Electron energy-loss spectroscopy of reconfigurable meta-atoms

PhD Thesis
Artyom Assadillayev

December 2021
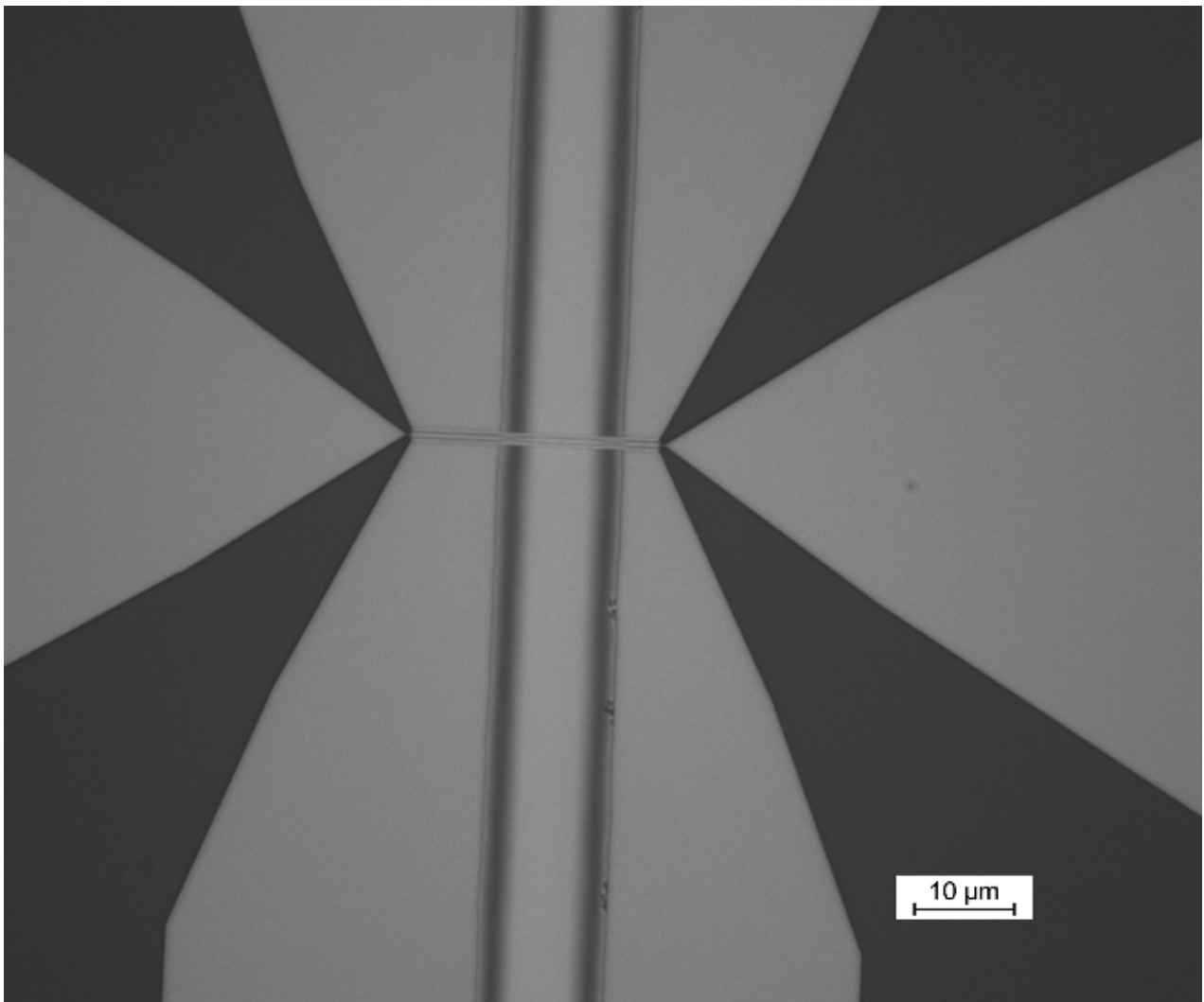
Front page image: Fabricated electromechanically actuated silicon beams.

Abstract

This thesis presents an investigation of optical meta-atoms and reconfigurable optical meta-atoms both via experiments and simulation. Electron energy-loss spectroscopy (EELS), an outstanding technique to characterize both near- and far-field optical properties, is extensively used in the thesis.

Optical meta-atoms based on silicon, boron phosphide, gold and nickel are considered in the thesis. We characterize the EELS response of Mie resonant silicon nanoparticles and place them on a thin gold film to efficiently launch surface plasmon polaritons. We excite the short-range surface plasmon polaritons of the thin metal film via electron beam and show its scattering by a silicon nanoparticle. Using cathodoluminescence spectroscopy at low acceleration voltages, we show the interference effects from the transition radiation. We introduce boron phosphide material as a promising candidate for UV photonics and demonstrate experimentally that boron phosphide nanoparticles can support Mie modes. We investigate the localised surface plasmon hybridization effect with another localised surface plasmon in gold dimers, and with the interband transition in nickel. We shift the hybridized plasmon modes in gold nanodimers into the visible and show experimentally an approach to fine-tune these resonances by a thin silver shell. For nickel nanoparticles, we demonstrate the interband hybridization effect with multipole order localised surface plasmons in individual particles.

We investigate reconfigurable meta-atoms based on two effects, thermo-optic effect and electromechanical tuning. We utilize the thermo-optic effect to spectrally tune the resonances in silicon nanoparticles in the visible range and show one linewidth tuning for the magnetic quadrupole mode. Then, using the electron energy-loss intensity maps, we demonstrate the tuning between the near-fields of different Mie modes. We fabricate silicon nanobeams separated by a gap and perform electromechanical tuning of the resonance associated with the coupled nanobeams.

Resumé

Denne afhandling præsenterer en undersøgelse af optiske metaatomer og rekonfigurerbare optiske metaatomer både via eksperimenter og simulering. Elektron energitab spektroskopi (EELS), en fremragende teknik til at karakterisere både nær- og fjernfelts optiske egenskaber, anvendes i stor udstrækning i afhandlingen.

Optiske metaatomer baseret på silicium, bor phosphid, guld og nikkel behandles i denne afhandling. Vi karakteriserer EELS signalet af silicium nanopartikler, som understøtter Mie resonanser, og placerer dem på en tynd guld film for effektivt at anslå overfladeplasmon polaritoner. Vi anslår kort-distance overfladeplasmon polaritonerne af den tynde metalfilm via elektronstrålen og viser dens spredning af en silicium nanopartikel. Ved hjælp af katodeluminescens spektroskopi ved lave accelerationsspændinger viser vi interferenseffekterne fra overgangsstrålingen. Vi introducerer bor phosphid som en lovende kandidat til UV fotonik og demonstrerer eksperimentelt, at bor phosphid nanopartikler kan understøtte Mie resonanser. Vi undersøger hybridiseringen af en lokaliseret overfladeplasmon med en anden lokaliseret overfladeplasmon i en guld dimer og med interbåndsovergangen i nikkel. Vi forskyder de hybridiserede plasmontilstande i guld nanodimer til det synlige spektralområde og viser eksperimentelt en tilgang til at finjustere disse resonanser med en tynd sølvskal. I nikkel nanopartikler demonstrerer vi interbånd hybridisering med lokaliserede overfladeplasmoner af forskellige multipolsordner i individuelle partikler.

Vi undersøger rekonfigurerbare metaatomer baseret på to effekter, den termooptiske effekt og elektromekanisk justering. Vi bruger den termooptiske effekt til spektralt at justere resonanserne i silicium nanopartikler i det synlige og demonstrerer en linjebreddejustering på én for den magnetiske quadrupol tilstand. Derefter demonstrerer vi ved hjælp af den rumlige fordeling af elektron energitab intensiteten at nærfelterne af forskellige Mie tilstande kan kontrolleres. Vi fremstiller silicium nanotråde adskilt med et gab og udfører elektromekanisk justering af resonansen forbundet med de koblede nanotråde.

Preface and acknowledgements

The work presented in this thesis has been carried out at the Department of Physics at the Technical University of Denmark during the period from September 2018 to December 2021. My initial department was the Department of Micro and Nanotechnology which was later rebranded and I moved to my current department. The PhD project has been supervised by Assoc. Prof. Søren Raza, Assoc. Prof. Tim Booth and Prof. Jakob Birkedal Wagner. During the project, I used the cleanroom and electron microscopy facilities at DTU Nanolab for nanofabrication and characterization of my samples.

I would like to thank my main supervisor Søren Raza for his support, useful discussions and a positive working environment, Tim Booth for his useful insights and personal help in some of the experiments, and Jakob Birkedal Wagner for his help in the initial steps of this PhD project. I could not imagine excelling in this PhD project without Søren Raza who introduced me to low-loss EELS characterization, helped me in simulations and assisted in the preparation of my first publication. I thank him for being available for discussions at any point in time even though the COVID limitations were in full strength during a large part of my PhD project.

I would like to thank the staff of the DTU Nanolab for their assistance in fabrication and equipment training in the cleanroom: Karen, Elena, Matthias, Jonas, Berit, Majken, and Patama. Also, I would like to thank Jens Kling for his invaluable help with electron microscopy resolving many issues with EELS equipment.

I am grateful to N. Asger Mortensen for a research stay opportunity at his group at the University of Southern Denmark. I thank Christian Wolff for his help, Martin Thomaschewski and Saskia Fiedler for their help with the experiments.

Additionally, I would like to thank our collaborators for our productive endeavours: Tatsuki Hinamoto, Minoru Fujii, Hiroshi Sugimoto, Mark L. Brongersma, Mark Kamper Svendsen, Daisuke Shima, Kristian S. Thygesen, P. Elli Stamatopoulou, Christos Tserkezis, Fatih Nadi Gür, Mihir Dass, Tim Liedl, Ihar Faniayeu, and Alexander Dmitriev.

Finally, I would like to thank my parents, Ruslan and Natalya, who are always there to support me.

<div align="right">

Artyom Assadillayev

December 2021

</div>

List of publications

Peer-reviewed journal publications

[**A**] **Assadillayev, A.**, Hinamoto, T., Fujii, M., Sugimoto, H., Brongersma, M. L., Raza, S. Plasmon launching and scattering by silicon nanoparticles. *ACS Photonics* **8**, 1582–1591 (2021).

[**B**] Fiedler, S., Stamatopoulou, P. E., **Assadillayev, A.**, Wolff, C., Sugimoto, H., Fujii, M., Mortensen, N. A., Raza, S., Tserkezis, C. Disentangling cathodoluminescence spectra in nanophotonics: particle eigenmodes vs transition radiation. *AarXiv preprint arXiv:* **2112.04931** (2021).

[**C**] Svendsen, M. K., Sugimoto, H., **Assadillayev, A.**, Shima, D., Fujii, M., Thygesen, K. S., Raza, S. Ultraviolet Mie resonances in computationally discovered boron phosphide nanoparticles. *AarXiv preprint arXiv:* **2112.13600** (2021).

[**D**] **Assadillayev, A.**, Hinamoto, T., Fujii, M., Sugimoto, H., Raza, S. Thermal near-field tuning of silicon Mie nanoparticles. *Nanophotonics* **10**, 4161–4169 (2021).

Conference Proceedings

[**E**] **Assadillayev, A.**, Hinamoto, T., Fujii, M., Sugimoto, H., Brongersma, M. L., Raza, S. Electron energy-loss spectrocopy of hybrid silicon-on-gold nanoresonators. Poster presented at META 2021, Warsaw, Poland.

x

Contents

1 Introduction

Optical meta-atoms are the elemental building blocks of optical metamaterials, the artificial materials with engineered optical properties which are not obtainable with natural media. The properties of these artificial atoms which can be effectively tailored by their shape, size or material composition combined with their particular arrangement in the metamaterial define the outcome functionality of the resulting devices, allowing such novel applications as optical cloaking [1, 2], optical metasurfaces [3, 4] or negative index of refraction [5]. The meta-atoms are even utilized separately as nanoresonators in nanoantennas [6, 7] or nonlinear optics [8, 9]. This broad range of possible applications dictates the need to tailor their properties even further. In most current applications, the meta-atoms and metamaterials are operated statically, i.e. their response cannot be actively modulated after their fabrication. However, there is a growing need to obtain actively modulated optical elements or reconfigurable meta-atoms, the response of which can be controlled with an external stimulus [10, 11].

The meta-atoms can be split into three large groups based on their material composition, high-refractive-index semiconductor or dielectric materials [6, 8], metals [7, 12] and hybrid dielectric-metal [13, 14, 15]. The first is characterized by a high refractive index with low non-radiative losses and support of multiple dielectric resonances, while the metals are characterized by low refractive indices with non-negligible radiative losses but they support free-electron oscillations, plasmons which can be coupled to light, leading to sub-wavelength plasmon polaritons. The hybrid meta-atoms combines the advantages of both material types. In this thesis, we consider several examples of meta-atoms of both material types, silicon and boron phosphide in the case of high-refractive-index materials, gold and nickel for metals, as well as we consider silicon on a thin gold layer hybrid system.

We focus our investigation on the reconfigurable meta-atoms based on the high-refractive-index materials. Various active tuning mechanisms of dielectric meta-atoms have already been demonstrated, including photothermal [16, 17], electromechanical [18, 19, 20], via photocarrier generation [21, 22], coupling to liquid crystals [23, 24, 25], using phase change materials [26, 27, 28, 29, 30], and through the thermo-optic effect [31, 32]. In this regard, we further explore two tuning mechanisms, through the thermo-optic effect and electromechanical tuning. In both cases, we utilise silicon as a material for dynamic tuning due to its combination of high refractive index, CMOS compatibility, high thermo-optic coefficient [33], and moderate Young's modulus [34].

There are several different experimental techniques to study the response of the meta-atoms with photon [35, 36] and electron excitation sources [37, 38, 39]. We broadly utilize electron energy-loss spectroscopy to study our optical metaatoms. This near-field technique which is performed with an electron excitation in a scanning transmission electron microscope provides excellent spatial and good energy resolution [40]. The near-field nature allows us to directly map the modes which are characteristic of a particular meta-atom that can be used to characterize its near-field properties. Moreover, since reconfigurable meta-atoms often involve a change in the geometry of the structure it allows us both to track these changes in real-time both spectrally and via imaging ultimately characterizing the stability of our actuation method. The ability to perform the actuation in the TEM microscope is enabled by a new generation of TEM holders which allow electrical biasing, changing chemical environment and heating.

1.1 Thesis outline

The outline of this thesis is as follows:

- **Chapter 2. Scattering by small particles**

  In this chapter, we perform a brief theoretical introduction to the scattering by small spherical particles, fundamental examples of optical meta-atoms, using the Mie theory. We show the main difference between the metal and high-refractive-index particles.

- **Chapter 3. Characterization Techniques**

  This chapter describes the characterization techniques which have been utilized for the fabricated structures. First, we describe film thickness measurement techniques, ellipsometry and profilometry. Then, we perform a general introduction to electron microscopy and consider the types of signals which can be excited by the electron beam. We introduce three spectroscopic electron techniques, electron energy loss spectroscopy (EELS), energy-dispersive X-ray spectroscopy and cathodoluminescence spectroscopy with a particular focus on EELS where we describe its simulation and experimental data post-processing steps.

- **Chapter 4. Meta-atoms**

  The chapter covers meta-atoms based on four materials, silicon, boron phosphide, gold and nickel. We perform EELS characterization of Mie resonances in silicon nanospheres. Then, we place them on a thin gold film and show plasmon launching and scattering effects. Using CL characterization at low acceleration voltages we show non-negligible transition radiation interference effects for the silicon spheres. We numerically discover a promising optical material in the UV range, boron phosphite and demonstrate its Mie resonances using EELS. Using the laser reshaping method, we propose a way to achieve spherical BP particles and experimentally demonstrate it. Then, we consider gold dimer geometry and demonstrate the shift of its resonances into the visible range, as well as demonstrate EELS profiles of symmetrical and antisymmetric modes supported by the dimer geometry. Using a thin silver shell, we suggest a way to fine-tune these resonances. In the case of nickel nanoparticles, we show the dependence of the bulk and surface electron losses on the electron beam position and demonstrate the coupling between different multipoles orders of localized surface plasmons and interband transition supported by the nickel.

- **Chapter 5. Reconfigurable meta-atoms**

  Here, we consider two active tuning mechanisms for silicon meta-atoms, thermal tuning and electromechanical tuning. We perform thermal tuning using the thermo-optic effect in silicon shifting the Mie resonances in resonance energies. Then, we show near-field tuning between different Mie modes utilizing the characteristic EELS maps. We perform electromechanical tuning of silicon nanobeams shifting the resonance associated with the coupled nanobeams in resonance energy.

- **Chapter 6. Conclusions and Outlook**

  We conclude the thesis in this chapter and present an outlook for future developments related to the investigation presented in this thesis.

2 Scattering by small particles

For a homogeneous isotropic spherical particle with a radius r illuminated by a plane wave polarized along x direction and propagating along z direction, the scattered electromagnetic field at any point in space $\mathbf{r}$ can be calculated as an expansion into vector spherical harmonics according to the Mie-Lorenz theory [41]:

$$\mathbf{E}_s(\mathbf{r}) = \sum_{n=1}^{\infty} E_n(ia_n\mathbf{N}_{eln}^{(3)}(k\mathbf{r}) - b_n\mathbf{M}_{oln}^{(3)}(k\mathbf{r}))$$

$$\mathbf{H}_s(\mathbf{r}) = \sqrt{\frac{\epsilon}{\mu}} \sum_{n=1}^{\infty} E_n(ib_n\mathbf{N}_{oln}^{(3)}(k\mathbf{r}) - a_n\mathbf{M}_{eln}^{(3)}(k\mathbf{r}))$$

(2.1)

where a_n and b_n are the Lorentz-Mie scattering coefficients of the n-th order electric and magnetic multipole terms; $\mathbf{N}_{eln}$, $\mathbf{M}_{oln}$, $\mathbf{N}_{oln}$, $\mathbf{M}_{eln}$ are vector spherical harmonics; k is the wavenumber of the surrounding medium; ϵ and μ are the relative electric permittivity and the relative magnetic permeability of the sphere respectively; $E_n = i^n E_0(2n+1)/n(n+1)$ where E_0 is the amplitude of the incident wave.

Assuming the same relative magnetic permeability inside and outside the particle, the Lorentz-Mie scattering coefficient are given by the following expressions:

$$a_n = \frac{m\psi_n(mx)\psi_n'(x) - \psi_n(x)\psi_n'(mx)}{m\psi_n(mx)\xi_n'(x) - \xi_n(x)\psi_n'(mx)}$$

$$b_n = \frac{\psi_n(mx)\psi_n'(x) - m\psi_n(x)\psi_n'(mx)}{\psi_n(mx)\xi_n'(x) - m\xi_n(x)\psi_n'(mx)}$$

(2.2)

where $m = N_1/N$ is the complex relative refractive index with N_1 and N being the complex refractive indices of the particle and surrounding medium respectively; $x = 2\pi Na/\lambda$ is the size parameter with a being the particle radius and λ being the wavelength of incident light; ψ_n and ξ_n are the spherical Ricatti-Bessel functions.

The extinction cross-section of a sphere is given by the following expression:

$$C_{ext} = \frac{2\pi}{k^2} \sum_{n=1}^{\infty} (2n+1)Re(a_n + b_n)$$

(2.3)

Figure 2.1 shows the extinction cross-section from two nanoparticles made of two typical optical materials, high-refractive-index silicon and metal gold for the same particle radius of $a = 75$nm. The cross-section is decomposed to the contributions from first two multipole orders, $n = 1$ dipole and $n = 2$ quadrupoles. The resonances of the silicon nanoparticles are confined inside the particle volume and they are called Mie resonances while the resonances of the gold particles are confined on the particle surface and are called localised surface plasmon resonances due to the presence of electron oscillations on the metal surface. In the case of a silicon nanoparticle, we observe peaks from both magnetic and electric contributions, while gold only supports electric multipole resonances
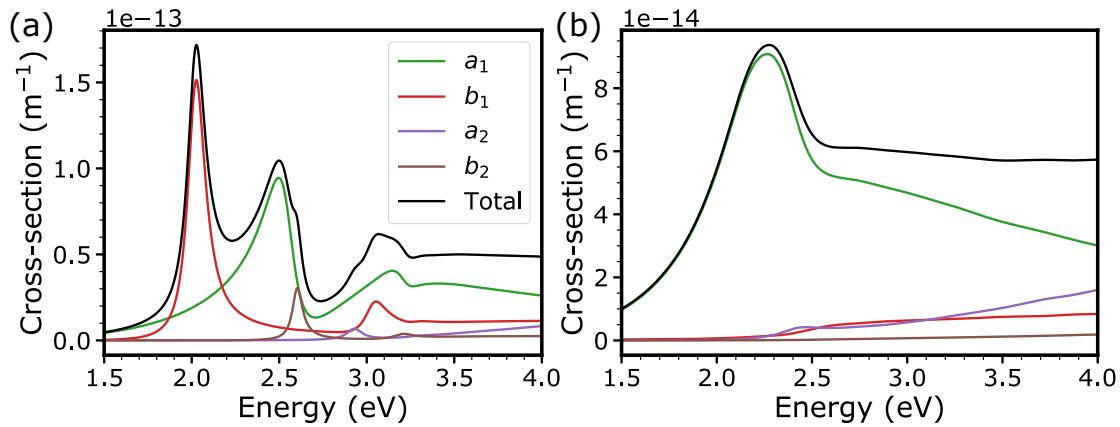
Figure 2.1: Extinction cross-section of spherical particles with $r = 75$ nm for (a) silicon and (b) gold.

which are significantly broader due to optical damping present in metals. This simple example shows that typical spherical metal nanoparticles do not support magnetic resonances while typical high-refractive-index nanoparticles have resonances of both types, and, for the same particle radius, the typical spherical metal nanoparticles support less multipole contributions. The support of different multipole order resonances, as well as both magnetic and electric resonances in high-refractive-index particles, allows them to be efficiently utilized in multimode engineering strategies giving rise to new resonance types such as Huygen dipole, Janus dipole, circular dipole or anapole modes [42] while typical metal particles lack these features.

3 Characterization Techniques

This chapter describes the characterization techniques which are used throughout the thesis. We use ellipsometry to determine the thickness of thin layers (from 10 nm up to 2 um) in the intermediate or final steps of the fabrication process. The thickness of thicker layers is quantified by profilometry. We use electron microscopy for both visualization and characterization of the samples. We mainly characterize the spectral response of the samples using electron energy-loss spectroscopy (EELS) in a scanning transmission electron microscope (STEM). In some studies, we use cathodoluminescence spectroscopy in a scanning electron microscope as an alternative to EELS. Lastly, we use energy-dispersive X-ray spectroscopy in a STEM microscope to observe the compositional changes in some of the samples.

3.1 Film thickness

3.1.1 Ellipsometry

Ellipsometry is an optical technique that measures the change in the polarization state of light upon reflection or transmission from a sample. We use ellipsometry in a reflection setup to identify the thickness of fabricated thin layers. A typical setup consists of a light source, the light from the sources passes through a polarization state generator (PSG) and reaches the sample. Then, the light which is reflected from the sample goes through a polarization state detector (PSD) and reaches a detector. PSG and PSD are a set of polarizers, retarders or photoelectric modulators which change the polarization state of the light. The resulting electromagnetic wave is decomposed into s- and p-polarized components and the complex relative amplitude attenuation is given by [43]:

$$\rho = \frac{r_s}{r_p} = \tan \psi \mathrm{e}^{i\Delta} \tag{3.1}$$

where r_s and r_p are the complex amplitudes of s and p components respectively, $\tan \psi$ is relative amplitude attenuation, Δ is a relative phase change.

The $\tan \psi$ and Δ are measured for several angles of incidence and fitted to a theoretical model to find the optical constants and thicknesses of the thin layers. As such, ellipsometry is an indirect technique to measure the thickness, however, combined with the appropriate model of the structure and well-understood nature of the light reflection from surfaces, it gives quite precise results [44].

3.1.2 Profilometry

Profilometry is an experimental technique that uses a diamond stylus to obtain topographical data of the sample's surface. To obtain the data, a stylus is lowered in contact with a sample surface and the contact force during the scanning is kept constant. We use this technique to measure the thickness of layers for which not enough light is collected in ellipsometry or to check the etch depth during the fabrication of TEM membranes. The thickness of the layers is measured by measuring the step between the area with and without the layer of interest. We use Dektak 150 surface profiler with a large vertical range of up to 1 mm and a resolution of not less than 16 nm.

3.2 Electron microscopy

Electron microscopy is a technique that uses the interaction of electrons with matter to obtain high-resolution images of a sample. The high resolution of electron microscopy stems from the significantly smaller wavelength of an electron in comparison to the optical microscopy, at an acceleration voltage of 300 kV the electron wavelength is around 1 pm. This, however, comes with a disadvantage of high vacuum requirement to ensure low interaction with air molecules and possible material degradation due to beam-induced damage of the sample [45].

Electron microscopy benefits from various signals generated from the interaction of the swift electrons with a sample which are illustrated in Figure 3.1. For the thin samples of a few hundred nanometers thickness, we can detect the electrons which pass through the sample, the transmitted electron beam which undergoes no scattering events, and elastically and inelastically scattered electrons. Elastically scattered electrons can change their direction, but do not lose their energy, while inelastic scattering involves both changes in direction and energy. These electrons are used to obtain transmission (TEM) or scanning transmission electron microscopy (STEM) images of the sample. In the former case, the image is a projection of an electron beam onto the sample, while the latter technique utilizes tightly focused electron beams to perform raster scanning of the sample. The spectroscopic data of these electrons can also be utilized in electron energy-loss spectroscopy (EELS) to obtain a spectroscopic response of the sample, i.e. the dependence of the energy loss and electron count. It should be noted that for sufficiently thick samples, these signals cannot be detected since the electrons lose all their energy in the bulk of the sample.
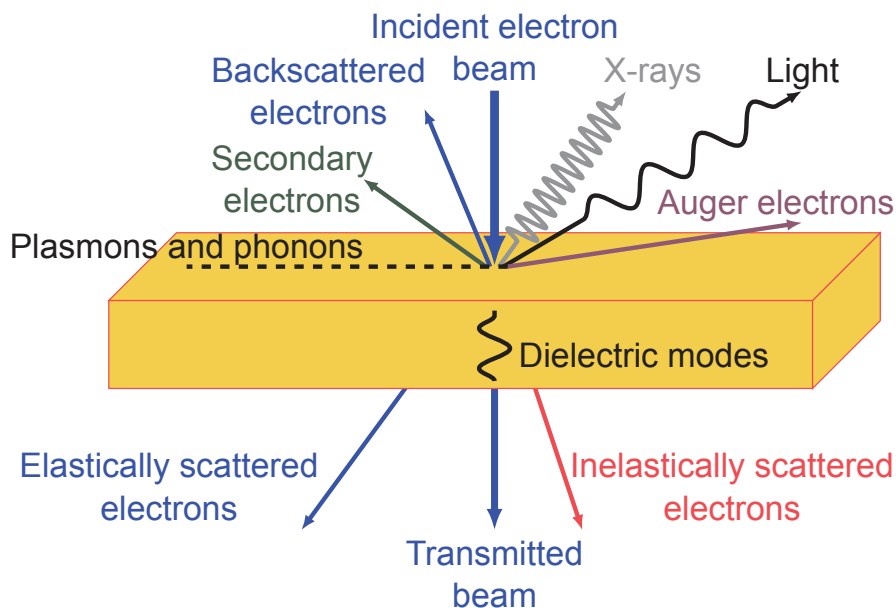
Figure 3.1: Interaction of an incident electron beam with a thin sample. The interaction of the incident beam with a thin sample results in the transmitted, backscattered, elastically and inelastically scattered electrons. The inelastic scattering can result in multiple relaxation processes: excitation of plasmons, phonons, dielectric modes, generation of electromagnetic radiation (X-rays, UV and visible light), secondary and Auger electrons. The respective signals for three electron spectroscopy techniques used in the thesis: elastically and inelastically scattered electrons for EELS, UV and visible radiation for CL, X-rays for EDX.

Some elastically scattered electrons can undergo a reflection from the sample and result in the backscattered electrons, while the inelastic scattering of electrons transfers some energy to the sample and this can result in multiple kinds of relaxation processes: secondary electrons, Auger electrons, electromagnetic radiation (X-rays, visible or UV light), excitation of dielectric resonances, plasmon and phonon generation. The backscattered, secondary and Auger electrons are used in scanning electron microscopy (SEM) to obtain high-resolution images of the sample. The main difference between the secondary and Auger electrons is that the secondary electrons are generated by the process of knocking out the electrons from their shell positions by incident electrons, while Auger electrons are the results of the atom relaxation processes after the generation of secondary electrons. Depending on the energy of the generated secondary electron, there can be multiple relaxation processes where the electron in the higher energy shell relaxes to the lower energy shell producing the excess energy. This excess energy can result in the generation of Auger electrons or electromagnetic radiation which characterizes the shell transitions in the atom.

It should also be noted that electromagnetic radiation can be generated via transition [46] or Cherenkov radiation [47]. Transition radiation is electromagnetic radiation when a charged particle passes an inhomogeneous medium, and Cherenkov radiation is radiation when a charged particle travels through a dielectric medium at a speed greater than the phase velocity. These combined radiation processes due to atom relaxation, Cherenkov and transition radiation, can lie in different wavelength ranges: X-rays, UV or visible light. The X-rays can be detected via energy-dispersive X-ray spectroscopy (EDX), and visible or UV light in cathodoluminescence spectroscopy (CL).

Excitation of plasmons, phonons or dielectric modes by the electron beam can be measured via the scattered electrons using EELS. CL can also be used for this purpose if the modes can emit the electromagnetic radiation in the UV or visible range, or via some outcoupling mechanism for the plasmon modes to emit this radiation.

In the current thesis, three electron spectroscopic techniques are used for sample characterization: EELS, EDX and CL with a particular focus on EELS characterization. These techniques are considered in the next respective sections.

3.3   Electron energy-loss spectroscopy

EELS is an experimental technique that measures the loss of kinetic energy of the electron beam which traverses a thin sample. The typical EELS spectrum consists of a high-intensity zero-loss peak that incorporates transmitted and elastically scattered electrons, a low-loss and core-loss regions. The low-loss region lies at energies up to a few tens of electronvolts containing peaks due to excitation of phonons [48, 49], plasmons [50, 51, 52], dielectric modes [53, 54] and slow secondary electrons [55, 56] where the latter is generated through the process of knocking out loosely bound conduction and valence band secondary electrons. The core-loss region lies at a few hundred electronvolts energies containing the peaks due to excitation of the fast secondary electrons characterizing the inner shell transitions of the element. In our work, we probe the low-loss energy range of different plasmonic and dielectric structures to characterize their optical modes.

A typical low-loss EELS spectrum from a dielectric nanostructure is presented in Figure 3.2. We probe a silicon nanocylinder located on a silicon nitride membrane. The highest intensity feature is a zero-loss (ZL) peak. It has a finite width which characterizes the energy resolution of the experimental setup. A signal of interest is typically hundreds

of times smaller, and for this particular example lies in the energy range between 1 and 3 eV. Multiple peaks can be observed in this spectral range which are the results of excitation of the characteristic Mie modes of this particular nanostructure. It should be noted that the low energy phonon modes (10-100 meV) are not visible due to the limited resolution of our EELS setup.
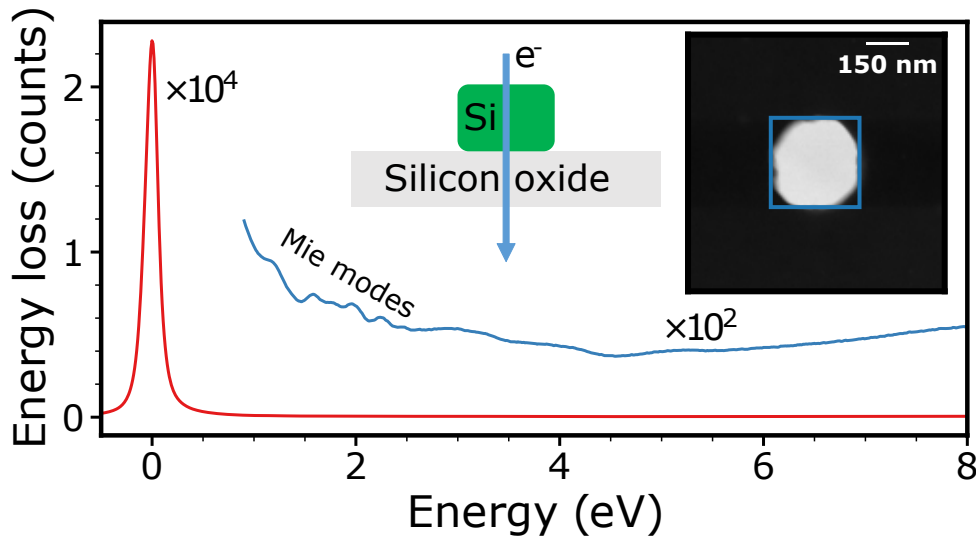
Figure 3.2: Typical low-loss EELS spectrum. The spectrum is taken from a cylindrical silicon nanoparticle with $r = 158$ nm and $h = 200$ nm on a 200 nm silicon oxide membrane. The spectrum is integrated in the square region indicated on the STEM image inset. The side view of the structure is demonstrated in the schematic inset.

3.3.1 Experimental details

We perform EELS in a monochromated and aberration-corrected FEI Titan operated in STEM mode at an acceleration voltage of 300 kV. The high acceleration voltage allows the electron beam to penetrate the samples up to approximately 1000 nm [57]. This thickness is further limited by multiple scattering events, which in the case of metal structures can be as small as around 150 nm to avoid multiple plasmon scattering [57]. The final applicable thickness changes from the particular sample composition and geometry, and microscope operating conditions, such as acceleration voltage or collection angle.

A typical STEM EELS system schematic is presented in Figure 3.3. The system consists of an electron gun, which is a field emission gun emitting electrons with an energy spread of around 0.4 eV (as measured by the full-width at half-maximum of the zero-loss peak). The gun is directly followed by a monochromator, which further improves the energy resolution. The monochromator system in our FEI Titan is a double Wien filter [58] and can provide an energy resolution up to 0.08 eV. The double Wien filter disperses the energy of the electron beam, and the aperture selects the electrons with a particular energy. Then, the electrons are projected onto a thin sample by a set of condenser and objective lenses. The beam is raster-scanned by a set of deflection coils. Projective lenses focus the electrons that are scattered at high angles onto an annular detector to form a STEM image of a sample, while the electron scattered at low angles are projected onto a dispersive prism. The dispersive prism is a magnetic prism that disperses and focuses the interacted beam onto a CCD detector to obtain an EELS spectrum.
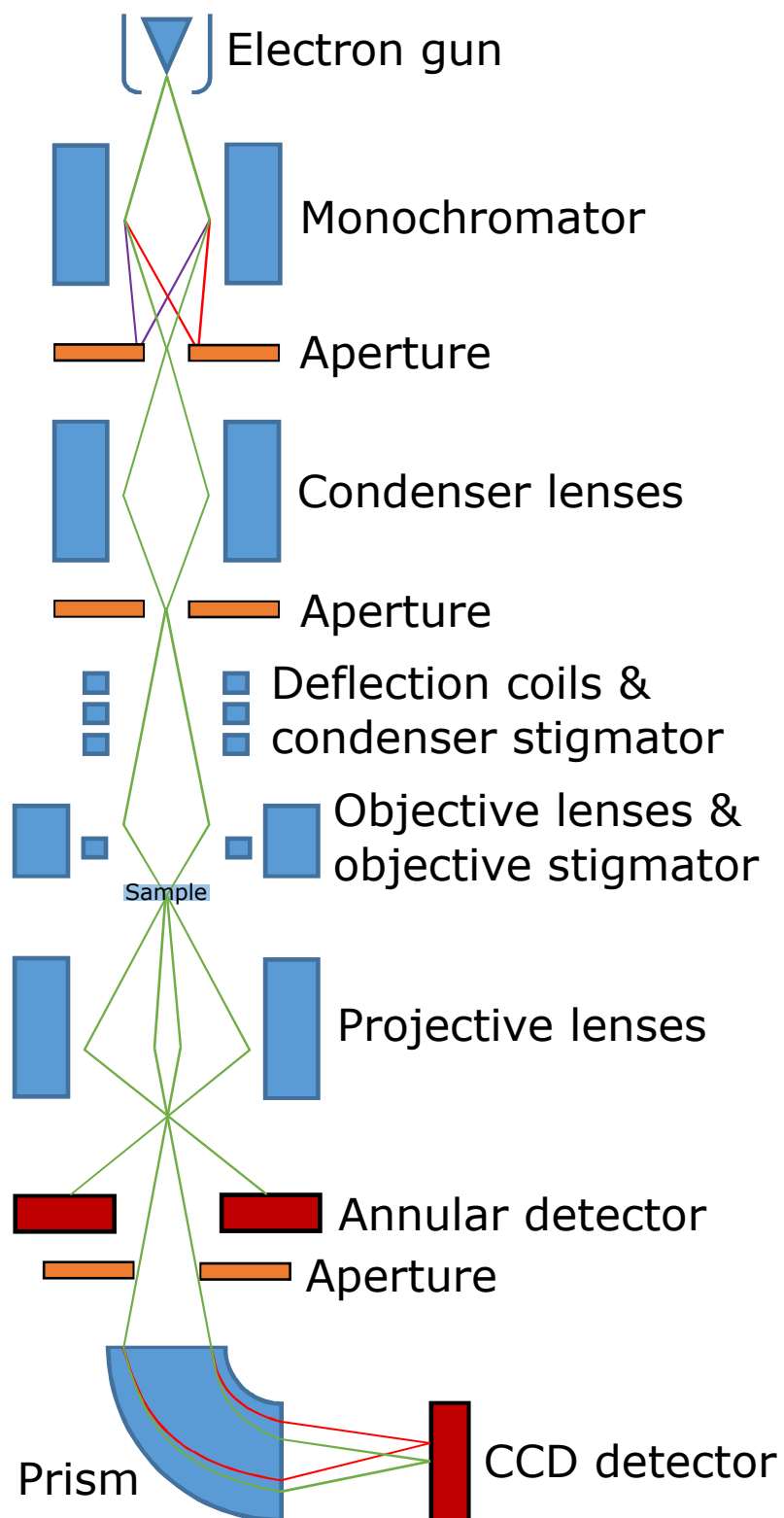
Figure 3.3: Schematic of a STEM EELS system.

The spatial resolution is typically limited by the aberrations present in the electron beam. The condenser and objective stigmators assist in improving the spatial resolution. The stigmators are quadrupole lenses that typically correct the astigmatism of the system due to imperfections in the other lenses. In FEI Titan, there are multiple condenser stigmators that also correct for spherical aberrations and can provide the spatial resolution ~ 0.5 nm with an excited monochromator.

3.3.2 Experimental data post-processing: Zero-loss

To improve the signal to noise ratio and highlight the resonances in optical nanostructures obtained with our system, we employ several manipulations steps with a low-loss EELS spectrum:

1. Zero-loss centring
2. Zero-loss normalization
3. Zero-loss deconvolution

Zero-loss centring is a procedure of shifting all EELS spectra for different beam scan positions in energy to centre at the signal maximum and shifting this maximum to 0 eV which is in case of the low loss spectrum is zero loss. This is required to correct for the energy drift during the EELS acquisition, which can be unpredictable drifts due to energy changes in the beam of electrons or predictable drifts such as drifts appearing during the scanning with the electron probe. For our setup, the main contributor to the drift is the latter which is typical for the microscopes without double deflection coils. This energy drift is the result of the change in the entrance angle into the EELS spectrometer as the beam
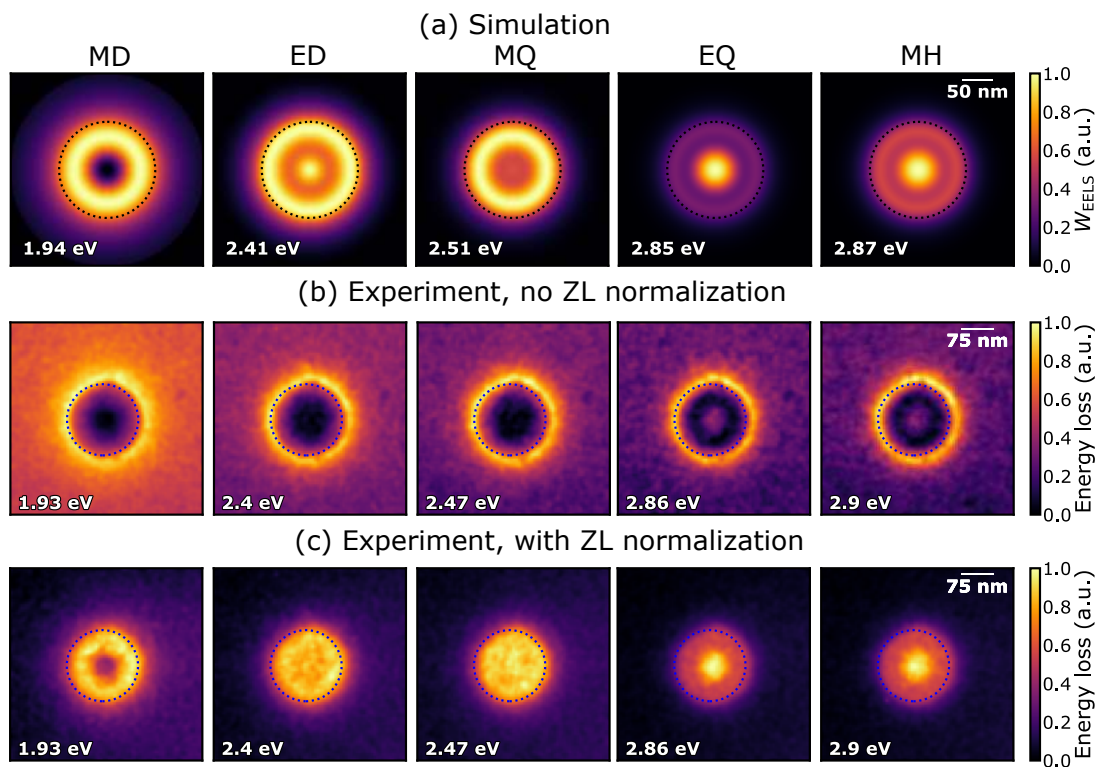
Figure 3.4: EELS maps of different Mie modes for a silicon nanosphere with radius $r = 80$ nm on top of a 40 nm silicon nitride membrane. (a) COMSOL simulation of EELS maps. (b) Experimental EELS maps without zero-loss normalization. (c) Experimental EELS maps with zero-loss normalization.

scans the sample [59]. The typical value of the energy drift for the 250 by 250 nm scan is a 1.5 eV energy difference in the zero-loss maximum position between the opposite spatial edge points of the EELS map. We align the zero-loss peak using python hyperspy implementation which performs the alignment with subpixel energy resolution.

Zero-loss normalization is the process of normalizing the zero loss to the same maximum for all spatial points in the EELS map. It is typically required to account for the thickness dependence of the EELS signal. First, we show the simulated EELS maps for a typical silicon nanosphere in Figure 3.4(a) (For simulation method, check Section 3.3.4). Then, we plot zero-loss centred experimental EELS maps in Figure 3.4(b) and compare it with the simulation. It can be seen that the simulation does not account for the thickness dependence of the EELS signal and holds only the probabilistic nature of exciting the Mie modes in the silicon nanoparticle. We perform zero-loss normalization in Figure 3.4(c) to remove the thickness dependence and observe a close match between the simulation and experiment.

Zero-loss deconvolution is the process of reduction in the energy blurring/spreading of the resulting spectrum affected by the limited resolution of the system, i.e. limitations and fluctuations in the EELS system. The following equations show how the true data is affected by the response of the EELS system [60]:

$$I(i) = \sum_{j} P(i - j)O(j) \tag{3.2}$$
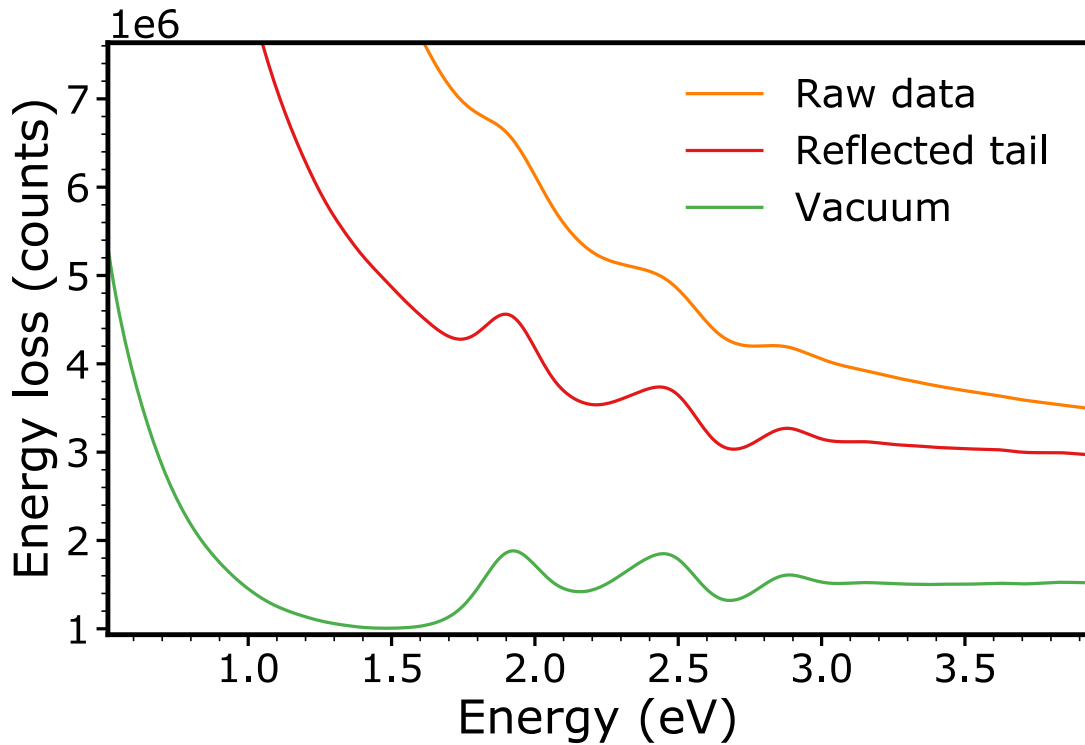
Figure 3.5: Zero-loss deconvolution. ZL centered and normalized EELS data: raw data (orange), RL deconvoluted with two different PSF inputs, reflected tail method (red) and the zero-loss obtained in vaccum (green).

where $I(i)$ is the experimentally obtained EELS spectrum, $P(i - j)$ is the point spread function (PSF) of the EELS setup which describes how the point representing specific energy spreads over multiple channels of the CCD detector, $O(j)$ is the original unblurred spectrum.

Richardson-Lucy (RL) deconvolution approach can be used to deconvolute the response of the system and significantly sharpen the features of interest. We show the results of this approach in Figure 3.5. We compare the raw ZL centred and normalized data with its deconvolutions using two types of input as the PSF. We fix the deconvolution threshold parameter for both cases at 0.01 [61]. First, we use the reflected tail approach [62, 63] where the ZL function is generated as the mirror to the negative range of the actual EELS measured data in each spatial point, then this artificially generated signal is fitted with a combination of Lorentzian and Gaussian functions in each spatial point of the EELS measurement and used as the PSF to deconvolute with the actual EELS signal at the same spatial positions. We see that a significant part of the original ZL is still present in the reflected tail approach. Then, we show a second approach where the ZL peak measured in vacuum [64], i.e. with the sample removed from the path of the electron beam in the STEM EELS system, is used as a PSF for the deconvolution process. We can see a significant improvement in the resulting spectrum using this approach. In conclusion, it can be stated that the use of the ZL measured in a vacuum is a more precise and physically correct approach to approach the deconvolution process. The reflected tail approach can be used for symmetric ZL peaks response, which in the general case is not true for the EELS system due to asymmetries present in the original zero-loss or PSF of the system.

3.3.3 Experimental data post-processing: Spectra and maps

We perform further post-processing for the EELS spectra and maps. For the EELS spectra, we typically integrate the signal around some locations of the structure to increase the signal-to-noise ratio (Figure 3.2). The typical integration regions used throughout the thesis are square, circle and annulus. An example with circle and annulus-shaped integration regions can be found in Figure 4.3. The integration is followed by spectra smoothing with a Gaussian function ($\sigma = 0.03$ eV).

The EELS maps are obtained by summing the deconvoluted EELS data in a spectral window of 0.02 eV width centred at the resonance energies. To improve the signal-to-noise ratio, the maps are spatially binned, reducing the effective number of pixels by a factor of 2 in each row and column, i.e., a factor of 4 in total. Afterwards, a Gaussian filter with $\sigma = 0.8$ pixels is applied to smooth the image. For spherical geometries, we perform integration of the maps along an azimuth angle at the coordinates located at the same distance from the centre of the geometry. Figure 3.6 shows typical changes in the EELS maps after each step of the process. The result of the post-processing can be directly compared with the simulation in Figure 3.4(a). It demonstrates that with each step, we achieve closer correspondence of the experimental data with the simulation as a consequence of the improved signal-to-noise ratio.

3.3.4 Numerical simulation

We express the energy loss as the mean energy dissipation within a volume V [65]:

$$W_{\text{EELS}}(\omega) = -\frac{1}{2} \int_V \text{Re}\left[\mathbf{j}^*(\mathbf{r}, \omega) \cdot \mathbf{E}(\mathbf{r}, \omega)\right] dV \tag{3.3}$$

where $\mathbf{j}(\mathbf{r}, \omega)$ and $\mathbf{E}(\mathbf{r}, \omega)$ is the current density and electric field in frequency domain.
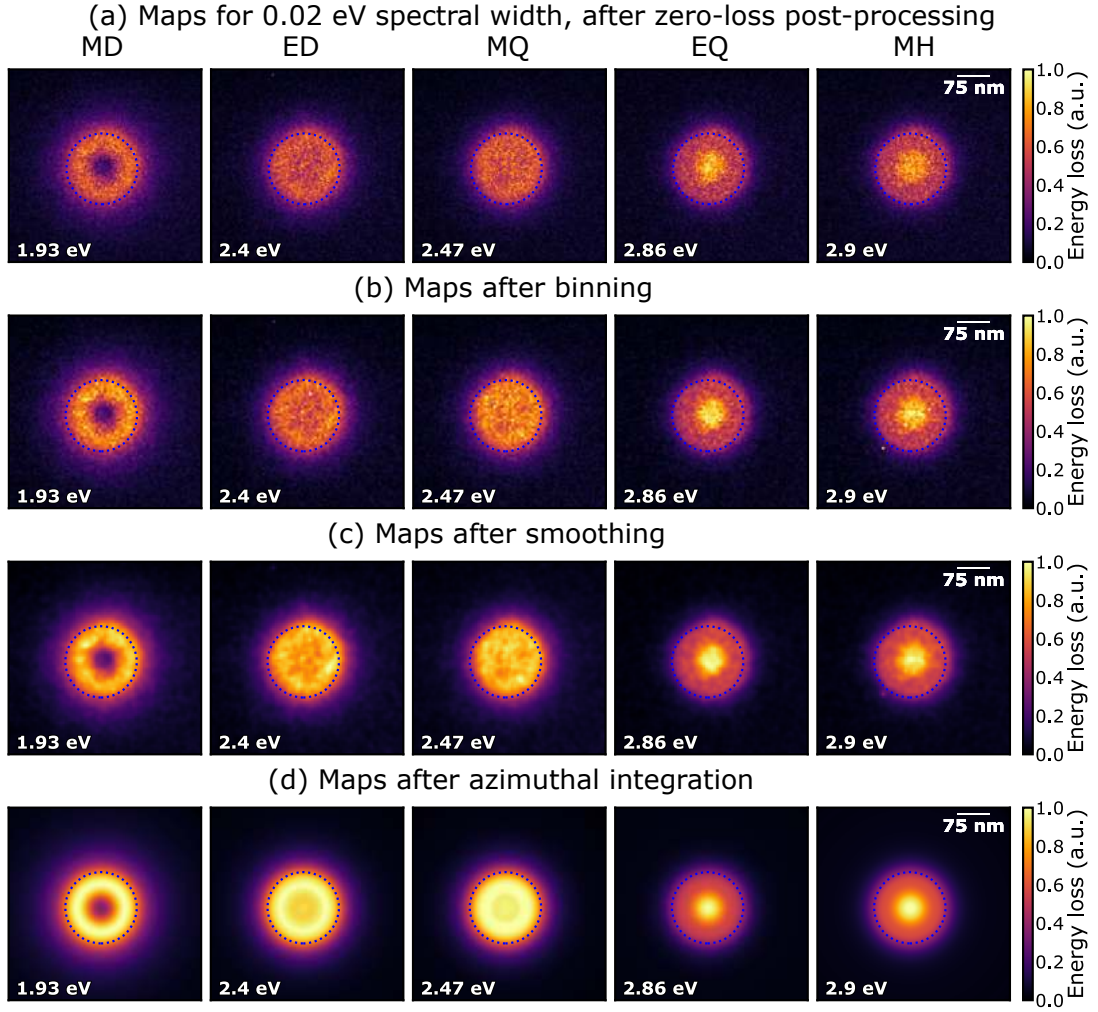
Figure 3.6: Post-processing of EELS maps.

In the case of an electron beam that propagates along z-direction and generates an induced electric field by dielectric or plasmonic structure on itself, we can simplify the energy loss to one-dimensional integral:

$$W_{\text{EELS}}(\omega) = \frac{1}{2} \int_z \text{Re} \left[\mathbf{j}^*(\mathbf{r_e}, z, \omega) \cdot \mathbf{E}^{\text{ind}}(\mathbf{r_e}, z, \omega) \right] dz. \tag{3.4}$$

Where $\mathbf{j}(\mathbf{r_e}, z, \omega) = -e\hat{\mathbf{z}}\delta(\mathbf{r} - \mathbf{r_e})e^{i\omega z/v}$ is the frequency domain representation of the current density of an electron moving at a speed v along the z-direction, and $\mathbf{r_e} = (x_e, y_e)$ is the in-plane position of the electron beam.

We solve the Maxwell's equations in COMSOL Multiphysics using edge current boundary condition for the electron beam and obtain the induced field as the difference between the electric fields with and without the structure $\mathbf{E}_e^{\text{ind}}(\mathbf{r}_e, z, \omega) = \mathbf{E}_e^{\text{air}}(\mathbf{r}_e, z, \omega) - \mathbf{E}_e^{\text{str}}(\mathbf{r}_e, z, \omega)$

The energy-loss W_{EELS} is directly related to the energy-loss probability Γ_{EELS} [40] where the electron beam is considered as a charged particle moving in time and the loss probability is expressed as a force exerted by the induced electric field onto the electron. Both approaches are reduced to calculating the induced electric field along the electron trajec-

tory.

3.4 Energy-dispersive X-ray spectroscopy

We perform energy-dispersive X-ray spectroscopy (EDX) characterization in the same FEI Titan system as the EELS characterization. To increase the EDX signal, we do not excite the monochromator which leads to higher electron currents. The X-rays produced by the interaction of the electron beam with a sample are collected by an X-ray detector located above the sample.

The collected X-rays characterize the inner shell transitions inside the sample, allowing to perform elemental analysis of the sample based on well-known and unique inner shell transitions for different chemical elements. A typical EDX spectrum is presented in Figure 3.7. We measure the EDX spectrum from a silicon nanoparticle on top of a silicon nitride membrane. Using the tabulated values of characteristic energy transitions of N, O, Si, P elements we assign the peaks to the corresponding elements and identify the chemical composition of the sample.
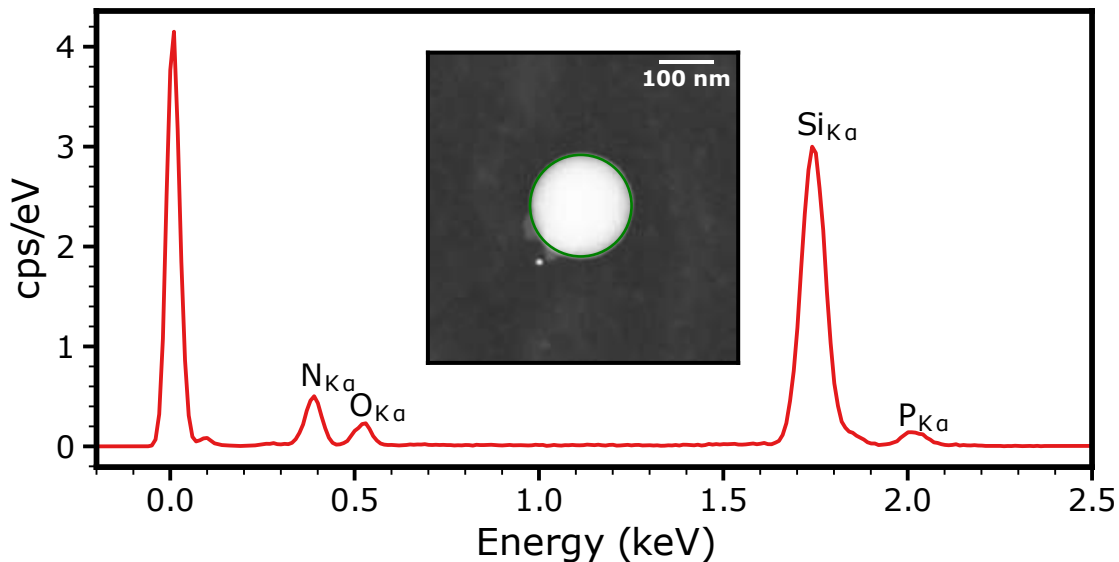
Figure 3.7: Typical EDX spectrum from a silicon nanoparticle on top of a silicon nitride membrane. The inset is a STEM image of the nanoparticle, where the green circular region represents the integration region for the EDX signal.

3.5 Cathodoluminescence spectroscopy

We perform CL characterization in a Tescan Mira3 scanning-electron microscope (SEM) operated at an acceleration voltage up to 30 kV. A typical schematic of an SEM CL system is presented in Figure 3.8. The system features a Schottky emitter as an electron source, which is a field-assisted thermionic source of electrons. The electron beam is projected onto a thin sample by a set of condenser and objective lenses and raster-scanned by a set of deflection coils. The interaction of the electron beam with the sample results in the emission of multiple signals. In particular, an SEM image is formed by collecting the secondary electrons, while the CL signal is focused by an ellipsoidal mirror onto a CL detector to obtain a spectroscopic response of a sample.
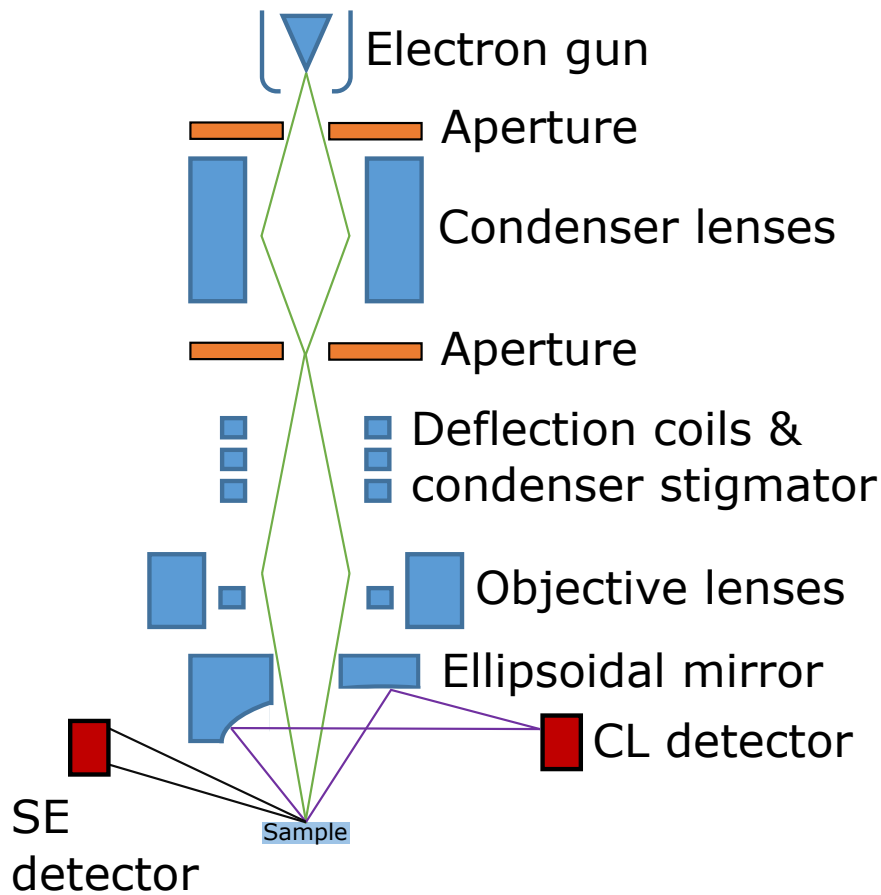
Figure 3.8: Schematic of a SEM CL system.

The spatial resolution in the SEM system is typically limited by the size of the electron spot, which in turn depends on the acceleration voltage and the electro-optical system that produces the scanning beam, and further electron spreading in the material, the interaction volume of the electrons. For the typical 30 kV scanning voltage, the electron wavelength is very small in comparison to the effects of the electro-optical system. The typical spot size is ~ 8 nm for the beam currents of 1.7 nA.

The electron spreading in the material is material and voltage dependant and at 30 kV voltage does not have a significant effect. Figure 3.9 shows a Monte-Carlo simulation of the beam scattering events inside the 150 nm silicon on a 30 nm silicon nitride two-layer system. It can be seen that the interaction volume of the electrons with the sample does not spread significantly in comparison to the entrance beam size. For the SEM images where SE are detected, the SE which reach the detector are typically in the first 100 nm sample thickness, so the effect of spreading is even less significant. However, the CL signal typically escapes the structure from the depth of several micrometres, so the spatial resolution should be less than for SEM imaging and should be affected by the whole interaction volume.
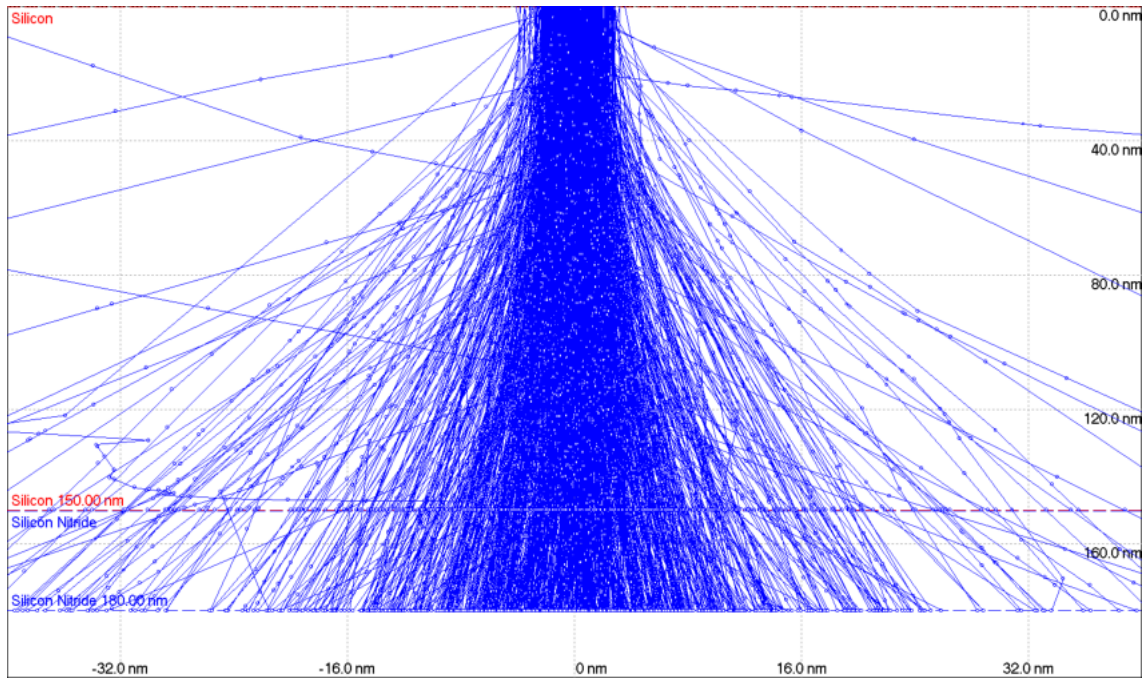
Figure 3.9: Monte-Carlo simulation of electron trajectory in 150 nm silicon - 30 nm silicon nitride two-layer system. The acceleration voltage is 30 kV. The electron spread is simulated in the Monte Carlo program CASINO [66].

4 Meta-atoms

This chapter is dedicated to the elemental building blocks of the reconfigurable optical systems: the meta-atoms. We consider different optical nanostructures based on two main groups of optical materials, high-refractive-index materials and metals.

We consider nanoparticles based on two high-refractive-index materials, silicon and boron phosphide. In the case of silicon nanoparticles, we characterize their EELS response to identify and map their Mie resonances and employ them in a combination with a 10 nm thin gold layer to launch and scatter surface plasmon polaritons. Moreover, we perform their CL characterization and show resonant interference effects from the transition radiation coming as a result of comparatively low acceleration voltages.

Then, we investigate the nanoparticles based on the BP material, a material that has the potential to be utilized in UV nanophotonic devices. Using EELS we demonstrate that BP nanoparticles with a random shape support the UV Mie resonances. We suggest an approach to obtain nanoparticles with a more defined spherical shape and perform its experimental validation.

The next two sections deal with two metal meta-atoms, namely gold nanodimers and nickel nanospheres. We utilize both structures to achieve the hybridization between two localized surface plasmons in the case of gold and hybridization between a localized surface plasmon and interband transition in the case of nickel. For the gold nanostructures, we propose a way to fine-tune the resonances via utilizing a thin silver shell, while for the nickel nanostructures we show the hybridization between localised surface plasmon of different multipoles orders and the interband transitions.

4.1 Silicon nanoparticles

The work presented in this section is based on Paper A and B.

4.1.1 Introduction

Dielectric meta-atoms have high refractive index and low absorption, and support multiple possible optical resonances such as Mie resonances [36, 67], Fano resonances [68, 69], bound states in the continuum [70]. They have been utilized in various applications such as dielectric nanoantennas [6, 71, 72, 73], resonant nonlinear optics [74, 75, 76] and metasurfaces [77, 78, 79, 80]. In this section, we consider the Mie resonant nanoparticles which have both strong magnetic and electric response and can support modes in the broad wavelength range based on silicon material.

The Mie resonant silicon nanoparticles have been studied by several optical techniques with light excitation [35, 36], as well as an optical technique with electron excitation, cathodoluminescence [37], and only recently, there have been reports on their EELS response in Ref. [38, 39] and our work in Paper A. Ref. [38, 39] deal with disk, triangular or rectangular geometries while we consider the response of silicon nanospheres which are symmetrical in all three dimensions providing the most simple, yet representative, picture of dielectric Mie modes. Using the near-field nature of EELS, we experimentally map and differentiate between spectrally close Mie resonances of silicon nanospheres, as well as track their resonance energy - particle size dependence in a broad spectral range.

4.1.2 Fabrication

We can separate the fabrication of the samples for characterization of silicon nanoparticles properties into three main steps: fabrication of the TEM membranes, fabrication of the silicon nanoparticles and deposition of the nanoparticles on the TEM membranes. The samples which are used to characterize launching and scattering of SPPs with silicon nanoparticles have an additional step of gold deposition which is mentioned in the fabrication of TEM membranes.

TEM membranes. We deposit a low-stress silicon-rich nitride layer on top of an n-type (phosphor) $\langle 100 \rangle$ double-side polished silicon wafer (350 μm thickness) by low-pressure chemical vapour deposition (LPCVD). The resulting thickness determined by ellipsometry is around 33 nm, with a 1 nm native silicon oxide below the nitride. Using UV lithography, we create a photoresist pattern for the membrane windows on one side of the wafer. Afterwards, we dry etch the silicon nitride using the lithographic pattern. The dry etching is followed by a photoresist strip, wet KOH etching of the silicon, and water:HCl 4:1 cleaning. The water:HCl etching is required to remove the iron oxide particles depositing onto the surface of the sample during KOH etching [81].

For the samples with a thin metal layer, this is followed by a step of gold layer deposition. The wafers are submerged into a solution of 95% isopropanol, 2.5% water and 2.5% APTMS for 3 hours to achieve a 1 nm APTMS layer, followed by two steps of isopropanol-water rinsing. Sputter deposition is used to produce a 10 nm thick gold layer. Both AFM and ellipsometry confirm the thickness of the gold layer to be 9-10 nm. The root mean squared roughness of the gold surface as measured by AFM is around 1.5 nm. The method produces high-quality metal films with negligible influence on the APTMS layer on the SPP propagation [82].

Afterwards, we cover the wafer with a protective layer of a photoresist. In the case of the samples with silicon nanoparticles only, we introduce grooves along the lattice planes with a high power laser and manually break the wafer into smaller TEM chips. For the samples with a thin metal film, we perform saw dicing through the whole wafer. The laser cutting is not performed on the gold samples due to damage introduced to the thin gold layer by the procedure.

The detailed process flow for both samples types can be found in Table A.1.

Fabrication of silicon nanoparticles. The crystalline silicon nanoparticles of spherical shape are produced by thermal annealing of silicon suboxide (SiO_x) and extraction into methanol by our collaborators, the procedure is described in Ref. [73].

Deposition of silicon nanoparticles. We remove the protective photoresist and clean the TEM membranes in acetone followed by isopropanol solutions for 10 minutes in both steps. Then, we ash the chips without the gold layer in oxygen plasma for 5 minutes. The samples with a thin gold layer are not ashed since the process introduces damage to the gold layer. The methanol solution with nanoparticles in a vial is submerged into an ultrasound bath for 5 minutes to disperse the particles. We drop cast 10 μL solution of silicon nanoparticles in methanol onto the membranes. After 1 minute wait time, this can be followed by an optional step of ethanol rinsing to reduce the concentration of the particles on the sample surface. However, we do not perform this step since the resulting concentration of the nanoparticles is satisfactory in our STEM measurements. The membrane is nitrogen dried at the end of the process.

4.1.3 Size analysis of silicon nanoparticles

In the STEM-EELS experiment, we determine the radii of the silicon nanoparticles using their STEM images. First, we consider processing performed for a particle without a gold film in Figure 4.1(a). We use image processing operations implemented in the Python scikit-image library. Initially, we manually determine the approximate particle radius, expected radius r_{exp}. For the samples without the gold layer, a Canny filter with $\sigma = 3$ pixels is applied to find the particle edges (Figure 4.1(b)). Then, we remove the false edge pixels by a combination of two morphological operations, diameter $0.7r_{exp}$ and area $1.4\pi r_{exp}$ opening, which remove small edge boundaries (Figure 4.1(c)). We use the Hough circle transform on the edge map to find the best fit for the radius and particle centre (Figure 4.1(d)). The Hough circle transform is performed by positioning a circle with a particular radius on each pixel of the edge map, and calculating how many circles with a particular radius intersect at some point, usually a centre point of the resulting fitted circle. The radii which are analyzed in this process lie in the provided radii range $r_{exp} \pm r_{range}$. We demonstrate the obtained best fit result overlaid on top of a STEM image in Figure 4.1(e) where the radius of the particle is determined to be 93 nm. Then, we use the number of intersections-radius dependence from the circle Hough transform to determine the uncertainty in the radius determination (Figure 4.1(f)). We fit the dependence with a bimodal distribution of 2 Gaussians. The uncertainty is taken as the standard deviation of the smaller Gaussian or the width of the edges determined with Canny filtering (1 pixel wide edges are the image resolution) if the edge width is larger than the standard deviation. In the example provided in Figure 4.1(f), we get the final uncertainty in the particle radius of 3.29 nm.

Then, we enlarge the edge map (Figure 4.1(c)) by 2 pixels in width and perform the circle Hough transform and Gaussians fitting again. This results in the new best-fit circle parameters and the uncertainty. If the uncertainty is smaller than the previous value and not larger than the image resolution of 3 pixels, it is taken as a new true value, otherwise, the previous values are preserved. This procedure is repeated multiple times resulting in edges that are increased by 2 pixels every step. For the particular example in Figure 4.1, we perform two enlargement operations and the result is shown in 4.1(g-h) with a final particle radius $r = 90 \pm 2$ nm. Qualitatively, if we compare Figure 4.1 (e) and (g), we can see a clear improvement in the quality of the fit.

The samples with the gold layer follow a similar procedure with some modifications. In the beginning, we predetermine the particle edges with a $\sigma = 20$ pixels Canny edge detector. Knowing that the particle is located approximately in the centre of the image (particle centre coordinates c_x and c_y are in the centre of the image), all the edges after $2r_{exp}$ are removed. We fit the resulting edge map using the Hough circle transform resulting in the intermediate radius r_{int}, and intermediate particle center coordinates c_{xi} and c_{yi}. Then, we find the particle edges with $\sigma = 10$ pixels Canny edge detector. Assuming the particle center is located at c_{xi} and c_{yi}, all edges before $0.8r_{int}$ and after $1.3r_{int}$ are removed, followed by a diameter $0.1r_{exp}$ opening. Finally, the Hough circle transform is applied on the last edge map to find the best fit for the radius and particle centre. The procedure of predetermining the particle edges is required to decrease computational cost since the gold film produces multiple false edges. We can decrease the number of false edges by using a Canny filter with a comparatively strong smoothing to define a rough location of the particle and use this rough location with a weaker smoothing to remove excessive false edges. The determination of the particle size uncertainty and the final best fit to the circle follows the same procedure as for the samples without the gold layer.

In the SEM-CL experiment, we determine the particle size following the same procedure
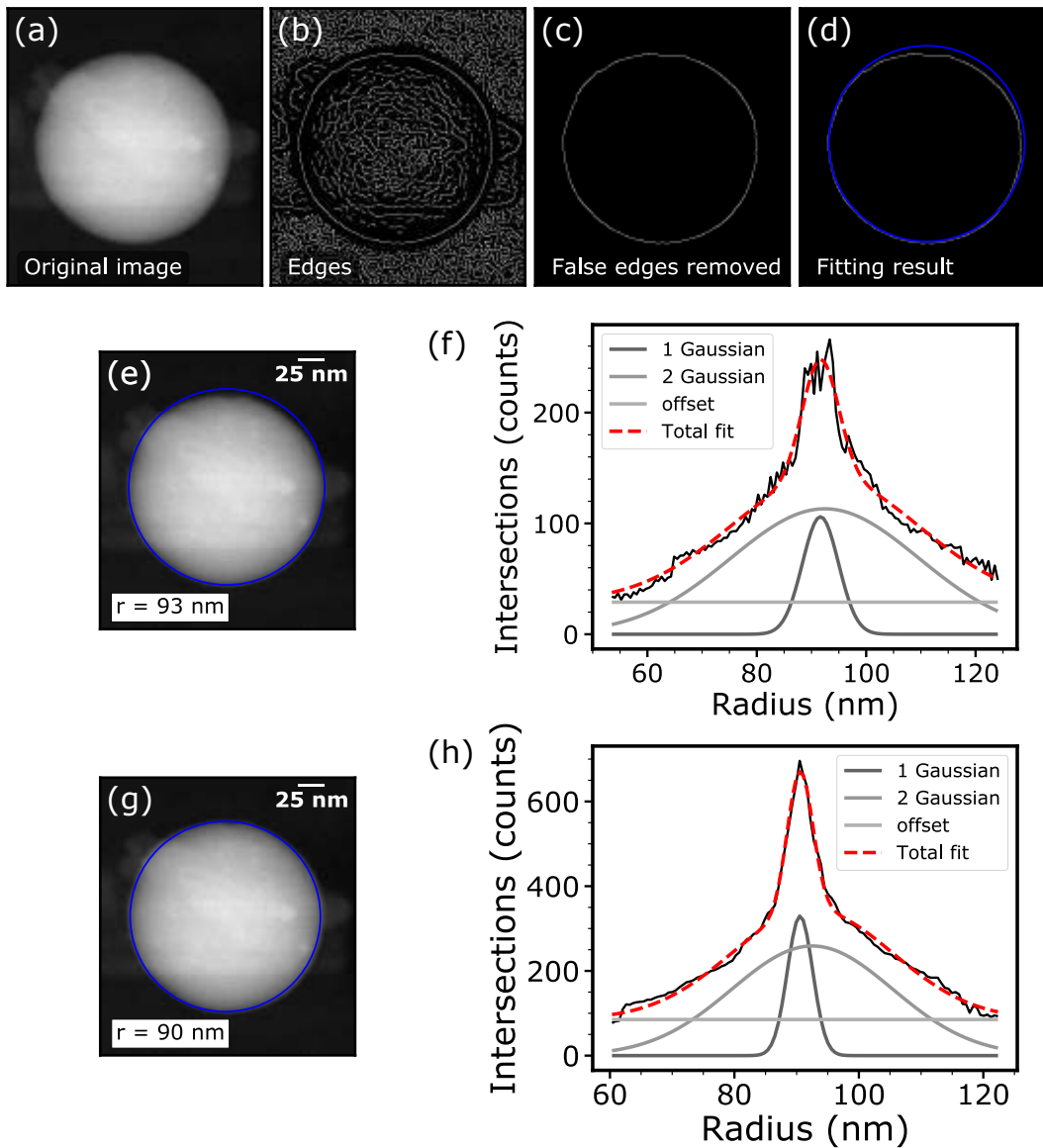
Figure 4.1: Size analysis of silicon nanoparticles. (a) STEM image of a silicon nanoparticle. (b) Edges after Canny filtering. (c) Edges after diameter and area opening. (d) Best fit from Hough transform. (e) STEM image of the nanoparticle with the best fit which shows the radius of $r = 93$ nm. (f) Result of the Hough transform, number of intersecting points as a function of the particle radius. The dependence is fitted with a distribution of two Gaussians with $\sigma_1 = 3.29$ nm and $\sigma_2 = 17.19$ nm. The width of the edges after Canny filtering is 0.28 nm (1 pixel). (g) STEM image of the nanoparticle with the best fit after two edge enlargement procedures which shows the radius of $r = 90$ nm. (h) Result of the Hough transform, number of intersecting points as a function of the particle radius, after two edge enlargement procedures. The dependence is fitted with a distribution of two Gaussians with $\sigma_1 = 2.04$ nm and $\sigma_2 = 12.92$ nm. The width of the edges is 1.42 nm (5 pixels).

as for the silicon on gold STEM-EELS case with the $\sigma = 30$ pixels Canny pre-processing filter and the final $\sigma = 5$ pixels Canny filter. The uncertainty is taken as the width of the electron beam in the experiments (8 nm at 30 kV).

4.1.4 EELS response of silicon nanoparticles

The schematic of the EELS measurements of a silicon nanoparticle is presented in Figure 4.2(a). The system consists of a silicon nanoparticle of a variable radius r on top of a silicon nitride membrane with a 30 nm fixed thickness and an electron beam which allows us to probe the EELS response of a particle. The electron beam can be moved around the particle resulting in the impact parameter b change. Figure 4.2(b) shows a typical EELS response from a silicon nanoparticle with $r = 54.6 \pm 1.1$ nm obtained by positioning the electron beam outside the particle. In the theoretical spectrum, the electron beam is positioned at a precise location $b = 75$ nm, while the experiments involve the summation of the EELS signal in the $b = 74.6 \pm 10$ nm range to increase the signal-to-noise-ratio of the resulting spectrum. The outside location of the electron beam allows us to have a direct comparison with the analytical theory for the EELS probability of a swift electron in the external vicinity of a vacuum-embedded dielectric sphere [83] (theoretical spectrum) which exists only outside the particle. As can be seen from Figure 4.2(b) we observe two clear peaks in the spectrum. Using the analytical solution, we identify them as the two lowest Mie modes of the nanoparticle, 2.54 eV magnetic and 2.97 eV electric dipoles. Experimental and theoretical resonance energies are in quantitative agreement, while the experimental peaks are broadened by the EELS setup. This can be accounted for by convolution of the theoretical spectrum with a Lorentzian function (area curve) [84].

We extend the considered electron beam positions including the electron beam inside the particle by using the simulation method discussed in Section 3.3.4. Figure 4.3(a) and (b) shows typical simulated and experimental spectra from a larger silicon nanoparticle which supports more Mie modes with $r = 90 \pm 2.0$ nm. The STEM image of the investigated structure is presented in Figure 4.3(c) which identifies the experimental integration regions and simulated points for the EELS spectra. The depicted EELS spectra are obtained by integrating the deconvoluted EELS data around the experimental impact parameter b_{exp}. For the disk-shaped integration regions, the experimental impact parameter denotes the
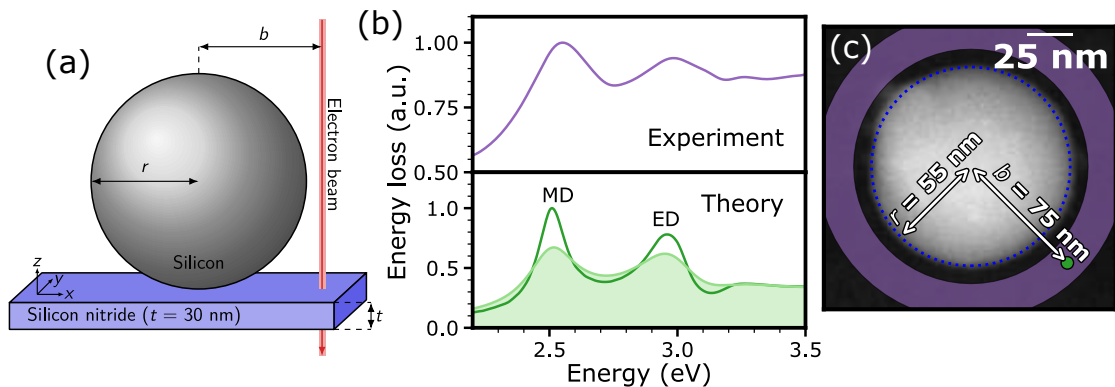
Figure 4.2: EELS measurements of Mie resonances in silicon nanoparticles. (a) Schematic of a silicon nanoparticle of radius r placed on a silicon nitride membrane and excited by an electron beam. The impact parameter b denotes the distance between the electron beam and the centre of the nanoparticle. (b) Experimental (top) and theoretical (bottom) EELS spectra of a silicon nanoparticle with radius $r = 54.6 \pm 1.1$ nm, acquired from the electron beam positions shown in (c). The area curve represents a convolution with a Lorentzian function. (c) STEM image of the nanoparticle, where the purple region represents the integration region for the experimental spectrum, and the green point depicts the location of the electron beam in the simulation. Adapted from paper A.

centre of the disk. For the annulus-shaped regions, the experimental impact parameter denotes the mean of the inner and outer radii.

Using the localized nature of the electron beam which quantifies the efficiency of mode excitation depending on its position [51], we distinguish between spectrally close ED and MQ resonances, as well as EQ and MH resonances. From the EELS simulation (Figure 4.3a), we find that the ED mode is efficiently excited by positioning the electron beam outside the nanoparticle ($b = 145$ nm)), while the MQ mode dominates for impact parameters inside the nanoparticle ($b = 60$ nm). In the case of EQ and MH modes, EQ is dominant in the particle centre ($b = 0$ nm) and MH inside the particle approximately halfway to the particle edge ($b = 60$ nm). This change in excitation efficiency shifts the experimental EELS peak, enabling us to identify multiple resonance energies from each silicon nanoparticle (Figure 4.3b). In contrary to the identification of spectrally-close plasmonic modes which are strongly excited near the particle surface [84] and, hence, don't have a pronounced spatial dependence, Mie resonances localize light both inside and outside the nanoparticle. This allows us to harness the spatial dependence of the electron beam to identify the resonance energies of Mie modes while distinguishing neighbouring plasmonic modes with EELS usually requires the highest energy resolution [61].

We map the first five Mie modes both numerically and experimentally (Figure 4.3d-h). Using the near-perfect spherical shape, we perform azimuthal averaging of the resulting EELS maps (Section 3.3.3). The MD mode (Figure 4.3d) has a doughnut-like field profile with a maximum intensity of approximately two-thirds inside the nanoparticle and a complete minimum at the centre. This demonstrated that the MD mode cannot be excited when the electron beam is positioned in the particle centre. The MQ mode (Figure 4.3f) shows a similar intensity map with a stronger localization to the nanoparticle and a weaker minimum in the centre. In contrast, the ED mode (Figure 4.3e) shows a weak peak in the centre and maximum inside the particle near its surface. Compared to the MQ mode, the ED mode extends further outside the particle, which we exploited to distinguish their spectrally close resonance energies. The higher-order EQ and MH modes (Figure 4.3g,h) both have a maximum in the particle centre and a small peak two-thirds inside the nanoparticle. The MH mode shows a stronger peak than the EQ mode and we use this difference to find their resonance energies in the experimental data. We note that the EELS maps of neighbouring Mie modes are influenced by the broad nature of the Mie resonances, and, for the experimental maps, also by the energy resolution of the EELS setup. The resolution of the EELS setup can be accounted for by plotting the simulated EELS maps of Lorentzian smoothed EELS spectra (area curves in 4.3(a)) in Figure 4.3(d-h)(bottom). We find reasonable agreement between experimental and simulated EELS maps, which shows that EELS can be successfully applied to detect the rich field profiles of Mie resonances.

As an outcome of both positioned-dependant EELS spectra plotting and mapping, we specify the spatial regions which are used for the identification of mode resonance energies in Table 4.1. The table shows the ranges of electron beam impact parameters that are used to integrate the experimental EELS signal. The resonance energies of Mie modes are identified from the resulting spectrum.
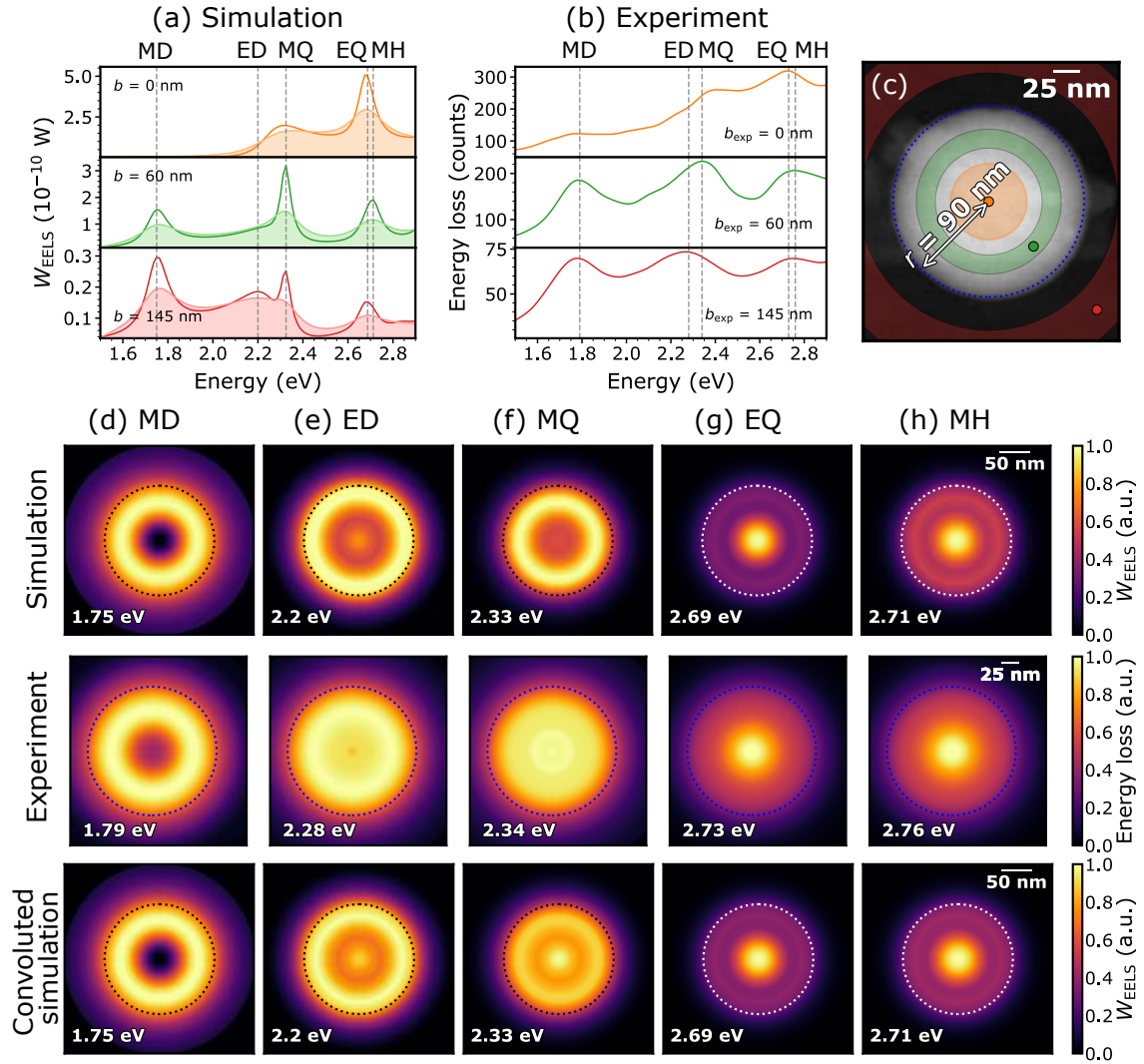
Figure 4.3: EELS mapping of Mie resonances. (a) Simulated EELS spectra of a silicon nanoparticle with radius $r = 90$ nm at different impact parameters b. The area curves depict the simulated spectra convoluted with a Lorentzian function. (b) Experimental EELS spectra for a particle with radius $r = 90.5 \pm 2.0$ nm acquired from the regions shown in (c). (c) STEM image of the nanoparticle, where the coloured areas represent the integration regions for the experimental EELS signal, and the coloured points are the position of the electron beam in the simulation. (d-h) Simulation (top), experiment (middle), simulation convoluted with a Lorentzian function (bottom) of EELS intensity maps of the first five Mie modes. The EELS maps are individually normalized. Adapted from paper A.

Table 4.1: Spatial ranges for Mie mode identification with EELS.

Mode	Impact parameter range
MD	$[0r, 0.8r]$
ED	$[1.3r, 2r]$
MQ	$[0.4r, 0.8r]$
EQ	$[0r, 0.4r]$
MH	$[0.55r, 0.75r]$
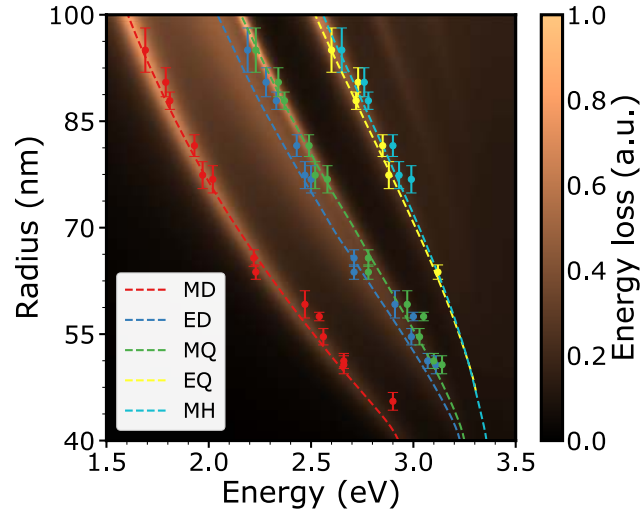
Figure 4.4: EELS measurements of Mie resonances in silicon nanoparticles. Measured resonance energies as a function of particle radius for the first five Mie resonances in silicon nanoparticles. The colour plot shows the EELS simulation for an impact parameter $b = r + 20$ nm and the dashed curves indicate the theoretical Mie resonance energies. Adapted from paper A.

Using these experimental results and analytical Mie theory [83], we measure the Mie resonance energies of silicon nanoparticles over a broad size range from 40 nm to 100 nm (Figure 4.4). The coloured points show the experimentally measured resonance energies of the first five Mie resonances. The colour plot depicts the calculated EELS probability using the same analytical theory as in Figure 4.2(b), while the dashed curves show the first maxima of the different Mie scattering coefficients, which indicate the position of the resonance energies. We find excellent quantitative agreement between experiment and theory across the wide span of particle sizes, even though the theory does not account for the presence of a thin substrate. The strong match evidences that the silicon nitride membrane has negligible influence on the Mie resonances, which is in agreement with earlier theoretical studies on the influence of substrates on Mie resonances [85, 86]. In addition, we highlight that the tightly confined electromagnetic field of the electron beam couples stronger to higher-order Mie resonances than the plane-wave field used in optical measurements [87, 36], which enables us to detect them even in small particles.

4.1.5 Plasmon launching with silicon nanoparticles

We utilize the silicon nanoparticles as launchers and scatterers of surface plasmon polaritons (SPP) in thin metal films. SPPs supported by metal films guide and localize the light at subwavelength scales [88] which is desirable to reduce the footprint and energy consumption of integrated photonics devices [89, 90] as well as realizing two-dimensional manipulation of light [91]. However, the momentum mismatch between the surface plasmon and incoming light does not allow a direct excitation of the SPP waves. Typically, this is achieved by total internal reflection, such as Kretschmann or Otto prism coupling, or diffractive effects, such as grating couplers [92]. The former approach is usually bulky which compromise the miniaturization of the resulting device, while the latter requires patterning of the metal film compromising the quality of the resulting film. This motivates the utilization of subwavelength scatterers for SPP launching. In this approach, a significant modal overlap between the field of the resonant nanostructure and the SPP supported by the metal film is required to achieve efficient SPP launching. However, there has

been little attention in the literature on improving the modal overlap to boost the plasmon excitation efficiency where both plasmonic [93, 94] and dielectric [95, 96] resonant nanostructures have been considered. Optically-thick metal films have been used to achieve plasmon coupling, whose fields are optimized to overlap with neither plasmonic nor dielectric nanostructures [97, 98].

Here, we experimentally show that Mie resonances supported by silicon nanoparticles strongly hybridize with the highly-confined SPPs in 10-nm-thin gold films. The strong hybridization between the SPPs in metal film and Mie resonances in silicon nanoparticles leads to the formation of hybrid dielectric-plasmon resonances [98] where the SPPs provide the out-of-plane confinement, while the Mie resonances provide the in-plane confinement of the hybrid resonances. Such hybrid resonances also occur for optically-thick metal films, where they offer light confinement with low losses, however, they typically have high radiation efficiency into free-space light [98, 99], hence, low excitation efficiencies. In contrast, we show hybrid dielectric-plasmon resonances with strong modal overlap between the Mie resonances of a silicon nanoparticle and the SPP supported by optically-thin gold films which have most of the incoming light coupled into SPP rather than the free space light. This proves a promising platform for efficient nanoscale plasmon generation.

We place silicon nanoparticles on top of a 10 nm gold - 30 nm silicon nitride layers stack (Figure 4.5(a)) to excite the hybrid resonances and launch SPPs. A thin metal film can support two SPP modes by itself, long-range and short-range SPPs, however, the asymmetric dielectric composition of the two layers stack turns the long-range SPP into a leaky mode [91], and only the short-range SPP remains (Figure 4.5(b), green line). We can directly excite the short-range SPP, i.e. using the layers stack without a nanoparticle, via the electron beam which results in a broad peak at 1.3 eV in the EELS spectrum (Figure 4.5(c)). The broadband nature of the electron source allows the electron beam to couple to the SPP of the films at different energies and wavenumbers resulting in large bandwidth of the ELLS peak. The possibility to couple at multiple energies and wavenumbers combined with the dispersion relation of the short-range SPP defines the resulting peak energy in the EELS spectrum [100].

A combined system which includes a silicon nanoparticle produces a narrower and red-shifted peak (Figure 4.5(d)). This peak is due to a hybrid dielectric-plasmon mode and, for the particle with the radius $r = 54.1 \pm 0.8$ nm, lies at the energy of 1.22 eV. The peak energy can be accounted in a dispersion relation of a three layers system consisting of an additional layer of silicon (silicon-gold-silicon nitride) with the thickness of the nanoparticle diameter (Figure 4.5(b), purple line). The dispersion relation is then sampled at specific wavenumbers k_{lm} defined by the resonance condition of zero round trip phase [98], which is given by the relation:

$$k_{lm}r \approx j_{lm} \qquad (4.1)$$

Where j_{lm} denotes the m-th zero of the spherical Bessel function of order l. Physically, the indices (l, m) correspond to the field variations in the radial and azimuthal directions, respectively. The two lowest quantized wavenumber given by Eq. (4.1) are shown in Figure 4.5(b) as dashed vertical lines.

We find that the resonance energy given by the lowest-order $(0, 1)$ mode matches with the energy of the EELS peak excited in the silicon on gold system. The field profile which corresponds to this mode is depicted in the inset of Figure 4.5(d). We elaborate on the

nature of the hybrid resonance in Figure 4.5(e) where we show how the fields of the short-range SPP residing in the gold-silicon nitride films and ED Mie mode of the silicon nanoparticle hybridize to form the hybrid resonance. The substantial spatial field overlap of the resulting system results in an efficient excitation of the SPP mode.

The strong hybridization can also be observed in the spectral shift between the ED resonance of a bare silicon nanoparticle (Figure 4.2(b)) and the hybrid resonance of the silicon of gold system. For particles with a similar size of $r \approx 54$ nm, the ED resonance of the bare particle at 2.97 eV shifts to the hybrid resonance energy at 1.22 eV. It can be concluded that the hybrid resonance localizes the light on a smaller scale than the lowest-order MD resonance of a silicon nanoparticle. An increase in light confinement by a factor of $\lambda_H/\lambda_{MD} \approx 2$ can be routinely achieved when we compare the hybrid resonance wavelength λ_H and the MD resonance wavelength λ_{MD} of the same particle size. The increase in the light confinement comes from the fact that the SPP confinement defines the confinement of the hybrid resonances, while the Mie resonances arise due to the confinement of light inside silicon. This shows that a substantially higher effective refractive index
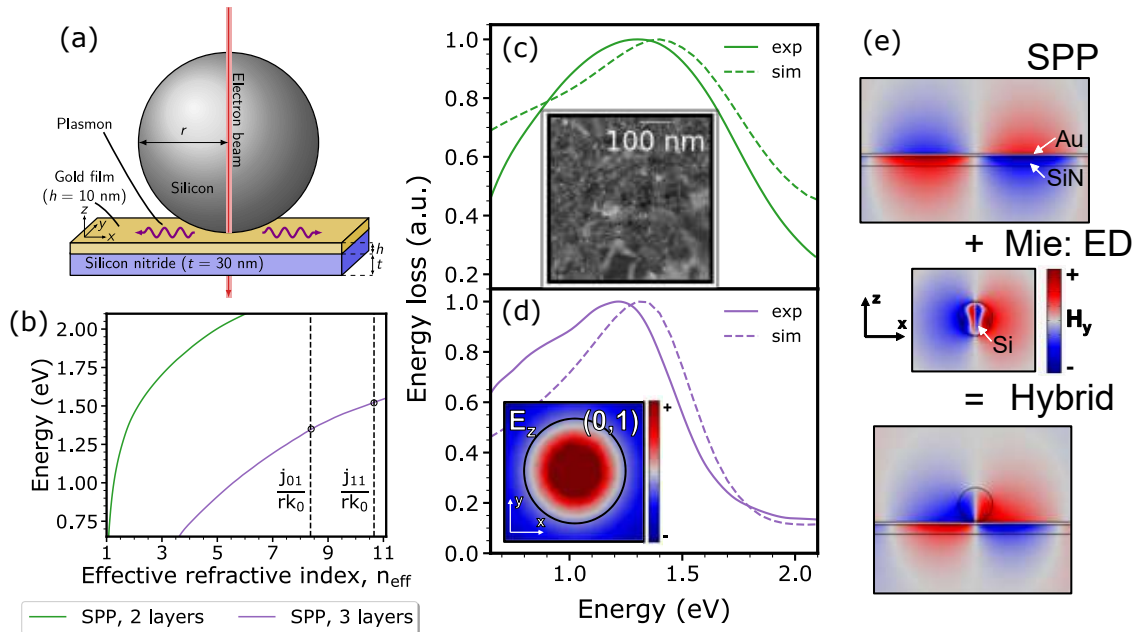
Figure 4.5: Hybrid dielectric-plasmon resonances. (a) Schematic of a silicon nanoparticle placed on a thin layer stack consisting of 10 nm gold film on top of a 30 nm silicon nitride membrane. The structure is probed by an electron beam penetrating the centre of the nanoparticle ($b = 0$ nm). (b) Dispersion relation of the short-range SPP supported by the gold-silicon nitride stack (green line) as well as the silicon-gold-silicon nitride stack (purple). In the latter, the silicon thickness is 110 nm, corresponding to the diameter of the nanoparticle. The two lowest-order resonance conditions given by Eq. (4.1) are depicted as vertical lines. (c,d) Experimental and simulated EELS spectra of the structure without and with the silicon nanoparticle, respectively. The radius of the particle is $r = 54.1 \pm 0.8$ nm. The inset in (d) shows the z component of the electric field of the $(0,1)$ hybrid mode in the xy-plane at the top gold surface. (e) Cross-sectional magnetic field profiles of the short-range SPP mode without the nanoparticle (top), the electric dipole mode of an isolated silicon nanoparticle (middle), and the hybrid dielectric-plasmon mode (bottom). Adapted from paper A.

can be achieved in the hybrid system compared to purely dielectric materials, leading to a way to shrink the dielectric scatterers below their diffraction limit.

The importance of a *thin* gold layer for efficient plasmon excitation is further elaborated in Figure 4.6. We decompose the electric field generated by an electric dipole placed above a silicon nanoparticle on top of the gold-silicon nitride layers (Figure 4.6(a)) into free-space (FS) and SPP radiation [101]. The simulation shows that the field is coupled to $(0, 1)$ mode which is the same case as for the electron beam. We vary the thickness of the gold layer and show the coupling efficiency into SPP (Figure 4.6(b)) and FS radiation (Figure 4.6(c)). The results show the increase in SPP coupling efficiency for smaller gold layer thickness, while the FS efficiency decreases. This fact highlights the importance of thin gold films for efficient SPP coupling showing an increase in SPP coupling efficiency from 1 % in the case of a 50 nm film to around 70 % in the case of a 10 nm film.

As the next step, we analyze the EELS response of silicon on gold structure when we change the impact parameter, i.e. move the electron beam. Figure 4.7(a-c) shows that when the beam is radially moved from the particle centre to the edge or outside locations, the hybrid resonance energy experiences a redshift of around 50 nm. We perform Cartesian multipole decomposition [102] of the induced electromagnetic field and plot electric dipole moment of the hybrid mode (Figure 4.7(f)). We observe the change in the orientation of the electric dipole as the beam moved further from the particle centre. The change in orientation slightly shifts the resonance conditions of the hybrid mode and this results in the redshift of the hybrid mode.

When we move further from the particle, the hybrid mode intensity drops almost completely. However, other resonances are appearing in the energy range above the hybrid mode. These resonances are due to plasmon scattering effects and they are considered in the next section. We also perform EELS mapping of the hybrid mode in Figure 4.7(d-e) which, as expected, shows that the hybrid mode is localized to the particle volume and it drops completely when the beam is far from the particle. The increase in the intensity on the edges of the map are due to the broad modes appearing outside the particle which are considered in the next section.

We extend the hybrid mode analysis to particles in a broad size range (Figure 4.7 (g)).
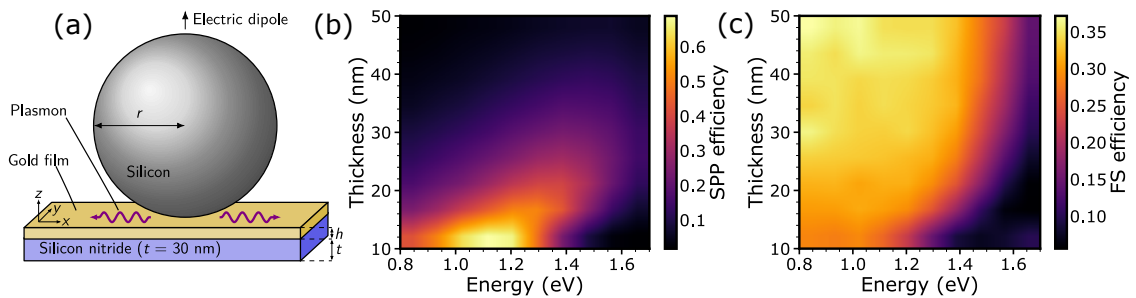
Figure 4.6: SPP coupling efficiency of the hybrid dielectric-plasmon mode as a function of gold thickness. (a) Schematic of a silicon nanoparticle placed on the gold-silicon nitride stack, which is probed by an electric dipole oriented along the z direction and located above the centre of the nanoparticle at a 1 nm gap. (b) Efficiency of SPP and free-space (FS) coupling of the $(0, 1)$ hybrid dielectric-plasmon mode for increasing gold layer thickness. The efficiency is taken as a ratio of the SPP or FS power to the power radiated by the electric dipole in a vacuum. Adapted from paper A.
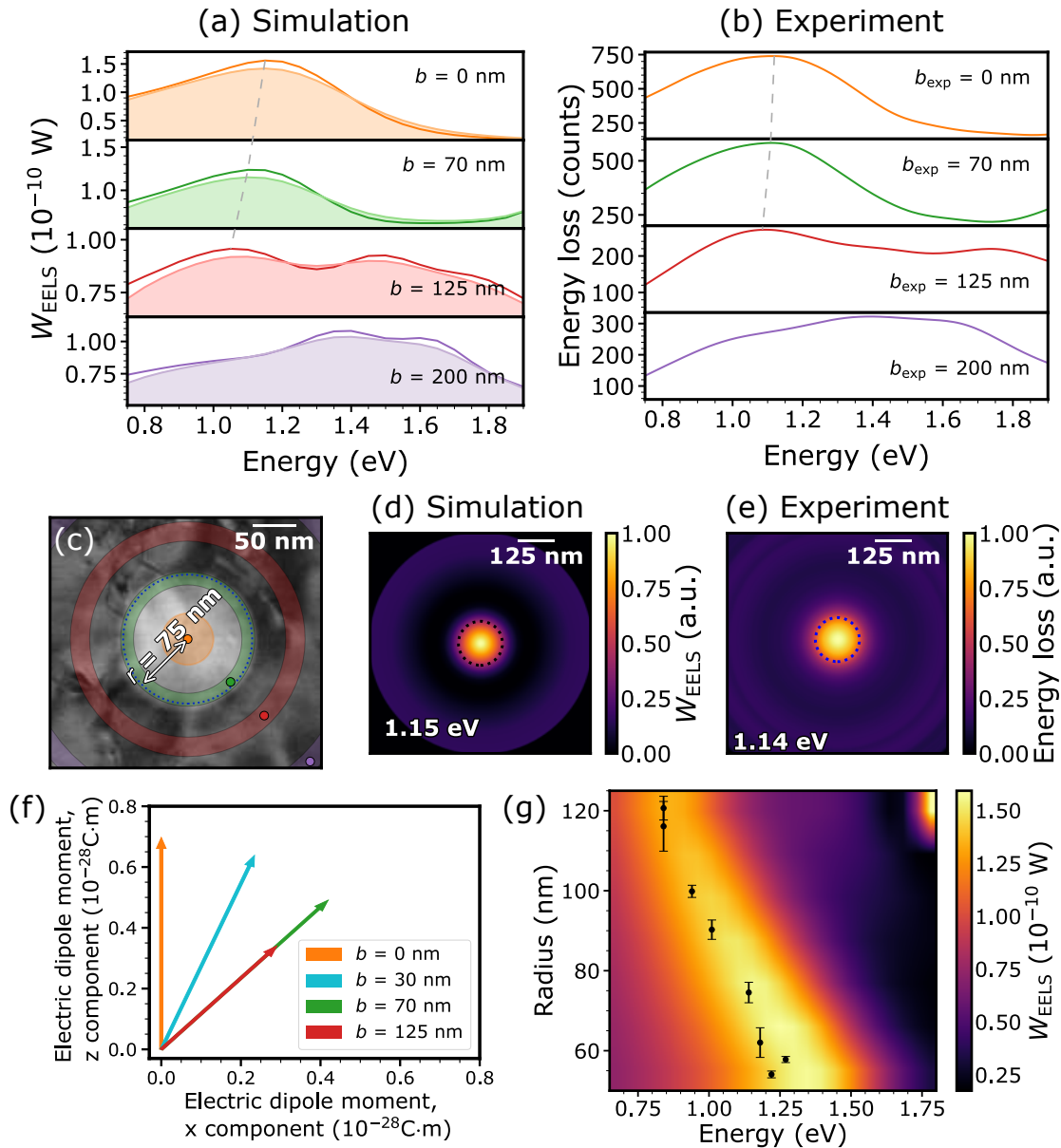
Figure 4.7: Plasmon launching. (a) Simulated EELS spectra of a silicon nanoparticle ($r = 75$ nm) on a thin gold-silicon nitride stack at different impact parameters b. The area curves depict the simulated spectra convoluted with a Lorentzian function. The grey dashed line shows a change in peak energy of the hybrid mode as the beam moves. (b) Experimental EELS spectra for a particle with radius $r = 74.5 \pm 2.6$ nm acquired from the regions shown in (c). (c) STEM image of the nanoparticle, where the coloured areas represent the integration regions for the experimental EELS signal, and the coloured points are the position of the electron beam in the simulation. (d,e) Simulated and experimental EELS maps of the $(0,1)$ hybrid mode. (f) The electric dipole moment of the $(0,1)$ hybrid mode at different impact parameters, which shows the change in dipole direction as the electron beam is moved away from the centre of the particle. (g) Measured resonance energies of the $(0,1)$ hybrid mode as a function of particle radius acquired by positioning the electron beam in the nanoparticle centre. The colour plot shows the EELS simulation for an impact parameter of $b = 0$ nm. Adapted from paper A.

The results show that the $(0, 1)$ hybrid mode resonance energy can be effectively tuned from the near-infrared to telecommunication wavelengths by changing the nanoparticle size. The resonance energies obtained in the experiment are in agreement with our EELS simulations (colour plot), which also show a linewidth broadening of the resonance at
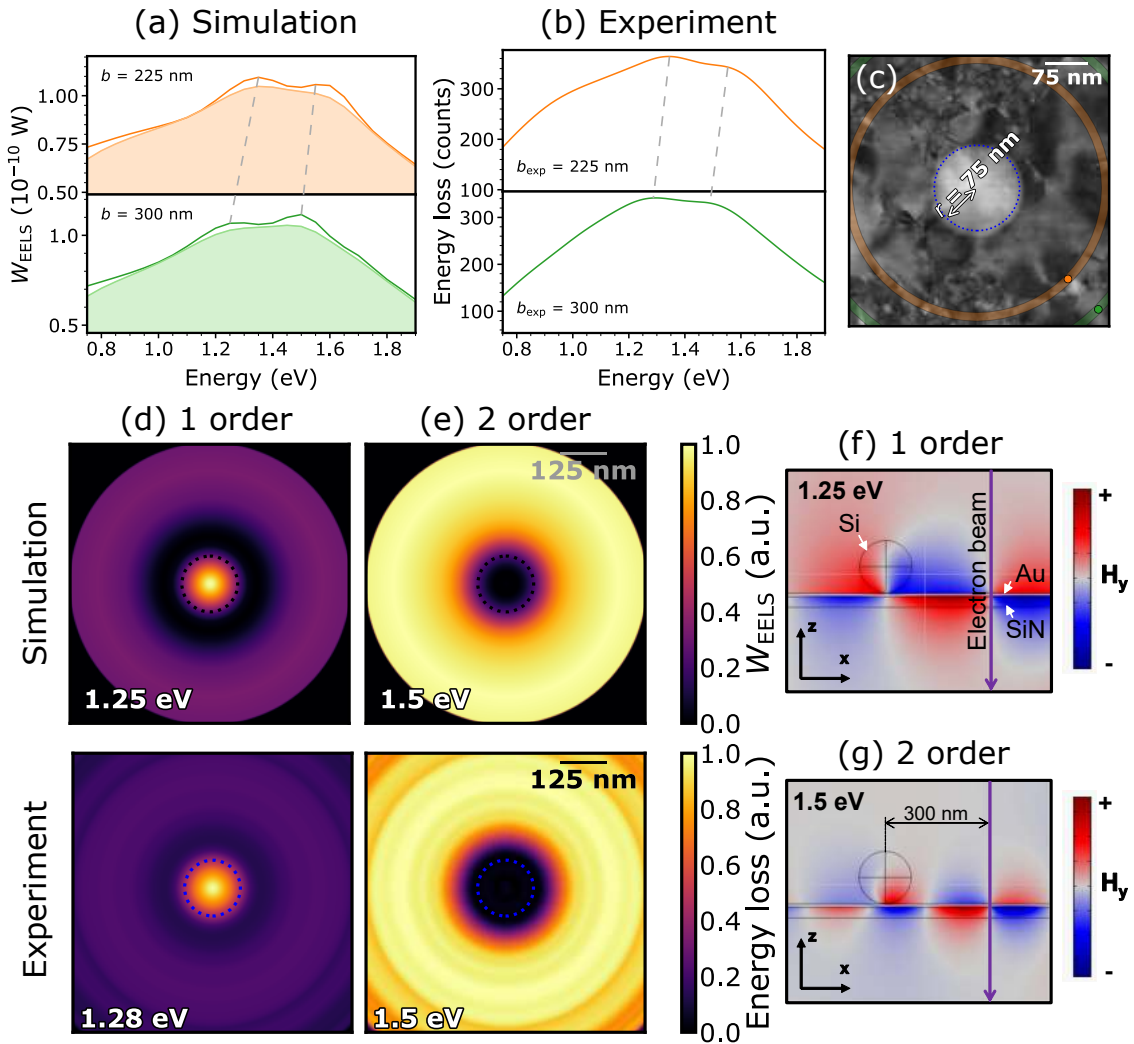
Figure 4.8: Plasmon scattering. (a) Simulated EELS spectra of a silicon nanoparticle ($r = 75$ nm) on a thin gold-silicon nitride stack at different impact parameters b. The area curves depict the simulated spectra convoluted with a Lorentzian function. The grey dashed lines shows the change in peak energy of the first and second-order reflection as the beam moves. (b) Experimental EELS spectra for a particle with radius $r = 74.5 \pm 2.6$ nm acquired from the regions shown in (c). (c) STEM image of the nanoparticle, where the coloured areas represent the integration regions for the experimental EELS signal, and the coloured points are the position of the electron beam in the simulation. (d,e) Simulated (top) and experimental (bottom) EELS maps of the plasmon reflection at two separate energies, which correspond to either (d) the first-order reflection (half-wavelength of SPP) or (e) second-order reflection (one-wavelength of SPP).(f,g) Cross-sectional magnetic field profiles of the reflected SPP mode for (f) first and (g) second interference orders, respectively. In both cases, the reflection occurs at the nanoparticle centre. Adapted from paper A.

higher energies due to decreasing SPP propagation length.

4.1.6 Plasmon scattering with silicon nanoparticles

We consider the case where the electron beam is outside the particle. As was mentioned in the previous Section new resonances are appearing outside the particle at the energy range higher than the hybrid mode. We demonstrate theoretical and experimental spectra for such case in Figure 4.8(a-c). We can observe two peaks that also move to lower energy when the electron beam is positioned further from the particle. These peaks occur due to the plasmon reflection from the particle. Since we can efficiently couple to the SPP of the bare thin films of gold and silicon nitride with an electron beam, we launch this SPP when we are outside the particle, the launched wave is resonantly reflected from the particle resulting in an interference effect with the original wave. Therefore, we can observe multiple peaks which are due to different interference order maxima. When the beam moves further from the particle, the interference condition changes, therefore we see a decrease in the peaks resonance energies. We perform EELS mapping for two interference orders in Figure 4.8(d-e) which show a maximum at the same distance from the particle of b = 300 nm. We further prove the interference effect in Figure 4.8(f-g) where we plot the resulting magnetic field from the simulation in Figure 4.8(a). It shows a standing wave pattern for the first and second-order interference having half and full wavelength standing wave patterns respectively. By describing the SPP waves as one-dimensional plane waves with wavelength λ_{SPP}, we find the phase relation:

$$b = \frac{(2\pi q - \phi)}{4\pi}\lambda_{SPP}. \qquad (4.2)$$

Where ϕ is the reflection phase and q is a positive integer, which denotes the interference order. We find that the SPP reflection occurs at the nanoparticle centre using the ELLS simulations (4.8(f-g)). Therefore, a part of the phase pickup occurs in silicon, which differs from the phase pickup outside the nanoparticle due to the refractive index of silicon. In
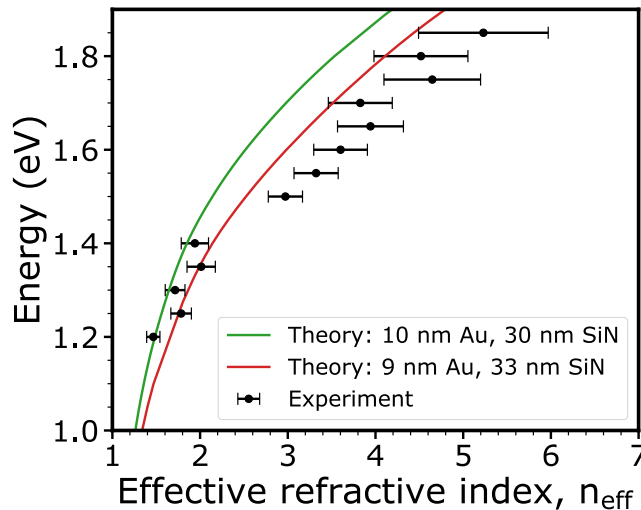
Figure 4.9: Experimental and theoretical dispersion relations of the short-range SPP supported by the gold-silicon nitride stack. Experimental data points are determined by using Equation (4.2) on the SPP reflection EELS maps of the nanoparticle in Figure 4.8(d-e). Adapted from paper A.

Equation (4.2), we assume that this difference is small and describe the nanoparticle as a reflecting boundary located at the nanoparticle centre.

We measure the distance b from the ring-shaped EELS maps at different energies. Using Equation (4.2), we assume a zero phase shift upon reflection and extract the SPP dispersion relation of the short-range SPP supported by the gold-silicon nitride stack (Figure 4.9). For energies below approximately 1.5 eV, first-order interference ($q = 1$) is the main contributor in the reconstruction of the experimental dispersion curve, when the second-order interference is dominant for the larger energies. This is mainly limited by the limited spatial range in the experiment. The dispersion curve obtained in the experiment has a good agreement with a theoretical dispersion curve at low energies, but has a slight deviation at higher energies, even if we consider the different layer thicknesses within our fabrication tolerance. It should be noted that similar results can be obtained for particles of other sizes. The difference between the theory and experiment at higher energies can be explained by an additional phase pickup inside the nanoparticle which contributes more for shorter wavelengths or higher energies and which is not accounted for in Equation 4.2. Nevertheless, the dispersion diagram reconstructed from the plasmon reflection phenomenon shows that silicon nanoparticles reflect short-range SPP in a broad energy range.

4.1.7 Mie modes in silicon nanoparticles on a thin gold film

We also track how Mie modes of the silicon nanoparticle are affected by the presence of a thin gold film. Using the same particle with $r = 74.5 \pm 2.6$ nm as in Figure 4.7 and 4.8 we plot the simulated and experimental spectra in Figure 4.10(b-d) for the energy range of Mie resonances. It can be seen that for the positions inside the particle we observe similar Mie mode peaks as in Figure 4.3 (a-b). When the beam is moved outside the particle the resonances of the gold film start to dominate the spectrum and cover the Mie resonances. However, we do not observe any energy shifts in the Mie modes of the silicon nanoparticle themselves, and it can be concluded that the presence of the thin gold layer does alter them significantly.
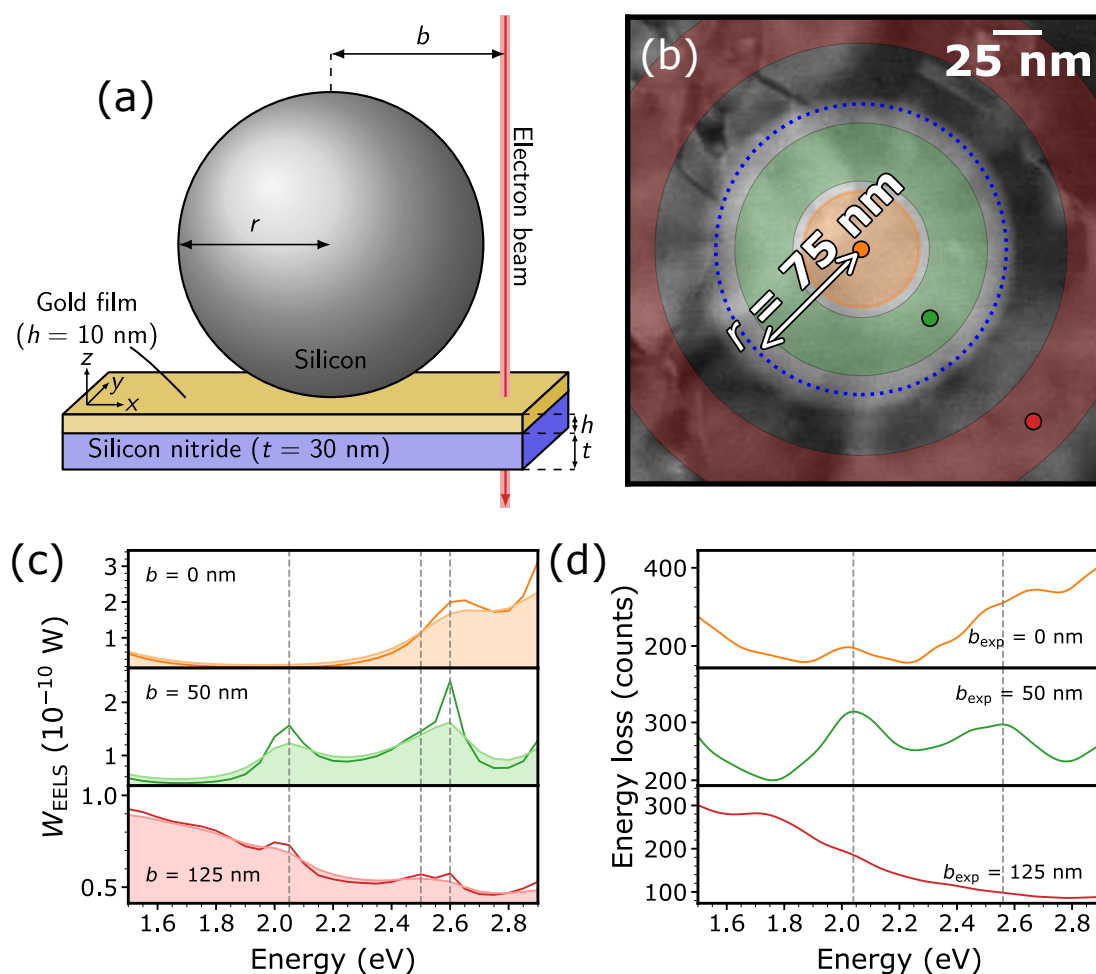
Figure 4.10: Mie resonances in silicon nanoparticles on a 10 nm thin gold film. (a) Schematic of a silicon nanoparticle placed on a thin layer stack consisting of 10 nm gold film on top of a 30 nm silicon nitride membrane. (b) STEM image of the nanoparticle, where the coloured areas represent the integration regions for the experimental EELS signal, and the coloured points are the position of the electron beam in the simulation. (c) Simulated EELS spectra of a silicon nanoparticle ($r = 75$ nm) on a thin gold-silicon nitride stack at different impact parameters b. The area curves depict the simulated spectra convoluted with a Lorentzian function. (d) Experimental EELS spectra for a particle with radius $r = 74.5 \pm 2.6$ nm acquired from the regions shown in (b). Adapted from paper A.
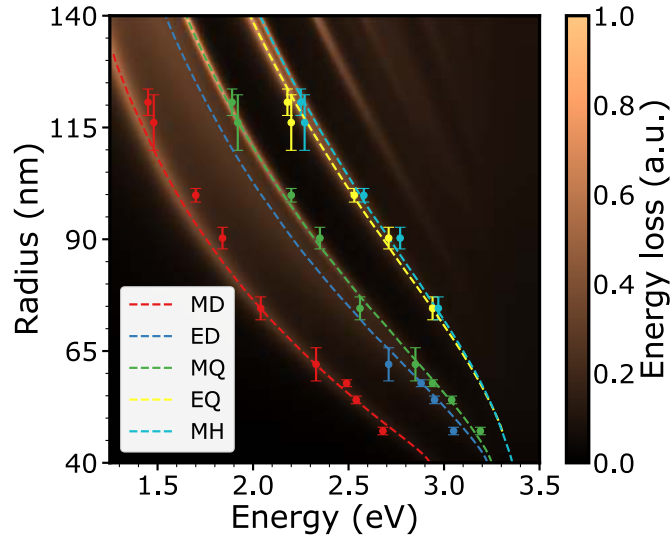
Figure 4.11: Measured resonance energies as a function of particle radius for the first five Mie resonances in silicon nanoparticles on the gold-silicon nitride stack. The colour plot shows the EELS simulation of a *vacuum-embedded* silicon sphere for an impact parameter $b = r + 20$ nm and the dashed curves indicate the free-space theoretical Mie resonance energies. Adapted from paper A.

The effect of masking of low energy Mie resonances makes it impossible to experimentally identify the position of the ED mode in larger particle sizes. However, for smaller particle sizes, the ED resonance energy occurs at much larger energies than the SPP, allowing us to identify the ED resonance. This is summarized in Figure 4.11 where we show the peak energies of the Mie resonances in a broad particle size range for the silicon on gold structures determined experimentally as colour points, and compare them with the colour plot and dashed lines of the bare silicon nanoparticles. The strong agreement between theory and experiments show that the Mie resonances remain largely unaffected by the presence of the thin gold film.

4.1.8 Transition radiation in CL response of silicon nanoparticles

As an alternative to EELS, we use cathodoluminescence spectroscopy to probe the response of silicon nanoparticles in an SEM microscope. Contrary to EELS, it collects the light emitted by the structure as a result of the electron scattering, when EELS deals with measuring these scattered electrons. As such, CL is an invaluable technique to measure the radiative modes of the structure when EELS probes both dark and radiative modes [103, 104]. As a consequence of lower acceleration voltages in SEM microscopes, we discover a non-negligible contribution from the transition radiation in the resulting CL spectrum. We show that the transition radiation generates new distinctive resonances by itself resulting from the constructive and destructive interference effects. These effects are the result of the electron excitation of dipole resonances at two interfaces of the nanoparticle which are separated in time by the electron flight through the particle and interfere with each other. Therefore, specific care must be taken when interpreting the CL results.

Figure 4.12 shows a typical CL response from a particle with $r = 92 \pm 8$ nm at an acceleration voltage of 30 kV. We plot the first two maxima of the Mie coefficients for ED and MD modes, and the first one maxima for MQ, EQ and MH modes as dashed vertical lines. We can identify the ED and MQ modes from the centre position of the electron beam which is
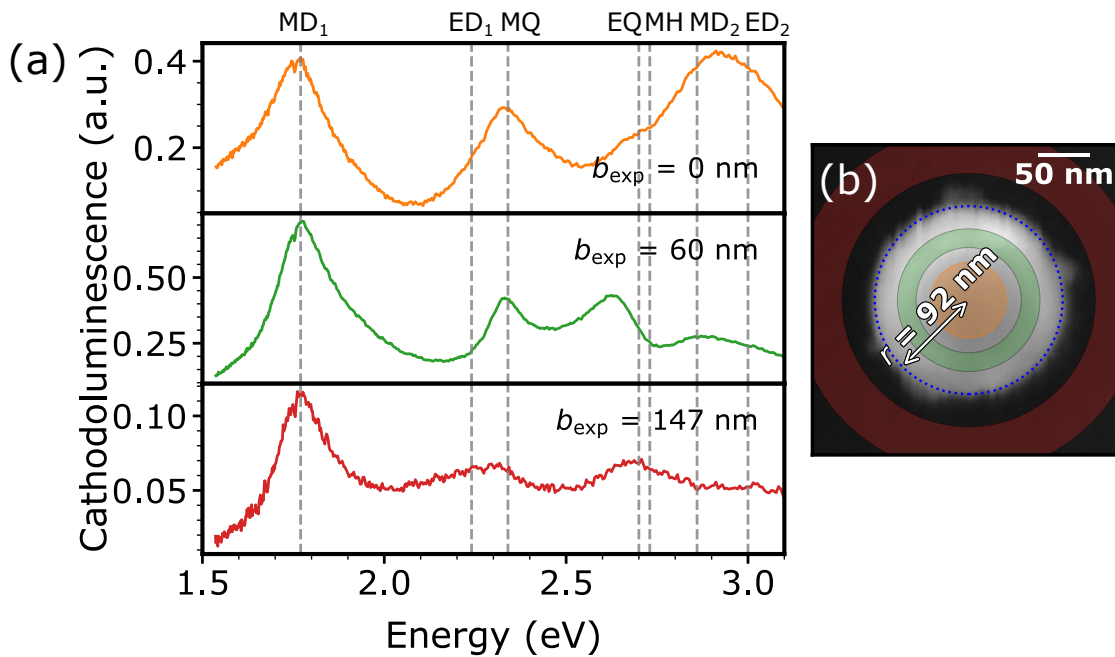
Figure 4.12: CL response of a silicon nanoparticle. (a) Experimental EELS spectra for a particle with radius $r = 92\pm8$ nm acquired from the regions shown in (b) at an acceleration voltage of 30 kV. The vertical dashed lines show theoretical Mie resonance energies of a particle with $r = 89$ nm. (b) SEM image of the nanoparticle, where the colored areas represent the integration regions for the experimental CL signal. Adapted from paper B.

in agreement with our EELS analysis. The clear shift in energy as we move further from the particle at the energy spectrally close to the MQ mode can be attributed to the ED mode which is larger in the CL intensity outside the particle. This is also characteristic of EELS as we have shown in the previous section. However, new resonances are appearing at 2.6 and 2.9 eV inside the particle which does not correspond to any theoretical Mie
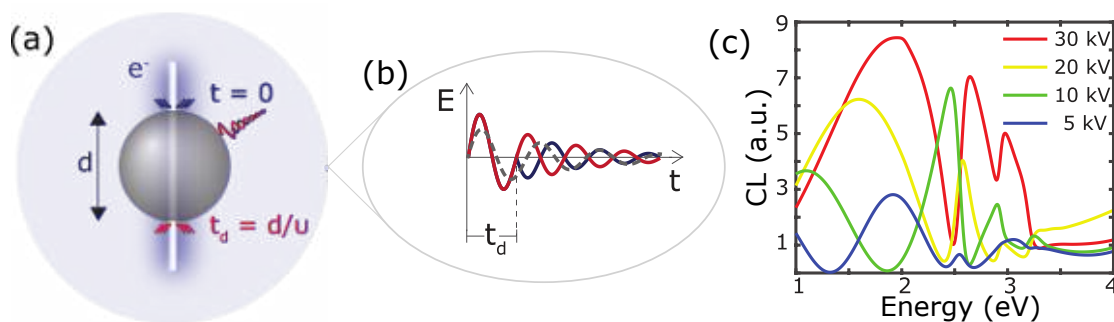
Figure 4.13: Transition radiation in a silicon nanoparticle. (a) Emergence of the two collapsing dipoles at the upper and lower surfaces of an NP crossed by an electron beam through its centre. (b) Time-domain sketch of the electric far-field amplitude due to the two excitation events (red and blue lines) and an NP Mie resonance (grey dashed line). (c) Calculated CL spectra for a Si sphere with $r = 75$ nm at the different acceleration voltages, at $b = 5$ nm. Adapted from paper B.
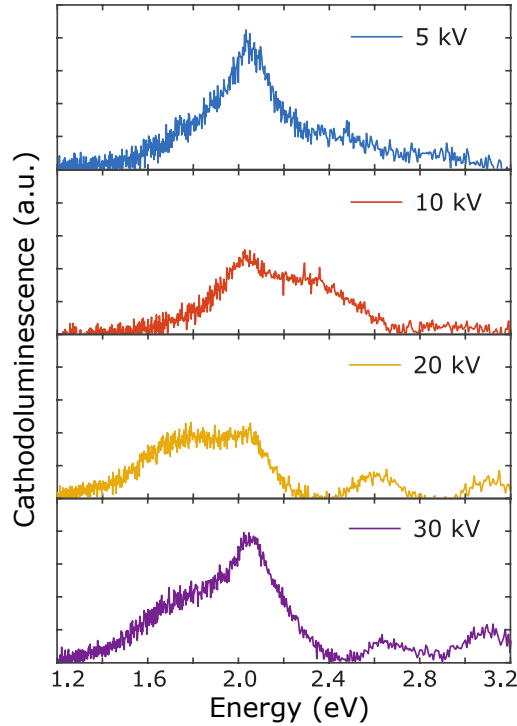
Figure 4.14: Experimental CL spectra for an electron beam passing through the centre of a Si nanosphere with $r = 75$ nm, for acceleration voltages ranging from 5 kV (upper panel) to 30 kV (lower panel). Adapted from paper B.

modes. We attribute these resonances to transition radiation effects which are significant for comparatively low acceleration voltage and thick particles.

We explain this effect in Figure 4.13(a). When the electron approaches the nanoparticle one at a time, it collapses with its image charge [105, 106, 107] at the nanoparticle surface leading to a formation of an electric dipole and resulting in transition radiation. This effect is repeated at the other particle boundary with a time delay $t_d = d/v$ (where d is the electron path inside the particle, v is the electron velocity). These two dipoles can interfere constructively or destructively resulting in the oscillations in the resulting CL spectrum which is overimposed on the original CL spectrum of Mie resonances. The corresponding oscillations in time are sketched in Figure 4.13(b) with the NP Mie resonance (dashed grey line). Calculated CL spectra of a $r = 75$ nm particle for different acceleration voltages are shown in Figure 4.13(c). At a low voltage of 5 kV, the signal comes mainly from the transition radiation, when the voltage is increased, the contribution of Mie resonances increases. The Mie resonances are superimposed with the transition radiation leading to new peaks in the CL spectrum.

We perform an experimental verification by collecting CL spectrum from $r = 75$ nm sphere at different acceleration voltages in Figure 4.14. We can observe traces of the oscillations related to transition radiation. For example, we observe four resonance at 1.8, 2 (MD), 2.6 (MQ) and 3.1 eV for 20 kV acceleration voltage, where the resonances at 1.8 eV and 3.1 eV are not a result of Mie theory. Noticeably, there are broad shoulders at 2.3 eV for 10 kV and 1.8 eV at 20-30 kV acceleration voltages which appear and disappear when the voltage is varied. We believe that this is a clear feature of transition radiation interference effects which have oscillatory behaviour in the resulting spectrum.

4.1.9 Concluding remarks

We have used EELS to measure and map the Mie resonances in silicon nanospheres in a broad size range. Using the position dependant excitation of the Mie modes by the electron beam, we obtain the resonance energies of the first five Mie modes, some of which are located closer in energy than the resolution of our EELS setup. Each map shows a field profile unique to a particular Mie mode. We perform the full-wave EELS simulations and find excellent quantitative agreement with our experimental studies. Our results contribute to EELS investigation of high-index nanophotonics and can be potentially utilized to shed more light on important interference phenomena such as anapole states and bound states in the continuum [54, 108, 109].

When we place the silicon nanoparticle on top of a thin gold film, a new class of hybrid dielectric-metal resonances appear with the original Mie resonances in the silicon nanoparticle remaining largely unchanged. These hybrid resonances depend both on the short-range SPP of the gold film and the Mie resonance of the dielectric nanoparticle. The hybrid mode shows efficient SPP excitation and stronger light confinement than the Mie resonances supported by the isolated nanoparticle. We show both experimentally and via simulation that the hybrid resonance energy can be modulated by the particle size providing a simple approach to excite the SPP at the desired wavelength. Multipole decomposition of the induced field shows that the optical response of the hybrid mode corresponds to an electric dipole. The orientation of the electric dipole is sensitive to the position of the electron beam. Having a vertical orientation at the nanoparticle centre, it gradually tilts toward the gold surface with an increase in the electron distance. The tilt leads to a slight redshift of the hybrid mode. The tilted electric dipole can be potentially utilized to realize directional SPP launching by exciting the nanoparticle with circularly polarized light [110].

We also demonstrate that the short-range SPPs are scattered by the silicon nanoparticle. The scattering results in an interference pattern characterized by the EELS intensity maxima. We derive a simple theoretical expression that describes SPP propagation and reflection and utilize it to experimentally reconstruct the dispersion relation of the short-range SPP supported by the thin film. Our results show the scattering properties of the high-index nanostructures, which can be utilized in the design of new SPP optical elements.

Finally, we perform CL characterization of silicon nanoparticles. Because of the lower acceleration voltage below 30 kV, we identified a significant transition radiation contribution to the CL spectrum. The transition radiation leads to an interference effect generated from the excitation of two electric dipoles on two boundaries of the nanoparticle penetrated by the electron beam. This interference effect is overimposed on the Mie resonances leading to ambiguous, possibly erroneous, assignment of modal characters to spectral features. Therefore, we would advise care when interpreting the CL results or possibly any other electron-based technique at low acceleration voltage.

4.2 Boron phosphide nanoparticles

The work presented in this section is based on Paper C.

4.2.1 Motivation

We find that boron phosphide can be a promising candidate for dielectric meta-atoms. It has a high refractive index and low absorption not only in the visible but also in the ultraviolet range, which is not typical for commonly used materials, such as silicon [111], gallium phosphide [112], and titanium dioxide [113], which have been extensively used

in the visible and infrared ranges. The small direct bandgap edge of these materials limits their application in the UV range since it results in an increased absorption loss in the energy range of interest. Diamond has been suggested to be utilized in the UV spectral range [114, 115], however, it has a moderate refractive index and its integration with nanofabrication techniques is relatively challenging [116]. BP can potentially offer a solution since it has a high refractive index with low losses in the UV.

4.2.2 Fabrication

The samples with BP particles and laser-reshaped spherical BP particles on top of 8 nm silicon oxide membranes are produced by our collaborators and the procedure is described in Paper C.
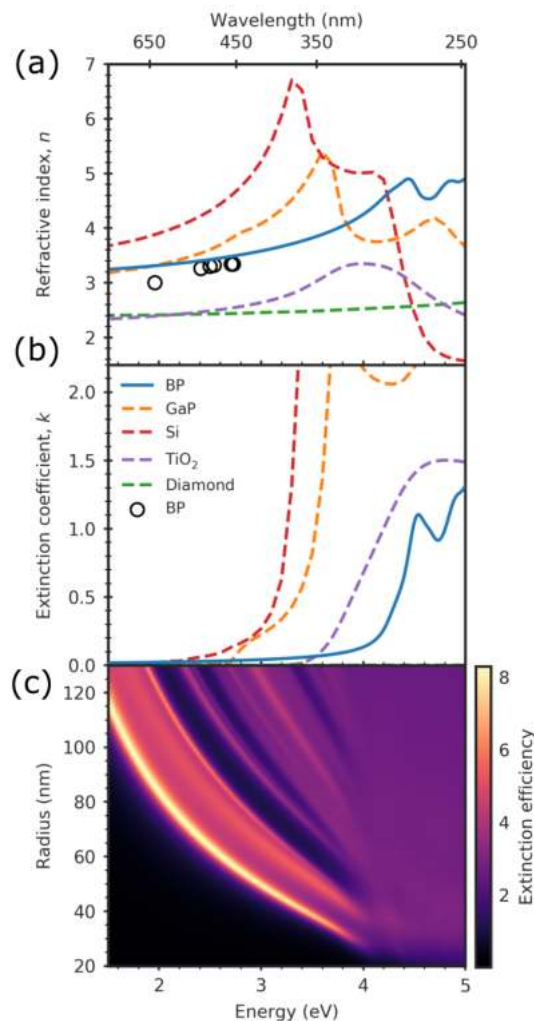
Figure 4.15: Optical response and Mie resonances of BP. (a) Refractive index n and (b) extinction coefficient k of BP calculated using the f-sum corrected BSE method compared with that of some of the commonly used dielectrics in the visible and ultraviolet spectral regions. (c) Extinction efficiency map of BP spheres of varying radii calculated using Mie theory, which demonstrates that Mie resonances can be sustained in the visible and ultraviolet. Adapted from paper C. The refractive indices of GaP, Si, TiO$_2$, diamond and experimental BP are taken from Ref. [117], [117], [118], [119], and [120] respectively.

4.2.3 Optical response

The experimental synthesis of BP crystals have been reported as early as 1957 [121], yet there is limited data on its refractive index [120, 122]. Using the ab initio calculation performed by our collaborators which is described in Paper C, we perform a quantitative comparison of the refractive index of the BP with some common optical materials in Figure 4.15. We observe a high refractive index in the visible and UV range on par with GaP, only slightly smaller than silicon near the violet end of the visible range, but higher in most of the UV range (Figure 4.15(a)). The most noticeable difference lies in its extinction coefficient which is lower than most other materials with an absorption edge lying significantly higher than silicon or GaP (Figure 4.15(b)). The extinction coefficient is comparable to TiO_2 material and higher than the transparent diamond, however, they both have a significantly lower refractive index which needs to be high for compact nanostructures [123]. As such, BP shows a promise for its utilization in the visible range giving a similar performance as silicon or GaP with an extension to the broad UV range - the range which is not achievable by commonly used materials. We demonstrate its broadband operation in extinction efficiency calculations for spheres with variable radii using Mie theory in
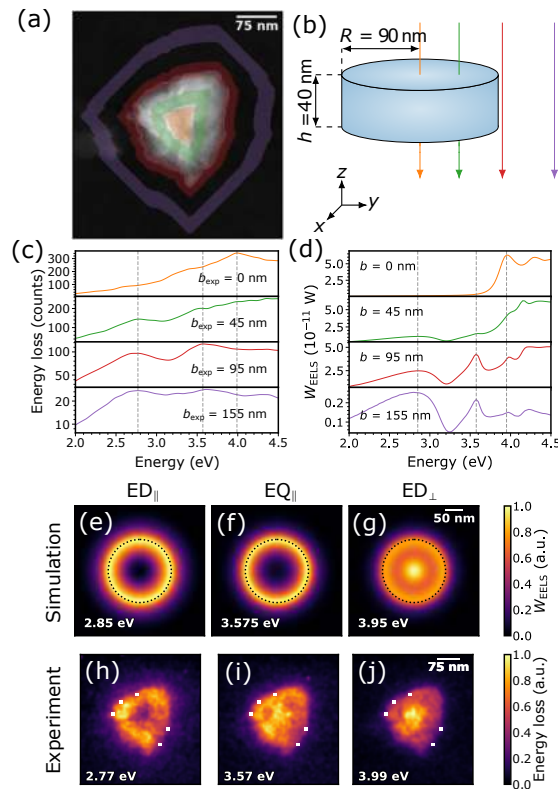
Figure 4.16: Electron energy-loss spectroscopy of BP nanoparticles (a) Experimental STEM image and (b) theoretical set-up depicting the electron beam positions b used to acquire the measured and simulated EELS spectra of (c) and (d), respectively. The triangular-shaped BP nanoparticle is characterized by an effective radius of $R = 90$ nm. Several EELS peaks due to Mie resonances are observed. (e-g) Simulated and (h-j) experimental EELS intensity maps at the Mie resonance energies. The Mie modes are identified as the in-plane electric dipole ($ED_\parallel$), in-plane electric quadrupole ($EQ_\parallel$), and out-of-plane electric dipole ($ED_\perp$) using a multipole decomposition. Adapted from paper C.

Figure 4.15(c) which show clear Mie resonances in the broad spectral region.

4.2.4 Near-field characterization

We perform experimental validation of BP Mie resonances using EELS. Figure 4.16(a) shows a typical STEM image of a triangular-shaped BP nanoparticle with its spectra depicted in Figure 4.16(c). The particle is characterized with an effective radius of 90 nm determined from the effective area of the particle ($A_{eff} = \pi * r_{eff}^2$). The depicted spectra are recorded from different regions which can be used to characterize position-dependant mode excitation. In particular, we can identify two resonances at 2.77 and 3.57 eV when the electron beam is positioned outside the particle, and for the beam in the centre, we have a resonance at 3.99 eV. We perform EELS simulation of a silicon nanodisk geometry (Figure 4.16(b)) to identify the origin of these resonances (Figure 4.16(d)). We fix the radius of the simulated disk at 90 nm and find an optimum height of the nanoparticle to have a close spectral position to the experimental resonance energies (h = 40 nm). The simulated spectra show the same tendencies with two resonances at 2.85 and 3.58 eV outside the particle and a mode at 3.95 eV inside the particle. We perform multipole decomposition [124] of the induced electric field by the electron beam (Figure 4.17) and identify the three resonances by their highest multipole contributions as an in-plane electric dipole (ED$_\parallel$), in-plane electric quadrupole (EQ$_\parallel$), and out-of-plane electric dipole (ED$_\perp$) from low to high energy respectively. The simulated and measured spatial EELS
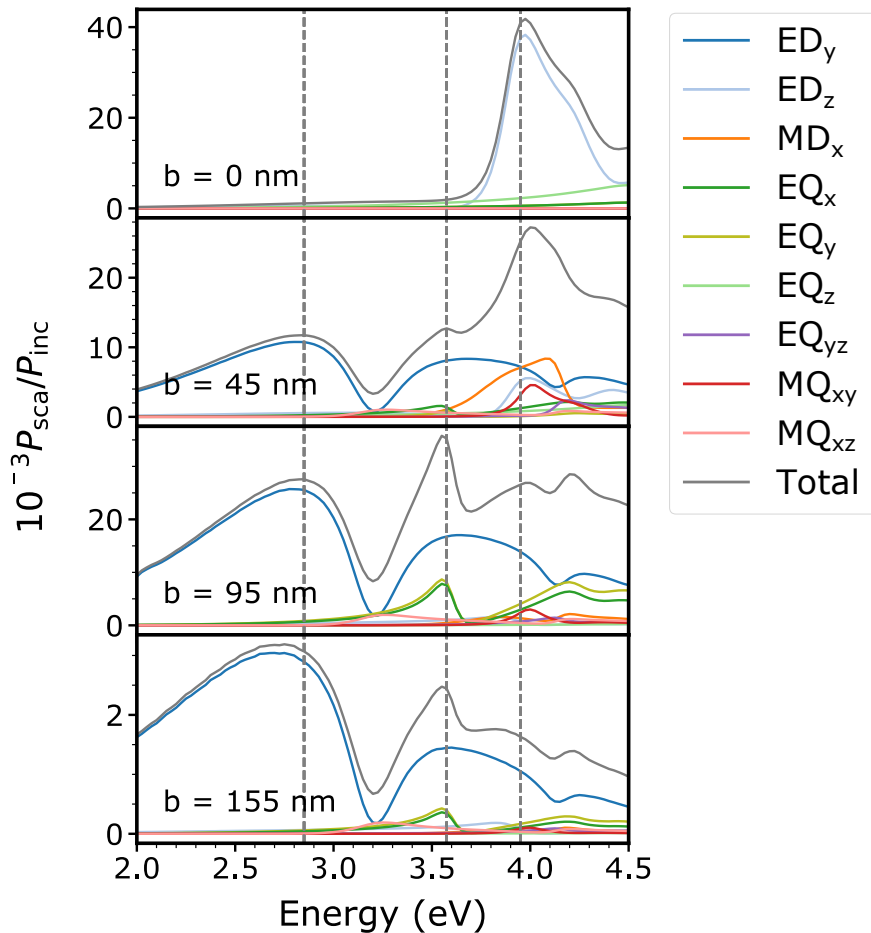
Figure 4.17: Multipole decomposition of the electric field calculated in Figure 4.16(b). Adapted from paper C.

maps (Figure 4.16(e-j)) of the highest and lowest Mie modes are in good agreement, with the 3.6 eV mode lacking a minimum in the particle centre for the experimental maps. The difference in maps can be attributed to the experimental broadening of the resulting spectrum by the EELS setup.

The good agreement between theory and experiment demonstrates the validity of the refractive index calculation and the possibility to utilize the BP material in the UV range.
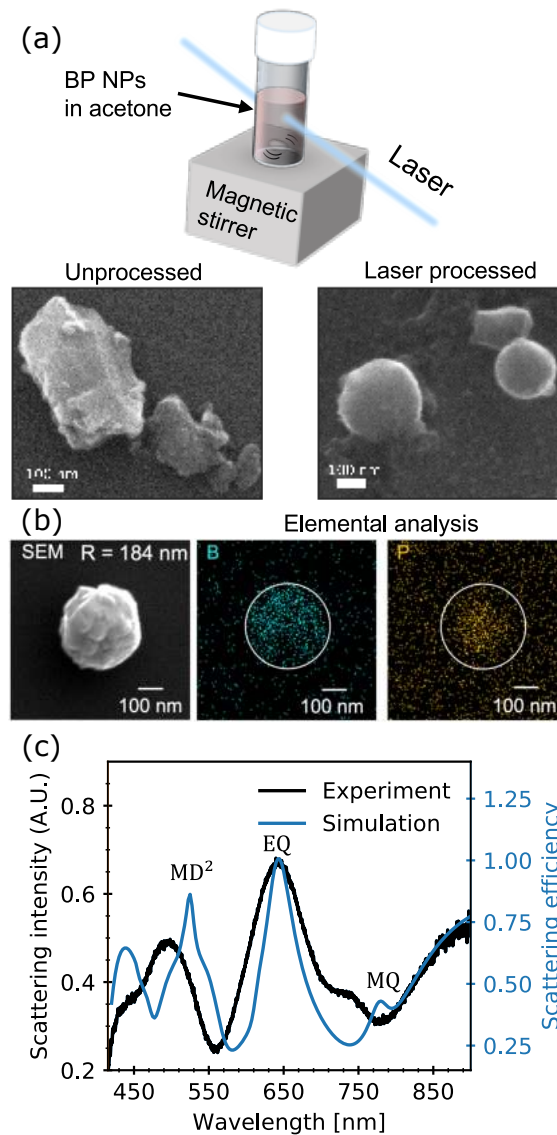
Figure 4.18: Laser reshaping of BP nanoparticles. (a) (top) Reshaping of the BP nanoparticles is achieved by pulsed laser irradiation of unprocessed BP nanoparticles in acetone. The SEM scans of a BP particle (bottom left) before and (bottom right) after the irradiation. (b) Scanning electron microscopy image and energy-dispersive x-ray analysis of reshaped BP nanoparticle, showing a spherical shape without change in composition. (c) Scattering spectrum recorded from the BP nanoparticle in (b) and simulated spectrum for a BP nanosphere with radius $r =165$ nm with multipole decomposition revealing the excitation of the magnetic quadrupole (MQ), electric quadrupole (EQ), and radial higher-order magnetic dipole (MD^2). Adapted from paper C.

We demonstrated Mie resonances at energies as high as 4 eV which is not achievable with silicon nanoparticles.

4.2.5 Spherical BP nanoparticles

Typically, the BP particles have random irregular shapes after their deposition. We suggest an approach to achieve BP particles with spherical shapes by pulsed laser irradiation in an acetone solution (Figure 4.18(a)). The method results in spherically-shaped BP particles with both B and P still present in the nanoparticle after laser irradiation ((Figure 4.18(b)). We perform dark-field scattering characterisation of a typical resulting particle in Figure 4.18(c). The spectrum consists of multiple scattering peaks with the lowest order Mie resonances lying outside the measurement range of our setup which is the result of a relatively large particle size ($r = 184$ nm). We demonstrate the full-field simulation of the particle with a slightly smaller radius $r = 165$ nm where we account for the substrate and the measurement setup which shows a good agreement with the experiment. Using multipole decomposition we find that the scattering peaks are due to the excitation of the magnetic quadrupole MQ, the electric quadrupole EQ, and radial higher-order magnetic dipole MD^2 modes confirming the Mie-resonant nature of spherically-shaped BP nanoparticles.

4.2.6 Concluding remarks

Using an ab initio calculation of the dielectric function of the BP material, we show its high refractive index ($n > 3$) and low extinction coefficient ($k < 0.1$) up to ultraviolet photon energies of 4 eV. We identify the BP as a promising candidate for high-refractive nano-optics in the UV range and perform an experimental demonstration of the Mie resonances supported by the BP nanoparticles in the UV and visible. Combined with a simple demonstrated technique to generate BP nanospheres, our work proposes a solution to advance the nanoscale Mie optics to the ultraviolet range.

4.3 Gold-silver core-shell nanodimers

4.3.1 Motivation

Metal meta-atoms supporting localised surface plasmon resonances produce high absorption and scattering peaks as well as localize and enhance light at subwavelength scales. These effects strongly depend on the material, size and geometry of the device making them attractive for various practical application including sensing [125, 126], nanolenses [127], light guiding [128, 129], medicine [130] and catalysis [131]. Typically, plasmonic devices are optimized to work in a single wavelength band, but there is a growing need for the devices which operate in multiple bands which can be utilized in such fields as wavelength multiplexing or multiphoton nonlinear devices [132]. This is achievable in spatially hybridized nanostructures [133] where the modes of two or several simple plasmon building blocks in close proximity interact and couple to give rise to new modes at distinct energies. One of the structures which support this effect is a metal nanorod dimer [134, 135, 136]. The two nanorods at a small spatial gap can couple resulting in two distinct modes, symmetric and antisymmetric localized surface plasmons with the latter mode having a magnetic character [136, 137]. In particular, we consider the gold dimer structure with an offset [137] where the offset is used for energy separation of the resulting modes. The nanometer-sized offset and gap control can be demanding for the current fabrication methods. One of the approaches to achieve this fine degree of control and have high reproducibility of the devices is a DNA nanofabrication method [138, 139] which we also utilize in our work. We expand the work in Ref. [137] by shifting the magnetic localized surface plasmon resonance into visible and suggest the usage of silver

shells for gold cores [140] to provide an additional mechanism to finely tune the magnetic mode.

4.3.2 Fabrication

We fabricate gold nanodimers with and without a silver shell in four main steps: synthesis of gold nanorods, (with shell) silver coating combined with DNA functionalization or (without shell) DNA functionalization only, conjugation of DNA-functionalized nanostructures with DNA origami and their deposition on TEM membranes. The first three steps are performed by our collaborators and the procedure can be found in Ref. [140]. The fourth step is described below.

Deposition. We deposit the conjugated dimer nanostructures onto 10 nm thick commercially available silicon nitride TEM membranes (TEMwindows). The silicon nitride TEM grids are plasma-treated for 3 min. Next, we functionalize the membrane's surface by application of 10 µL of Poly-L-Ornithine solution (0.01 %) and incubate it for 30 s. The membranes are rinsed with ultrapure water with the excess water being removed with a filter paper. We drop cast 5-7 µL of conjugated dimer nanostructures onto the membrane's surface and incubate for 2 min. Then, we wash the TEM grids once more with ultrapure water with the excess water being removed with filter paper. The samples are left for drying.

4.3.3 Magnetic dipole in the visible

We characterize our structures with electron energy-loss spectroscopy to resolve nanometer gaps present in our devices as well as to investigate their near field properties. For this purpose, we deposit the gold dimers on top of a 10 nm thick silicon nitride membrane. First, we show the EELS response of a single 77×24 nm gold rod (Figure 4.19(a)). Using the position-dependent excitation of the modes by an electron beam, we can identify three modes in the gold rod: a longitudinal surface plasmon (1.77 eV), transverse surface plasmon (2.28 eV) and bulk surface plasmon (2.42 eV) modes. We also map these three modes to obtain their characteristic field profiles in Figure 4.19(b-d). The longitudinal mode depicts two maxima located at the two edges along the length of the rod demonstrating a localised surface plasmon excitation along the long axis of the rod while the transverse mode has one maximum located in the middle of the structure demonstrating the excitation of the localised surface plasmon mode along the short axis, the bulk mode is distributed at the whole volume of the particle which is typical for the bulk plasmon mode. Then, we perform characterization of a gold dimer with a 2.5 nm gap and 43 nm offset (Figure 4.19(e)). As for the single rod case, we can identify three modes (1.57, 2.34, 2.46 eV) with a new mode excited at 1.95 eV. The longitudinal mode (1.57 eV) is redshifted due to an increase in the effective length of the combined structure and shows two maxima at the furthest edges of the combined structure (Figure 4.19(f)). This proves that the gap is sufficiently small to allow plasmon hybridization and shows the symmetric plasmon coupling nature of this mode. The EELS maps of the new mode at 1.95 eV demonstrate two maxima at the closest longitudinal edges between two rods (Figure 4.19(g)). It is characteristic of the magnetic dipole mode which is a result of asymmetric plasmon coupling [137]. Both transverse and bulk modes exhibit a slight blue shift compared to the single rod case which can be due to slightly smaller average widths of two rods. The transverse mode EELS map shows two maxima in the middle of the rods with a slight overlay of the map from the magnetic dipole mode (Figure 4.19(h)). The bulk mode, as expected is distributed around the whole volume of the rods (Figure 4.19(i)).

We deposit silver shells around our gold rods to fine-tune the gold dimers and perform their characterization. The presence of the silver shell modifies the EELS response of the
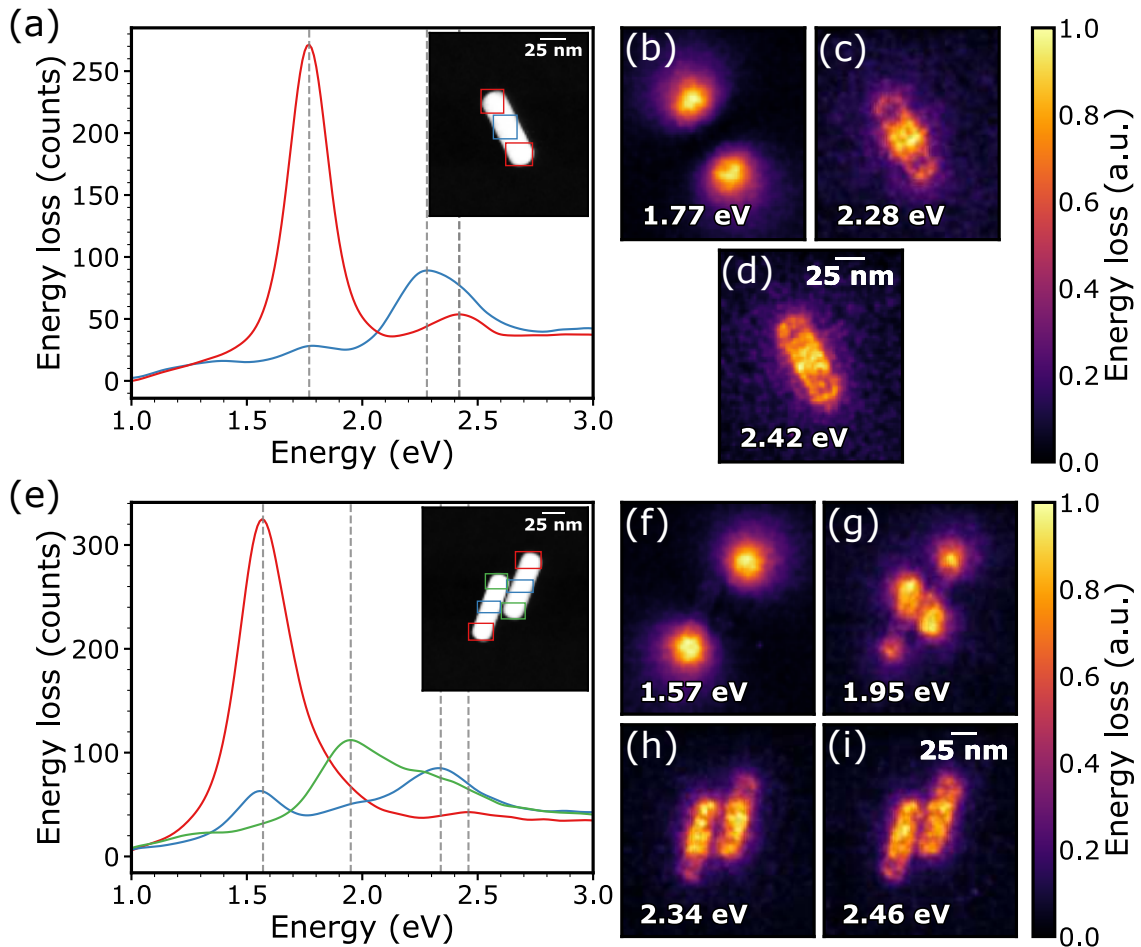
Figure 4.19: EELS of a gold dimer. (a) Experimental EELS spectrum of a 77×24 nm Au single rod acquired from the electron beam positions indicated in the STEM image inset. (b-d) Experimental EELS maps of an Au single rod for three rod modes. (e) Experimental EELS spectrum of a (77×22 (left), 77×24 (right)) nm Au dimer (2.5 nm gap, 42 nm offset) acquired from the electron beam positions indicated in the STEM image inset. (f-i) Experimental EELS maps of an Au dimer for four dimer modes.

single rod (Figure 4.20(a)). The longitudinal mode at 2.17 eV experiences a large blue shift of 0.4 eV in comparison to the gold rod case. As expected, it has two maxima along the length of the rod (Figure 4.20(b)). The transverse and volume modes mask each other which makes it not possible to differentiate between these modes. We expect to have 1 transverse and 2 volume modes of gold and silver respectively in the 2.5-4 eV energy range. Even plotting the near-field profiles (Figure 4.20(c,d)) at the edges of the combined broad peak does not allow us to safely separate the modes. The spectral response of the gold dimers with a silver shell also exhibits energy shifted peaks in comparison to the gold dimers ((Figure 4.20(e))). Both the longitudinal and transverse modes show a large blue shift of 0.22 and 0.34 eV respectively. They have their typical EELS maps ((Figure 4.20(f,g))) as for the gold case. The others modes are also masked by each other as for the single rod with a shell case. There are some minor alterations in the EELS maps at the energy edges of the combined EELS peak (Figure 4.20(h, i)), which can be mainly due to the presence of the strong magnetic dipole mode.
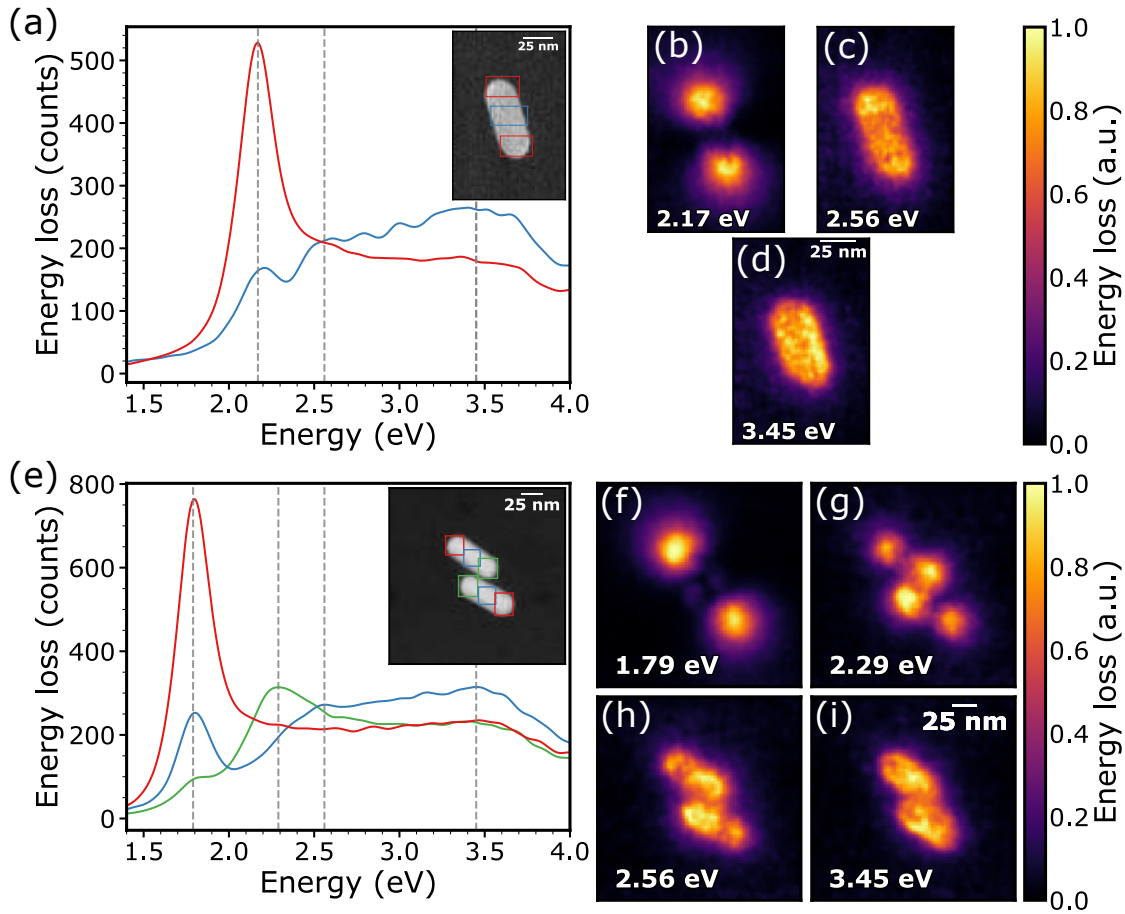
Figure 4.20: EELS of a gold dimer with a thin silver shell. (a) Experimental EELS spectrum of a 67×26 nm Au single rod with a thin silver shell acquired from the electron beam positions indicated in the STEM image inset. (b-d) Experimental EELS maps of an Au single rod with a thin silver shell for three rod modes. (e) Experimental EELS spectrum of a (64×26 (top), 67×27 (bottom)) nm Au dimer (4 nm gap, 29 nm offset) with a thin silver shell acquired from the electron beam positions indicated in the STEM image inset. (f-i) Experimental EELS maps of an Au dimer with a thin silver shell for four dimer modes.

4.3.4 Concluding remarks

We shift the magnetic mode supported by the gold dimer nanostructure and characterize it via EELS. EELS allows us to obtain near field maps of the symmetric and antisymmetric modes present in this type of structure which can be used to perform the mode identification. We suggest and experimentally demonstrate a fine-tuning mechanism of the dimer modes by depositing a thin silver shell.

4.4 Nickel nanospheres

4.4.1 Motivation

Another approach to achieve hybridized plasmonic systems is the usage of interband transitions (IBT) in some metal nanoparticles where the hybridization is achieved via the interaction between the localized surface plasmon and IBT [141]. Contrary to the previous case of metal dimers, the resonator is coupled to itself since it supports both resonances that couple to each other. This hybridization effect have been demonstrated in such metals as Al [142] and Ni [143]. While the latter demonstrates the hybridization effect without

consideration of different multipole resonances and does not investigate the response from individual particles, we shed the light on hybridization effect between different order multipoles and the IBT transition of individual nickel particles. STEM EELS is particularly well suited for this purpose since it allows us to study the response of isolated particles and access the deep UV spectral range where we investigate these resonances.

4.4.2 Fabrication

We use commercial nickel nanospheres of 99.7 % purity in a nanopowder form with radii of 40-180 nm. We add around 1 g of this nanopowder to acetone and ultrasonicate for
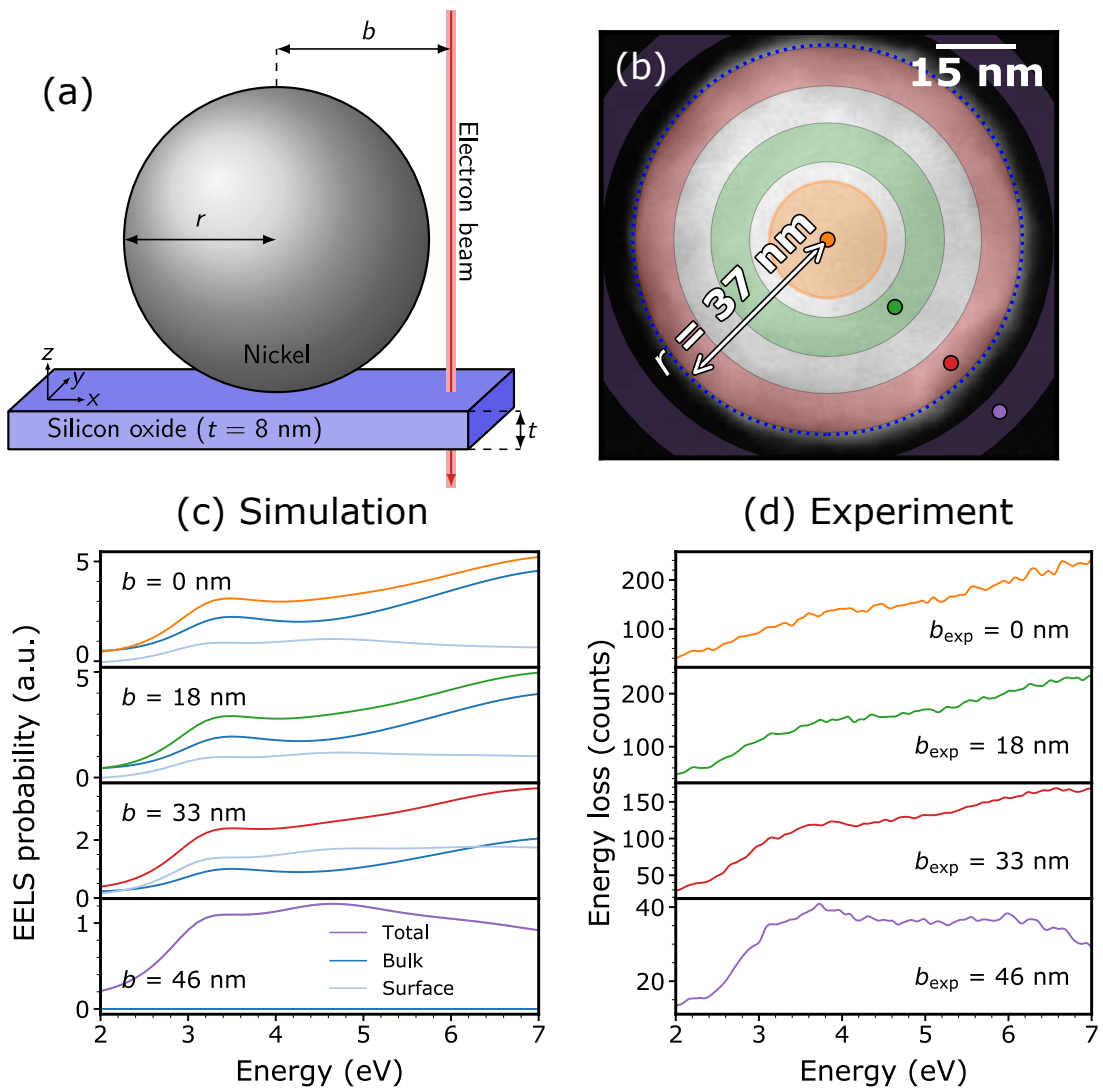
Figure 4.21: Bulk and surface contributions to EELS signal of a nickel nanosphere. (a) Schematic of a nickel nanoparticle placed on an 8 nm silicon oxide membrane. (b) STEM image of the nanoparticle, where the coloured areas represent the integration regions for the experimental EELS signal, and the coloured points are the position of the electron beam in the simulation. (c) Simulated EELS spectra of a nickel nanoparticle ($r = 37$ nm) at different impact parameters b from the colour points shown in (b). Each EELS spectrum is separated into bulk and surface contributions. (d) Experimental EELS spectra for a particle with radius $r = 36.8 \pm 0.8$ nm acquired from the regions shown in (b).

10 min to ensure nanospheres separation. We drop cast the Ni nanospheres in acetone onto the substrate with an 8 nm thick silicon dioxide membrane and wait for the acetone to evaporate.

4.4.3   Electron excitation: bulk vs surface losses

We use electron energy-loss spectroscopy to characterize the resonances of nickel nanoparticles present in a broad spectral range. Figure 4.21(a) shows a schematic of the experiment where we probe a nickel nanoparticle with radius r on top of an 8 nm silicon oxide membrane with an electron beam displaced from the particle centre by an impact parameter b. We probe a nanoparticle with $r = 36.8 \pm 0.8$ nm at different impact parameters inside and outside the nanoparticle indicated in Figure 4.21(b) and show simulated EELS spec-
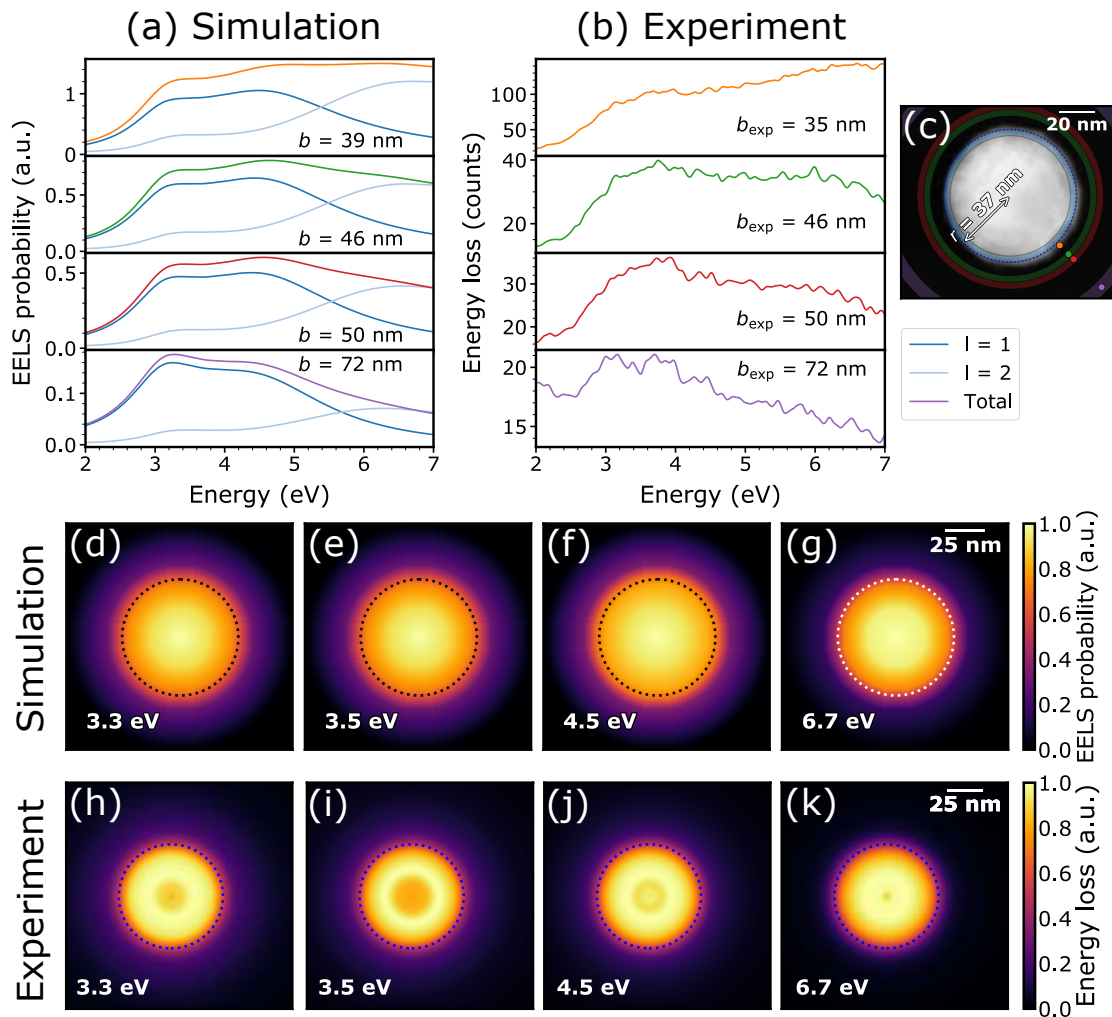
Figure 4.22: Interaction of multipoles with IBT. (a) Simulated EELS spectra of a nickel nanoparticle ($r = 37$ nm) at different impact parameters b from the colour points shown in (c). Each EELS spectrum is separated into contributions for the first two azimuthal $l = 1, 2$ numbers. (b) Experimental EELS spectra for a particle with radius $r = 36.8 \pm 0.8$ nm acquired from the regions shown in (c). (c) STEM image of the nanoparticle, where the coloured areas represent the integration regions for the experimental EELS signal, and the coloured points are the position of the electron beam in the simulation. (d-k) Simulated (top) and experimental (bottom) EELS intensity maps of the four resonances supported by the Nickel nanoparticle. The EELS maps are individually normalized.
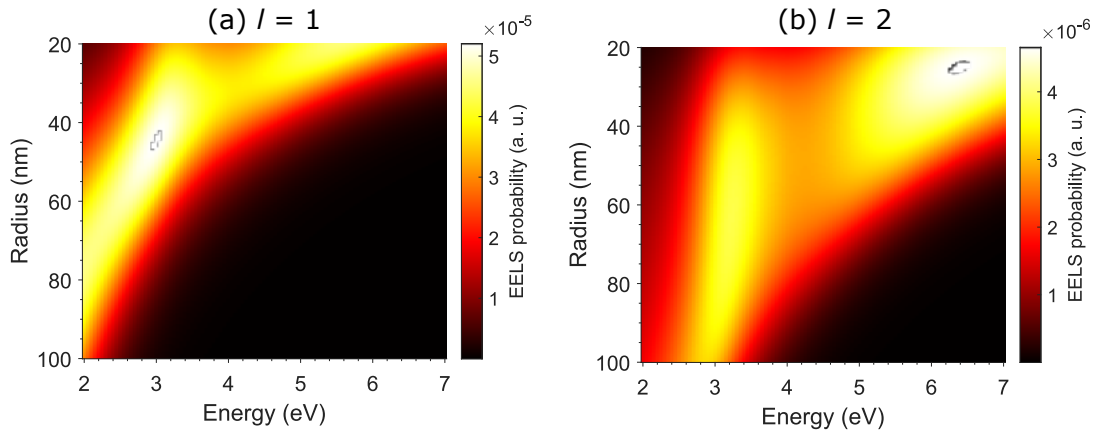
Figure 4.23: EELS simulation at the impact parameter $b = 3r$ as a function of the nickel particle radius r for (a) $l = 1$ and (b) $l = 2$.

tra of $r = 37$ nm nickel nanoparticle in vacuum in Figure 4.21(c). Here, we separate the EELS signal into bulk and surface contributions and demonstrate their dependence on the impact parameter. The bulk contribution dominates in the particle centre having a peak at 3.5 eV due to interband transition. As we move further from the particle, the surface contribution becomes more pronounced with two peaks at 3.4 and 4.7 eV which is indicative of the hybridization between the IBT and localized surface plasmon of the particle. The total EELS signal, therefore, is rather complicated due to position dependant weighting of bulk and surface contributions which lead to apparent shits in the EELS signal. We can neglect the effect of the bulk contribution if we limit ourselves to the spatial range where the electron beam position is outside the particle which we use to demonstrate and discuss the hybridization effect in more detail in the next section. The experimental data in Figure 4.21(d) shows similar trends having a very broad peak at the particle centre and more two more pronounced resonances when the beam is outside the particle.

4.4.4 Interaction of multipoles with IBT

Figure 4.22(a-c) shows simulated and experimental EELS spectra of the same nickel nanoparticle as in Figure 4.21. We separate the simulated EELS spectra into different azimuthal contributions $l = 1, 2$ and show the dependence on the impact parameter (Figure 4.22(a)). Both $l = 1$ dipole and $l = 2$ quadrupole multipoles show two peaks at 3.3 and 4.5 eV ($l = 1$) or 3.5 and 6.7 eV ($l = 2$). The shift in the energy of the dipole mode at 3.3 eV compared to the 3.5 eV IBT can be indicative of the hybridization effect between the IBT and the dipole LSPRs supported by the particle. For the quadrupole, the energy shift is not observable due to the large energy separation between the IBT and the quadrupole. The impact parameter dependence shows a decrease in the contribution of higher energy modes when the beam is moved further from the particle for both multipoles. This is also accompanied by a decrease in the contribution of the higher-order multipoles to the EELS spectrum. This is expected as higher energy modes are typically localized closer to the nanoparticle surface. The experiment shows a similar trend in the overall EELS spectrum with some apparent shifts in the EELS spectrum with the change in the impact parameter. We perform EELS mapping at four energies in Figure 4.22(d-k) both via simulation and experiment which show higher localization of the field to the particle surface for higher-order modes.

We demonstrate the influence of the particle radius in the IBT - LSPR hybridization in Figure 4.23(a-b) where we plot the change in the EELS signal for dipole and quadrupole

multipoles as a function of the nickel particle radius at the impact parameter $b = 3r$. Both multipoles show two resonances starting from a particular radius where LSPR lie higher than the IBT with no second peak observable when the LSPR resonance is lying much lower than the IBT. When the LSPR approaches the IBT, the peak splits into two resonances which can be indicative of the hybridization of the LSPR and IBT modes. As can be expected, this condition shifts to larger radii for the higher-order modes.

4.4.5 Concluding remarks

Using EELS, we characterize individual nickel nanoparticles and demonstrate the contributions from bulk and surface EELS signals when the beam is moved around the particle. We show the complex shape of the EELS signal with multiple possible resonances and identify a region to simplify the characterization of the coupling effect between the LSPRs and IBT. Using the outside beam positions with zero bulk contributions, we experimentally show a hybridization effect in a nickel sphere between the LSPRs of different multipole orders and the IBT supported by a nanosphere which gives rise to two hybridized resonances for a particular particle radius range. We also demonstrate that hybridization of higher-order multipoles with the IBT involves the increase in the particle size since larger particles support more multipoles.

5 Reconfigurable meta-atoms

This chapter is dedicated to reconfigurable meta-atoms. We perform a modification of spectral response from the meta-atoms using two physical effects, the thermo-optic effect and electromechanical tuning. We use the thermo-optic effect to modify the response from spherical silicon nanoparticles by application of temperature. We also perform thermal near-field tuning between different Mie modes using the characteristic EELS near-field maps. In the case of electromechanical tuning, we fabricate silicon beams with a nano-sized cross-section and tune their response by electromechanical bending.

5.1 Thermal tuning of silicon nanoparticles
The work presented in this section is based on Paper D.

5.1.1 Motivation
The thermo-optic effect is a change in the refractive index of a material n with temperature T. It is proved to be an appealing tuning mechanism because of its reversibility and ability to provide continuous and large spectral shifts. Far-field optical response of nanoparticles and metasurfaces based on such materials as silicon, germanium, lead telluride [31, 33, 144, 145, 146] and hybrid silicon-gold [147] has been effectively tuned using this effect. In this regard silicon which has a high refractive index, high thermo-optic coefficient dn/dT [33] and CMOS compatibility is an attractive candidate for thermal tuning. So far, thermal tunning of silicon have been performed in nano- and micron-sized structures with resonances in the infrared spectral ranges where moderate tunability can be achieved. We would like to perform thermal tuning of the resonances in the visible range where we predict an increase in the tuning range due to an increased thermo-optic coefficient near the direct bandgap edge.

Moreover, many important photonics applications rely on the modification of the near-field, such as nonlinear processes [148, 76], Raman scattering [149, 150, 151], and light emission [152, 153, 154], thus the dynamic tuning of the near-field can provide new applications in these areas. However, tuning in dielectric components have been mostly demonstrated in the far-field with little attention given to the near-field. Here, we demonstrate a reversible thermal tuning of both far- and near-fields of Mie resonances in silicon nanoparticles in the visible range.

5.1.2 Fabrication
We deposit 10 µL of the silicon nanoparticles in methanol (fabrication of Si nanoparticles is described in Section 4.1.2) onto commercially available thermal E-chips produced by Protochips and nitrogen dry them after 1 minute wait time. The chips have membranes composed of a silicon carbide heating layer on top of a 40 nm thick silicon nitride layer. The silicon carbide can be heated up to 1473 K with a temperature accuracy over 95.5% (example: 1073±48 K) and a 99.5% homogeneous temperature profile across the entire chip. The membrane has nine 8 µm holes where only the silicon nitride layer is present. The experimental characterization is performed on these areas.

5.1.3 Thermal tuning of silicon Mie resonances
Figure 5.1(a) shows a schematic of the experiment, where an isolated silicon nanoparticle with a radius r on top of a 40 nm silicon nitride membrane is heated from room temperature to 1073 K using a ceramic heater (not shown). The heating leads to the change in the refractive index of silicon due to the thermo-optic effect shown in Figure 5.1(b). The

real part of the refractive index increases up to 0.6 at 1100 K in comparison to room temperature due to the positive thermo-optic coefficient in the 1.5 eV to 3 eV energy range. The positive thermo-optic coefficient is a result of temperature-induced changes in the electronic transitions in silicon [156], It should be noted that silicon also demonstrates a negative thermo-optic coefficient at energies higher than the temperature-dependent direct bandgap edge (3.4 eV at room temperature [155]), or for a non-negligible concentration of thermally-generated free carriers [145]. The imaginary part of the refractive index also increases, but mainly due to an increase in the phonon population with temperature. This results in an increased probability of indirect transitions, thus, increased light absorption [157]. The effect is more prominent at 3 eV because of its proximity to the direct bandgap energy of silicon.

We perform EELS characterization of a typical silicon nanoparticle with $r = 82.4 \pm 1.9$ nm at different temperatures in Figure 5.1(c-d) where the electron beam is positioned at the locations indicated in Figure 5.1(e). The two locations are selected for efficient ED exci-
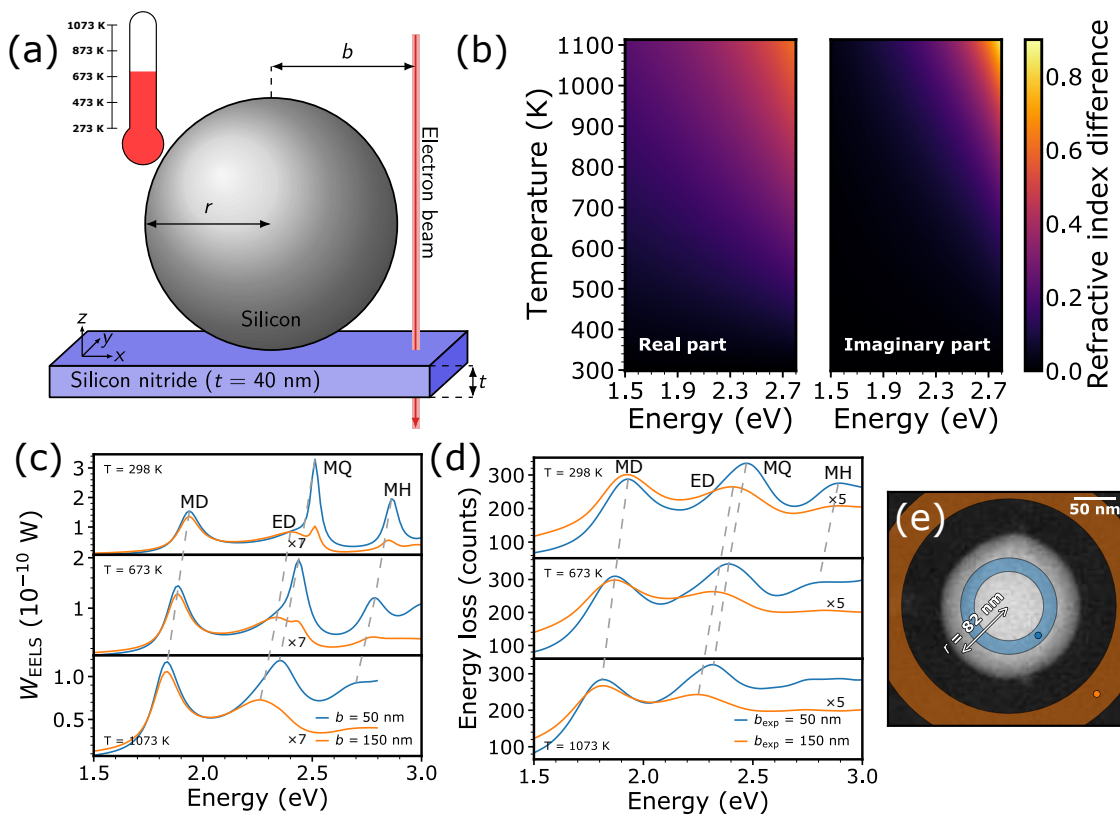
Figure 5.1: Thermal tuning of Mie resonances in silicon nanoparticles. (a) Schematic of a silicon nanoparticle of radius r placed on a silicon nitride membrane and excited by an electron beam. The impact parameter b denotes the distance between the electron beam and the centre of the nanoparticle. The temperature is applied to the nanoparticle by a ceramic heater located around the nitride membrane. (b) Temperature modulation of the silicon refractive index taken from Ref. [155]. (c) Simulated and (d) experimental EELS spectra of a silicon nanoparticle with a radius $r = 82.4 \pm 1.9$ nm acquired from the electron beam positions shown in (e). (e) STEM image of the nanoparticle, where the coloured areas represent the integration regions for the experimental EELS signal, and the coloured points are the position of the electron beam in the simulation. Adapted from paper D.
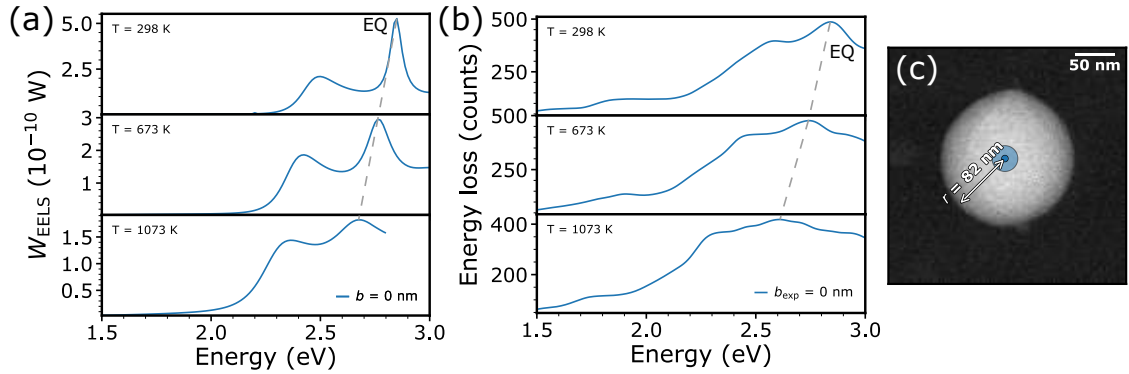
Figure 5.2: Thermal tuning of the EQ Mie resonance in a silicon nanoparticle. (a) Simulated and (b) experimental EELS spectra of a silicon nanoparticle with a radius $r = 82.4 \pm 1.9$ nm acquired from the electron beam positions shown in (c). (c) STEM image of the nanoparticle, where the coloured area represents the integration region for the experimental EELS signal, and the coloured point is the position of the electron beam in the simulation. Adapted from paper D.

tation outside the particle and efficient MQ and MH inside the particle (see Section 4.1.4). The increase in temperature leads to the redshift of all Mie resonances (MD, ED, MQ, MH) due to the increase in the real part of the refractive index, while the increase in the imaginary part of the refractive index leads to the broadening of the Mie resonances with the MH mode, located close to the direct bandgap edge, barely detectable at temperatures higher than 673 K in the experiment. The MD resonance energy is shifted by around 0.1 eV as the temperature is elevated from room temperature to 1073 K, while the higher-order ED, MQ and MH modes demonstrate larger shifts of around 0.15 eV each. The electric quadrupole (EQ) which is efficiently excited in the particle centre shows a comparable shift of 0.15 eV and similar to MH mode is barely detectable at the temperature higher than 673 K (Figure 5.2). Both EELS simulation and experiment are in good agreement with broader modes in the experiment due to the energy resolution of the EELS setup.

We perform EELS mapping of the $r = 82.4 \pm 1.9$ nm silicon nanoparticle Mie modes at the lowest and highest temperatures in Figure 5.3. Overall, the EELS maps follow similar EELS intensity distributions as in Section 4.1.4. The main difference is that the EELS maps of the spectrally close Mie modes pairs (ED and MQ, EQ and MH) at 1073 K obtain even more features from each other. This leads to almost non-distinguishable EELS maps of EQ and MH modes at 1073 K with ED and MQ still looking unique. Both simulation and experiment closely follow each other, however, there are some differences caused by the energy resolution of the EELS setup, which influences the experimental field profiles of spectrally-close Mie modes.

We extend the analysis of Mie resonances thermal tuning for different particle sizes in Figure 5.4(a). We show the change in the first five Mie modes (MD, ED, MQ, EQ, MH) resonance energies both via theory and experiment for the silicon nanoparticle with 40-100 nm radii. The good agreement between the theory and experiment demonstrates an ability to thermally tune all Mie resonances by up to 0.15 eV at the elevated temperature of 1073 K with the modes around 3 eV having a lower shift of around 0.1 eV. The different spectral shifts for Mie modes are caused by the nonlinear dependence of the refractive index with energy and temperature. From Figure 5.1(b), we have a larger change in the
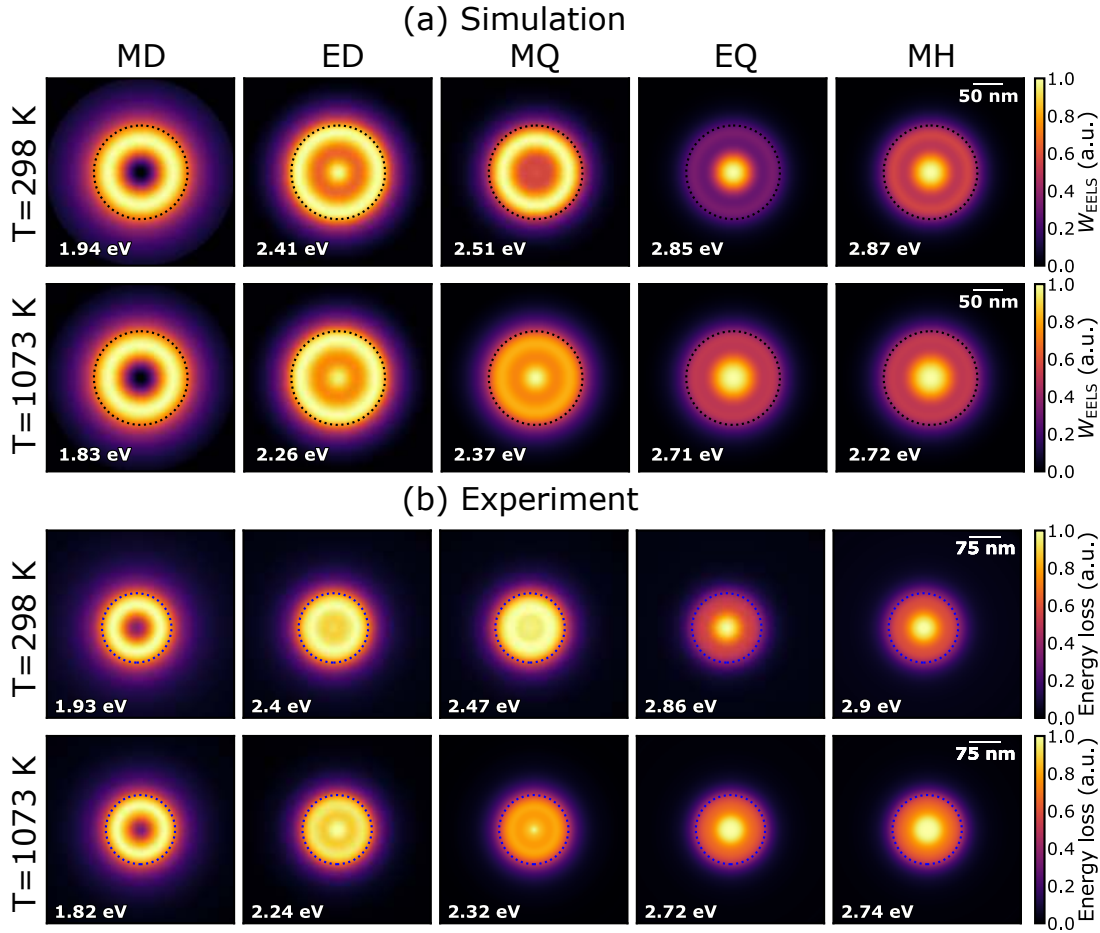
Figure 5.3: EELS mapping of a silicon nanoparticle Mie modes at different temperatures. (a) Simulated EELS maps of a silicon nanoparticle with a radius $r = 80$ nm at different temperatures (rows) and different Mie resonances (columns). (b) Experimental EELS maps of a silicon nanoparticle with a radius $r = 82.4 \pm 1.9$ nm at different temperatures (rows) and different Mie resonances (columns). Note that, the EQ and MH resonance energies at $T = 1073$ K can not be resolved in the experimental spectra due to thermal-induced damping of the modes. Hence, we assume that the EQ and MH modes undergo the same thermally-induced spectral shift as seen in the simulations and depict the experimental EELS signal at the energies 2.72 eV and 2.74 eV, respectively. Adapted from paper D.

real part of the refractive index at higher energies which leads to larger spectral shifts of Mie modes with higher resonance energies. The combined effect of the increased imaginary part of refractive index at elevated temperatures and the energy resolution of our EELS setup makes it impossible to identify the resonances energies of some Mie modes located above 2.5 eV. In particular, the MD resonance cannot be experimentally resolved for the smallest particle (42 nm radius) at temperatures above 673 K, the MH and EQ resonances are not observable for the average-sized nanoparticles (82 nm radius) at the same temperatures, while large nanoparticles (99 nm radius) are not affected.

We quantify the thermal tunability using the linewidth tunability $\Delta\lambda/\mathrm{FWHM}$ which is defined as the spectral shift of the Mie resonance wavelength at elevated temperatures relative to the room temperature, normalized by its full-width at half-maximum at the el-
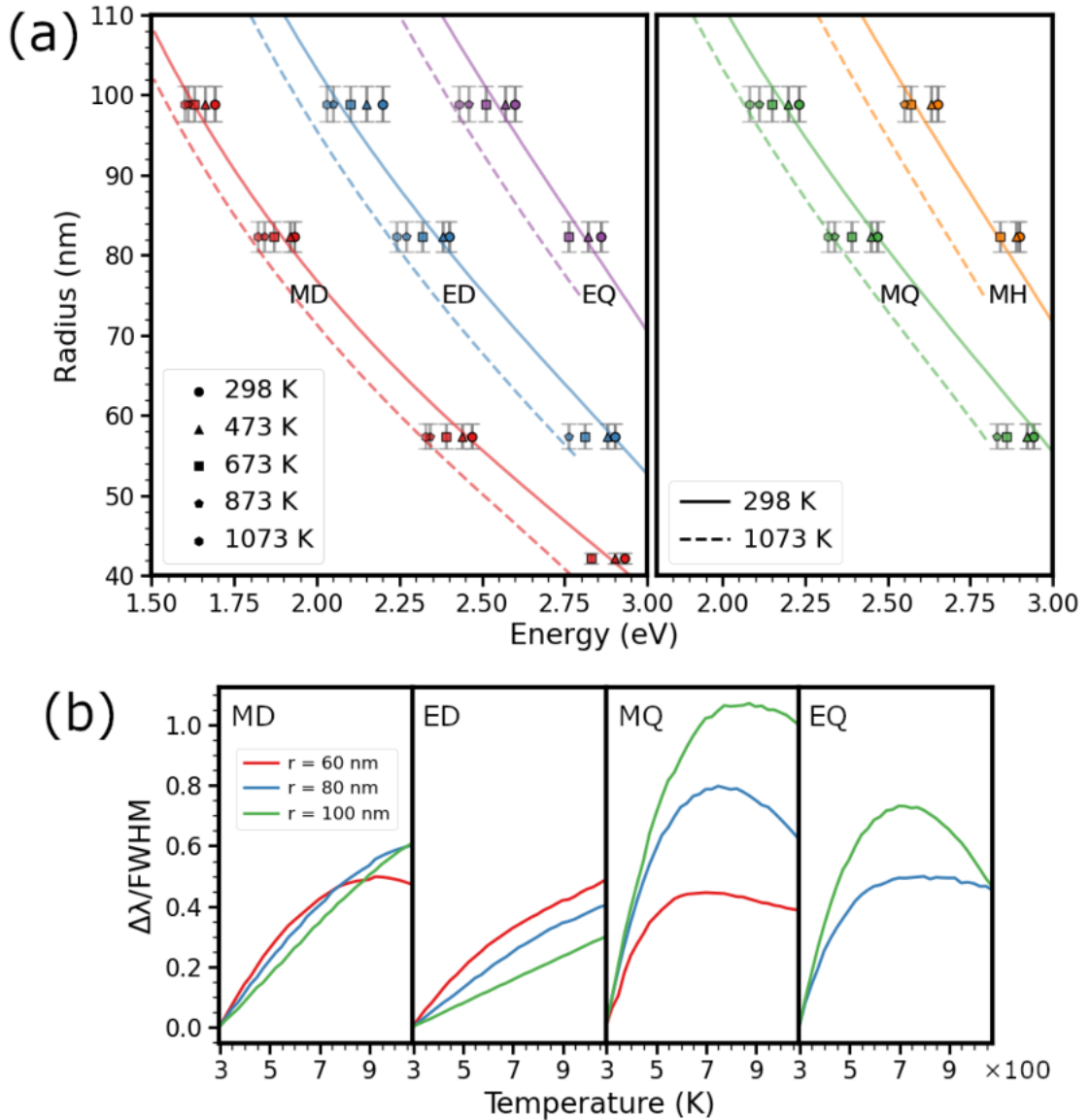
Figure 5.4: Tunability of Mie resonances. (a) Measured resonance energies as a function of particle radius and temperature for the first five Mie resonances in silicon nanoparticles. The colour points represent experimental values, and the colour lines show the first maxima of the different Mie scattering coefficients. ED/EQ and MQ/MH resonances are separated into two plots for clarity. (b) Simulated linewidth tunability as a function of temperature for the first four Mie modes supported by silicon nanoparticles with different radii. Adapted from paper D.

evated temperature. The linewidth tunability above one corresponds to more than one linewidth tuning of the resonance wavelength. We calculate it from the theoretical EELS spectra of a silicon sphere at fixed impact parameters $b = 2r$ [83]. The theoretical EELS spectra are calculated for separate azimuthal coefficients l = 1,2. Then, we fit them with two Lorentzian functions, resulting in the parameters for different couples of multipoles (MD and ED for l = 1, MQ and EQ for l = 2). We fix the resonance wavelength at the first maximum of the Mie scattering coefficient for a respective multipole and find the full-width at half-maximum of the Lorentzian from the fit. We use a split Lorentzian function (width of

the distribution is different between left and right slopes) for the ED mode, while we utilize symmetrical Lorentzian function for the rest of the modes. The fit is performed using the python package LMFIT.

The linewidth tunability of the Mie resonances has a non-linear dependence on their resonance energies defined by the particle radius since the resonance experience both the increase in the real and imaginary parts of the refractive index at elevated temperatures. Figure 5.4(b) shows the numerically calculated linewidth tunability of the first four Mie modes supported by silicon nanoparticles in the 60-100 nm radii range. The linewidth tunability of the MD resonance increases continuously by up to 0.6 except for the 60 nm particle, which peaks at 923 K and decreases slightly. The ED resonance shows a similar trend of increasing with temperature with larger particles having smaller overall tunability. The higher-order MQ resonance demonstrates the largest linewidth tunability, reaching its peak value at a higher temperature with the increase in particle size (700 K and 0.44 tuning for 60 nm nanoparticle, 820 K and 1.07 tuning for 100 nm nanoparticle). The further increase in the temperature leads to a continuous decrease in the linewidth tunability due to thermally-induced broadening of the direct bandgap edge in silicon. The EQ linewidth tunability has a similar lineshape with an approximately 1.5 times smaller peak value. These results show the ability to optimize the thermal tuning of fundamental Mie
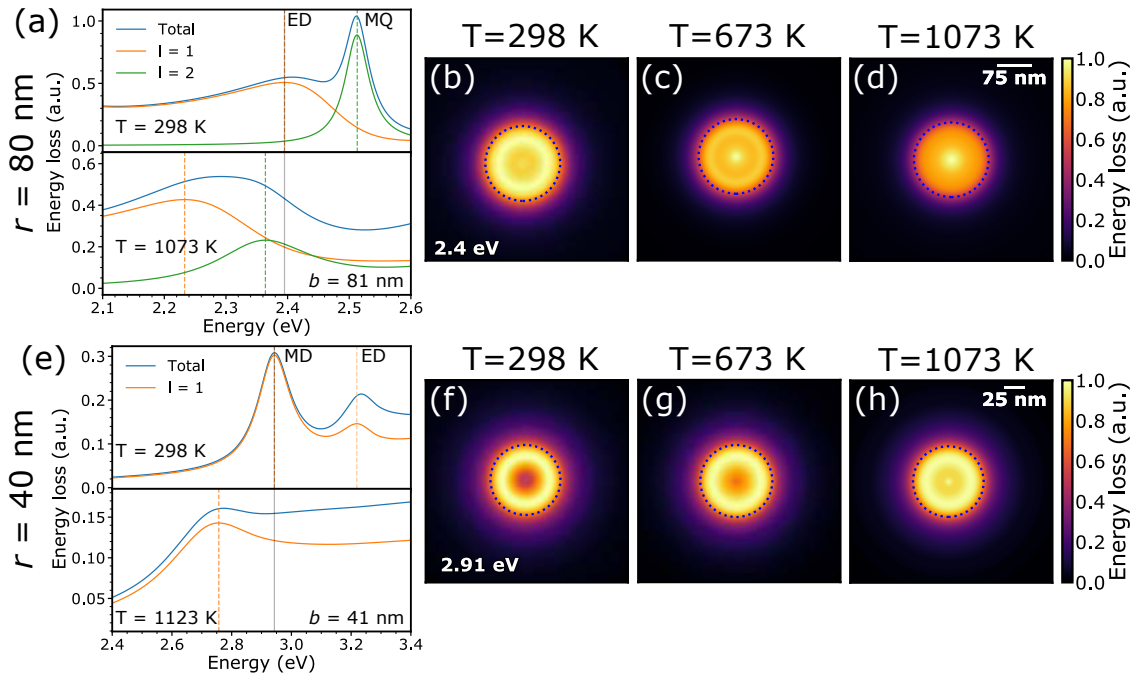
Figure 5.5: Thermal near-field tuning of silicon Mie modes. (a) Multipole decomposition of the EELS signal into different azimuthal contributions l for a particle with $r = 80$ nm. The decomposition is performed at two temperatures for the impact parameter $b = 81$ nm. (b-d) Experimental EELS maps of a particle with $r = 82.4 \pm 1.9$ nm for a fixed energy of 2.4 eV (ED at the room temperature) at different temperatures. (e) Multipole EELS decomposition at two temperatures for a particle with $r = 40$ nm with impact parameter $b = 41$ nm. (f-h) Experimental EELS maps of a particle with $r = 42.2 \pm 0.7$ nm for a fixed energy of 2.91 eV (MD at the room temperature) at different temperatures. Note, that the refractive index in (e) is taken from Ref. [158] due to a limited energy range of the refractive index in Ref. [155]. Adapted from paper D.

resonances to achieve the large tuning values above unity.

5.1.4 Thermal near-field tuning of silicon Mie resonances

We use the near-field maps of different Mie modes (Figure 5.3) to show near-field tuning of the EELS field profiles at the energy of interest. Figure 5.5 demonstrates near-field tuning with temperature for two nanoparticle sizes. For a $r = 80$ nm silicon nanoparticle, a multipole decomposition of the EELS spectrum [83] shows that there are two main contributions coming from the first two azimuthal components $l = 1$ and $l = 2$ (Figure 5.5(a)). Each azimuthal component with $l = 1$ ($l = 2$) contains two resonances: the MD and ED for $l = 1$ (MQ and EQ for $l = 2$). We consider the energy of interest of 2.4 eV which is the ED resonance energy at room temperature. When the temperature is increased to 1073 K, the multipole decomposition shows that the energy crosses the MQ resonance energy. We show the accompanying changes in the experimental EELS intensity maps at different temperatures (5.5(b-d)) which reveals that the near field is tuned from the ED mode at room temperature to the MQ mode at 1073 K.

For the particle with the radius $r = 40$ nm, the EELS spectrum mainly consists of only $l = 1$ contribution (Figure 5.5(e)). We fix the energy of interest at 2.91 eV which is the MD resonance energy at room temperature. At the elevated temperature of 1073 K, the energy of interest is in the flat region of the spectrum. We plot the near-field changes in the EELS maps in Figure 5.5(f-h) which show that even without having spectral features, the near-field tuning remains accessible, where we shift the EELS intensity map from the characteristic of the MD mode EELS maps to the ED mode EELS map at the elevated temperature.

5.1.5 Stability

In-situ EELS allow us to track the morphological changes in the nanoparticle upon heating via STEM imaging. The morphological changes can be attributed to the nanoparticle size and shape changes due to temperature treatment, such as melting. The morphological data from STEM imaging combined with the spectral response from the EELS characterization allows us to ensure stable and reversible operation of the nanoparticles under the temperature treatment.

Figure 5.6(a-d) shows the STEM images of a typical silicon nanoparticle at different temperatures. The STEM images are taken with several minutes time gaps after the heating to the temperature of the interest to ensure the thermally stable condition of the TEM chip. Using the image analysis (Section 4.1.3) we find no change in the particle radius for temperatures up to 1073 K which proves that there are no thermal expansion effects in silicon. When the particle is heated further (Figure 5.6(d)), we observe irreversible changes in the particle shape resulting in a more faceted particle in the beginning. It should be noted that the changes in the particle geometry are time dependant, i.e. the particle shape is constantly modified under the temperature treatment at temperatures higher than 1073 K, leading to a total melting of the particle. We extend this procedure to 31 silicon nanoparticles with different sizes in Figure 5.6(e) where we show that approximately two-thirds of the particles remain stable up to 1073 K temperature with all particles being stable for 100 K lower temperature. This shows that the majority of the particles can be safely operated up to 1073 K temperature without any changes in the nanoparticle morphology. To the best of our knowledge, this is the highest operating temperature of the thermally actuated silicon nanoparticles, however, it is nonetheless smaller than the melting point of the crystalline silicon (1688 K). The possible reasons for the lower melting point of our nanoparticles can be attributed to the size-dependent melting effects, electron beam induced heating, pollycrystallinity or doping. Size-dependent melting should
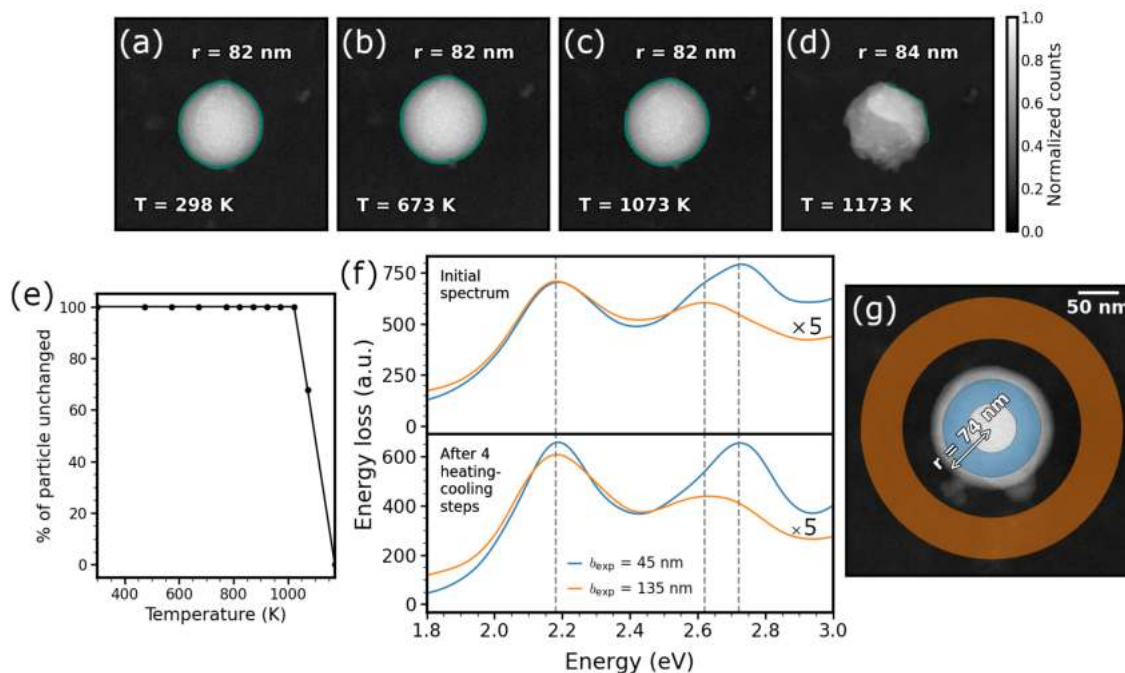
Figure 5.6: Stability of thermally tuned nanoparticles. (a-d) STEM images of a silicon nanoparticle with $r = 82.4 \pm 1.9$ nm at different temperatures. The green selection represents the boundary of the particle. (e) Systematic investigation of morphology changes for 31 different nanoparticles with radii spanning 40-100 nm at elevated temperatures. (f) Experimental EELS spectra of a silicon nanoparticle with a radius $r = 73.8 \pm 2.3$ nm (top) with no heating applied and (bottom) after four heating to 1073 K-cooling to 298 K procedures. The spectra are acquired from the electron beam positions shown in (g). (g) STEM image of the nanoparticle, where the coloured areas represent the integration regions for the EELS signal. Adapted from paper D.

not play any role for the comparatively large nanoparticles investigated here (larger than 40 nm radii) [159]. The electron beam induced heating [160] effect can be safely discarded since the particles which are not affected by the electron beam also change their shape upon heating. We attribute the lower melting point to particle pollycrystallinity and doping of our nanoparticles. Doped polycrystalline silicon is known to have grain growth at relatively low temperatures below 1173 K because of self-diffusion effects enhanced by doping [161]. Moreover, the highly spherical shapes of our particles involve the presence of crystal planes with high Miller indices on the particle surface. These crystal planes are known to grow into low-index planes upon heating [162]. Indeed, the reported temperatures near or above 1073 K for grain growth and reconstruction into low-index planes in silicon is consistent with the temperatures of the shape and facet changes recorded in our experiments.

We also demonstrate that the thermal tuning is stable and reversible spectrally via EELS measurements. In particular, we apply four heating and cooling processes and record the EELS spectra before and after the whole process trying to detect any changes in the EELS spectrum (Figure 5.6(f-g)). We observe no changes in the EELS spectrum and conclude that the nanoparticle remains stable and is not affected by the multiple heating processes. As such, the majority of the silicon nanoparticles can be safely operated up to 1073 K without their operation failure in a reversible manner.
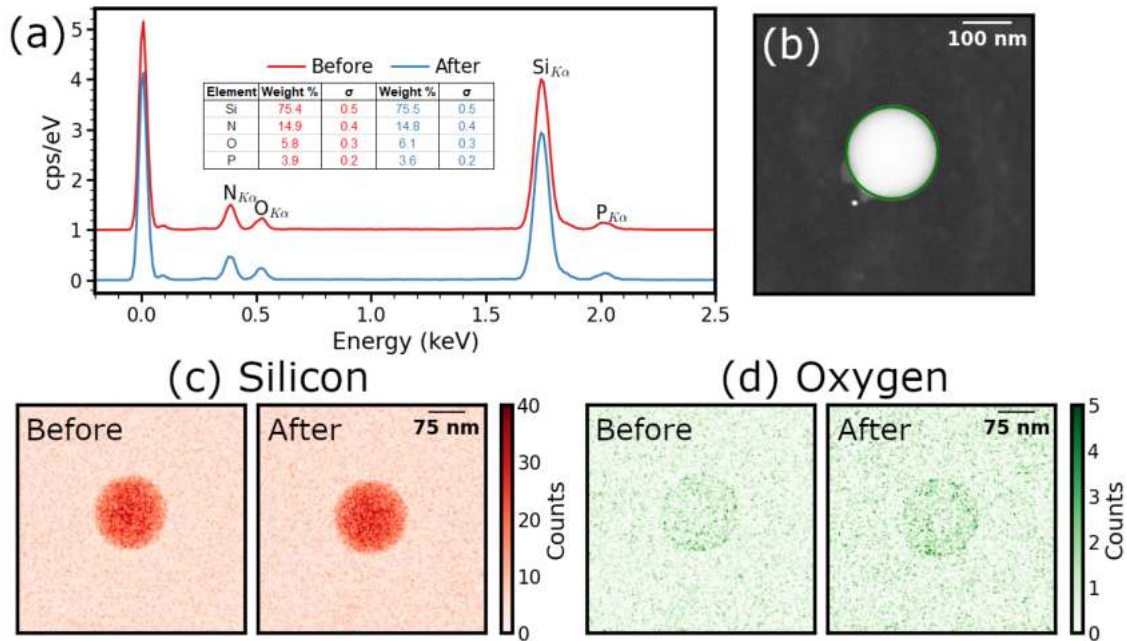
Figure 5.7: STEM EDX analysis of a silicon nanoparticle. (a) EDX spectra before the heating to 1073 K and after the cooling to 298 K obtained in the region indicated in (b). Note, that the top spectral line is shifted by one unit for clarity. (b) STEM image of the nanoparticle, where the green circular region represents the integration region for the EDX signal. (c-d) EDX mapping of (c) silicon and (d) oxygen before the heating and after the cooling. Adapted from paper D.

We further confirm the stability of the thermally modulated silicon nanoparticles by STEM EDX measurements which characterize the chemical composition of the nanoparticles (Figure 5.7). From both, spectral (Figure 5.7(a-b)) and mapping (Figure 5.7(c-d)) experimental EDX data, we can conclude that there are no significant changes in the chemical composition of the particle after its heating to 1073 K.

5.1.6 Concluding remarks

We have experimentally shown the thermal tuning of the silicon nanoparticles Mie modes in the 40-100 nm radii range using the thermo-optic effect. We tune the Mie modes in the visible range by up to 0.15 eV for the smallest particle of 40 nm radius. The MQ mode can be thermally tuned beyond one linewidth by particle size optimization, with the MD, ED and EQ modes offering the linewidth tunability in the 0.3 to 0.7 range. The linewidth tunability at high energies (2.8-3 eV) is limited by the silicon losses which can be beneficial for switching devices with turn on-off functionalities.

We exploited the large spectral shifts of Mie resonances to thermally tune the near-field profile of the Mie modes and showed the thermal switching between the near-field profiles of different Mie modes. Noticeably, the near-field changes can be observed even when there are no spectral features in the EELS spectrum. As such, the near-field switching between different Mie modes can be achieved via thermal tuning, proving to be a promising approach for photonics applications where near-field tuning is required.

We show no significant changes in the spectral response or morphology for the majority of silicon nanoparticles as they are heated to temperatures up to 1073 K (973 K for all particles) using the combination of STEM imaging and EELS spectral characterization. In

addition, we perform EDX STEM analysis to show no chemical changes in the nanoparticle composition upon heating. Thus, we conclude that the Mie modes in our silicon nanoparticles can be thermally tuned stably and reversibly up to 1073 K temperature.

5.2 Silicon electromechanical beams

5.2.1 Motivation

Electromechanical actuation is another approach that can be utilized to modify the optical response of a photonics system due to precise control of the mechanically moveable elements, allowing such applications as tunable lenses [20], light steering [163], tunable lasers [164] as well as reconfigurable meta-atoms [18, 19]. This approach of achieving reconfigurable meta-atoms is particularly attractive due to its low power requirements and an ability to provide high-frequency dynamic operation of the moveable elements [165].

Dielectric nanowires which support multiple Mie-like resonances [166] can be effectively combined into pairs to modulate their response via changing the spatial gap between them. They show a significant shift and appearance of new Mie type resonances when they are positioned at different distances[167]. We combine the dielectric nanowires or beams made of silicon in an electromechanical system to show the modulation of the optical response. Silicon is attractive for this application because of its compatibility with lithographic techniques, ability to be doped to increase the conductivity, hence allowing the electric signal to be directly applied and outstanding mechanical properties.

5.2.2 Device concept

We conceptualize the device for electromechanical actuation of silicon beams in Figure 5.8(a). We place two silicon beams separated by a gap g over a hole produced in a silicon oxide thin layer on top of a silicon substrate. The hanging silicon beams have their ends attached to the silicon oxide layer, the beams are also connected to the electrodes for biasing. When no bias is applied, the beams are separated by a gap g. The beams start to deflect when voltage bias is applied snapping into contact at a pull-in voltage U_{PI}. Figure 5.8(b) shows the COMSOL simulation of two electromechanically actuated silicon beams fixed on both ends with following parameters: $g = w = h$ = 205 nm, L = 15 μm. We see a typical pull-in behaviour for electrostatic actuation of the mechanical beams[168] at a pull-in voltage of around 13 V with an achievable deflection of around 85 nm before the pull-in. It should be noted that this voltage is easily accessible by the TEM electrostatic holder which can be biased by up to around 200 volts.

5.2.3 Fabrication

We use commercially available 6 inch SOI wafers produced by Shin-Etsu Handotai which feature a $\langle 100 \rangle$ 205 ± 20 nm thick p-doped (boron) silicon layer on top of a 200 ± 10 nm thick silicon oxide layer and a $\langle 100 \rangle$ 625 μm thick n-doped (phosphorous) silicon substrate. The production is performed in the following steps which are also represented in Figure 5.9:

1. Fabrication of silicon beams.

Using deep UV lithography on the thin silicon layer side of the SOI wafer, we create a photoresist pattern of two silicon beams separated by a small gap with the smallest dimensions of 200 nm wide beams and 200 nm wide gaps (Figure 5.9(a)). Then, we perform the deep reactive ion etching of the silicon layer using the lithographic pattern. The dry etching is followed by a photoresist strip (Figure 5.9(b)).

2. Fabrication of silicon nitride mask.

We perform RCA cleaning of the wafer before its further processing in a furnace. The RCA cleaning consists of two 10 minutes cleaning steps in each chemical solution: $H_2O:NH_4OH:H_2O_2$
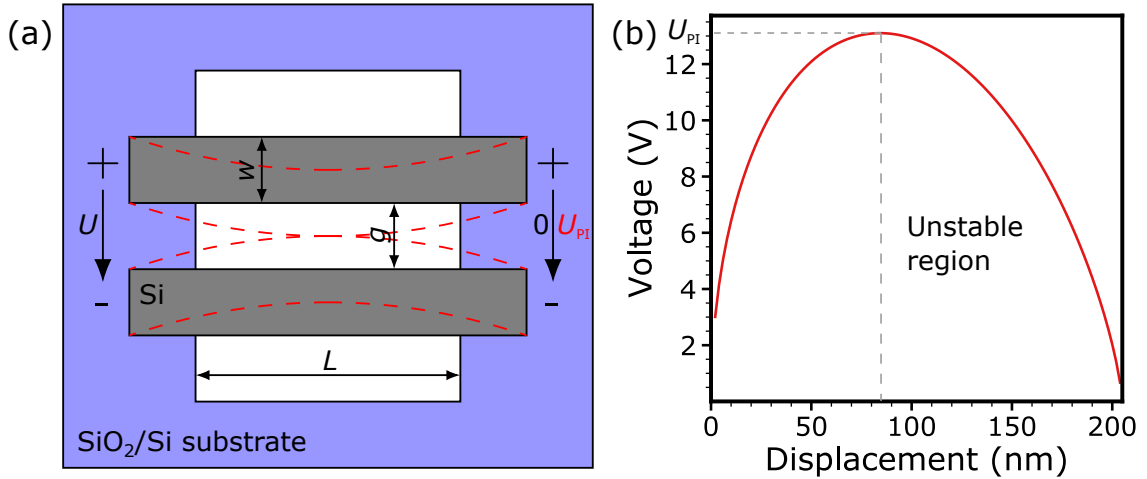
Figure 5.8: Electromechanical actuation of silicon beams. (a) Schematic of the device: two silicon beams separated by a gap g actuated by an applied bias U. Each beam has length L, width w and height h (not shown). At 0 bias, there is no beam deflection, while red dashed lines represent the snapping of the beam at the pull-in voltage U_{PI}. (b) Numerical simulation of the displacement-applied bias dependence for two silicon beams with following parameters: $g = w = h$ = 205 nm, L = 15 µm. The beams are fixed on both ends. Note, that at U_{PI} the beams snap into contact.
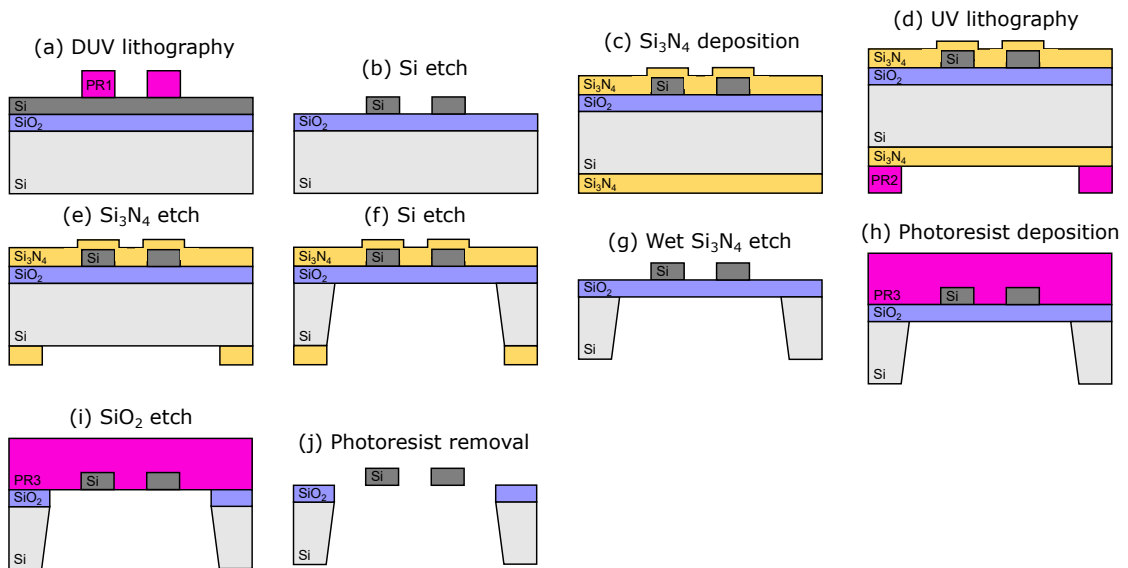
Figure 5.9: Schematic representation of of the silicon electromechanical beams after some fabrication steps which are indicated under (a-j) labels.

5:1:1 and H_2O:HCl:H_2O_2 5:1:1 solutions. Afterwards, we deposit 60 nm of a low-stress silicon-rich nitride layer on both sides of the wafer by low-pressure chemical vapour deposition (LPCVD) (Figure 5.9(c)). The LPCVD nitride layer acts both as a protection of the top device layer and the bottom mask for the creation of TEM membranes. Using UV lithography on the silicon substrate side of the SOI wafer, we create a photoresist pattern of the TEM membranes (Figure 5.9(d)). This is followed by an etch of the silicon nitride layer through the lithographic pattern and a subsequent strip of the resist (Figure 5.9(e)).

It should be noted that we have also tested the silicon nitride layer deposited via plasma-enhanced chemical vapour deposition (PECVD). However, the layer performed worse as protection and mask during KOH etching due to a higher amount of pinholes generated in the silicon nitride layer during the etching. Even more important fact is that this deposition method results in platten patterns in the device silicon layer which is enriched by nitrogen in some areas. The subsequent removal of the silicon nitride layer results in some areas of the wafer still having silicon nitride made of the device silicon layer enriched by nitrogen.

3. Fabrication of silicon oxide membrane.

We perform the wet KOH etching of the silicon substrate through the LPCVD silicon nitride mask (Figure 5.9(f)). Then, we remove the LPCVD silicon nitride layer from both sides of the wafer using wet H_3PO_4 etching at 160°C (Figure 5.9(g)).

4. Release of silicon beams.

First, we deposit a protective photoresist on the device side of the wafer (Figure 5.9(h)) and perform wet BHF etching to remove the silicon oxide layer under the TEM windows (Figure 5.9(i)). Afterwards, we introduce grooves along the lattice planes with a high power laser and manually break the wafer into smaller chips. To remove the protective photoresist layer, these chips are further processed in acetone solution for 10 minutes, followed by several isopropanol solutions for 5 minutes in each one. We try to avoid sample drying when transferring the sample between different solutions. Then, we perform critical point drying of sample in the last isopropanol solution and plasma ash the sample for 5 minutes (Figure 5.9(j)).

It should be noted that the photoresist delaminates in some areas during the BHF etching of the silicon oxide layer. This can be explained by the pin-holes introduced by KOH etching. The BHF solution can penetrate in these areas lifting the photoresist and resulting in flakes with the photoresist. Even more importantly, it seems that the photoresist bends the beams when the silicon oxide layer is removed. An alternative way of releasing the silicon beams which needs to be tested is to perform the dicing after photoresist deposition, remove the photoresist, and remove the silicon oxide layer directly followed by a critical point drying.

The detailed process flow for the fabrication of silicon beams is shown in Table A.2.

5.2.4 Size analysis

We use the STEM image of the silicon beams for the size analysis (Figure 5.10(a)). First, we apply a canny edge detection filter with $\sigma = 1$ pixel on the STEM image and perform a diameter opening operation to remove all edges shorter than the 0.4 of the length of STEM image taken along the beams (Figure 5.10(b)). Then, we perform Hough line transform to find four best-fitting lines to the edges with the minimal distance separation between the fitted lines of 5 pixels (Figure 5.10(c)). We utilize Python scikit-image library to perform all these operations. We assume the orientation of the beams to be along one of the coordinates which are along y in Figure 5.10. Then, we evaluate the x coordinate of each fitted line at the top and bottom of the image and find the location of each edge of the silicon beam as an average of these two coordinates. The width of each silicon beam and the gap are calculated as the difference between pairs of edge locations with the final results indicated in Figure 5.10(c).

5.2.5 Electromechanical actuation and EELS response.

Figure 5.11(a) shows a part of free-standing silicon beams with a total length of approximately 15 μm. The fabricated silicon beams have a curvature which results in a non-

(a) Input image   (b) Edges   (c) Detected lines

150 nm

205.7 nm   204.2 nm

104 nm
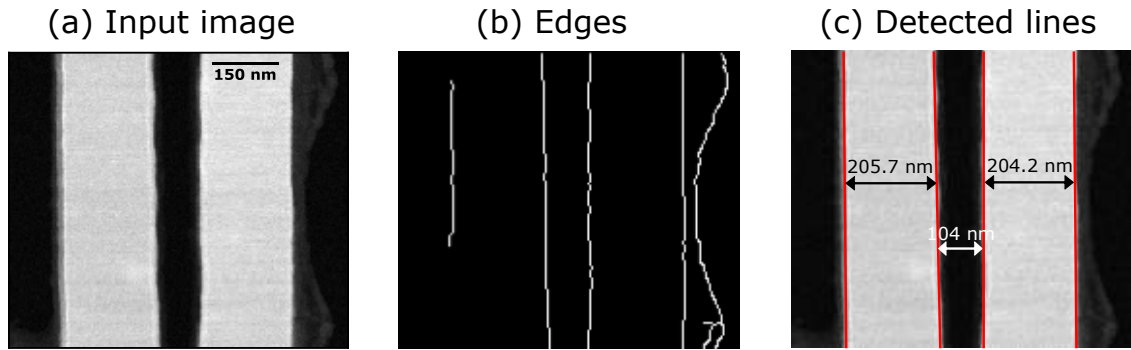
Figure 5.10: Size analysis of silicon beams. (a) STEM image of two silicon beams at a gap. (b) Canny edge detection. (c) Fitted lines to the edges via Hough line transform.

uniform gap between the beams. We perform the characterization of the beams at the shortest gap of 104 nm shown in Figure 5.11(b). When the voltage is applied and increased, the beams snap to the gap of 23 nm at a pull-in voltage of 43 V (Figure 5.11(c)) indicating the smallest possible gap. Figure 5.11(d) shows the dependence of the gap between the silicon beams on the applied voltage. The beams can be moved linearly from a gap of 104 nm to 84 nm with a pull-in effect at 43 V which decreases the gap sharply to 23 nm. It should be noted that when the voltage is removed, the beams return to their original position demonstrating a reversible operation of the device.

We perform the EELS characterization of electromechanically actuated silicon beams shown in Figure 5.12(a). We integrate the EELS spectrum along the length of the silicon beams and show the resulting spectrum of the unbiased silicon beams in Figure 5.12(b). We can observe multiple possible Mie-type resonances which are excited by the electron beam. The energies of some resonances are indicated by the grey dashed lines. Noticeably, we can resolve some resonances at energies around 3 eV which is not the case for silicon nanoparticles studied in Section 4.1 which can be explained by the crystalline

(a)

0 V: g = 104 nm

(b)

43 V: g = 23 nm

(c)

(d)

2 µm

0.2 µm
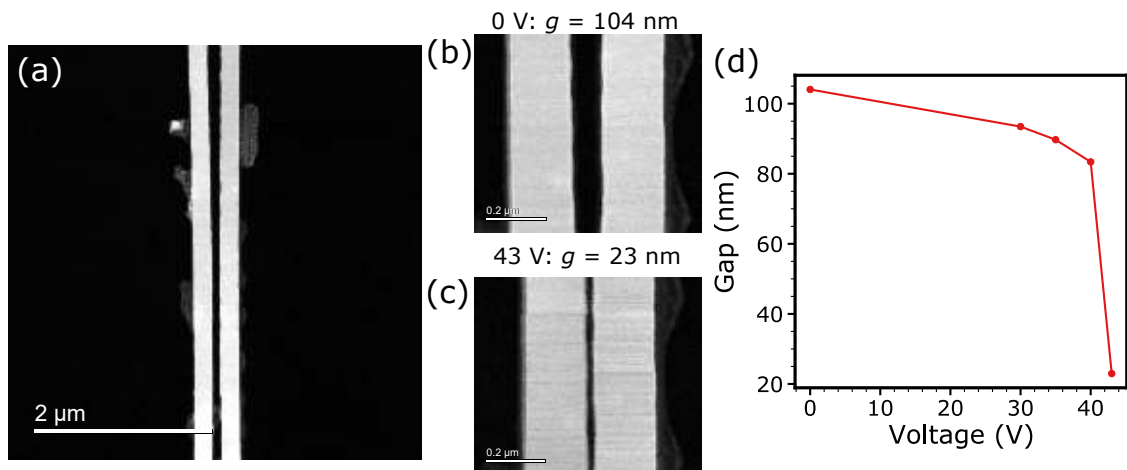
Figure 5.11: Electromechanical actuation of silicon beams. (a) Overview STEM image of silicon beams. (b) STEM image of silicon beams at no applied voltage and a gap of 104 nm. (c) STEM image silicon beams at a pull-in voltage and a gap of 23 nm. The average width of the silicon beam is 204 nm. (d) The gap between silicon beams as a function of an applied voltage. The pull-in voltage is 43 V.
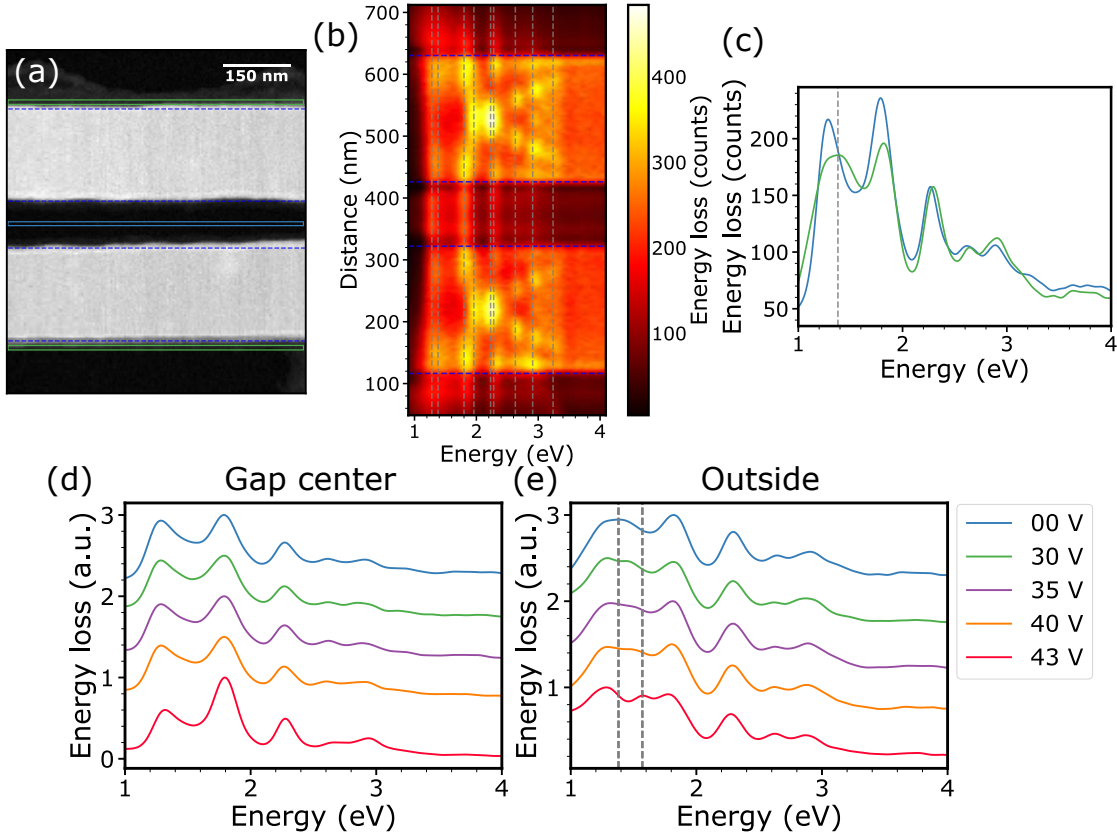
Figure 5.12: EELS response of silicon beams. (a) STEM image of the silicon beams at no applied bias with squared regions representing the integration areas of the EELS signal shown in (c). (b) Experimental EELS signal integrated along the length of beams. (c) Experimental EELS signal integrated in the regions indicated in (a). (d) Experimental EELS signal integrated in center of the gap (blue square region in (a)) at different applied voltages. (e) Experimental EELS signal integrated in outside the beams (green square region in (a)) at different applied voltages.

nature of the silicon beams. The optical mode of interest for reconfiguration purposes lies at 1.38 eV which can be efficiently excited only outside the silicon beams (Figure 5.12(c)).

We perform the electromechanical actuation of the silicon beams combined with EELS characterization in Figure 5.12 (d-e) where we show the EELS signal integrated around the gap centre ($g_{centre} \pm$ 5 nm) and at a fixed outside location of 15 ± 5 nm. The significant difference in the EELS spectrum can be observed for the outside location of the electron beam where we actively tune the mode from 1.38 eV for no applied bias to 1.57 eV at the pull-in voltage. This demonstrates a 0.19 eV or 100 nm possible actuation range.

5.2.6 Concluding remarks

We have fabricated electromechanically actuated silicon beams with nanometer-sized cross-sections. The fabrication resulted in non perfectly shaped beams due to the release step of the silicon beam, therefore, we suggest an alternative approach to achieve more improve the resulting shape of the silicon nanobeams.

We performed the electromechanical actuation of the silicon beams by voltage modulating the gap from 104 nm to 84 nm with a pull-in distance of 23 nm. The beams return to the original shape when we remove the voltage showing a reversible nature of their operation.

By positioning the electron beam outside the silicon beams, we can excite the mode which is the result of the coupling of two silicon beams. We show 0.19 eV or 100 nm spectral tuning of the resulting mode by electromechanical actuation.

6 Conclusions and Outlook

This thesis "Electron energy-loss spectroscopy of reconfigurable meta-atoms" investigates some optical meta-atoms and reconfigurable optical meta-atoms using in-depth electron energy-loss analysis.

We consider several optical meta-atoms based on two groups of materials, dielectric and metals. In the case of dielectrics, we consider the EELS response of silicon Mie resonant nanoparticles in a broad size range. In particular, we obtain the resonance energies of the first five Mie modes where we utilize position-dependant EELS signals to differentiate between spectrally close modes. We place the silicon nanoparticle on top of a thin gold layer to excite the hybrid dielectric-metal resonances. The thin gold layer ensures efficient plasmon launching due to strong field overlap between the electric dipole Mie mode of the silicon and the short-range SSP supported by the metal film. We change the resonance energy of the hybrid resonance by changing the nanoparticle size allowing us to launch the SPP at the energy of interest. The hybrid mode resonance energy also depends on the location of the electron beam where we show that the electron beam movement from the particle centre leads to the change in the orientation of the electric dipole modifying the resonance condition and leading to a redshift in the resonance. We also demonstrate the SPP scattering by the silicon nanoparticle where we directly excite the short-range SPP of the thin gold film by the electron beam and show the interference effect resulting from the combination of scattered and launched waves. Using a simple relation, we experimentally reconstruct the dispersion relation of the short-range SPP. We also characterize the silicon nanoparticles using CL SEM. Due to low acceleration voltage, we show a significant contribution from the transition radiation interference effects.

The second dielectric meta-atom we consider is based on boron-phosphide. Using an ab initio calculation of the dielectric function of the BP material, we show its potential as a UV material. We characterize the randomly shaped BP particles via EELS to experimentally demonstrate that they can support the Mie resonances at the energies of interest. We suggest a simple approach to achieve spherical BP nanoparticles and experimentally demonstrate its validity.

We also consider meta-atoms based on two metal materials, gold and nickel. In both materials, we observe the hybridization effects leading to the resonances at new distinct energies. In the case of gold material, we examine gold dimer geometry which has a hybridization between two localised surface plasmon resonances (LSPR) of separate rods. We shift the resulting symmetric and antisymmetric modes to the visible range and characterize it via EELS. We suggest an approach to fine-tune the resonances via depositing a thin silver shell.

The nickel nanoparticles with spherical shapes have a hybridization effect between the LSPR and the interband transition. Using EELS, we show the hybridization effect between the different order multipole LSPRs and IBT in isolated nickel particles where the hybridization condition depends on the LSPR resonance energy which is defined by the particle radius.

Then, we investigate two reconfigurable meta-atoms. First, using the results from the silicon nanoparticles we considered earlier, we fine-tune their Mie resonances via the thermo-optic effect. We tune the Mie modes in the visible range by up to 0.15 eV for the smallest particle of 40 nm radius. We show numerically that the MQ mode can be

thermally tuned beyond one linewidth by particle size optimization, with the MD, ED and EQ modes offering the linewidth tunability in the 0.3 to 0.7 range. Using the near-field nature of EELS, we show thermal tuning between the near-field profiles of different Mie modes. We utilize a combination of STEM, EELS and EDX characterization to show a stable operation of the majority of the nanoparticles up to 1073 K.

Finally, we consider a reconfigurable meta-atom based on electromechanically actuated silicon beams separated by a small gap. We fabricated such silicon beams with nanometer-sized cross-sections and demonstrated their electromechanical actuation shifting the mode of interest by 0.19 eV or 100 nm.

6.0.1 Outlook

In the case of two dielectric materials, we suggest utilizing the silicon nanoparticles in a combination with other optical materials, for example, two-dimensional materials [169]. Boron phosphide needs new developments in the fabrication methods to obtain meta-atoms with various precisely defined shapes and geometries.

We suggest utilizing the metal dimers in electromechanically actuated devices to tune the gap and offset, and hence the optical response of the meta-atom. We show the hybridization effects in the nickel nanoparticles, however, the possibility to utilize them in a strong coupling regime still needs some consideration.

Reconfigurable meta-atoms based on the thermo-optic effect could benefit on investigation and discovery of new materials. In the case of electromechanically actuated beams, the fabrication sequence should be perfected to achieve well-defined shapes. Then, this can be extended into the fabrication of electromechanically actuated devices with a higher number of silicon beams.

Bibliography

[1] Cai, W., Chettiar, U. K., Kildishev, A. V. & Shalaev, V. M. Optical cloaking with metamaterials. *Nat. Photonics* **1**, 224–227 (2007).

[2] Shin, D. *et al.* Broadband electromagnetic cloaking with smart metamaterials. *Nat. Commun.* **3**, 1–8 (2012).

[3] Kang, L., Jenkins, R. P. & Werner, D. H. Recent progress in active optical metasurfaces. *Adv. Opt. Mater* **7**, 1801813 (2019).

[4] Bar-David, J. & Levy, U. Nonlinear diffraction in asymmetric dielectric metasurfaces. *Nano Lett.* **19**, 1044–1051 (2019).

[5] Shalaev, V. M. Optical negative-index metamaterials. *Nat. Photonics* **1**, 41–48 (2007).

[6] Krasnok, A. E., Miroshnichenko, A. E., Belov, P. A. & Kivshar, Y. S. All-dielectric optical nanoantennas. *Opt. Express* **20**, 20599–20604 (2012).

[7] Krasnok, A. E. *et al.* Optical nanoantennas. *Physics-Uspekhi* **56**, 539 (2013).

[8] Sain, B., Meier, C. & Zentgraf, T. Nonlinear optics in all-dielectric nanoantennas and metasurfaces: a review. *Adv. photonics* **1**, 024002 (2019).

[9] Gürdal, E. *et al.* Enhancement of the second harmonic signal of nonlinear crystals by a single metal nanoantenna. *Nanoscale* **12**, 23105–23115 (2020).

[10] Shaltout, A. M., Shalaev, V. M. & Brongersma, M. L. Spatiotemporal light control with active metasurfaces. *Science* **364**, eaat3100 (2019).

[11] Zou, C., Sautter, J., Setzpfandt, F. & Staude, I. Resonant dielectric metasurfaces: Active tuning and nonlinear effects. *J. Phys. D: Appl. Phys.* **52**, 373002 (2019).

[12] Ginzburg, P. *et al.* Plasmonic resonance effects for tandem receiving-transmitting nanoantennas. *Nano Lett.* **11**, 220–224 (2011).

[13] Ho, J. *et al.* Highly directive hybrid metal–dielectric yagi-uda nanoantennas. *ACS nano* **12**, 8616–8624 (2018).

[14] Sugimoto, H. & Fujii, M. Broadband dielectric–metal hybrid nanoantenna: Silicon nanoparticle on a mirror. *ACS Photonics* **5**, 1986–1993 (2018).

[15] Barreda, A. *et al.* Metal, dielectric and hybrid nanoantennas for enhancing the emission of single quantum dots: A comparative study. *J. Quant. Spectrosc. Radiat. Transf.* **276**, 107900 (2021).

[16] Zograf, G. P. *et al.* Resonant nonplasmonic nanoparticles for efficient temperature-feedback optical heating. *Nano Lett.* **17**, 2945–2952 (2017).

[17] Zhang, T. *et al.* Anapole mediated giant photothermal nonlinearity in nanostructured silicon. *Nat. Commun* **11**, 3027 (2020).

[18] Gutruf, P. *et al.* Mechanically tunable dielectric resonator metasurfaces at visible frequencies. *ACS Nano* **10**, 133–141 (2015).

[19] Holsteen, A. L., Raza, S., Fan, P., Kik, P. G. & Brongersma, M. L. Purcell effect for active tuning of light scattering from semiconductor optical antennas. *Science* **358**, 1407–1410 (2017).

[20] Arbabi, E. *et al.* Mems-tunable dielectric metasurface lens. *Nat. Commun.* **9**, 1–9 (2018).

[21] Lee, K. *et al.* Linear frequency conversion via sudden merging of meta-atoms in time-variant metasurfaces. *Nat. Photonics* **12**, 765–773 (2018).

[22] Xiang, J. *et al.* Modifying Mie Resonances and Carrier Dynamics of Silicon Nanoparticles by Dense Electron-Hole Plasmas. *Phys. Rev. Appl.* **13**, 014003 (2020).

[23] Sautter, J. *et al.* Active tuning of all-dielectric metasurfaces. *ACS Nano* **9**, 4308–4315 (2015).

[24] Parry, M. *et al.* Active tuning of high-Q dielectric metasurfaces. *Appl. Phys. Lett.* **111**, 053102 (2017).

[25] Li, S. Q. *et al.* Phase-only transmissive spatial light modulator based on tunable dielectric metasurface. *Science* **364**, 1087–1090 (2019).

[26] Wang, Q. *et al.* Optically reconfigurable metasurfaces and photonic devices based on phase change materials. *Nat. Photonics* **10**, 60–65 (2016).

[27] Tian, J. *et al.* Active control of anapole states by structuring the phase-change alloy $Ge_2Sb_2Te_5$. *Nat. Commun* **10**, 396 (2019).

[28] Liu, H. *et al.* Rewritable color nanoprints in antimony trisulfide films. *Sci. Adv.* **6**, eabb7171 (2020).

[29] Zhang, Y. *et al.* Electrically reconfigurable non-volatile metasurface using low-loss optical phase-change material. *Nat. Nanotechnol.* **16**, 661–666 (2021).

[30] Lu, L. *et al.* Reversible tuning of mie resonances in the visible spectrum. *ACS nano* (2021).

[31] Lewi, T., Evans, H. A., Butakov, N. A. & Schuller, J. A. Ultrawide thermo-optic tuning of PbTe meta-atoms. *Nano Lett.* **17**, 3940–3945 (2017).

[32] Berto, P. *et al.* Tunable and free-form planar optics. *Nat. Photonics* **13**, 649–656 (2019).

[33] Lewi, T. *et al.* Thermally reconfigurable meta-optics. *IEEE Photon. J.* **11**, 1–16 (2019).

[34] Wortman, J. & Evans, R. Young's modulus, shear modulus, and poisson's ratio in silicon and germanium. *J. Appl. Phys.* **36**, 153–156 (1965).

[35] Kuznetsov, A. I., Miroshnichenko, A. E., Fu, Y. H., Zhang, J. & Luk'Yanchuk, B. Magnetic light. *Sci. Rep.* **2**, 1–6 (2012).

[36] Kuznetsov, A. I., Miroshnichenko, A. E., Brongersma, M. L., Kivshar, Y. S. & Luk'yanchuk, B. Optically resonant dielectric nanostructures. *Science* **354**, aag2472 (2016).

[37] Coenen, T., van de Groep, J. & Polman, A. Resonant modes of single silicon nanocavities excited by electron irradiation. *ACS Nano* **7**, 1689–1698 (2013).

[38] Alexander, D. T., Flauraud, V. & Demming-Janssen, F. Near-field mapping of photonic eigenmodes in patterned silicon nanocavities by electron energy-loss spectroscopy. *ACS nano* **15**, 16501–16514 (2021).

[39] Kordahl, D., Alexander, D. T. & Dwyer, C. Waveguide modes spatially resolved by low-loss stem-eels. *Phys. Rev B* **103**, 134109 (2021).

[40] García de Abajo, F. J. Optical excitations in electron microscopy. *Rev. Mod. Phys.* **82**, 210–256 (2010).

[41] Bohren, C. F. & Huffman, D. R. *Absorption and scattering of light by small particles* (John Wiley & Sons, 2008).

[42] Liu, T., Xu, R., Yu, P., Wang, Z. & Takahara, J. Multipole and multimode engineering in mie resonance-based metastructures. *Nanophotonics* **9**, 1115–1137 (2020).

[43] Muller, R. H. Definitions and conventions in ellipsometry. *Surf. Sci.* **16**, 14–33 (1969).

[44] Bu-Abbud, G. H. & Bashara, N. M. Parameter correlation and precision in multiple-angle ellipsometry. *Appl. Opt.* **20**, 3020–3026 (1981).

[45] Egerton, R. F., Wang, F. & Crozier, P. A. Beam-induced damage to thin specimens in an intense electron probe. *Microsc. Microanal.* **12**, 65–71 (2006).

[46] Yamamoto, N., Toda, A. & Axaya, K. Imaging of transition radiation from thin films on a silicon substrate using a light detection system combined with TEM. *J. Electron Microsc.* **45**, 64–72 (1996).

[47] Naoki, Y., Hiroki, S. & Akio, T. Cherenkov and transition radiation from thin plate crystals detected in the transmission electron microscope. *Proc. R. Soc. Lond. A.* **452**, 2279–2301 (1996).

[48] Egoavil, R. *et al.* Atomic resolution mapping of phonon excitations in STEM-EELS experiments. *Ultramicroscopy* **1–7**, 147 (2014).

[49] Govyadinov, A. A. *et al.* Probing low-energy hyperbolic polaritons in van der Waals crystals with an electron microscope. *Nat. Commun.* **8**, 95 (2017).

[50] Nelayah, J. *et al.* Mapping surface plasmons on a single metallic nanoparticle. *Nat. Phys.* **3**, 348–353 (2007).

[51] Raza, S. *et al.* Electron energy-loss spectroscopy of branched gap plasmon resonators. *Nat. Commun.* **7**, 13790 (2016).

[52] Smith, K. C. *et al.* Direct observation of infrared plasmonic Fano antiresonances by a nanoscale electron probe. *Phys. Rev. Lett.* **123**, 177401 (2019).

[53] Alexander, D. T. L., Flauraud, V. & Demming-Janssen, F. Near-field mapping of photonic eigenmodes in patterned silicon nanocavities by electron energy-loss spectroscopy. *ACS Nano* **15**, 16501–16514 (2021).

[54] Dong, Z. *et al.* Photonic bound-states-in-the-continuum observed with an electron nanoprobe. *arXiv preprint arXiv:2105.04220* (2021).

[55] Brockt, G. & Lakner, H. Nanoscale EELS analysis of dielectric function and bandgap properties in GaN and related materials. *Micron* **31**, 435–440 (2000).

[56] Park, J. *et al.* Bandgap measurement of thin dielectric films using monochromated STEM-EELS. *Ultramicroscopy* **109**, 1183–1188 (2009).

[57] Egerton, R. F. Electron energy-loss spectroscopy in the TEM. *Rep. Prog. Phys.* **72**, 016502 (2009).

[58] Martinez, G. & Tsuno, K. Design of Wien filters with high resolution. *Ultramicroscopy* **100**, 105–114 (2004).

[59] Hunt, J. & Williams, D. Electron energy-loss spectrum-imaging. *Ultramicroscopy* **38**, 47–73 (1991).

[60] Gloter, A., Douiri, A., Tencé, M. & Colliex, C. Improving energy resolution of EELS spectra: an alternative to the monochromator solution. *Ultramicroscopy* **96**, 385–400 (2003).

[61] Bellido, E. P., Rossouw, D. & Botton, G. A. Toward 10 mev electron energy-loss spectroscopy resolution for plasmonics. *Microsc. Microanal.* **20**, 767–778 (2014).

[62] Lazar, S., Botton, G., Wu, M.-Y., Tichelaar, F. & Zandbergen, H. Materials science applications of hreels in near edge structure analysis and low-energy loss spectroscopy. *Ultramicroscopy* **96**, 535–546 (2003).

[63] Scholl, J. A., Koh, A. L. & Dionne, J. A. Quantum plasmon resonances of individual metallic nanoparticles. *Nature* **483**, 421–427 (2012).

[64] Colliex, C., Kociak, M. & Stéphan, O. Electron energy loss spectroscopy imaging of surface plasmons at the nanometer scale. *Ultramicroscopy* **162**, A1–A24 (2016).

[65] Novotny, L. & Hecht, B. *Principles of nano-optics* (Cambridge University Press, 2006).

[66] Drouin, D. *et al.* CASINO v2.42 — a fast and easy-to-use modeling tool for scanning electron microscopy and microanalysis users. *Scanning* **29**, 92–101 (2007).

[67] Evlyukhin, A. B. *et al.* Demonstration of magnetic dipole resonances of dielectric nanospheres in the visible region. *Nano Lett.* **12**, 3749–3755 (2012).

[68] Limonov, M. F., Rybin, M. V., Poddubny, A. N. & Kivshar, Y. S. Fano resonances in photonics. *Nat. Photon.* **11**, 543–554 (2017).

[69] Cui, C. *et al.* Multiple fano resonances in symmetry-breaking silicon metasurface for manipulating light emission. *ACS Photonics* **5**, 4074–4080 (2018).

[70] Koshelev, K., Favraud, G., Bogdanov, A., Kivshar, Y. & Fratalocchi, A. Nonradiating photonics with resonant dielectric nanostructures. *Nanophotonics* **8**, 725–745 (2019).

[71] Krasnok, A. E., Simovski, C. R., Belov, P. A. & Kivshar, Y. S. Superdirective dielectric nanoantennas. *Nanoscale* **6**, 7354–7361 (2014).

[72] Feng, T., Zhang, W., Liang, Z. & Xu, Y. Unidirectional emission in an all-dielectric nanoantenna. *J. Phys.: Condens. Matter* **30**, 124002 (2018).

[73] Sugimoto, H. & Fujii, M. Colloidal dispersion of subquarter micrometer silicon spheres for low-loss antenna in visible regime. *Adv. Opt. Mater.* **5**, 1–8 (2017).

[74] Shcherbakov, M. R. *et al.* Enhanced third-harmonic generation in silicon nanoparticles driven by magnetic response. *Nano Lett.* **14**, 6488–6492 (2014).

[75] Smirnova, D., Smirnov, A. I., & Kivshar, Y. S. Multipolar second-harmonic generation by Mie-resonant dielectric nanoparticles. *Phys. Rev. A* **97**, 013807 (2018).

[76] Koshelev, K. *et al.* Subwavelength dielectric resonators for nonlinear nanophotonics. *Science* **367**, 288–292 (2020).

[77] Moitra, P. *et al.* Large-scale all-dielectric metamaterial perfect reflectors. *ACS Photonics* **2**, 692–698 (2015).

[78] Arbabi, A., Horie, Y., Bagheri, M. & Faraon, A. Dielectric metasurfaces for complete control of phase and polarization with subwavelength spatial resolution and high transmission. *Nat. Nanotechnol.* **10**, 937–943 (2015).

[79] Khorasaninejad, M. *et al.* Metalenses at visible wavelengths: Diffraction-limited focusing and subwavelength resolution imaging. *Science* **352**, 1190–1194 (2016).

[80] Vaskin, A. *et al.* Manipulation of magnetic dipole emission from Eu^{3+} with Mie-resonant dielectric metasurfaces. *Nano Lett.* **19**, 1015–1022 (2019).

[81] Bergenstof Nielsen, C., Christensen, C., Pedersen, C. & Thomsen, E. V. Particle precipitation in connection with koh etching of silicon. *J. Electrochem. Soc.* **151**, G338–G342 (2004).

[82] Sukham, J., Takayama, O., Lavrinenko, A. & Malureanu, R. High-quality ultrathin gold layers with an APTMS adhesion for optimal performance of surface plasmon polariton-based devices. *ACS Appl. Mater. Interfaces* **9**, 25049–25056 (2017).

[83] García de Abajo, F. J. Relativistic energy loss and induced photon emission in the interaction of a dielectric sphere with an external electron beam. *Phys. Rev. B* **59**, 3095–3107 (1999).

[84] Raza, S. *et al.* Multipole plasmons and their disappearance in few-nanometre silver nanoparticles. *Nat. Commun.* **6**, 8788 (2015).

[85] Sugimoto, H., Hinamoto, T. & Fujii, M. Forward to backward scattering ratio of dielectric–metal heterodimer suspended in almost free-space. *Adv. Opt. Mater.* **7**, 1900591 (2019).

[86] Markovich, D. L., Ginzburg, P., Samusev, A. K., Belov, P. A. & Zayats, A. V. Magnetic dipole radiation tailored by substrates: numerical investigation. *Opt. Express* **22**, 10693 (2014).

[87] Zywietz, U., Evlyukhin, A. B., Reinhardt, C. & Chichkov, B. N. Laser printing of silicon nanoparticles with resonant optical electric and magnetic responses. *Nat. Commun.* **5**, 3402 (2014).

[88] Schuller, J. A. *et al.* Plasmonics for extreme light concentration and manipulation. *Nat. Mater.* **9**, 193–204 (2010).

[89] Cheben, P., Halir, R., Schmid, J. H., Atwater, H. A. & Smith, D. R. Subwavelength integrated photonics. *Nature* **560**, 565–572 (2018).

[90] Haffner, C. *et al.* Low-loss plasmon-assisted electro-optic modulator. *Nature* **556**, 483–486 (2018).

[91] Han, Z. & Bozhevolnyi, S. I. Radiation guiding with surface plasmon polaritons. *Rep. Prog. Phys.* **76**, 016402 (2013).

[92] Zayats, A. V., Smolyaninov, I. I. & Maradudin, A. A. Nano-optics of surface plasmon polaritons. *Phys. Rep.* **408**, 131–314 (2005).

[93] Smolyaninov, I. I., Mazzoni, D. L. & Davis, C. C. Imaging of surface plasmon scattering by lithographically created individual surface defects. *Phys. Rev. Lett.* **77**, 3877–3880 (1996).

[94] Liu, Y. *et al.* Compact magnetic antennas for directional excitation of surface plasmons. *Nano Lett.* **12**, 4853–4858 (2012).

[95] Landreman, P. E. & Brongersma, M. L. Deep-subwavelength semiconductor nanowire surface plasmon polariton couplers. *Nano Lett.* **14**, 429–434 (2014).

[96] Sinev, I. *et al.* Steering of guided light with dielectric nanoantennas. *ACS Photonics* **7**, 680–686 (2020).

[97] Yang, Y. *et al.* Optically thin metallic films for high-radiative-efficiency plasmonics. *Nano Lett.* **16**, 4110–4117 (2016).

[98] Yang, Y., Miller, O. D., Christensen, T., Joannopoulos, J. D. & Soljačić, M. Low-loss plasmonic dielectric nanoresonators. *Nano Lett.* **17**, 3238–3245 (2017).

[99] Sugimoto, H. & Fujii, M. Broadband dielectric-metal hybrid nanoantenna: Silicon nanoparticle on a mirror. *ACS Photonics* **5**, 1986–1993 (2018).

[100] Bolton, J. P. R. & Chen, M. Electron energy loss in multilayered slabs. I. Normal incidence. *J. Phys. Condens. Matter* **7**, 3373 (1995).

[101] Yang, J., Hugonin, J. P. & Lalanne, P. Near-to-far field transformations for radiative and guided waves. *ACS Photonics* **3**, 395–402 (2016).

[102] Evlyukhin, A. B., Fischer, T., Reinhardt, C. & Chichkov, B. N. Optical theorem and multipole scattering of light by arbitrarily shaped nanoparticles. *Phys. Rev. B* **94**, 205434 (2016).

[103] Losquin, A. *et al.* Unveiling nanometer scale extinction and scattering phenomena through combined electron energy loss spectroscopy and cathodoluminescence measurements. *Nano Lett.* **15**, 1229–1237 (2015).

[104] Losquin, A. & Kociak, M. Link between cathodoluminescence and electron energy loss spectroscopy and the radiative and full electromagnetic local density of states. *ACS Photonics* **2**, 1619–1627 (2015).

[105] Ginzburg, V. L. & Frank, I. M. Radiation of a uniformly moving electron due to its transition from one medium to another. *J. Phys. USSR* **9**, 353–362 (1945).

[106] Goldsmith, P. & Jelley, J. V. Optical transition radiation from protons entering metal surfaces. *Philos. Mag.* **4**, 836–844 (1959).

[107] Kuttge, M. *et al.* Local density of states, spectrum, and far-field interference of surface plasmon polaritons probed by cathodoluminescence. *Phys. Rev. B* **79**, 113405 (2009).

[108] Hsu, C. W., Zhen, B., Stone, A. D., Joannopoulos, J. D. & Soljačić, M. Bound states in the continuum. *Nat. Rev. Mater.* **1**, 16048 (2016).

[109] Kruk, S. & Kivshar, Y. Functional meta-optics and nanophotonics governed by Mie resonances. *ACS Photonics* **4**, 2638–2649 (2017).

[110] Rodríguez-Fortuño, F. J., Martínez, A., Wurtz, G. A. & Zayats, A. V. Near-field interference for the unidirectional excitation of electromagnetic guided modes. *Science* **340**, 328–331 (2013).

[111] Staude, I. & Schilling, J. Metamaterial-inspired silicon nanophotonics. *Nat. Photonics* **11**, 274–284 (2017).

[112] Wilson, D. J. *et al.* Integrated gallium phosphide nonlinear photonics. *Nat. Photonics* **14**, 57–62 (2020).

[113] Chen, W. T. *et al.* A broadband achromatic metalens for focusing and imaging in the visible. *Nat. Nanotechnol.* **13**, 220–226 (2018).

[114] Gutiérrez, Y. *et al.* The quest for low loss high refractive index dielectric materials for UV photonic applications. *Appl. Sci.* **8**, 2065 (2018).

[115] Hu, J., Lawrence, M. & Dionne, J. A. High Quality Factor Dielectric Metasurfaces for Ultraviolet Circular Dichroism Spectroscopy. *ACS Photonics* **7**, 36–42 (2020).

[116] Aharonovich, I., Greentree, A. D. & Prawer, S. Diamond photonics. *Nat. Photonics* **5**, 397–405 (2011).

[117] Aspnes, D. E. & Studna, A. Dielectric functions and optical parameters of si, ge, gap, gaas, gasb, inp, inas, and insb from 1.5 to 6.0 ev. *Phys. Rev B* **27**, 985 (1983).

[118] Siefke, T. *et al.* Materials pushing the application limits of wire grid polarizers further into the deep ultraviolet spectral range. *Adv. Opt. Mater* **4**, 1780–1786 (2016).

[119] Phillip, H. & Taft, E. Kramers-kronig analysis of reflectance data for diamond. *Phys. Rev* **136**, A1445 (1964).

[120] Takenaka, T., Takigawa, M. & Shohno, K. Dielectric Constant and Refractive Index of Boron Monophosphide. *Jpn. J. Appl. Phys.* **15**, 2021–2022 (1976).

[121] Popper, P. & Ingles, T. A. Boron Phosphide, a III–V Compound of Zinc-Blende Structure. *Nature* **179**, 1075 (1957).

[122] Wettling, W. & Windscheif, J. Elastic constants and refractive index of boron phosphide. *Solid State Commun.* **50**, 33–34 (1984).

[123] Yang, J. & Fan, J. A. Analysis of material selection on dielectric metasurface performance. *Opt. Express* **25**, 23899–23909 (2017).

[124] Alaee, R., Rockstuhl, C. & Fernandez-Corbaton, I. An electromagnetic multipole expansion beyond the long-wavelength approximation. *Opt. Commun.* **407**, 17–21 (2018).

[125] Nath, N. & Chilkoti, A. Label free colorimetric biosensing using nanoparticles. *Journal of Fluorescence* **14**, 377–389 (2004).

[126] Liu, N. *et al.* Planar metamaterial analogue of electromagnetically induced transparency for plasmonic sensing. *Nano Lett.* **10**, 1103–1107 (2010).

[127] Stockman, M. I. Nanoplasmonics: past, present, and glimpse into future. *Opt. Express* **19**, 22029–22106 (2011).

[128] Quinten, M., Leitner, A., Krenn, J. R. & Aussenegg, F. R. Electromagnetic energy transport via linear chains of silver nanoparticles. *Opt. Lett.* **23**, 1331–1333 (1998).

[129] Gür, F. N. *et al.* Dna-assembled plasmonic waveguides for nanoscale light propagation to a fluorescent nanodiamond. *Nano Lett.* **18**, 7323–7329 (2018).

[130] Boca, S. C. *et al.* Chitosan-coated triangular silver nanoparticles as a novel class of biocompatible, highly effective photothermal transducers for in vitro cancer cell therapy. *Cancer Lett.* **311**, 131–140 (2011).

[131] Priecel, P., Salami, H. A., Padilla, R. H., Zhong, Z. & Lopez-Sanchez, J. A. Anisotropic gold nanoparticles: Preparation and applications in catalysis. *Chinese J. Catal* **37**, 1619–1650 (2016).

[132] Tali, S. A. S. & Zhou, W. Multiresonant plasmonics with spatial mode overlap: overview and outlook. *Nanophotonics* **8**, 1199–1225 (2019).

[133] Prodan, E., Radloff, C., Halas, N. J. & Nordlander, P. A hybridization model for the plasmon response of complex nanostructures. *Science* **302**, 419–422 (2003).

[134] Dey, D., Kohoutek, J., Gelfand, R. M., Bonakdar, A. & Mohseni, H. Integration of plasmonic antenna on quantum cascade laser facets for chip-scale molecular sensing. In *SENSORS, 2010 IEEE*, 454–458 (IEEE, 2010).

[135] Liu, J. *et al.* Tunable coupling-induced transparency band due to coupled localized electric resonance and quasiguided photonic mode in hybrid plasmonic system. *Opt. Express* **21**, 13386–13393 (2013).

[136] Christ, A. *et al.* Controlling the interaction between localized and delocalized surface plasmon modes: Experiment and numerical calculations. *Phys. Rev B* **74**, 155435 (2006).

[137] Yang, S. *et al.* Feedback-driven self-assembly of symmetry-breaking optical metamaterials in solution. *Nat. Nanotechnol* **9**, 1002–1006 (2014).

[138] Rothemund, P. W. Folding dna to create nanoscale shapes and patterns. *Nature* **440**, 297–302 (2006).

[139] Dey, S. *et al.* Dna origami. *Nature Reviews Methods Primers* **1**, 1–24 (2021).

[140] Nguyen, L. *et al.* Chiral assembly of gold–silver core–shell plasmonic nanorods on dna origami with strong optical activity. *ACS nano* **14**, 7454–7461 (2020).

[141] Pakizeh, T. Optical absorption of plasmonic nanoparticles in presence of a local interband transition. *J. Phys. Chem. C* **115**, 21826–21831 (2011).

[142] Canales Ramos, A. I. *Light-Interband transitions coupling in Aluminum*. Master's thesis (2018).

[143] Pirzadeh, Z., Pakizeh, T., Miljkovic, V., Langhammer, C. & Dmitriev, A. Plasmon–interband coupling in nickel nanoantennas. *ACS Photonics* **1**, 158–162 (2014).

[144] Rahmani, M. *et al.* Reversible thermal tuning of all-dielectric metasurfaces. *Adv. Funct. Mater* **27**, 1700580 (2017).

[145] Lewi, T., Butakov, N. A. & Schuller, J. A. Thermal tuning capabilities of semiconductor metasurface resonators. *Nanophotonics* **8**, 331–338 (2019).

[146] Kamali, K. Z. *et al.* Reversible image contrast manipulation with thermally tunable dielectric metasurfaces. *Small* **15**, 1805142 (2019).

[147] Ward, J. *et al.* High-contrast and reversible scattering switching via hybrid metal-dielectric metasurfaces. *Beilstein J. Nanotechnol.* **9**, 460–467 (2018).

[148] Grinblat, G. *et al.* Efficient ultrafast all-optical modulation in a nonlinear crystalline gallium phosphide nanodisk at the anapole excitation. *Sci. Adv.* **6**, eabb3123 (2020).

[149] Caldarola, M. *et al.* Non-plasmonic nanoantennas for surface enhanced spectroscopies with ultra-low heat conversion. *Nat. Commun.* **6**, 7915 (2015).

[150] Baranov, D. G., Verre, R., Karpinski, P. & Käll, M. Anapole-Enhanced Intrinsic Raman Scattering from Silicon Nanodisks. *ACS Photonics* **5**, 2730–2736 (2018).

[151] Raza, S. & Kristensen, A. Raman scattering in high-refractive-index nanostructures. *Nanophotonics* **10**, 1197–1209 (2021).

[152] Cihan, A. F., Curto, A. G., Raza, S., Kik, P. G. & Brongersma, M. L. Silicon Mie resonators for highly directional light emission from monolayer MoS_2. *Nat. Photonics* **12**, 284–290 (2018).

[153] Liu, S. *et al.* Light-Emitting Metasurfaces: Simultaneous Control of Spontaneous Emission and Far-Field Radiation. *Nano Lett.* **18**, 6906–6914 (2018).

[154] Vaskin, A. *et al.* Directional and Spectral Shaping of Light Emission with Mie-Resonant Silicon Nanoantenna Arrays. *ACS Photonics* **5**, 1359–1364 (2018).

[155] Jellison, G. E., Modine, J. & Modine, F. A. Optical functions of silicon at elevated temperatures. *J. Appl. Phys* **76**, 3758–3761 (1994).

[156] Lautenschlager, P., Garriga, M., Vina, L. & Cardona, M. Temperature dependence of the dielectric function and interband critical points in silicon. *Phys. Rev. B* **36**, 4821 (1987).

[157] Jellison Jr., G. E. & Modine, F. A. Optical absorption of silicon between 1.6 and 4.7 ev at elevated temperatures. *Appl. Phys. Lett.* **41**, 180 (1982).

[158] Šik, J., Hora, J. & Humlíček, J. Optical functions of silicon at high temperatures. *J. Appl. Phys.* **84**, 6291–6298 (1998).

[159] Talyzin, I. V., Samsonov, M. V., Samsonov, V. M., Pushkar, M. Y. & Dronnikov, V. V. Size dependence of the melting point of silicon nanoparticles: Molecular dynamics and thermodynamic simulation. *Semiconductors* **53**, 947–953 (2019).

[160] Asoro, M. A., Kovar, D. & Ferreira, P. J. In situ transmission electron microscopy observations of sublimation in silver nanoparticles. *ACS Nano* **7**, 7844–7852 (2013).

[161] Wada, Y. & Nishimatsu, S. Grain growth mechanism of heavily phosphorus☐implanted polycrystalline silicon. *J. Electrochem. Soc.* **125**, 1499 (1978).

[162] Tsong, T., Feng, D. & Liu, H. Atomic structures in reconstruction of high index surfaces of silicon. *Surf. Sci.* **199**, 421–438 (1988).

[163] Li, H., Liu, Q. & Li, M. Electromechanical brillouin scattering in integrated planar photonics. *APL Photonics* **4**, 080802 (2019).

[164] Huang, M. C., Zhou, Y. & Chang-Hasnain, C. J. A nanoelectromechanical tunable laser. *Nat. Photonics* **2**, 180–184 (2008).

[165] Zheludev, N. I. & Plum, E. Reconfigurable nanomechanical photonic metamaterials. *Nat. Nanotechnol* **11**, 16–22 (2016).

[166] Cao, L. *et al.* Engineering light absorption in semiconductor nanowire devices. *Nat. Mater.* **8**, 643–647 (2009).

[167] Li, Q., Wu, T., van de Groep, J., Lalanne, P. & Brongersma, M. L. Structural color from a coupled nanowire pair beyond the bonding and antibonding model. *Optica* **8**, 464–470 (2021).

[168] Zhang, W.-M., Yan, H., Peng, Z.-K. & Meng, G. Electrostatic pull-in instability in mems/nems: A review. *Sens. Actuator A Phys.* **214**, 187–218 (2014).

[169] Cihan, A. F., Curto, A. G., Raza, S., Kik, P. G. & Brongersma, M. L. Silicon mie resonators for highly directional light emission from monolayer mos 2. *Nat. Photonics* **12**, 284–290 (2018).

A Process flows

Table A.1: Fabrication of TEM membranes

Step	Equipment & procedure	Comments
1. Wafer purchase	4″, n-type (phosphor), $\langle 100 \rangle$ orientation, 350 μm thickness, double side polished	
2. SiN deposition	Furnace LPCVD nitride 6 inch: 5 min 30 sec deposition time	
3. Inspection	Ellipsometer: 33 nm thickness and 2.1 refractive index of SiN with 1 nm of native oxide underneath	
UV lithography: KOH windows		
4.1. Photoresist deposition	Gamma UV Spin Coater: 1411 recipe (4″ wafer, 1.5 μm MiR 701 resist, HMDS priming)	
4.2. Exposure	MA6–2 Aligner: 13 mW/cm^2, 17.2 sec, channel 2, contact mode, 10 sec stabilization time	
4.3 Development	TMAH UV-lithography developer: 3001 recipe (4″ wafer, post-exposure baking (PEB) for 60 sec at 110°C, single puddle (SP) development for 60 sec)	
5. SiN etching	Advanced Oxide Etcher (AOE): NANOTECH/ERIJ/SRNETCH2 recipe, 1 minute, platen temperature is 0°C	Visual test: the colour of SiN areas should change
6. Resist strip	Plasma Asher 2: 30 min, 400 ml/min oxygen, 70 ml/min nitrogen, 1000 W, 1.222 mbar	
7. Inspection	Profilometer DektakXTA: 45-40 nm was etched (centre-edge location on the wafer)	
8. Si etching	Si Etch 1 (KOH): wet 28 % KOH etching at 80°C for 4 h 31 min. Rinsing: 2 program (water overflow only). The wafers are left for drying (no spin drying)	Ellipsometer is used in the middle of the etching process to check the etch rate (1.29 μm/min)
9. Wafer cleaning	HCl:water 4:1 solution for 10 min	Check with an optical microscope. If a noticeable number of FeO particles is still present, repeat the process
Gold layer deposition		

10.1. APTMS layer deposition	Fumehood: Solution of 95% isopropanol, 2.5% water and 2.5% APTMS. The wafers are immersed into the solution for 3 hours to get a 1 nm layer of APTMS. The solution holder is covered with a piece of plastic. After 3 hours, the wafers are cleaned in subsequent steps with the following solutions: isopropanol, water; isopropanol, water	It is important to do all cleaning steps immediately one after another
10.2. Gold layer deposition	Sputter-System (Lesker), parameters: 300 watt, 3 mTor, 10 sec	The expected deposition rate is 1 nm/second
10.3. Inspection	Ellipsometer: gold layer thickness of 9-10 nm	Model with 10 nm Au / 1 nm SiO_2 / 30 nm Si rich SiN / Si substrate has been created and used
10.4. Inspection	AFM: gold layer is scratched and step measured: 9-10 nm. AFM gold surface roughness: 1 nm	AFM and SEM show two types of gold grains (large and small) which is to be expected

Back-end		
11. Protective photoresist deposition	Spin coater Labspin 2: AZ 4562 resist, 2000 rpm, 2000 rpm/s, 60 sec. Bake for 60 sec at 100°C. Expected thickness: 9 μm	The temperature of the hot plate is set to 110°C to account for the additional metal plate on top
12.a. Wafer dicing, silicon only	Laser Micromachining Tool: 50 W picosecond laser manufactured by Time Bandwidth (TBW) with 1064 nm / 255 mm objective. Recipe: /artas/Simembranes/4inchSi_membrane	Use a test wafer of a similar thickness to check how easy it is to break the wafer after cutting. Modify the cutting parameters if needed
12.b. Wafer dicing, with a gold layer	Disco Saw, dicing recipe: modified 10 by 10 cm recipe with 0.1 mm blade height, 20 mm/s speed, appropriate dicing period and number of cuts	Since no alignment marks are present, membranes are used for alignment

Table A.2: Fabrication of silicon beams

Step	Equipment & procedure	Comments
1. Wafer purchase	SOI, 6″, substrate (n type (phosphor), $\langle 100 \rangle$ orientation, 625 µm thickness), silicon oxide (200 ± 10 nm thickness), silicon (p type (boron), $\langle 100 \rangle$ orientation, 205 ± 20 nm thickness)	
Fabrication of silicon beams		
2.1. Deep UV resist and BARC spin coating	SÜSS Spinner-Stepper: 1201 recipe (DCH 150 mm BARC 65 nm deposition) followed by 1301 recipe (DCH 150 mm M230Y 360 nm dispense 3 ml at 1000 rpm, spin-off 30 sec at 2500 rpm, soft bake 90 sec at 130°C)	
2.2. Deep UV resist exposure	DUV Stepper: simulated dose	
2.3. Deep UV resist development	Developer TMAH Stepper: 1002 recipe (DCH PEB 60 sec and DEV 60 sec, 60 sec baking at 130°C followed by 60 sec single puddle development)	
2.4. Inspection	Optical microscope: check pattern and alignment marks	
2.5. Silicon and BARC deep reactive ion etching	Pegasus 1: 30 sec of barc205 removal, followed by Nano1.42 recipe with endpoint detection tracking (SF_6 and SiF_4 concentrations tracking) for around 120 sec	Use endpoint detection to precisely stop the etching of silicon
2.6. Inspection	Ellipsometer: no silicon left in exposed areas	
2.7. Inspection	Optical microscope: check pattern and alignment marks	
2.8. Resist strip	Plasma Asher 2: 30 min, 400 ml/min oxygen, 70 ml/min nitrogen, 1000 W, 1.222 mbar	
Fabrication of silicon nitride mask		
3.1. Cleaning before furnace	2 step RCA cleaning	No HF step since silicon oxide is present on the wafer
3.2. LPCVD nitride deposition	Furnace LPCVD nitride 6 inches: 10 min deposition time	Test wafer, measured silicon nitride thickness is 58.43 nm, measured refractive Index is 2.16 (ellipsometry)
3.3. UV resist coating	Spin Coater (Gamma UV): 1611 recipe (DCH 150 mm MiR 701, 1.5 µm HMDS)	Backside of the wafer
3.4 UV resist exposure	Aligner (Maskless 03): AZ MiR 701 resist type, 1.5 µm thickness, quality exposure mode, 250 mJ/cm^2 dose, -2 defocus	Backside of the wafer

3.5. UV resist development	Developer (TMAH UV-lithography): 3010 recipe (DCH 150 mm PEB 60 sec at 110°C SP 60 sec)	Backside of the wafer
3.6. Silicon nitride etch	ICP Metal: SiO_2 etch with carrier recipe, 60 nm etch depth, 65 nm/min etch rate, etch for 1 min 30 sec to be sure	Backside of the wafer
3.7. Resist strip	Plasma Asher 2: 30 min, 400 ml/min oxygen, 70 ml/min nitrogen, 1000 W, 1.222 mbar	
3.8. Inspection	Optical microscope: check the resulting window sizes	Backside of the wafer

	Fabrication of silicon oxide membrane	
4.1. Si etching	Si Etch 1 (KOH): wet 28 % KOH etching at 80°C for 6 h 26 min followed by an additional 1 h 28 min. Rinsing: 2 program (water overflow only). The wafers are left for drying (no spin drying)	Ellipsometer is used after 6 h 26 min of etching to check the etch rate (1.3 µm/min).
4.2. Silicon nitride removal	Wet H_3PO_4 etching: 20 min at 160°C	Eching rate is approximately 3.3 nm/min
4.3. Inspection	Ellipsometer: no silicon nitride left	

	Release of silicon beams	
5.1 Resist deposition for device protection	Spray coater: acetone: Mir 701 3:1 solution, PGMEA solvent for cleaning, soft baking is done at 90°C for 90 sec. Spray coating parameters: speed 40 mm/s, line spacing 3 mm, z point 40, flow rate 1000 ul/min, 1 pass	The resulting thickness is around 9.6 µm
5.2. Silicon oxide removal	Wet BHF etch: 3 min 30 sec	Expected etch rate of wet thermal oxide: 75-80 nm/min
5.3. Inspection	Optical microscope: a lot of flakes from the spray-coated resist, some of the silicon beams are destroyed after or during the etch	
5.4. Dicing	Laser Micromachining Tool: 50 W picosecond laser manufactured by Time Bandwidth (TBW) with 1064 nm / 255 mm objective. Recipe: /artas/Simembranes/4inchSi_membrane	Use a test wafer of a similar thickness to check how easy it is to break the wafer after cutting and the width of the trenches (avoid destruction of the electrical contacts). Modify the cutting parameters if needed.
5.5. Samples separation	Break the sample along the introduced trenches	
5.6. Resist removal with critical point drying	Acetone solution for 10 min. This is followed by 2-3 different isopropanol solutions for 5 min in all steps. Transport directly in isopropanol solution for critical point drying. Then, plasma ash for 5 min	Don't clean in water in between acetone and isopropanol cleaning since it seems it leaves a lot of resist

Paper A

Assadillayev, A., Hinamoto, T., Fujii, M., Sugimoto, H., Brongersma, M. L., Raza, S.

Plasmon launching and scattering by silicon nanoparticles

Author Contributions

S.R. and M.L.B. conceived the experiments. A.A. fabricated the samples and performed the EELS measurements. A.A. performed the image and EELS data analyses. A.A. and S.R performed the simulations. T.H., H.S., and M.J. fabricated the silicon nanoparticles. A.A. and S.R. prepared figures and wrote the manuscript. S.R. supervised the project. All authors discussed the results and contributed to the preparation of the manuscript.

Article

Plasmon Launching and Scattering by Silicon Nanoparticles

Artyom Assadillayev, Tatsuki Hinamoto, Minoru Fujii, Hiroshi Sugimoto, Mark L. Brongersma, and Søren Raza*

Read Online

| ACCESS | | Metrics & More | | Article Recommendations | | Supporting Information |

ABSTRACT: Resonant optical nanomaterials with a high refractive index, such as silicon, have become key elements for controlling free-space light. Here, we show that silicon nanoparticles can manipulate highly confined guided waves in the form of surface plasmon polaritons (SPPs) on a subwavelength scale. Using electron energy-loss spectroscopy in a transmission electron microscope, we demonstrate that SPPs in ultrathin metal films can be efficiently launched due to the strong coupling between the Mie resonances of the nanoparticle and the SPP modes. We find that the SPP excitation wavelength can be tuned across the entire near-infrared by varying the particle size. For insight into the coupling mechanism, we also measure the electron-beam-induced response of the Mie resonances in isolated silicon nanostructures in a broad size range. Finally, we show that the silicon nanoparticles act as scatterers of the SPPs supported by the film. Our results may pave the way for using high-refractive-index dielectric nanoantennas as compact elements for manipulating highly confined SPPs.

KEYWORDS: high-refractive-index nanostructures, Mie resonances, surface plasmon polaritons, electron energy-loss spectroscopy, hybrid dielectric−plasmon resonances
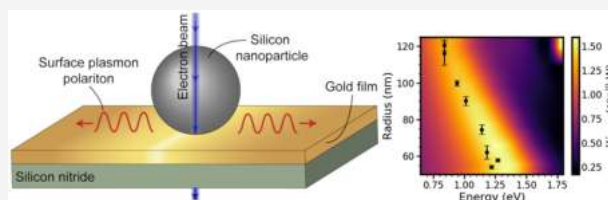
Surface plasmon polaritons (SPPs) supported by metal films have been the subject of intense research since their first prediction by Ritchie,[1] as they enable the localization and guiding of light at subwavelength scales.[2] These properties are desirable for reducing the footprint and energy consumption of integrated photonic devices[3,4] as well as realizing two-dimensional manipulation of light.[5] Several different passive SPP components, such as lenses, prisms, and graded-index structures, have already been realized.[6,7] However, SPPs cannot be directly excited due to the momentum mismatch between the impinging light and the SPP. The most common excitation techniques are based on either total internal reflection, such as Kretschmann or Otto prism coupling, or diffractive effects, such as grating couplers.[8] While prism coupling is suitable for investigating fundamental SPP properties, it is usually bulky and not amenable to miniaturization. On the other hand, grating coupling requires patterning the metal film on a scale several times larger than the wavelength of light, which may compromise the quality of the film. This can be particularly detrimental in high-quality atomically thin materials[9] and passivated metal films.[10] These considerations have prompted an interest in launching SPPs using subwavelength light scatterers, which provide access to a broad range of momenta. In this scheme, a key parameter for achieving efficient SPP launching is a significant modal overlap between the field of the resonant nanostructure and the SPP supported by the metal film. While a broad range of different plasmonic[11,12] and dielectric[13,14] resonant nanostructures have been considered, there has been little attention on modifying

the SPP to improve the modal overlap and thereby boost the coupling to SPPs. So far, studies have focused on coupling to the SPP of optically thick metal films, whose field is not optimized to overlap with either plasmonic or dielectric nanostructures.[15,16]

In this work, we experimentally demonstrate that geometric Mie resonances[17] supported by silicon nanoparticles hybridize strongly with the highly confined SPPs in 10-nm-thin gold films. The strong hybridization leads to the formation of a new class of hybrid dielectric−plasmon resonances,[16] where the out-of-plane confinement is enabled by the SPP, while the in-plane confinement is provided by the silicon nanoparticle. Such hybrid resonances also occur for optically thick metal films, where they offer light confinement with low losses and high radiation efficiency into free-space light.[16,18] In contrast, the hybrid dielectric−plasmon resonance reported here has a strong modal overlap with the SPP supported by the thin gold film, providing a promising platform for efficient nanoscale plasmon generation.

We perform the experimental characterization with electron energy-loss spectroscopy (EELS) in a transmission electron
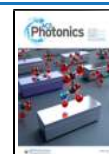
microscope (TEM), which can measure the optical response of nanophotonic structures with nanometer spatial resolution and meV energy resolution.[19,20] This powerful technique has been used to characterize the plasmonic response of a range of metal nanostructures[21−23] as well as low-energy phonon excitations.[24] The simultaneous high spatial and spectral resolution enables us to perform position-dependent spectral investigation over the area of the silicon nanoparticles to characterize the hybrid dielectric−plasmon resonances as well as the Mie resonances. We present near-field profiles of the Mie resonances and map their resonance energies across a broad range of nanoparticle sizes. We show that the presence of an ultrathin gold film beneath the silicon nanoparticles produces a hybrid resonance due to SPP coupling with a near-field profile distinctly different from those of the Mie resonances. Notably, we find that the hybrid resonance confines light on a deep-subwavelength scale of $\sim\lambda/10$ (where λ is the wavelength in free space), which is beyond the diffraction limit of silicon. The hybrid resonance and thereby the SPP excitation wavelength can be tuned across the entire near-infrared wavelength range, including telecommunication wavelengths, by varying the nanoparticle size. Finally, we exploit the capability of the electron beam to directly excite SPPs to demonstrate that silicon nanoparticles act as SPP scatterers. Our results show that silicon nanoparticles act as compact plasmon launchers and scatterers, which may enable nanoscale plasmon circuitry for on-chip applications without compromising the metal film quality.

■ RESULTS

Mie Resonances. The Mie resonances of silicon nanoparticles have been studied with a variety of optical techniques[17] as well as cathodoluminescence,[25,26] but, to the best of our knowledge, there have been no reports on their EELS response. It is therefore enlightening to first consider the EELS response of isolated silicon nanoparticles (Figure 1) before discussing the properties of the hybrid dielectric−plasmon resonance. We prepare crystalline silicon nanoparticles of spherical shape in a colloidal suspension[27] and carefully disperse them on a thin silicon nitride membrane (Methods). This produces well-separated silicon nanoparticles with a large size distribution, which enables us to perform all the measurements on the same sample under identical experimental conditions. Figure 1b shows a typical EELS spectrum for a pristine silicon nanoparticle of radius $r = 54.6 \pm 1.1$ nm, which is obtained by averaging the EELS signal collected at an electron beam position of approximately 20 nm outside the nanoparticle surface (Figure 1c). We observe two clear peaks in the spectrum, which are due to the excitation of Mie resonances in the silicon nanoparticle. Using an analytical theory for the EELS probability of a swift electron in the external vicinity of a vacuum-embedded dielectric sphere,[28] we identify the low-energy peak at 2.54 eV as the magnetic dipole (MD) resonance, while the high-energy peak at 2.97 eV is attributed to the electric dipole (ED) resonance. The measured resonance energies are in quantitative agreement with theory, while the experimental peaks are broadened due to the energy resolution of our EELS setup. The effect of a finite experimental energy resolution can be mimicked in the theoretical spectra by convolution with a Lorentzian function,[29] which broadens the EELS resonances (see Methods). As shown in Figure 1b, the convoluted spectrum
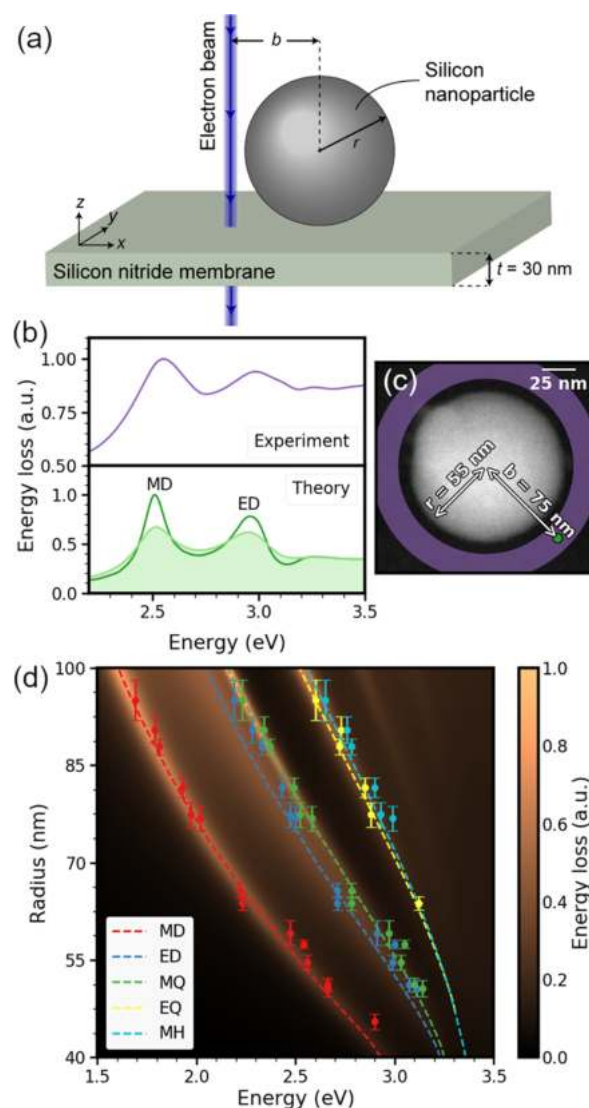
Figure 1. EELS measurements of Mie resonances in silicon nanoparticles. (a) Schematic of a silicon nanoparticle of radius r placed on a silicon nitride membrane and excited by an electron beam. The impact parameter b denotes the distance between the electron beam and the center of the nanoparticle. (b) Experimental (top) and theoretical (bottom) EELS spectra of a silicon nanoparticle with radius $r = 54.6 \pm 1.1$ nm, acquired from the electron beam positions shown in (c). The area curve represents a convolution with a Lorentzian function. (c) STEM image of the nanoparticle, where the purple region represents the integration region for the experimental spectrum and the green point depicts the location of the electron beam in the simulation. (d) Measured resonance energies as a function of particle radius for the first five Mie resonances in silicon nanoparticles. The color plot shows the EELS simulation for an impact parameter $b = r + 20$ nm, and the dashed curves indicate the theoretical Mie resonance energies.

captures both the resonance energies and linewidths observed in the experimental measurement.

We extend our analysis by measuring the Mie resonance energies of silicon nanoparticles over a broad size range (Figure 1d). The colored points show the experimentally measured resonance energies of the first five Mie resonances spanning a radius range from 40 to 100 nm. The color map
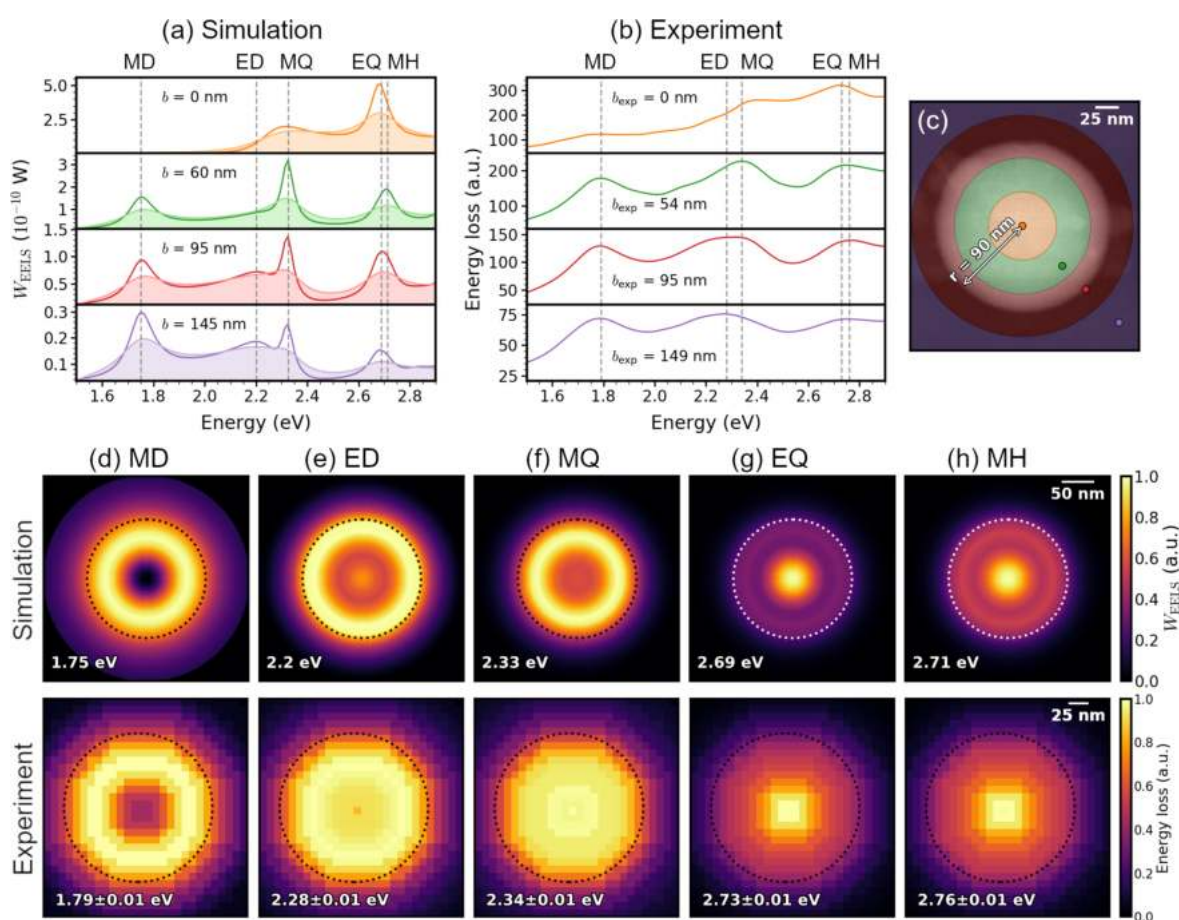
Figure 2. EELS mapping of Mie resonances. (a) Simulated EELS spectra of a silicon nanoparticle with radius $r = 90$ nm at different impact parameters b. The area curves depict the simulated spectra convoluted with a Lorentzian function. (b) Experimental EELS spectra for a particle with radius $r = 90.5 \pm 2.0$ nm acquired from the regions shown in (c). (c) STEM image of the nanoparticle, where the colored areas represent the integration regions for the experimental EELS signal, and the colored points are the position of the electron beam in the simulation. (d−h) Simulated (top) and experimental (bottom) EELS intensity maps of the first five Mie modes. The EELS maps are individually normalized.

depicts the calculated EELS probability using the same analytical theory as in Figure 1b, while the dashed lines show the first maxima of the different Mie scattering coefficients, which indicate the position of the resonance energies. We find excellent quantitative agreement between experiment and theory across the wide span of particle sizes, even though the theory does not account for the presence of the thin substrate. The strong match evidences that the silicon nitride membrane has a negligible influence on the Mie resonances, which is in agreement with earlier theoretical studies on the influence of substrates on Mie resonances.[30,31] In addition, we highlight that the tightly confined electromagnetic field of the electron beam couples stronger to higher-order Mie resonances than the plane-wave field used in optical measurements,[17,32] which enables us to detect them even in small particles.

The EELS signal is a measure of the efficiency to excite optical resonances by the electron beam,[22] which depends strongly on the position of the electron beam. We exploit this feature of EELS to identify the resonance energies of spectrally close Mie resonances. In particular, we distinguish the ED and magnetic quadrupole (MQ) modes as well as the electric quadrupole (EQ) and magnetic hexapole (MH) modes, even though their resonance energies are closer than the energy

resolution of our EELS setup (80 meV). In Figure 2a−c, we present EELS spectra acquired at different electron beam positions from a nanoparticle with a larger radius of $r = 90 \pm 2.0$ nm, which supports higher-order Mie resonances. From EELS simulations (Figure 2a), we find that the ED mode is efficiently excited by positioning the electron beam outside the nanoparticle ($b = 145$ nm), while the MQ mode dominates for impact parameters inside the nanoparticle ($b = 60$ nm). This difference in excitation efficiency shifts the experimental EELS peak to either the ED or MQ resonance energies, enabling us to identify both resonance energies from each silicon nanoparticle (Figure 2b). A similar analysis is performed to distinguish the EQ and MH modes by comparing the EELS signal acquired in the center of the particle ($b = 0$ nm) to that acquired approximately halfway through the particle (see Figure S1 for detailed comparison). While this unique property of EELS has also been used to distinguish spectrally close plasmonic modes,[29] the strong surface localization of plasmonic fields generally requires the electron beam to be positioned near the particle surface for efficient excitation. As such, distinguishing neighboring plasmonic modes with EELS often comes down to achieving the highest energy resolution possible.[33] In contrast, Mie resonances localize light both inside and outside the nanoparticle, enabling us to fully
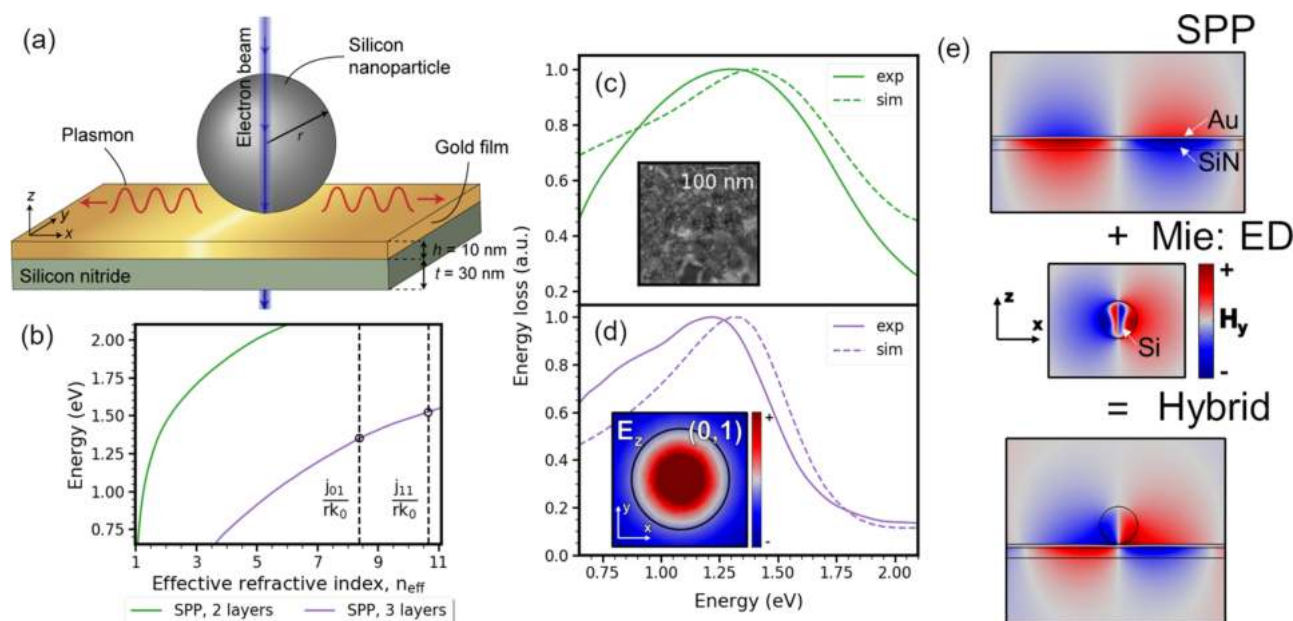
Figure 3. Hybrid dielectric−plasmon resonances. (a) Schematic of a silicon nanoparticle placed on a thin layer stack consisting of a 10 nm gold film on top of a 30 nm silicon nitride membrane. The structure is probed by an electron beam penetrating the center of the nanoparticle (b = 0 nm). (b) Dispersion relation of the short-range SPP supported by the gold−silicon nitride stack (green line) as well as the silicon−gold−silicon nitride stack (purple). In the latter, the silicon thickness is 110 nm, corresponding to the diameter of the nanoparticle. The two lowest-order resonance conditions given by eq 2 are depicted as vertical lines. (c, d) Experimental and simulated EELS spectra of the structure without and with the silicon nanoparticle, respectively. The radius of the particle is r = 54.1 ± 0.8 nm. The inset in (d) shows the z component of the electric field of the (0, 1) hybrid mode in the xy-plane at the top gold surface. (e) Cross-sectional magnetic field profiles of the short-range SPP mode without the nanoparticle (top), the electric dipole mode of an isolated silicon nanoparticle (middle), and the hybrid dielectric−plasmon mode (bottom).

capitalize on the highly localized nature of the electron beam source.

The EELS simulations shown in Figure 2a are performed in COMSOL Multiphysics, which allows us to go beyond the analytical solution provided in ref 28 by including thin substrate layers as well as obtaining EELS spectra for impact parameters inside the nanoparticle. The EELS signal is calculated as the work rate W_{EELS} done on the electron beam by the electromagnetic field induced by the optical structure $\mathbf{E}^{ind}$:

$$W_{EELS}(\omega) = \frac{1}{2} \int Re[\mathbf{j}^*(\mathbf{r}_e, z, \omega) \cdot \mathbf{E}^{ind}(\mathbf{r}_e, z, \omega)] \, dz \qquad (1)$$

Here, $\mathbf{j}(\mathbf{r}_e, z, \omega) = -e\hat{\mathbf{z}}\delta(\mathbf{r} - \mathbf{r}_e)e^{i\omega z/v}$ is the frequency domain representation of the current density of an electron moving at a speed v along the z-direction, and $\mathbf{r}_e = (x_e, y_e)$ denotes the in-plane position of the electron beam, which relates to the impact parameter as $b = |\mathbf{r}_e|$. The integral in eq 1 is performed along the line sustaining the incident current.[34]

Equipped with eq 1, we map the first five Mie modes both numerically and experimentally (Figure 2d−h). We harness the near-perfect spherical shape of the nanoparticles to average the experimental data along the in-plane azimuth angle, which results in a radial EELS profile with a high signal-to-noise ratio (Methods). The radial profile is then depicted in a two-dimensional plot for easy comparison with the simulated EELS maps (see Figure S2 for the unprocessed EELS maps). The MD mode (Figure 2d) shows a doughnut-like field profile with a maximum intensity approximately two-thirds inside the nanoparticle and a complete minimum at the center. This demonstrates that the radial electric field of the electron beam cannot excite the MD mode when the electron beam is

positioned at the particle center. A similar intensity map is observed for the MQ mode (Figure 2f), albeit with a stronger localization to the nanoparticle and a weaker minimum in the center. On the other hand, the ED mode (Figure 2e) shows a peak in the center and maximal intensity localized near the particle surface. Compared to the MQ mode, the ED mode extends further outside the particle, which we exploited to distinguish their close resonance energies. The higher-order EQ and MH modes (Figure 2g,h) both show a maximal EELS intensity in the particle center. However, the MH mode decreases continuously as the position of the beam is moved radially outward, while the EQ mode shows a dip halfway through the particle. This subtle difference in excitation efficiency is utilized to distinguish their resonance energies in the experimental data. We note that the EELS maps of neighboring Mie modes are influenced by the broad nature of the resonances and, for the experimental maps, also by the energy resolution of the EELS setup (see Figure S2 for the simulated EELS maps convoluted with a Lorentzian to account for the energy resolution of the EELS setup). Nonetheless, we find reasonable agreement between experimental and simulated EELS maps, which demonstrates that EELS can be successfully applied to detect the rich field profiles of Mie resonances.

Plasmon Launching. Placing silicon nanoparticles on metal films substantially changes the optical response due to the presence of SPPs. This coupling between SPPs and Mie resonances gives rise to hybrid dielectric−plasmon resonances. For optically thick metal films, the coupling into guided SPPs is weak, and the hybrid resonances radiate primarily into free-space photons.[16] In contrast, optically thin films support coupled SPPs which have a strong modal overlap with the

85
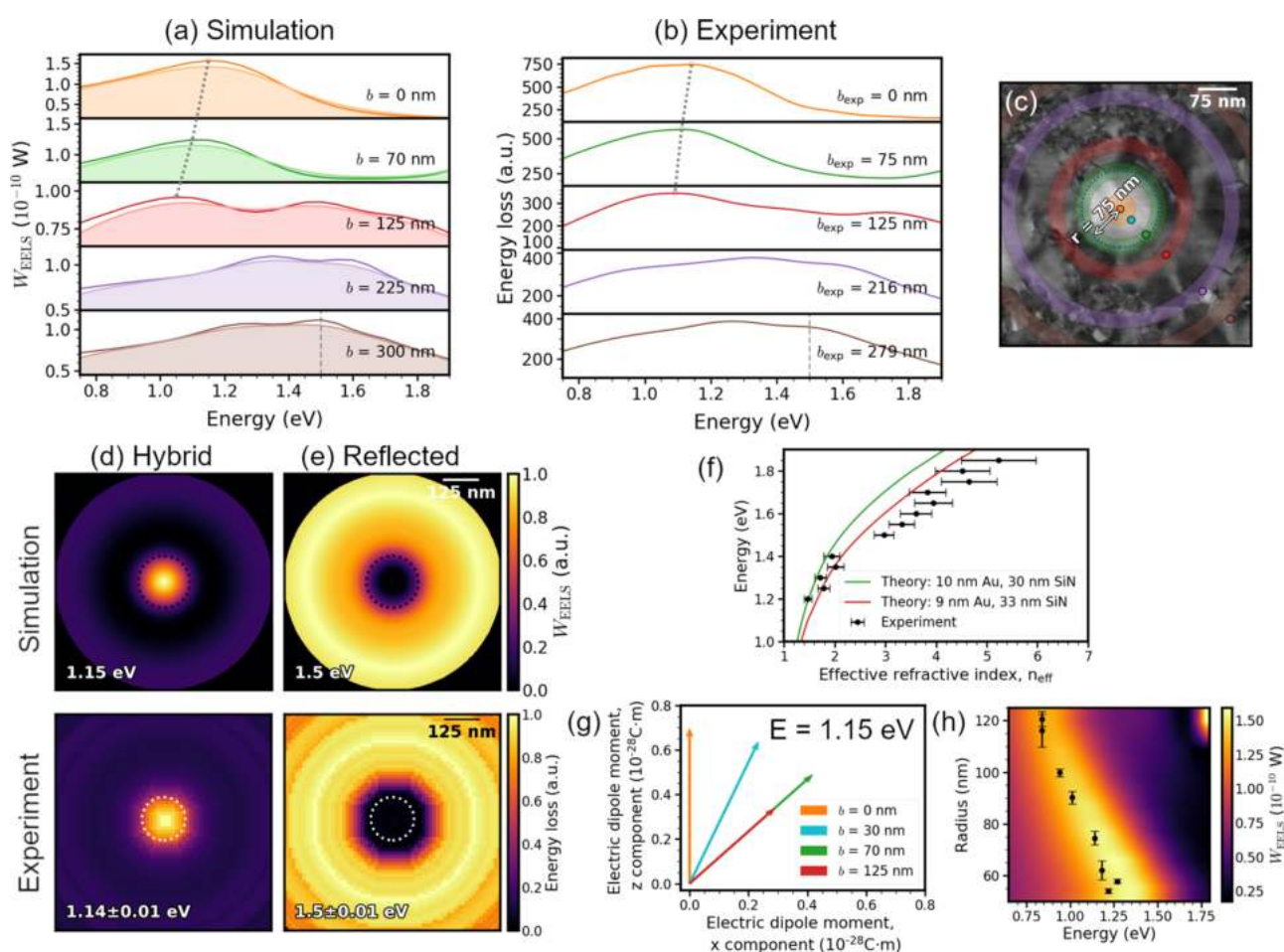
Figure 4. Plasmon launching and scattering. (a) Simulated EELS spectra of a silicon nanoparticle ($r = 75$ nm) on a thin gold−silicon nitride stack at different impact parameters b. The area curves depict the simulated spectra convoluted with a Lorentzian function. (b) Experimental EELS spectra for a particle with radius $r = 74.5 \pm 2.6$ nm acquired from the regions shown in (c). (c) STEM image of the nanoparticle, where the colored areas represent the integration regions for the experimental EELS signal, and the colored points are the position of the electron beam in the simulation. (d, e) Simulated (top) and experimental (bottom) EELS maps of the (0, 1) hybrid mode and the SPP reflection. (f) Experimental and theoretical dispersion relations of the short-range SPP supported by the gold−silicon nitride stack. Experimental data points are determined by using eq 3 on the SPP reflection EELS maps of the nanoparticle in (c). (g) Electric dipole moment of the (0, 1) hybrid mode at different impact parameters, which shows the change in dipole direction as the electron beam is moved away from the center of the particle. (h) Measured resonance energies of the (0, 1) hybrid mode as a function of particle radius acquired by positioning the electron beam in the nanoparticle center. The color plot shows the EELS simulation for an impact parameter of $b = 0$ nm.

hybrid resonance. Consequentially, the coupling into SPPs is boosted (see Figure S5). We construct such hybrid dielectric−plasmon resonances by placing silicon nanoparticles on a gold film of only 10 nm thickness (Figure 3a). The gold film is deposited on the silicon nitride membrane using an APTMS adhesion layer, which produces high-quality thin films with negligible influence on the SPP propagation[35] (Methods). In general, thin metal films can support two SPP modes, commonly referred to as the long-range and short-range SPPs, due to the hybridization of the SPPs at each metal surface. However, the asymmetric dielectric environment of our gold film turns the long-range SPP into a leaky mode,[5] while the short-range SPP remains below the light line and is strongly confined to the gold film (Figure 3b, green line). The short-range SPP can be excited directly by the electron beam without the nanoparticle, resulting in a broad response in the EELS spectrum with a peak at 1.3 eV (Figure 3c). The large linewidth (∼1 eV) of the EELS peak stems from the

broadband nature of the electron source, which may couple to the SPP at different energies and wavenumbers. This property combined with the dispersion relation of the short-range SPP specifies the peak energy in the EELS spectrum.[36]

On the other hand, the presence of the silicon nanoparticle gives rise to a notably narrow and red-shifted EELS peak (Figure 3d). The EELS peak is due to the formation of a hybrid dielectric−plasmon resonance, which, for the particle radius of $r = 54.1 \pm 0.8$ nm, has a resonance energy of 1.22 eV. The hybrid resonance can be conceptually understood as a standing wave of the short-range SPP residing beneath the nanoparticle. The SPP dispersion relation is influenced by the local presence of silicon and can to a good approximation be accounted for in a three-layer silicon−gold−silicon nitride model, where the thickness of the silicon layer is defined by the particle diameter (Figure 3b, purple line). The dispersion relation is then sampled at specific wavenumbers k_{lm} defined by

the resonance condition of zero round trip phase,[16] which is given by the relation

$$k_{lm}r \approx j_{lm} \tag{2}$$

Here, j_{lm} denotes the mth zero of the spherical Bessel function of order l. Physically, the indices (l, m) correspond to the field variations in the radial and azimuthal directions, respectively. The two lowest quantized wavenumbers given by eq 2 are depicted in Figure 3b. We find that the resonance energy of the lowest-order $(0, 1)$ mode, corresponding to the field profile shown in Figure 3d, matches accurately with the energy of the EELS peak in our measurements. The nature of the hybrid resonance is further elucidated in Figure 3e, which illustrates how the short-range SPP of the thin gold film hybridizes with the out-of-plane ED resonance of the silicon nanoparticle to form the hybrid resonance. Here, it is of value to note the similarity in the field profiles of the hybrid mode and the SPP mode. This substantial spatial field overlap facilitates an efficient excitation of the SPP mode.

Another signature of the strong hybridization is the spectral shift between the ED resonance of an isolated silicon nanoparticle (Figure 1b) and the hybrid resonance. Comparing silicon nanoparticles of the same size, the ED resonance of an isolated silicon nanoparticle shows a dramatic shift from 2.97 eV to the hybrid resonance energy of 1.22 eV. Consequentially, the hybrid resonance confines light on a scale even smaller than the lowest-order MD resonance, which is not altered significantly by the presence of the thin gold film (see Figure S3). Comparing the hybrid resonance wavelength λ_H with the MD resonance wavelength λ_{MD} of the same particle reveals an increase in light confinement by a factor $\lambda_H/\lambda_{MD} \approx 2$. The gain in light confinement stems from the fact that the hybrid resonance is formed due to the confinement of the SPP, while the Mie resonances arise due to the confinement of light inside silicon. Interestingly, this reveals that dielectric nanoparticles on thin metal films lead to a system with substantially higher effective refractive index than that available with purely dielectric materials, offering a route for shrinking dielectric scatterers below their diffraction limit.

The resonance energy of the hybrid mode is surprisingly dependent on the position of the electron beam (Figure 4), which is in contrast to the Mie resonances of isolated silicon nanoparticles (Figure 2). We observe that as the electron beam is moved radially outward from the center of the silicon nanoparticle, the hybrid resonance energy shows a red-shift of around 50 nm (Figure 4a−c). A Cartesian multipole decomposition[37] of the electromagnetic field induced by the electron beam reveals that the hybrid mode can be described by an electric dipole (Figure 4g). When the beam is positioned in the center of the particle, the electric dipole is oriented normal to the gold surface. As the beam is moved off-center, the red-shift of the hybrid mode is accompanied by a tilting of the electric dipole toward the gold surface. For impact parameters far away from the nanoparticle ($b \gtrsim 200$ nm), the EELS signal from the hybrid mode is not detected. This is also visible from the EELS maps of the hybrid mode (Figure 4d), which are different from the Mie modes of isolated silicon nanoparticles (Figure 2).

In addition to the dependence of the electron beam position, eq 2 reveals that the resonance energy of the hybrid modes can be tuned by changing the particle size. By collecting EELS data from different particles, we experimentally trace the $(0, 1)$ mode energy as a function of particle size (Figure 4h). We find

that the resonance energy can be effectively modulated from the near-infrared to telecommunication wavelengths. The resonance energies are in agreement with our EELS simulations, which also show a line width narrowing of the resonance at lower energies due to increasing SPP propagation length.

The hybridization between the Mie and the SPP modes is a key signature of their modal overlap and needs to be tailored to effectively use silicon nanoparticles as SPP launchers. In this regard, EELS offers a unique insight into the hybridization, as we can track both spectral shifts in a large energy range and changes in the near-field profiles of the modes. Such insight is not feasible in a standard far-field optical measurement. While our EELS results are important for near-field excitation sources, such as an electron beam or dipole emitter, it is also relevant to consider the properties of our system when excited by a plane wave. To this end, we perform additional plane-wave simulations of the scattering efficiency of the silicon nanoparticle, which are representative for optical measurements (see Figure S4). These simulations reveal that light couples to the $(1, 1)$ hybrid mode. By decomposing the scattered field into free-space and SPP radiation,[38] we find that the main contribution (>80%) to the scattering efficiency is the launching of SPPs. We also note that sending light at different angles of incidence provides a knob to fine-tune the SPP launching energy due to the reorientation of the electric dipole (Figure 4g), albeit with a reduction in the SPP coupling efficiency. This demonstrates that the hybrid dielectric−plasmon modes offer efficient nanoscale SPP launching regardless of the excitation source.

Plasmon Scattering. When the electron beam is positioned outside the particle, we observe additional peaks in the EELS spectra appearing at larger energies than the hybrid mode (Figure 4a,b). These peaks occur due to the reflection of the SPP from the silicon nanoparticle. As discussed in relation to Figure 3, the electron beam can directly excite SPPs in a broad energy range,[39] which are subsequently reflected by the nearby silicon nanoparticle. This results in an SPP interference pattern outside the nanoparticle with local electric field maxima producing regions of EELS signal with a larger amplitude.[40] We visualize this effect by mapping the EELS intensity at an energy of 1.5 eV (Figure 4e). Here, a clear ring structure is visible with a maximum EELS intensity approximately 200 nm from the nanoparticle center, which is in good agreement with the EELS simulations. The radial distance b from the EELS maximum to the nanoparticle center can be determined by tracking the SPP propagation and reflection phases,[22] providing physical insight into the simulations. By describing the SPP waves as one-dimensional plane waves with a wavelength λ_{SPP}, we find the phase relation

$$b = \frac{(2\pi q - \phi)}{4\pi}\lambda_{SPP} \tag{3}$$

Here, ϕ is the reflection phase and q is a positive integer, which denotes the interference order. From EELS simulations we find that the SPP reflection occurs at the nanoparticle center (see Figure S6). A part of the SPP propagation phase is therefore acquired inside the nanoparticle, which differs from the phase pickup outside the nanoparticle due to the refractive index of silicon. In the derivation of eq 3, we have assumed that this difference in phase pickup is small and described the nanoparticle as a reflecting boundary located at the nano-

particle center. As we show, this assumption is valid at low energies where the SPP wavelength is long.

By measuring the distance b from the ring-shaped EELS maps at different energies, we extract the SPP dispersion relation using eq 3 assuming a zero phase shift upon reflection (Figure 4f). For energies below approximately 1.5 eV, the ring-shaped EELS signal occurs due to the standing wave of half the SPP wavelength ($q = 1$), while for larger energies the standing wave corresponds to one SPP wavelength ($q = 2$) (see Figure S6). The experimentally extracted SPP dispersion agrees well with theory at low energies, but deviates at higher energies, even when we consider different layer thicknesses within our fabrication tolerance. Similar results are obtained when we extract the SPP dispersion from other nanoparticle sizes. The difference between theory and experiments observed at higher energies is due to the additional phase pickup upon propagation inside the nanoparticle, which is not accounted for in eq 3. Nonetheless, the SPP dispersion diagram demonstrates that silicon nanoparticles reflect the short-range SPP in a broad energy range.

At the resonance energy of the hybrid mode, the SPP reflection phase is expected to vary significantly due to the excitation of the hybrid resonance. To study this in more detail, we have simulated the SPP reflection from a silicon nanowire, which corresponds to the two-dimensional version of our system and also supports hybrid modes (see Figure S7). Here, we launch SPPs and detect the reflected SPP at the nanowire center. These simulations reveal that the SPP excitation of the hybrid mode coincides with both a varying reflection phase and an SPP reflectance minimum. The drop in the SPP reflectance is due to scattering of the SPP into free-space radiation through the hybrid mode. While we are not able to extract the reflection phase from our EELS measurements, we seem to qualitatively observe a weak drop in the EELS intensity of the interference pattern outside the nanoparticle at approximately 1.45 eV, which is close to the resonance energy of the (1, 1) hybrid mode (see Figure S8). However, an unambiguous experimental demonstration of the SPP scattering into free-space radiation due to the nanoparticle requires detecting the scattered light, such as in cathodoluminescence. Our EELS results show that silicon nanoparticles can be used to excite and reflect SPPs. This provides an exciting opportunity to design compact SPP optical elements with high-refractive-index nanostructures.

DISCUSSION AND CONCLUSIONS

Using EELS, we have measured and mapped the Mie resonances of spherical silicon nanoparticles in a broad radius range. Each Mie resonance shows unique field variations inside the nanoparticles, which we exploit in our EELS measurements. By careful positioning of the electron beam, we extract the resonance energies of the first five Mie resonances, even though some of the resonances are closer in energy than the energy resolution of our EELS setup. Full-wave EELS simulations corroborate our experimental findings and show excellent quantitative agreement. Our results expand the capabilities of EELS to include high-index nanophotonics and may in the future shed more light on important interference phenomena such as anapole states and bound states in the continuum.[41,42]

By placing silicon nanoparticles on a thin gold film, we find a new class of hybrid dielectric−plasmon resonances governed by both the short-range SPP of the gold film and the

nanoparticle material and size. The observed hybrid mode shows significantly stronger light confinement than the Mie resonances and couples efficiently to the SPP of the thin film. We experimentally demonstrate that the hybrid resonance energy can be controlled across the entire near-infrared by the particle size, providing a simple tuning mechanism to excite SPPs at a desired wavelength. By performing a multipole decomposition of the induced field, we find that the optical response of the hybrid mode corresponds to an electric dipole with a direction sensitive to the electron beam position. Positioning the beam in the nanoparticle center leads to an out-of-plane electric dipole moment, which is gradually tilted toward the gold surface as the beam is moved radially outward. This tilting is accompanied by a red-shift of the hybrid mode. We anticipate that the tilted electric dipole can be exploited in an optical setup to realize directional SPP launching by exciting the nanoparticle with circularly polarized light.[43]

Finally, we experimentally show that the short-range SPPs are scattered by the nearby silicon nanoparticle. The scattering process leads to an interference pattern with local field maxima producing regions of the EELS signal with a larger amplitude. By tracking the SPP propagation and reflection, we derive a simple theoretical relation, which enables us to experimentally extract the SPP dispersion relation in a broad energy range. Our results provide evidence for the SPP scattering properties of high-index nanostructures, opening up an avenue for new designs of SPP optical elements.

■ METHODS

Fabrication. *TEM Membranes.* A low-stress silicon-rich nitride layer is deposited on top of an n-type (phosphor) ⟨100⟩ double-side polished silicon wafer by low-pressure chemical vapor deposition (LPCVD). The resulting thickness determined by ellipsometry is around 33 nm, with a 1 nm native silicon oxide below the nitride. This is followed by a UV lithography step to create a photoresist pattern for the membrane windows on one side of the wafer. Afterward, the silicon nitride is dry etched using the lithographic pattern, followed by photoresist strip, wet KOH etching of the silicon, and water/HCl 4:1 cleaning.

For the gold samples, the wafers are submerged into a solution of 95% isopropanol, 2.5% water, and 2.5% APTMS for 3 h to achieve a 1 nm APTMS layer,[35] followed by two steps of isopropanol/water rinsing. Sputter deposition is used to produce a 10 nm thick gold layer. Both AFM and ellipsometry confirm the thickness of the gold layer to be 9−10 nm. The root mean squared roughness of the gold surface as measured by AFM is around 1.5 nm.

The wafers are then covered with a protective layer of photoresist. The wafer without (with) gold is laser cut (diced) into smaller TEM chips. Subsequently, the photoresist is removed in acetone followed by isopropanol for 10 min in both steps. The wafers without gold are also plasma ashed for 5 min. The plasma ashing and laser cutting are not performed on the gold samples due to damage introduced to the thin gold layer by these procedures.

Silicon Nanoparticles. The crystalline silicon nanoparticles of spherical shape are produced by thermal annealing of silicon suboxide (SiO$_x$) and extraction into methanol.[27] A silicon-rich SiO$_x$ film of 10−20 μm in thickness is prepared by co-sputtering of Si and SiO$_2$ together with B$_2$O$_3$ and P$_2$O$_5$. The film is annealed at 1500 °C in a nitrogen atmosphere for 30 min to grow silicon nanoparticles in a SiO$_2$ matrix. The silicon

nanoparticles are extracted from the matrix by hydrofluoric acid (46 wt %) etching and transferred to a methanol solution. The doping of boron and phosphor results in formation of a heavily boron and phosphor codoped layer on the nanoparticle surface and prevents agglomeration in the solution. In optical measurement, it has been shown that the scattering spectrum of the nanoparticle perfectly agrees with the Mie theory.[31] At the end of the fabrication, a 10 μL solution of silicon nanoparticles in methanol is drop-casted onto the membrane. The membrane is nitrogen dried after a 1 min wait time.

Image Analysis. The sizes of the silicon nanoparticles are determined from the STEM images using image processing operations with the Python scikit-image library. Initially, the particle size is predetermined manually resulting in an expected radius r_{exp}. For the samples without the gold layer, a Canny filter with $\sigma = 3$ pixels is applied to find the particle edges. This is followed by a diameter $0.7r_{exp}$ and area $1.4\pi r_{exp}$ opening morphological operations to remove the false edge pixels.

For the samples with the gold layer, the particle edges are predetermined with a $\sigma = 20$ pixels Canny edge detector. Knowing that the particle is located approximately in the center of the image (particle center coordinates c_x and c_y are in the center of the image), all the edges after $2r_{exp}$ are removed. The resulting edge map is fitted with the Hough circle transform, resulting in the intermediate radius r_{int} and intermediate particle center coordinates c_{xi} and c_{yi}. Then, the particle edges are found with a $\sigma = 10$ pixels Canny edge detector. Assuming the particle center is located at c_{xi} and c_{yi}, all edges before $0.8r_{int}$ and after $1.3r_{int}$ are removed, followed by a diameter $0.1r_{exp}$ opening. Finally, the Hough circle transform is applied on the last edge map to find the best fit for the radius and particle center.

The uncertainty in the radius is determined by fitting the number of intersections−radius dependence with a bimodal distribution of 2 Gaussians. The number of intersections−radius dependence is provided from the Hough circle transform since it draws circles with a particular radius centered on each pixel of the edge map and counts the number of their intersections at different locations on the map. The point with the highest number is taken as a center location of the particle. This process is performed for different radii in the provided radius range $r_{exp} \pm r_{range}$. The uncertainty is taken as the standard deviation of the smaller Gaussian or the image resolution if the resolution is larger than the standard deviation. Then, the final edge map is enlarged by 2 pixels, the circle Hough transform is performed, and Gaussians are fitted again, resulting in the new circle parameters and the uncertainty. If the uncertainty is smaller than the previous value and not larger than the image resolution of 3 pixels, it is taken as a new true value; otherwise, the previous values are preserved. This procedure can be repeated multiple times, resulting in edges that are increased by 2 pixels every step.

EELS Measurements and Analysis. The EELS measurements are performed in a monochromated and aberration-corrected FEI Titan operated in STEM mode at an acceleration voltage of 300 kV, providing a probe size of ~0.5 nm and an energy resolution of 0.08 eV (as measured by the full-width at half-maximum of the zero-loss peak). The zero-loss peak is removed using Richardson−Lucy deconvolution. As input for the point-spread function, we use the reflected tail method for samples without gold, while for the samples with gold we used an EELS spectrum obtained in a vacuum. Due to a small asymmetry in the zero-loss peak, the

deconvolution algorithm produced an artificial EELS peak in the energy range below 0.6 eV. However, the artificial peak did not overlap with any of the observed resonances and could be safely removed using a first-order logarithmic polynomial.

The depicted EELS spectra are obtained by integrating the deconvoluted EELS data around the experimental impact parameter b_{exp}. For the disk-shaped integration regions, the experimental impact parameter denotes the center of the disk. For the annulus-shaped regions, the experimental impact parameter denotes the mean of the inner and outer radii. The depicted EELS spectra are smoothed with a Gaussian function ($\sigma = 0.03$ eV).

The EELS maps are obtained by summing the deconvoluted EELS data in a spectral window of 0.02 eV width centered at the resonance energies. In order to improve the signal-to-noise ratio, the map was spatially binned, reducing the effective number of pixels by a factor of 2 in each row and column, i.e., a factor of 4 in total. Afterward, a Gaussian filter with $\sigma = 0.8$ pixels was applied to smooth the image. Exploiting the spherical symmetry of the nanoparticles, the maps are integrated along the azimuth angle at the coordinates located at the same distance from the nanoparticle center.

EELS Simulations. The EELS simulations are performed in COMSOL Multiphysics, which uses finite-element modeling to solve Maxwell's equations. The electron beam is simulated using an edge current with an amplitude of 1 μA. The induced electromagnetic field is determined by calculating the field with and without the optical structures in the simulation space and subsequently subtracting them. Using the obtained induced electric field, the energy loss can be calculated using eq 1. To mimic the experimental energy resolution, we also perform a convolution with a Lorentzian function with a full-width at half-maximum of 0.1 eV. The complex refractive indices for silicon, gold, and silicon nitride are taken from refs 44−46, respectively. The silicon nitride layer is not included in the simulation of the silicon nanoparticle without the gold layer (Figure 2).

■ ASSOCIATED CONTENT

Ⓢ Supporting Information

The Supporting Information is available free of charge at https://pubs.acs.org/doi/10.1021/acsphotonics.0c01554.

> Positioning of the electron beam for distinguishing the spectrally close EQ and MH Mie resonances; additional spatial EELS maps for Figure 2; EELS measurements of Mie resonances in silicon nanoparticles on a thin gold film; plane-wave excitation of the hybrid dielectric−plasmon mode at varying angles of incidence; SPP coupling efficiency of the hybrid dielectric−plasmon mode as a function of gold thickness; SPP reflection for different interference orders (PDF)

■ AUTHOR INFORMATION

Corresponding Author

Søren Raza − *Department of Physics, Technical University of Denmark, DK-2800 Kongens Lyngby, Denmark;* ⓞ orcid.org/0000-0002-0296-7202; Email: sraz@dtu.dk

Authors

Artyom Assadillayev − *Department of Physics, Technical University of Denmark, DK-2800 Kongens Lyngby, Denmark*

Tatsuki Hinamoto − *Department of Electrical and Electronic Engineering, Kobe University, Kobe 657-8501, Japan*

Minoru Fujii − *Department of Electrical and Electronic Engineering, Kobe University, Kobe 657-8501, Japan;* ● orcid.org/0000-0003-4869-7399

Hiroshi Sugimoto − *Department of Electrical and Electronic Engineering, Kobe University, Kobe 657-8501, Japan;* ● orcid.org/0000-0002-1520-0940

Mark L. Brongersma − *Geballe Laboratory for Advanced Materials, Stanford University, Stanford, California 94305, United States;* ● orcid.org/0000-0003-1777-8970

Complete contact information is available at:
https://pubs.acs.org/10.1021/acsphotonics.0c01554

Author Contributions

S.R. and M.L.B. conceived the experiments. A.A. fabricated the samples and performed the EELS measurements. A.A. performed the image and EELS data analyses. A.A. and S.R performed the simulations. T.H., H.S., and M.J. fabricated the silicon nanoparticles. A.A. and S.R. prepared figures and wrote the manuscript. S.R. supervised the project. All authors discussed the results and contributed to the preparation of the manuscript.

Notes

The authors declare no competing financial interest.

■ REFERENCES

(1) Ritchie, R. H. Plasma losses by fast electrons in thin films. *Phys. Rev.* **1957**, *106*, 874−881.

(2) Schuller, J. A.; Barnard, E. S.; Cai, W.; Jun, Y. C.; White, J. S.; Brongersma, M. L. Plasmonics for extreme light concentration and manipulation. *Nat. Mater.* **2010**, *9*, 193−204.

(3) Cheben, P.; Halir, R.; Schmid, J. H.; Atwater, H. A.; Smith, D. R. Subwavelength integrated photonics. *Nature* **2018**, *560*, 565−572.

(4) Haffner, C.; et al. Low-loss plasmon-assisted electro-optic modulator. *Nature* **2018**, *556*, 483−486.

(5) Han, Z.; Bozhevolnyi, S. I. Radiation guiding with surface plasmon polaritons. *Rep. Prog. Phys.* **2013**, *76*, 016402.

(6) Bozhevolnyi, S. I.; Pudonin, F. A. Two-dimensional micro-optics of surface plasmons. *Phys. Rev. Lett.* **1997**, *78*, 2823−2826.

(7) Hohenau, A.; Krenn, J. R.; Stepanov, A. L.; Drezet, A.; Ditlbacher, H.; Steinberger, B.; Leitner, A.; Aussenegg, F. R. Dielectric optical elements for surface plasmons. *Opt. Lett.* **2005**, *30*, 893.

(8) Zayats, A. V.; Smolyaninov, I. I.; Maradudin, A. A. Nano-optics of surface plasmon polaritons. *Phys. Rep.* **2005**, *408*, 131−314.

(9) Basov, D. N.; Fogler, M. M.; García de Abajo, F. J. Polaritons in van der Waals materials. *Science* **2016**, *354*, aag1992.

(10) Wang, Y.; Yu, J.; Mao, Y. F.; Chen, J.; Wang, S.; Chen, H. Z.; Zhang, Y.; Wang, S. Y.; Chen, X.; Li, T.; Zhou, L.; Ma, R. M.; Zhu, S.; Cai, W.; Zhu, J. Stable, high-performance sodium-based plasmonic devices in the near-infrared. *Nature* **2020**, *581*, 401−405.

(11) Smolyaninov, I. I.; Mazzoni, D. L.; Davis, C. C. Imaging of surface plasmon scattering by lithographically created individual surface defects. *Phys. Rev. Lett.* **1996**, *77*, 3877−3880.

(12) Liu, Y.; Palomba, S.; Park, Y.; Zentgraf, T.; Yin, X.; Zhang, X. Compact magnetic antennas for directional excitation of surface plasmons. *Nano Lett.* **2012**, *12*, 4853−4858.

(13) Landreman, P. E.; Brongersma, M. L. Deep-subwavelength semiconductor nanowire surface plasmon polariton couplers. *Nano Lett.* **2014**, *14*, 429−434.

(14) Sinev, I.; Komissarenko, F.; Iorsh, I.; Permyakov, D.; Samusev, A.; Bogdanov, A. Steering of guided light with dielectric nano-antennas. *ACS Photonics* **2020**, *7*, 680−686.

(15) Yang, Y.; Zhen, B.; Hsu, C. W.; Miller, O. D.; Joannopoulos, J. D.; Soljačić, M. Optically thin metallic films for high-radiative-efficiency plasmonics. *Nano Lett.* **2016**, *16*, 4110−4117.

(16) Yang, Y.; Miller, O. D.; Christensen, T.; Joannopoulos, J. D.; Soljačić, M. Low-loss plasmonic dielectric nanoresonators. *Nano Lett.* **2017**, *17*, 3238−3245.

(17) Kuznetsov, A. I.; Miroshnichenko, A. E.; Brongersma, M. L.; Kivshar, Y. S.; Luk'yanchuk, B. Optically resonant dielectric nanostructures. *Science* **2016**, *354*, aag2472.

(18) Sugimoto, H.; Fujii, M. Broadband dielectric-metal hybrid nanoantenna: Silicon nanoparticle on a mirror. *ACS Photonics* **2018**, *5*, 1986−1993.

(19) Egerton, R. F. Electron energy-loss spectroscopy in the TEM. *Rep. Prog. Phys.* **2009**, *72*, 016502.

(20) García de Abajo, F. J. Optical excitations in electron microscopy. *Rev. Mod. Phys.* **2010**, *82*, 210−256.

(21) Nelayah, J.; Kociak, M.; Stéphan, O.; García de Abajo, F. J.; Tencé, M.; Henrard, L.; Taverna, D.; Pastoriza-Santos, I.; Liz-Marzán, L. M.; Colliex, C. Mapping surface plasmons on a single metallic nanoparticle. *Nat. Phys.* **2007**, *3*, 348−353.

(22) Raza, S.; Esfandyarpour, M.; Koh, A. L.; Mortensen, N. A.; Brongersma, M. L.; Bozhevolnyi, S. I. Electron energy-loss spectroscopy of branched gap plasmon resonators. *Nat. Commun.* **2016**, *7*, 13790.

(23) Smith, K. C.; Olafsson, A.; Hu, X.; Quillin, S. C.; Idrobo, J. C.; Collette, R.; Rack, P. D.; Camden, J. P.; Masiello, D. J. Direct observation of infrared plasmonic Fano antiresonances by a nanoscale electron probe. *Phys. Rev. Lett.* **2019**, *123*, 177401.

(24) Govyadinov, A. A.; Konečná, A.; Chuvilin, A.; Vélez, S.; Dolado, I.; Nikitin, A. Y.; Lopatin, S.; Casanova, F.; Hueso, L. E.; Aizpurua, J.; Hillenbrand, R. Probing low-energy hyperbolic polaritons in van der Waals crystals with an electron microscope. *Nat. Commun.* **2017**, *8*, 95.

(25) Coenen, T.; van de Groep, J.; Polman, A. Resonant modes of single silicon nanocavities excited by electron irradiation. *ACS Nano* **2013**, *7*, 1689−1698.

(26) McPolin, C. P.; Marino, G.; Krasavin, A. V.; Gili, V.; Carletti, L.; de Angelis, C.; Leo, G.; Zayats, A. V. Imaging electric and magnetic modes and their hybridization in single and dimer AlGaAs nanoantennas. *Adv. Opt. Mater.* **2018**, *6*, 1−6.

(27) Sugimoto, H.; Fujii, M. Colloidal dispersion of subquarter micrometer silicon spheres for low-loss antenna in visible regime. *Adv. Opt. Mater.* **2017**, *5*, 1−8.

(28) García de Abajo, F. J. Relativistic energy loss and induced photon emission in the interaction of a dielectric sphere with an external electron beam. *Phys. Rev. B: Condens. Matter Mater. Phys.* **1999**, *59*, 3095−3107.

(29) Raza, S.; Kadkhodazadeh, S.; Christensen, T.; di Vece, M.; Wubs, M.; Mortensen, N. A.; Stenger, N. Multipole plasmons and their disappearance in few-nanometre silver nanoparticles. *Nat. Commun.* **2015**, *6*, 8788.

(30) Markovich, D. L.; Ginzburg, P.; Samusev, A. K.; Belov, P. A.; Zayats, A. V. Magnetic dipole radiation tailored by substrates: numerical investigation. *Opt. Express* **2014**, *22*, 10693.

(31) Sugimoto, H.; Hinamoto, T.; Fujii, M. Forward to backward scattering ratio of dielectric-metal heterodimer suspended in almost free-space. *Adv. Opt. Mater.* **2019**, *7*, 1900591.

(32) Zywietz, U.; Evlyukhin, A. B.; Reinhardt, C.; Chichkov, B. N. Laser printing of silicon nanoparticles with resonant optical electric and magnetic responses. *Nat. Commun.* **2014**, *5*, 3402.

(33) Bellido, E. P.; Rossouw, D.; Botton, G. A. Toward 10 meV electron energy-loss spectroscopy resolution for plasmonics. *Microsc. Microanal.* **2014**, *20*, 767−778.

(34) Koh, A. L.; Fernández-Domínguez, A. I.; McComb, D. W.; Maier, S. A.; Yang, J. K. W. High-resolution mapping of electron-beam-excited plasmon modes in lithographically defined gold nanostructures. *Nano Lett.* **2011**, *11*, 1323−1330.

(35) Sukham, J.; Takayama, O.; Lavrinenko, A.; Malureanu, R. High-quality ultrathin gold layers with an APTMS adhesion for optimal performance of surface plasmon polariton-based devices. *ACS Appl. Mater. Interfaces* **2017**, *9*, 25049−25056.

(36) Bolton, J. P. R.; Chen, M. Electron energy loss in multilayered slabs. I. Normal incidence. *J. Phys.: Condens. Matter* **1995**, *7*, 3373.

(37) Evlyukhin, A. B.; Fischer, T.; Reinhardt, C.; Chichkov, B. N. Optical theorem and multipole scattering of light by arbitrarily shaped nanoparticles. *Phys. Rev. B: Condens. Matter Mater. Phys.* **2016**, *94*, 205434.

(38) Yang, J.; Hugonin, J. P.; Lalanne, P. Near-to-far field transformations for radiative and guided waves. *ACS Photonics* **2016**, *3*, 395−402.

(39) Schilder, N. J.; Agrawal, H.; Garnett, E. C.; Polman, A. Phase-Resolved Surface Plasmon Scattering Probed by Cathodoluminescence Holography. *ACS Photonics* **2020**, *7*, 1476−1482.

(40) Schoen, D. T.; Atre, A. C.; García-Etxarri, A.; Dionne, J. A.; Brongersma, M. L. Probing complex reflection coefficients in one-dimensional surface plasmon polariton waveguides and cavities using STEM EELS. *Nano Lett.* **2015**, *15*, 120−126.

(41) Kruk, S.; Kivshar, Y. Functional meta-optics and nanophotonics governed by Mie resonances. *ACS Photonics* **2017**, *4*, 2638−2649.

(42) Hsu, C. W.; Zhen, B.; Stone, A. D.; Joannopoulos, J. D.; Soljačić, M. Bound states in the continuum. *Nat. Rev. Mater.* **2016**, *1*, 16048.

(43) Rodríguez-Fortuño, F. J.; Martínez, A.; Wurtz, G. A.; Zayats, A. V. Near-field interference for the unidirectional excitation of electromagnetic guided modes. *Science* **2013**, *340*, 328−331.

(44) Aspnes, D. E.; Studna, A. A. Dielectric functions and optical parameters of Si, Ge, GaP, GaAs, GaSb, InP, InAs, and InSb from 1.5 to 6.0 eV. *Phys. Rev. B: Condens. Matter Mater. Phys.* **1983**, *27*, 985−1009.

(45) Johnson, P. B.; Christy, R. W. Optical constants of the noble metals. *Phys. Rev. B* **1972**, *6*, 4370−4379.

(46) Luke, K.; Okawachi, Y.; Lamont, M. R. E.; Gaeta, A. L.; Lipson, M. Broadband mid-infrared frequency comb generation in a Si3N4 microresonator. *Opt. Lett.* **2005**, *40*, 4823−4826.

Supporting Information: Plasmon launching and scattering by silicon nanoparticles

Artyom Assadillayev,[†] Tatsuki Hinamoto,[‡] Minoru Fujii,[‡] Hiroshi Sugimoto,[‡] Mark L. Brongersma,[¶] and Søren Raza[*,†]

†*Department of Physics, Technical University of Denmark, Fysikvej, DK-2800 Kongens Lyngby, Denmark*

‡*Department of Electrical and Electronic Engineering, Kobe University, Rokkodai, Nada, Kobe 657-8501, Japan*

¶*Geballe Laboratory for Advanced Materials, 476 Lomita Mall, Stanford University, Stanford, CA 94305, USA*

E-mail: sraz@dtu.dk

Figure S1: Distinguishing the spectrally-close EQ and MH Mie resonances. (a) Experimental EELS spectra of a silicon nanoparticle ($r = 90.5 \pm 2.0$ nm) on a thin silicon nitride membrane at the electron beam positions indicated in (b). Careful positioning of the electron beam enables us to shift the EELS peak to either the EQ or MH resonance energies. This allows us to measure both resonance energies from a single silicon nanoparticle, even though their energies are closer than the energy resolution of our EELS setup.
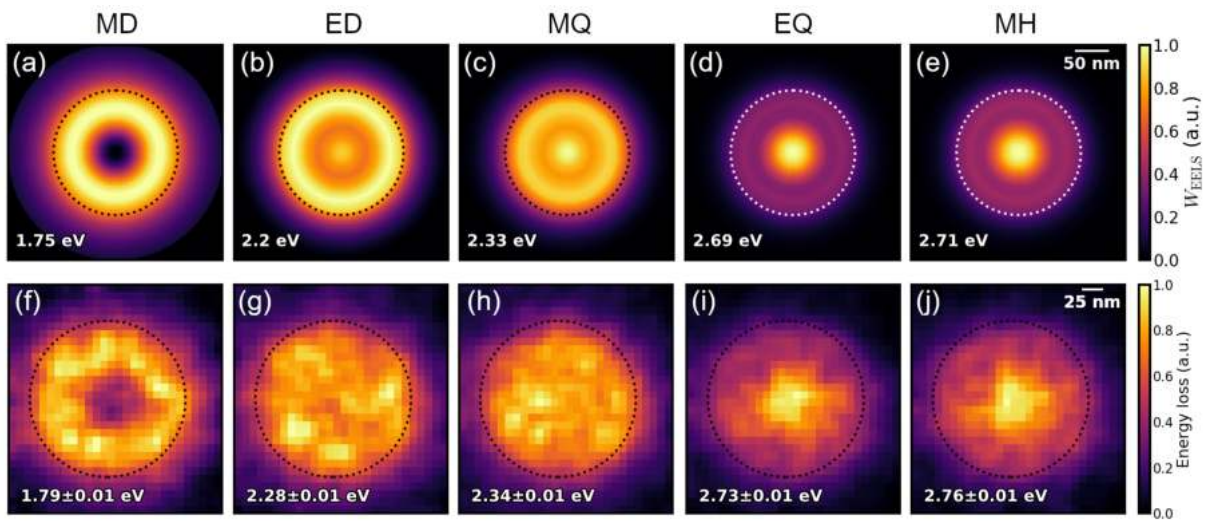
Figure S2: Additional spatial EELS maps for Figure 2 in the manuscript. (a-e) Simulated EELS maps for the EELS spectra convoluted with a Lorentzian function. A maximum appears in the nanoparticle center for the ED and MQ modes. This leads to closer correspondence with the experimental EELS maps shown in Figure 2. (f-j) Experimental EELS maps before spatial integration along the azimuth angle. While similar features may be observed in the unprocessed EELS maps, it is clear that exploiting the spherical symmetry of the nanoparticles to perform an azimuthal integration results in EELS maps with markedly improved signal-to-noise ratio.
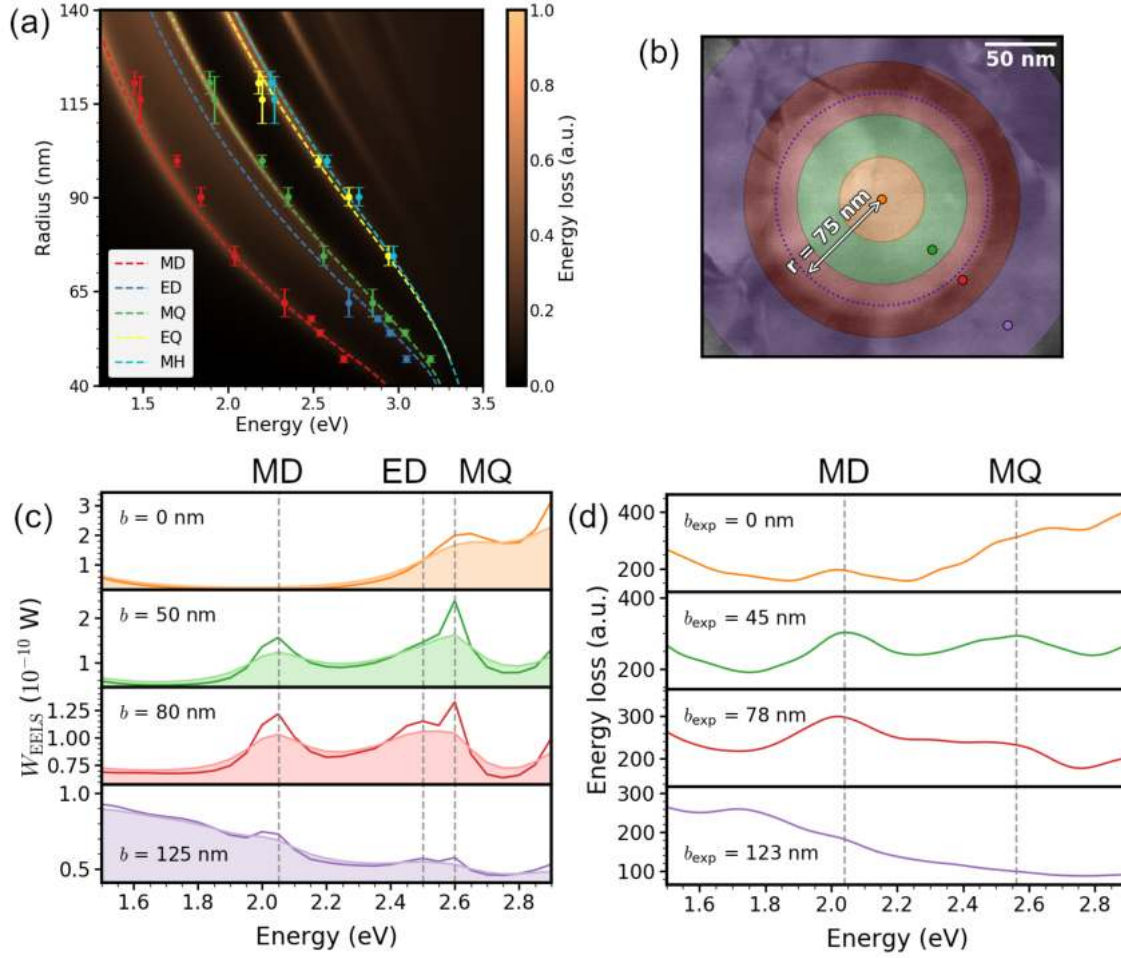
Figure S3: Mie resonances in silicon nanoparticles on a 10 nm thin gold film. (a) Measured resonance energies as a function of particle radius for the first five Mie resonances in silicon nanoparticles on the gold-silicon nitride stack. The colour plot shows the EELS simulation of a *vacuum-embedded* silicon sphere for an impact parameter $b = r + 20$ nm and the dashed curves indicate the free-space theoretical Mie resonance energies. The strong agreement between theory and experiments show that the Mie resonances remain largely unaffected by the presence of the thin gold film. (b) STEM image of the nanoparticle, where the colored areas represent the integration regions for the experimental EELS signal, and the colored points are the position of the electron beam in the simulation. (c) Simulated EELS spectra of a silicon nanoparticle ($r = 75$ nm) on a thin gold-silicon nitride stack at different impact parameters b. The area curves depict the simulated spectra convoluted with a Lorentzian function. (d) Experimental EELS spectra for a particle with radius $r = 74.5 \pm 2.6$ nm acquired from the regions shown in (b). The EELS spectra show that the Mie modes can be safely identified when the electron beam is positioned inside the particle. As the beam is moved outside the nanoparticle, the EELS signal from the SPP of the gold film starts to dominate the spectrum, which masks the signal from the ED mode in larger particle sizes. For smaller particle sizes, the ED resonance energy occurs at much larger energies than the SPP, allowing us to identify the ED resonance.

S-4
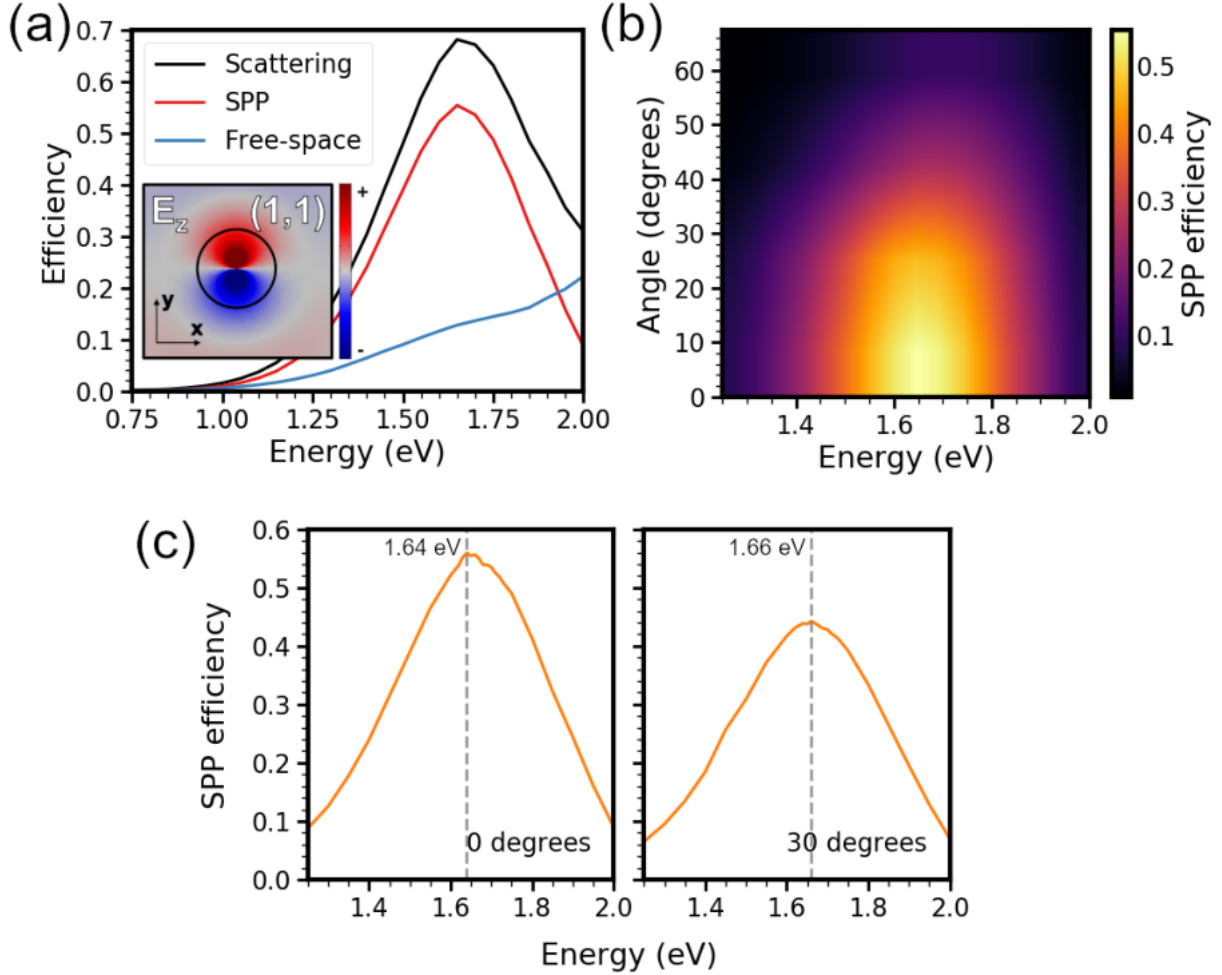
Figure S4: Plane-wave excitation of the hybrid dielectric-plasmon mode. (a) Plane-wave scattering efficiency of a silicon nanoparticle with radius $r = 55$ nm on top of a gold-silicon nitride stack. The scattering efficiency is decomposed into SPP and free-space radiation contributions. The incident plane wave impinges normal to the gold-silicon nitride stack. The inset shows the z component of the electric field of the $(1, 1)$ hybrid dielectric-plasmon mode in the xy-plane at the top gold surface. (b) SPP coupling efficiency as a function of the angle of incidence relative to the perpendicular plane of the gold-silicon nitride stack. (c) SPP efficiency for normally-incident and 30°-incident impinging plane-wave excitation. The SPP efficiency peak shows a delicate shift, consistent with the EELS measurements in Figure 4, accompanied by a modest decrease in efficiency due to a slight re-orientation of the induced electric dipole moment.
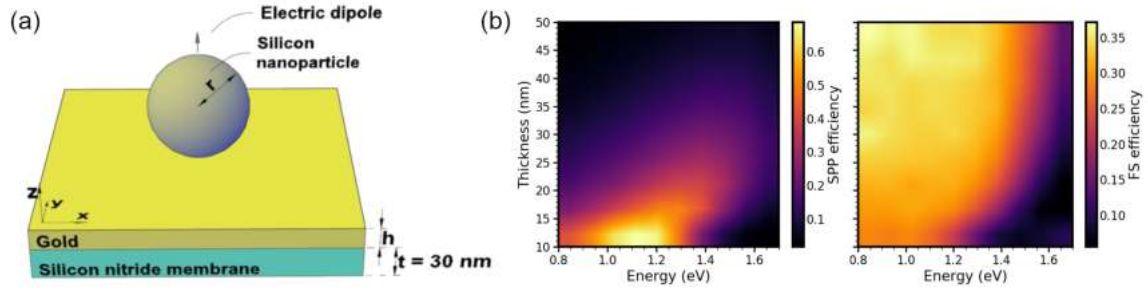
Figure S5: SPP coupling efficiency of the hybrid dielectric-plasmon mode as a function of gold thickness. (a) Schematic of a silicon nanoparticle placed on the gold-silicon nitride stack, which is probed by an electric dipole oriented along the z direction and located above the centre of the nanoparticle at a 1 nm gap. (b) Efficiency of SPP and free-space (FS) coupling of the $(0,1)$ hybrid dielectric-plasmon mode for increasing gold layer thickness. The efficiency is taken as a ratio of the SPP or FS power to the power radiated by the electric dipole in vacuum. The results show the increasing (decreasing) SPP (FS) efficiency for decreasing film thickness, highlighting the importance of thin gold films for efficient SPP coupling.
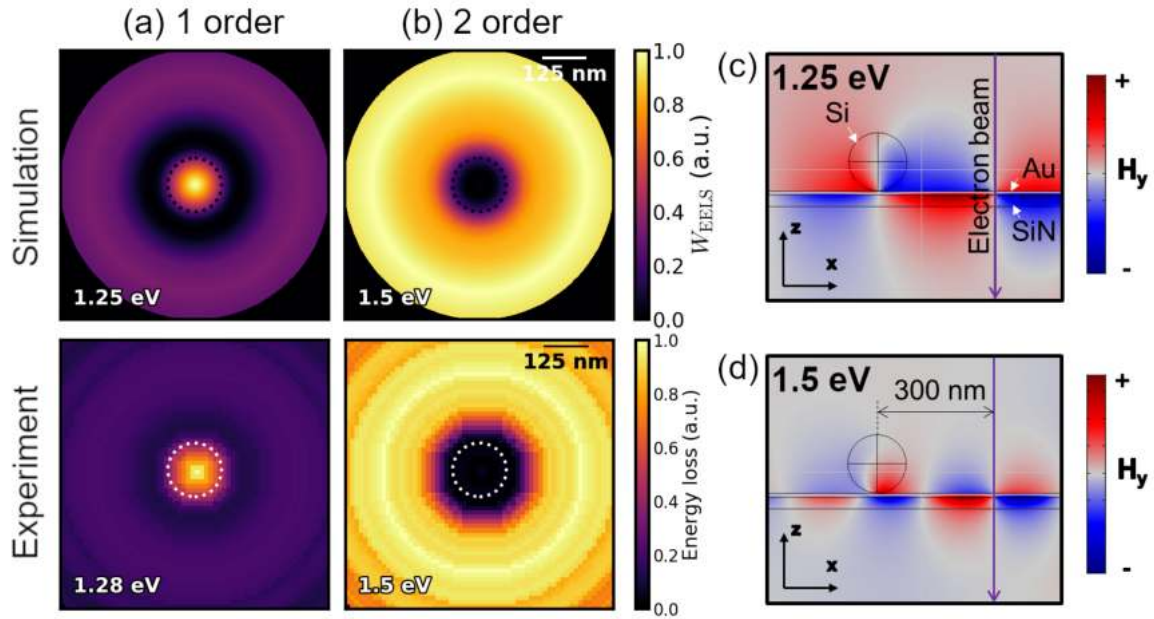
Figure S6: Plasmon reflection for different interference orders. (a,b) Simulated (top) and experimental (bottom) EELS maps of the plasmon reflection at two separate energies, which correspond to either (a) the first-order reflection (half-wavelength of SPP) or (b) second-order reflection (one-wavelength of SPP). The nanoparticle radius is $r = 75$ nm. (c,d) Cross-sectional magnetic field profiles of the reflected SPP mode for first and second interference orders, respectively. In both cases, the reflection occurs at the nanoparticle centre.

S-6
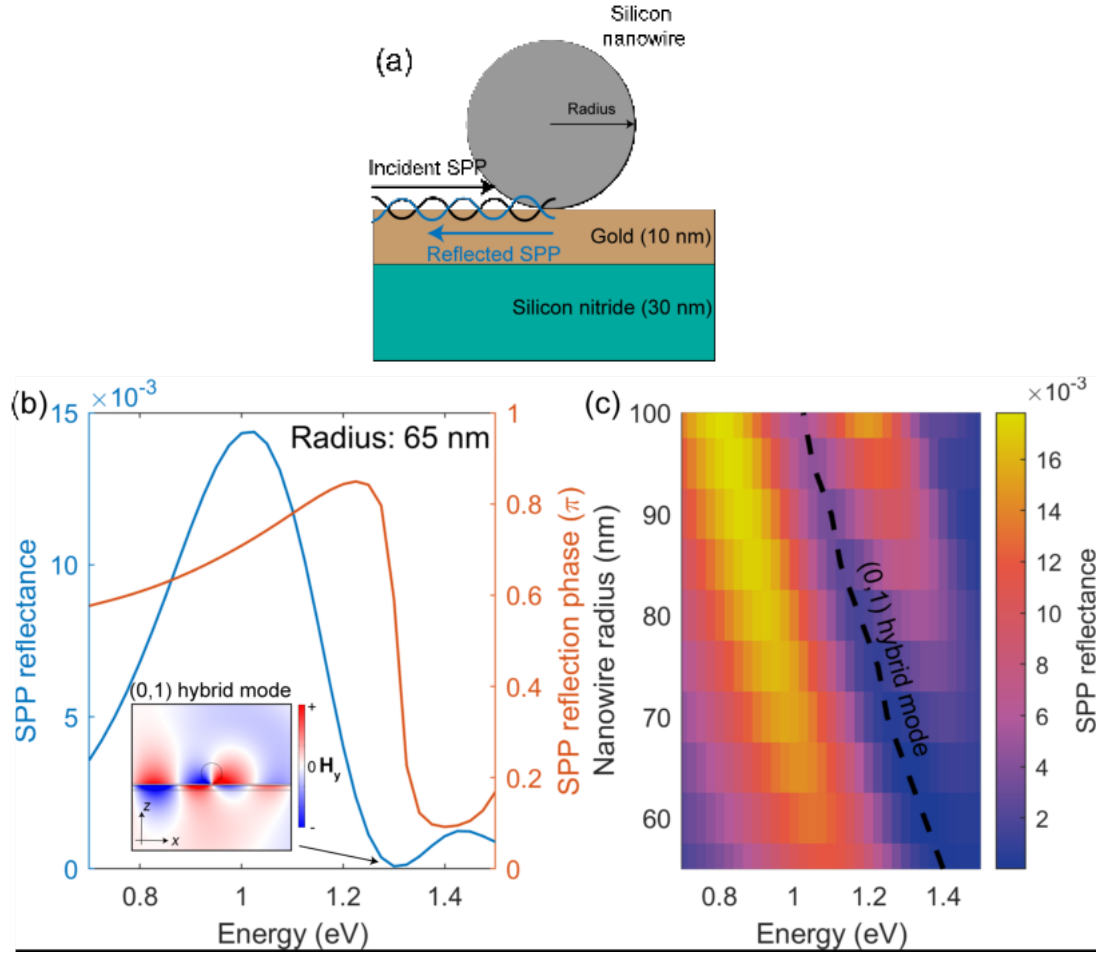
Figure S7: Simulated plasmon reflection from silicon nanowires. (a) The SPP supported by the gold-silicon nitride stack is incident on a silicon nanowire (2D). The incident SPP scatterers into different radiations channels, including reflected and transmitted SPPs as well as free-space radiation. Here, we track the reflected SPP as this is relevant for the EELS measurements in Figure 4. (b) SPP reflectance and reflection phase for a 65 nm radius silicon nanowire. The reflection is evaluated at the at the nanowire centre. The reflectance dip is accompanied by a rapid phase variation, signifying the excitation of the $(0, 1)$ hybrid dielectric-plasmon mode. The inset shows the out-of-plane magnetic field profile at the reflectance dip, which matches well with the field profile shown in Figure 3. The hybrid mode enables efficient outcoupling of the SPP, hence the low reflectance. (c) SPP reflectance map for varying nanowire radius, which shows that the hybrid mode redshifts for increasing radii, in accordance with the EELS measurements in Figure 4.

S-7
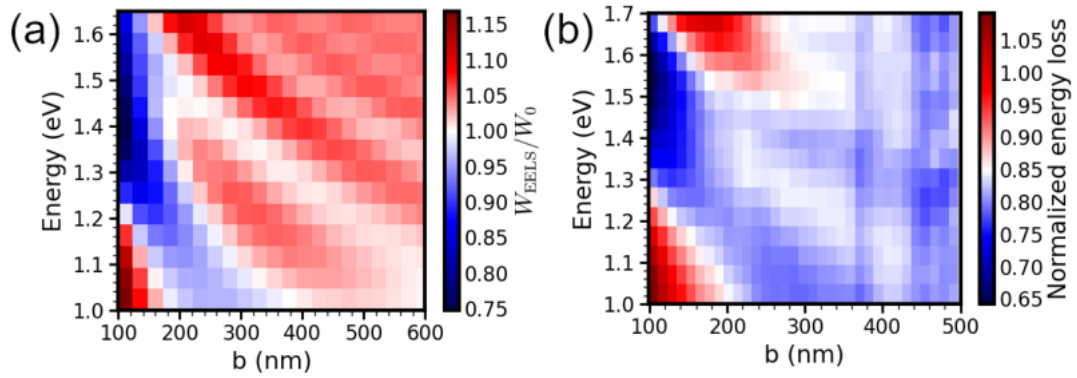
Figure S8: Surface plasmon reflection: EELS signal outside the silicon nanoparticle. (a) Simulated and (b) experimental normalized EELS signal as a function of energy and electron beam position b. The silicon nanoparticle has a radius of $r = 75$ nm and is located at the origin. In both simulations and measurements, the EELS signal outside the silicon nanoparticle is normalized to the signal from the gold-silicon nitride stack (i.e., without the particle). The regions of intense EELS signal correspond to maxima in the interference pattern due to the SPP reflection by the nanoparticle. The intense EELS signal seen at low energies and small impact parameters (lower left corners) is due to the hybrid mode. A weak drop in the intensity of the interference pattern is observed at approximately 1.4 eV (1.45 eV) in the simulations (measurements), which could potentially be due to outcoupling of the SPP to free space radiation.

Paper B

Fiedler, S., Stamatopoulou, P. E., **Assadillayev, A.**, Wolff, C., Sugimoto, H., Fujii, M., Mortensen, N. A., Raza, S., Tserkezis, C.

Disentangling cathodoluminescence spectra in nanophotonics: particle eigenmodes vs transition radiation

Author Contributions

A.A. engaged in the discussion on the conceptual framework, performed a part of the CL measurements, performed a part of SEM image and CL data analyses, fabricated the samples, prepared a CL figure, discussed the results with all co-authors.

Disentangling cathodoluminescence spectra in nanophotonics: particle eigenmodes *vs* transition radiation

Saskia Fiedler,[†] P. Elli Stamatopoulou,[†] Artyom Assadillayev,[‡,†] Christian Wolff,[†] Hiroshi Sugimoto,[¶] Minoru Fujii,[¶] N. Asger Mortensen,[†,§] Søren Raza,[*,‡] and Christos Tserkezis[*,†]

[†]*Center for Nano Optics, University of Southern Denmark, Campusvej 55, DK-5230 Odense M, Denmark*
[‡]*Department of Physics, Technical University of Denmark, Fysikvej, DK-2800 Kongens Lyngby, Denmark*
[¶]*Department of Electrical and Electronic Engineering, Kobe University, Rokkodai, Nada, Kobe 657-8501, Japan*
[§]*Danish Institute for Advanced Study, University of Southern Denmark, Campusvej 55, DK-5230 Odense M, Denmark*

E-mail: sraz@dtu.dk; ct@mci.sdu.dk

Abstract

Cathodoluminescence spectroscopy performed in an electron microscope has proven a versatile tool for analysing the near- and far-field optical response of plasmonic and dielectric nanostructures. Nevertheless, the transition radiation produced by electron impact is often disregarded in the interpretation of the spectra recorded from resonant nanoparticles. Here we show, experimentally and theoretically, that transition radiation can by itself generate distinct resonances which, depending on the time of flight of the electron beam inside the particle, can result from constructive or destructive interference in time. Superimposed on the eigenmodes of the investigated structures, these resonances can distort the recorded spectrum and lead to potentially erroneous assignment of modal characters to the spectral features. We develop an intuitive analogy that helps distinguish between the two contributions. As an example, we focus on the case of silicon nanospheres, and show that our analysis facilitates the unambiguous interpretation of experimental measurements on Mie-resonant nanoparticles.

Keywords

Cathodoluminescence, electron-beam spectroscopy, dielectric nanoparticles, Mie resonances, mode characterisation, transition radiation

Electron-based microscopy techniques that harness signals generated from the excitation of a material by a fast electron beam have proven essential for exploring the optical properties of matter,[1,2] offering one of the most efficient platforms for achieving subwavelength-resolution imaging.[3] They combine the possibility of spatial resolution optimisation[4] with efficient specimen excitation,[5] and have met with growing popularity in quantum- and nano-optics, e.g. to study quantum dots or quan-

102

tum confinement in semiconductors[6,7] and to image plasmons.[8] Depending on signal nature and detection process, electron microscopy and spectroscopy come in different flavours, such as electron energy-loss spectroscopy (EELS) and scanning electron microscopy (SEM).[2] Among these, cathodoluminescence (CL) spectroscopy, which collects the light emitted by the interaction of the electron beam with the sample, allows direct imaging of optical modes in plasmonic[9,10] or dielectric[11] nanoparticles (NPs), while enabling detection of optically dark excitations,[5] visualisation of the local density of optical states,[12,13] or even tomographic reconstruction of the optical near fields.[14] These successful endeavours have led to increasingly extended use of CL spectroscopy as a principal method for analysing photonic nanostructures, including the characterisation of plasmonic[15] or Mie-resonant dielectric NPs.[16]

Despite this success, particular care must be taken when interpreting CL measurements, since the recorded signal can originate from both excitation of eigenmodes and from transition radiation.[17–19] Here, we demonstrate how, in the case of electron beams traversing NPs, the presence of resonances resulting from interfering transition radiation emanating from the two NP sides with a time delay has the potential to hinder the unambiguous interpretation of measured spectra in terms of NP eigenmodes. The two competing mechanisms are, in principle, present in any CL experiment, and can lead to large discrepancies between anticipated and observed frequencies of NP resonances. We show that this behaviour is particularly relevant when the electron beam penetrates the NP at its centre and/or with low velocity, so that its time of flight in the NP is maximal, and provide an intuitive theoretical description based on the time delay between the consecutive excitation of radiating dipoles at the entering and exiting surfaces of the NP. While recent works have indeed proved CL a powerful tool in the study, design and monitoring of both dielectric- and plasmonic-based nanostructures,[20–25] most experiments and analyses have focused on non-penetrating electron beams accelerated at as high a voltage as possible (so as to excite NP

resonances more efficiently while limiting the electron beam spreading), and the emergence of additional interference mechanisms for penetrating beams —and the possible complications that accompany it— has remained unexplored.

In what follows, we choose to analyse the emission properties of Si NPs, because of their high refractive index and low Ohmic losses,[26] the multitude of co-existing modes in the visible[27,28] —with the field largely confined inside the NP, thus calling for traversing electron beams— and the relatively large sizes required for the full glory of all Mie resonances to unveil itself;[29] the combination of these features can significantly pronounce the interference effects under study. The spectra of Mie-resonant NPs are characterised by multipoles of both electric and magnetic character,[30] Fano resonances,[31] anapoles,[32] and bound states in the continuum,[33] and have enabled functionalities as diverse as directional light scattering[34,35] and emission,[36] directional couplers,[37,38] and Huygens-based metasurfaces.[39,40] All-dielectric nanodevices are thus proposed as promising alternatives to plasmonics, with possible applications in biosensing,[41,42] nanoantennas,[43,44] slow light,[45] thermo-optic tuning,[46] ultraviolet interband plasmonics,[47] fluorescence control,[48–50] and Mie-exciton strong-coupling phenomena.[51–54]

CL measurements are performed with the set-up shown schematically in the left-hand sketch of Figure 1a (see Methods for details). Si nanospheres of radius R (prepared in an agglomeration-free colloidal solution;[55] typical SEM image is shown in the middle panel of the figure), placed on a thin Si_3N_4 membrane, are exposed to swift electrons travelling at velocity v (with a corresponding relativistic factor $\beta = v/c$, where c is the speed of light in vacuum), for different impact parameters b (see right-hand schematic of Figure 1a), corresponding to either non-penetrating or penetrating electron beams. The colour map of Figure 1b shows experimental CL spectra for a relatively small NP ($R = 62$ nm) —for which modal characters should be straightforward to assign— as a function of impact parameter. With vertical dashed lines we show the energies where different mul-

2
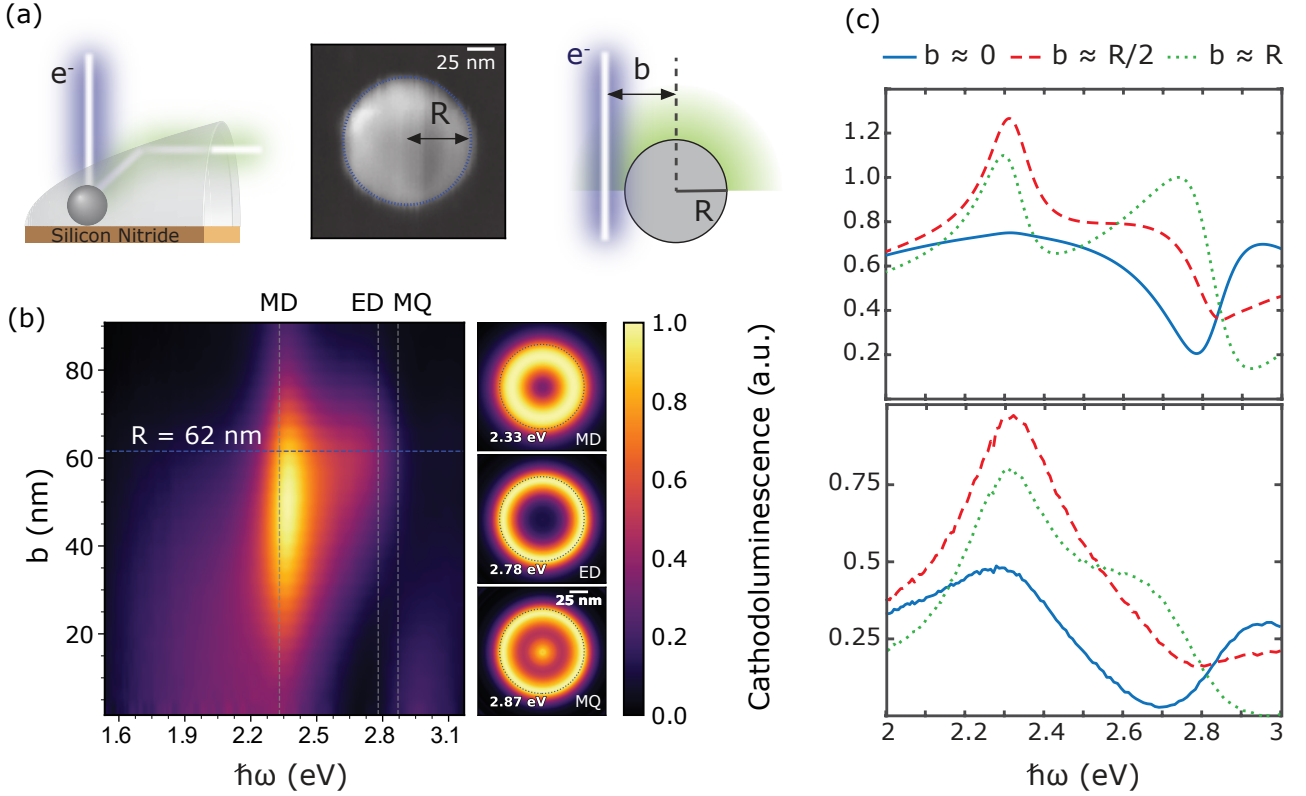
Figure 1: (a) Left: Schematic of the experimental set-up—a Si nanosphere of radius R, placed on a thin Si_3N_4 membrane, is excited by an electron beam. Scattered light is collimated and collected by a parabolic mirror. Middle: SEM image of a typical Si NP with $R = 62$ nm used in the experiments. Right: Sketch of the theoretical description—the electron beam comes at an impact parameter b, and scattered light is collected at the upper half-space (green-shaded area). (b) Experimental CL (colour map) as a function of photon energy $\hbar\omega$ and impact parameter. Vertical dashed lines denote the energies of the resonances predicted by analytic extinction calculations for the NP of (a). CL maps at the MD, ED, and MQ energies are shown on the right-hand side. In all measurements the acceleration voltage is 30 kV. (c) Theoretical (upper panel) and experimental (lower panel) CL spectra for the NP of (a) and three different impact parameter $b \simeq R$ (green dotted lines), $b \simeq R/2$ (red dashed lines), and $R \simeq 0$ (blue solid lines).

tipoles are predicted by Mie theory[49] for this NP size (for extinction spectra and their multipolar decomposition, see Supporting Information). Two resonances manifest clearly in the spectra for large impact parameters: a sharp magnetic dipole (MD) at about $\hbar\omega = 2.35$ eV, and a broader and less intense electric dipole (ED) around 2.75 eV. A magnetic quadrupole (MQ) is identified in the extinction spectra as a weak contribution to the total extinction at about 2.85 eV, but it is hardly discernible in CL due to losses and its short lifetime. These features are in good agreement with corresponding dark-field spectra from literature,[30] but this

agreement becomes worse for small impact parameters, close to the NP centre. Differences between theoretical extinction and experimental CL spectra might initially be attributed to NP shape imperfections and the presence of the thin yet non-negligible substrate,[56,57] but this turns out to be only a minor source of deviations, as we discuss below. To better illustrate the nature of the various resonances, in Figure 1b we also show experimental CL maps at the three energies analysed above.

To further analyse the CL spectra, and in order to identify where theoretical extinction calculations fail to interpret the measurements,

we compare in Figure 1c experimental spectra (lower panel) with a semi-analytic Mie-theory based CL calculation[16] (see Methods), for three characteristic impact parameters: a grazing electron beam ($b \simeq R$, green dotted lines), a penetrating beam passing halfway between the edge and centre of the NP ($b \simeq R/2$, red dashed lines), and one passing exactly through the centre (note that the theoretical calculations are performed for a small $b \simeq 5$ nm for convergence reasons; in any case, this is within the experimental electron-beam diameter). Different impact parameters are expected to excite different modes with different weights, while transition radiation also becomes relevant when penetrating beams are considered. Indeed, as the electron beam approaches the centre, the MD is less efficiently excited for symmetry reasons; in theory, for $b = 0$ the MD contribution should be exactly zero, but in practice the electron beam does not follow strictly a straight line (see Supporting Information for Monte Carlo maps of the electron trajectories). At the same time, the ED seems to shift in energy as b changes, while even stronger shifts are exhibited by the dip at about $2.7 - 2.9$ eV, identified as an anapole.[11] These shifts are not justified by the poles of the corresponding Mie coefficients (where eigenmodes are located), and their origin is the main focus of the remainder of this paper.

The spectra of Figure 1c already suggest that a multipolar decomposition in terms of Mie coefficients might not be straightforward. To better analyse the situation we shift in Figure 2 our attention to a larger NP with $R = 105$ nm, where higher-order multipoles are expected to contribute significantly (see corresponding extinction in the Supporting Information). The MD and ED modes have now moved to lower energies due to retardation, and additional higher-order multipoles are clearly visible in the CL spectra at higher energies (above ~ 2.5 eV), both in experimental (Figure 2a) and in theoretical (Figure 2b) spectra, while the agreement between measurements and calculations becomes more questionable, especially regarding the relative peak intensities. It is noteworthy that both the resonance peaks and the dips change intensities and positions as the impact parameter varies.
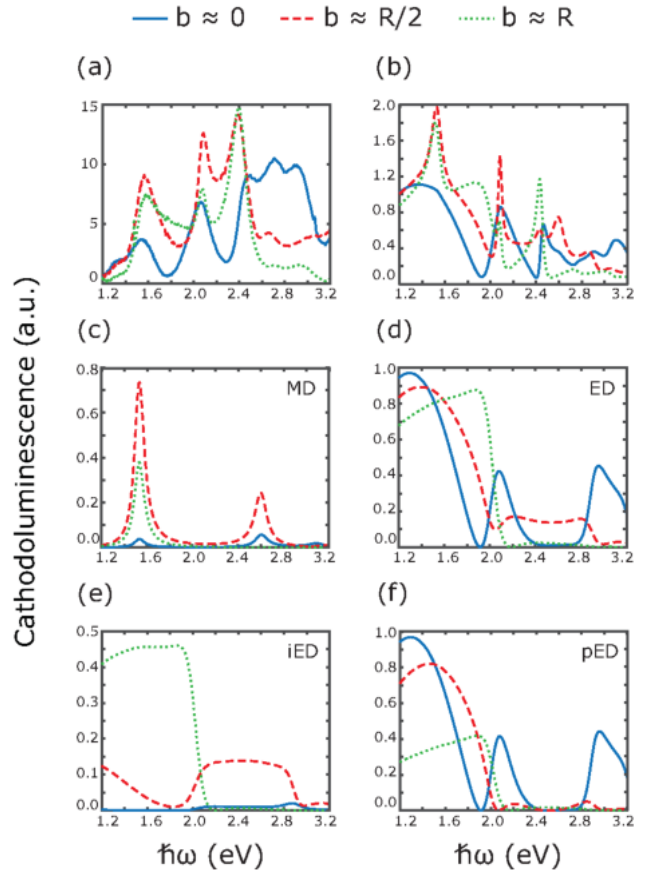
Figure 2: (a) Experimental and (b) theoretical CL spectra for a Si NP with $R = 105$ nm, for three different impact parameter $b \simeq R$ (green dotted lines), $b \simeq R/2$ (red dashed lines), and $R \simeq 0$ (blue solid lines). Theoretical (c) MD and (d) ED contribution to the CL spectra of (b), for the same impact parameters. The ED is further analysed into iED and pED in (e) and (f), respectively.

pact parameter varies. To assign a multipolar character to such rich spectra, the most natural approach is to use Mie theory to decompose them into independent contributions. Indeed, in Figure 2c the MD resonance at about 1.5 eV becomes weaker as the electron-beam trajectory approaches the NP centre, while remaining practically fixed at energy, as expected. At the same time, one can observe at higher energies, around 2.6 eV, the emergence of the first radial MD.[11] On the other hand, the ED contribution shown in Figure 2d is not straightforward to interpret: it appears as if the main ED keeps redshifting away from the actual pole of the scat-

4
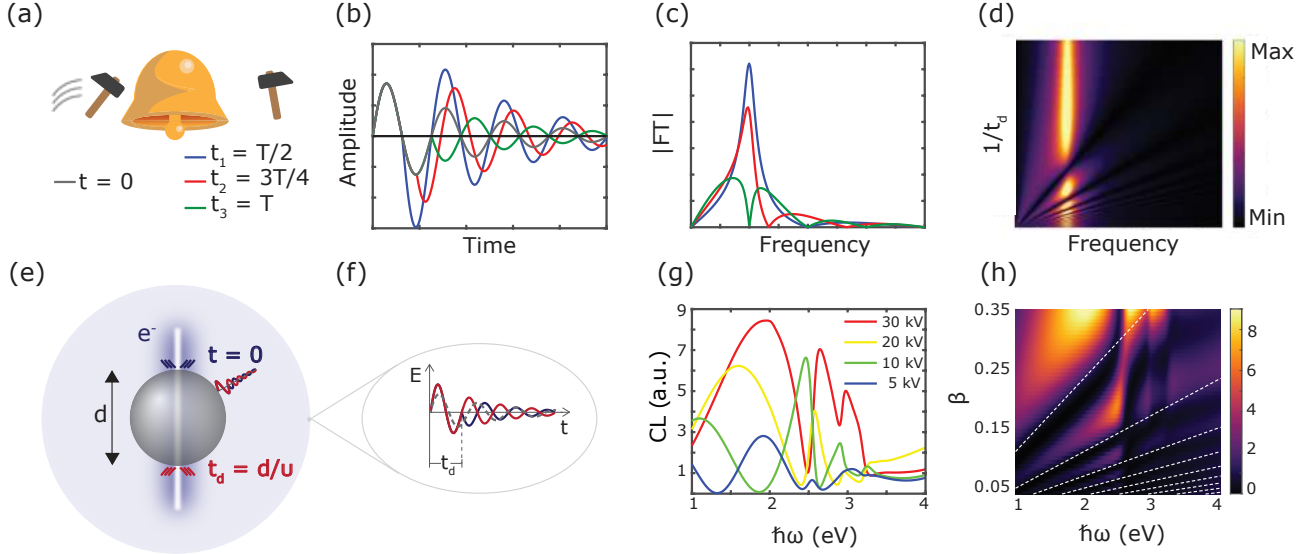
Figure 3: (a) A bell hit by two hammers from two opposite sides, with different time delays t_i comparable to the period T of the generated acoustic waves. (b) Time evolution of the amplitude of the individual acoustic waves produced by the two hammers in the far field. (c) FT of the total (sum of those at $t = 0$ and t_d) acoustic wave perceived by an observer. In both (b) and (c) coloured lines follow the notation of (a). (d) Colour map of the FT amplitude as a function of frequency and the inverse of the time delay t_d. Destructive interference conditions follow a linear dependence between frequency and inverse time delay. (e) Emergence of the two collapsing dipoles at the upper and lower surfaces of an NP crossed by an electron beam through its centre. (f) Time-domain sketch of the electric far-field amplitude due to the two excitation events (red and blue lines) and an NP Mie resonance (grey dashed line). (g) Calculated CL spectra for a Si sphere with $2R = d = 150$ nm at the different acceleration voltages given in the inset, at $b = 5$ nm. (h) Colour map of the calculated CL spectra, as a function of electron velocity in the NP. Thin white lines serve as guides to the eye for tracing the interference minima.

tering coefficient (see Methods) as the electron beam approaches the centre, while additional resonances that cannot be attributed to radial EDs appear in the energy window $2 - 3.5$ eV. This peculiar response is better illustrated in Figures 2e-f, where the ED spectrum is further decomposed into in-plane (iED, plane normal to the electron beam and parallel to the substrate in the experiment) and perpendicular (pED, normal to the substrate) EDs —since the electric field of the electron beam has non-negligible components in all directions, it can excite both kinds of dipolar modes. The most striking feature is the strong shift, accompanied by an increase in intensity, and the oscillatory response of the resonances in the case of the pED shown in Figure 2f. There is practically no mechanism that could shift an ED to such an

extent (the pole of the corresponding scattering matrix is at about 1.9 eV). Nevertheless, these oscillations are reminiscent of the transition radiation manifestation discussed by Pogorzelski and Yeh,[17] which (for $b = 0$) is characterised by a $\sin(x)/x$ (where $x = \omega R/v$, with ω being the angular frequency) behaviour for the low (far below the Cherenkov limit) electron velocities and the dipolar modes of interest here. As we will discuss next, this response emerges from the interference of the transition radiation emitted at the two points where the electron beam crosses the NP surface with the time delay required for the electron to traverse the NP from top to bottom, becoming stronger as the electron beam approaches the NP centre and the electron time of flight increases.

To obtain an intuitive understanding of the

effects discussed above, let us first focus on the classical analogue analysed in Figures 3a-d. Figure 3a shows a bell which, at time $t = 0$, is hit by a hammer on its left side, generating an acoustic wave in the far field, with period T. A second hammer hits the bell on the opposite side, with some time delay t_d. The amplitudes of the first and second acoustic waves are shown as a function of time in Figure 3b, where we plot three different time delays for the second signal, corresponding to $T/2$ (blue line), $3T/4$ (red line), and T (green line) —naturally, all waves decay in time. In Figure 3c we plot the Fourier transform (FT) of the total wave that reaches an observer (in this case listener), for the three different superpositions of initial plus delayed wave. The frequency-domain signal displays an oscillatory behaviour, with zero amplitude emerging whenever the conditions for destructive interference are met. The amplitude colour map of Figure 3d shows, for each time delay, where destructive interference dips at different frequencies are expected, superimposed over the natural Lorentzian frequency of the oscillator; a linear dependence between the inverse of the time delay and the frequency is predicted.

The same concept can equally well apply to the case of NPs excited by a penetrating electron beam. Thinking of the beam as one electron approaching the NP at a time, an image charge appears inside the NP. As the electron approaches the surface, so does the image charge[18,58,59] until, at contact, the two charges collapse, leading to the formation of an electric dipole and resulting transition radiation (Figure 3e). This collapse also occurs at the bottom side of the particle, with a time delay $t_d = d/v$ (where d is the electron path length in the NP). The two dipoles can interfere constructively or destructively, depending on the time delay of their emergence which, in turn, depends on the factors that determine the time of flight: v and d. The corresponding temporal oscillations (red and blue lines), together with an NP Mie resonance (dashed grey line) are sketched in Figure 3f. Exact calculations of CL spectra for different acceleration voltages (corresponding to different electron velocities) are shown in Fig-
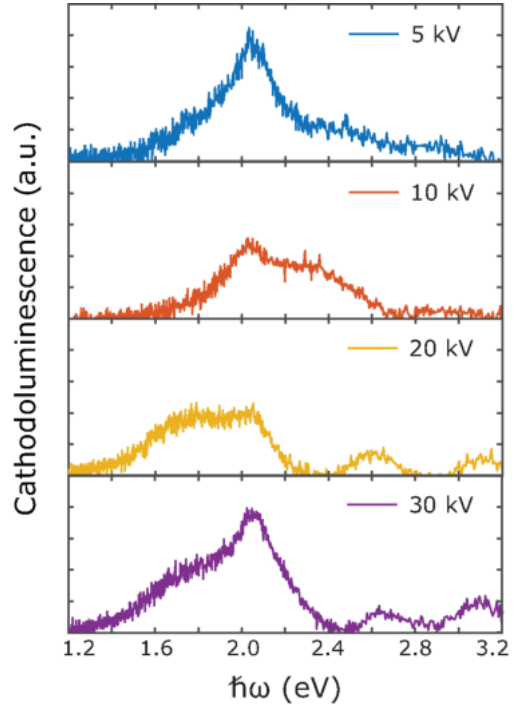
Figure 4: Experimental CL spectra for an electron beam passing through the centre of a Si nanosphere with $R = 75$ nm, for acceleration voltages ranging from 5 kV (upper panel) to 30 kV (lower panel).

ure 3g, in the range $5 - 30$ kV, which is experimentally feasible. For low voltages (see, e.g., the blue line for 5 kV) the only recorded signal originates from transition radiation. As the electron beam is further accelerated, the modes of the NP are more efficiently excited, leading to CL signals that emerge as a superposition of NP resonances and transition radiation. This complex interaction is displayed more clearly in the CL colour map of Figure 3h where, in addition to the linear response of the interference dips, one can see for higher electron velocities slight anticrossings when the NP Mie resonances are met. This behaviour strongly suggests that CL minima are extremely sensitive to transition radiation, and care must be taken so as not to assign to such dips an anapole character before further verification. Furthermore, the uneven spectral excitation implies that, even at high acceleration voltages, observed peaks may be noticeably shifted away from the natural Mie resonances, which must be kept in mind when interpreting CL measurements.

To verify our explanation, and indeed prove that transition radiation can be observed in experiments with small NPs (as in the case of thin films[60,61]) and affect the final spectra, we record in Figure 4 the CL spectra of a Si sphere with $R = 75$ nm at different acceleration voltages, for an electron beam passing through the NP centre ($b = 0$). While the spectra are affected by the fact that the electron trajectories are in practice not straight (see Supporting Information), thus leading to non-negligible contribution from MD terms, traces of the oscillations related to transition radiation can indeed be identified (see, e.g., the spectra for 20 kV, with four resonances at 1.8, 2, 2.6 and 3.1 eV, whereas extinction calculations only predict an MD at about 2 eV and an ED at 2.5 eV). The most remarkable feature is the behaviour of the energy dip at 2.5 eV for high acceleration voltage ($20 - 30$ kV); as the voltage decreases, this dip transforms into a peak at the same energy, with no correspondence to any NP eigenmode. Similarly, the shoulder around 1.75 eV observed at 5 kV, which disappears for 10 kV (and higher voltages not shown), only to reappear above 20 kV, also does not correspond to any pole of the scattering matrix of the NP. The above discussion finally sheds more light on the spectra of Figure 1c; for external beams, two Mie resonances are observed at 2.3 eV and 2.75 eV, while no traces of transition radiation are present. On the contrary, for penetrating beams, and particularly when the beam crosses the centre and some of the Mie modes are inactive for symmetry reasons, it is transition radiation that dominates the spectra.

Conclusions

In summary, we identified transition radiation in CL measurements as a possible source of interference with NP resonances, leading to ambiguous, possibly erroneous, assignment of modal characters to spectral features. When penetrating electron beams are used, two radiating dipoles are formed when the electron and its image charge collapse at the two opposite NP surfaces, with a time delay that is

related to the velocity of the electron and the length of its path inside the NP. These two parameters define whether the interference of the two dipoles will be constructive, leading to pronounced resonances that can mask those due to the NP, or destructive, leading to dips reminiscent of anapoles, but not necessarily of that nature. Care must thus be taken in the interpretation of CL measurements, especially when characterisation of NP properties is at question.

Methods

Cathodoluminescence spectroscopy CL spectroscopy is performed in a Tescan Mira3 scanning electron microscope operated at an acceleration voltage ranging from 5 kV to 30 kV, current of $400-470$ pA, and corresponding spot sizes between 4 nm and 15 nm. Light emitted from the sample is collected by a parabolic mirror and analysed using a Delmic SPARC CL detector equipped with an Andor Newton CCD camera. All CL spectra are corrected for the system response and the background of the thin SiN membrane. All CL maps are collected with activated sub-pixel scanning.

Analytic CL calculation The analytic theory for the interaction of spherical NPs with fast electron beams has been developed by García de Abajo.[1,16,20] The photon emission probability in the interaction of a Si sphere, described here by the experimental values of Green,[62] with an electron beam passing at impact parameter b with constant velocity v is described by the expression[16]

$$\Gamma_{\mathrm{CL}} = \frac{c\varepsilon_0}{\pi k^2 \hbar \omega} \sum_L \left| \psi_L^{\mathrm{ind}} \right|^2, \qquad (1)$$

where $k = \omega/c$ is the free-space wavenumber and ε_0 the vacuum permittivity. The summation over $L = \{P, l, m\}$ includes electric ($P = E$) and magnetic ($P = M$) multipoles, characterised by the angular momentum numbers l, m. Analytic expressions for the ψ_L^{ind} coefficients are provided in the Supporting Information.

Supporting Information Available

Details about the analytic CL calculation; Mie-theory extinction spectra; Monte Carlo simulations of electron trajectories, Sample degradation test.

References

(1) García de Abajo, F. J. Optical excitations in electron microscopy. *Rev. Mod. Phys.* **2010**, *82*, 209–275.

(2) Polman, A.; Kociak, M.; García de Abajo, F. J. Electron-beam spectroscopy for nanophotonics. *Nat. Mater.* **2019**, *18*, 1158–1171.

(3) Lazar, S.; Botton, G. A.; Zandbergen, H. W. Enhancement of resolution in core-loss and low-loss spectroscopy in a monochromated microscope. *Ultramicroscopy* **2006**, *106*, 1091–1103.

(4) García de Abajo, F. J.; Di Giulio, V. Optical excitations with electron beams: challenges and opportunities. *ACS Photonics* **2021**, *8*, 945–974.

(5) Koh, A. L.; Bao, K.; Khan, I.; Smith, W. E.; Kothleitner, G.; Nordlander, P.; Maier, S. A.; McComb, D. W. Electron energy-loss spectroscopy (EELS) of surface plasmons in single silver nanoparticles and dimers: influence of beam damage and mapping of dark modes. *ACS Nano* **2009**, *3*, 3015–3022.

(6) Rodt, S.; Schliwa, A.; Pötschke, K.; Guffarth, F.; Bimberg, D. Correlation of structural and few-particle properties of self-organized InAs/GaAS quantum dots. *Phys. Rev. B* **2005**, *71*, 155325.

(7) Yamamoto, N.; Bhunia, S.; Watanabe, Y. Polarized cathodoluminescence study of InP nanowires by transmission electron microscopy. *Appl. Phys. Lett.* **2006**, *88*, 153106.

(8) Vesseur, E. J. R.; de Waele, R.; Kuttge, M.; Polman, A. Direct observation of plasmonic modes in Au nanowires using high-resolution cathodoluminescence spectroscopy. *Nano Lett.* **2007**, *7*, 2843–2846.

(9) Chaturvedi, P.; Hsu, K. H.; Kumar, A.; Fung, K. H.; Mabon, J. C.; Fang, N. X. Imaging of plasmonic modes of silver nanoparticles using high-resolution cathodoluminescence spectroscopy. *ACS Nano* **2009**, *3*, 2965–2974.

(10) Sannomiya, T.; Konečná, A.; Matsukata, T.; Thollar, Z.; Okamoto, T.; García de Abajo, F. J.; Yamamoto, N. Cathodoluminescence phase extraction of the coupling between nanoparticles and surface plasmon polaritons. *Nano Lett.* **2020**, *20*, 592–598.

(11) Matsukata, T.; Matthaiakakis, N.; Yano, T.; Hada, M.; Tanaka, T.; Yamamoto, N.; Sannomiya, T. Selection and visualization of degenerate magnetic and electric multipoles up to radial higher orders by cathodoluminescence. *ACS Photonics* **2019**, *6*, 2320–2326.

(12) García de Abajo, F. J.; Kociak, M. Probing the photonic local density of states with electron energy loss spectroscopy. *Phys. Rev. Lett.* **2008**, *100*, 106804.

(13) Zu, S.; Han, T.; Jiang, M.; Liu, Z.; Jiang, Q.; Lin, F.; Zhu, X.; Fang, Z. Imaging of plasmonic chiral radiative local density of states with cathodoluminescence nanoscopy. *Nano Lett.* **2019**, *19*, 775–780.

(14) Atre, A. C.; Brenny, B. J. M.; Coenen, T.; García-Etxarri, A.; Polman, A.; Dionne, J. A. Nanoscale optical tomography with cathodoluminescence spectroscopy. *Nat. Nanotechnol.* **2015**, *10*, 429–436.

(15) Matsukata, T.; Wadell, C.; Matthaiakakis, N.; Yamamoto, N.; Sannomiya, T. Selected mode mixing and interference visualized within a single optical nanoantenna. *ACS Photonics* **2018**, *5*, 4986–4992.

(16) Matsukata, T.; García de Abajo, F. J.; Sannomiya, T. Chiral light emission from a sphere revealed by nanoscale relative-phase mapping. *ACS Nano* **2021**, *15*, 2219–2228.

(17) Pogorzelski, R.; Yeh, C. Diffraction radiation from a charged particle moving through a penetrable sphere. *Phys. Rev. A* **1973**, *8*, 137–144.

(18) Kuttge, M.; Vesseur, E. J. R.; Koenderink, A. F.; Lezec, H. J.; Atwater, H. A.; García de Abajo, F. J.; Polman, A. Local density of states, spectrum, and far-field interference of surface plasmon polaritons probed by cathodoluminescence. *Phys. Rev. B* **2009**, *79*, 113405.

(19) Schmidt, F.-P.; Losquin, A.; Horák, M.; Hohenester, U.; Stöger-Pollach, M.; Krenn, J. R. Fundamental limit of plasmonic cathodoluminescence. *Nano Lett.* **2021**, *21*, 590–596.

(20) García de Abajo, F. J. Relativistic energy loss and induced photon emission in the interaction of a dielectric sphere with an external electron beam. *Phys. Rev. B* **1999**, *59*, 3095–3107.

(21) Abuhassan, L. H.; Khanlary, M. R.; Townsend, P.; Nayfeh, M. H. Cathodoluminescence of small silicon nanoparticles under electron-beam excitation. *J. Appl. Phys.* **2005**, *97*, 104314.

(22) van de Groep, J.; Coenen, T.; Mann, S. A.; Polman, A. Direct imaging of hybridized eigenmodes in coupled silicon nanoparticles. *Optica* **2016**, *3*, 93–99.

(23) McPolin, C. P. T.; Marino, G.; Krasavin, A. V.; Gili, V.; Carletti, L.; De Angelis, C.; Leo, G.; Zayats, A. V. Imaging electric and magnetic modes and their hybridization in single and dimer AlGaAs nanoantennas. *Adv. Opt. Mater.* **2018**, *6*, 1800664.

(24) Peng, S.; Schilder, N. J.; Ni, X.; Van De Groep, J.; Brongersma, M. L.; Alù, A.; Khanikaev, A. B.; Atwater, H. A.; Polman, A. Probing the band structure of topological silicon photonic lattices in the visible spectrum. *Phys. Rev. Lett.* **2019**, *122*, 117401.

(25) Zouros, G. P.; Kolezas, G. D.; Mortensen, N. A.; Tserkezis, C. Monitoring strong coupling in nonlocal plasmonics with electron spectroscopies. *Phys. Rev. B* **2020**, *101*, 085416.

(26) García-Etxarri, A.; Gómez-Medina, R.; Froufe-Pérez, L. S.; López, C.; Chantada, L.; Scheffold, F.; Aizpurua, J.; Nieto-Vesperinas, N.; Sáenz, J. J. Strong magnetic response of submicron silicon particles in the infrared. *Opt. Express* **2011**, *19*, 4815–4826.

(27) Staude, I.; Miroshnichenko, A. E.; Decker, M.; Fofang, N. T.; Liu, S.; Gonzales, E.; Dominguez, J.; Luk, T. S.; Neshev, D. N.; Brener, I.; Kivshar, Y. Tailoring directional scattering through magnetic and electric resonances in subwavelength silicon nanodisks. *ACS Nano* **2013**, *7*, 7824–7832.

9

(28) Zenin, V. A.; Garcia-Ortiz, C. E.; Evlyukhin, A. B.; Yang, Y.; Malureanu, R.; Novikov, S. M.; Coello, V.; Chichkov, B. N.; Bozhevolnyi, S. I.; Lavrinenko, A. V.; Mortensen, N. A. Engineering nanoparticles with pure high-order multipole scattering. *ACS Photonics* **2020**, *7*, 1067–1075.

(29) Kruk, S.; Kivshar, Y. Functional meta-optics and nanophotonics govern by Mie resonances. *ACS Photonics* **2017**, *4*, 2638–2649.

(30) Evlyukhin, A. B.; Novikov, S. M.; Zywietz, U.; Eriksen, R. L.; Reinhardt, C.; Bozhevolnyi, S. I.; Chichkov, B. N. Demonstration of magnetic dipole resonances of dielectric nanospheres in the visible region. *Nano Lett.* **2012**, *12*, 3749–3755.

(31) Limonov, M. F.; Rybin, M. V.; Poddubny, A. N.; Kivshar, Y. S. Fano resonances in photonics. *Nat. Photon.* **2017**, *11*, 543–554.

(32) Gurvitz, E. A.; Ladutenko, K. S.; Dergachev, P. A.; Evlyukhin, A. B.; Miroshnichenko, A. E.; Shalin, A. S. The high-order toroidal moments and anapole states in all-dielectric photonics. *Laser Photon. Rev.* **2019**, *13*, 1800266.

(33) Azzam, S. I.; Kildishev, A. V. Photonic bound states in the continuum: from basics to applications. *Adv. Opt. Mater.* **2021**, *9*, 2001469.

(34) Fu, Y. H.; Kuznetsov, A. I.; Miroshnichenko, A. E.; Yu, Y. F.; Luk'yanchuk, B. Directional visible light scattering by silicon nanoparticles. *Nat. Commun.* **2013**, *4*, 1527.

(35) Person, S.; Jain, M.; Lapin, Z.; Sáenz, J. J.; Wicks, G.; Novotny, L. Demonstration of zero optical backscattering from single nanoparticles. *Nano Lett.* **2013**, *13*, 1806–1809.

(36) Cihan, A. F.; Curto, A. G.; Raza, S.; Kik, P. G.; Brongersma, M. L. Silicon Mie resonators for highly directional light emission from monolayer MoS$_2$. *Nat. Photon.* **2018**, *12*, 284–290.

(37) Assadillayev, A.; Hinamoto, T.; Fujii, M.; Sugimoto, H.; Brongersma, M. L.; Raza, S. Plasmon launching and scattering by silicon nanoparticles. *ACS Photonics* **2021**, *8*, 1582–1591.

(38) Gulkin, D. N.; Popkova, A. A.; Afinogenov, B. I.; A., S. D.; Kuršelis, K.; Chichkov, B. N.; Bessonov, V. O.; Fedyanin, A. A. Mie-driven directional nanocoupler for Bloch surface wave photonic platform. *Nanophotonics* **2021**, *10*, 2939–2947.

(39) Jahani, S.; Jacob, Z. All-dielectric metamaterials. *Nat. Nanotechnol.* **2016**, *11*, 23–36.

(40) Staude, I.; Schilling, J. Metamaterial-inspired silicon nanophotonics. *Nat. Photon.* **2017**, *11*, 274–284.

(41) García-Etxarri, A.; Dionne, J. A. Surface-enhanced circular dichroism spectroscopy mediated by nonchiral nanoantennas. *Phys. Rev. B* **2013**, *87*, 235409.

(42) Yavas, O.; Svedendahl, M.; Dobosz, P.; Sanz, V.; Quidant, R. On-a-chip biosensing based on all-dielectric n1anoresonators. *Nano Lett.* **2017**, *17*, 4421–4426.

(43) Krasnok, A. E.; Miroshnichenko, A. E.; Belov, P. A.; Kivshar, Y. S. All-dielectric optical nanoantennas. *Opt. Express* **2012**, *20*, 20599–20604.

(44) Li, S. V.; Baranov, D. G.; Krasnok, A. E.; Belov, P. A. All-dielectric nanoantennas for unidirectional excitation of electromagnetic guided modes. *Appl. Phys. Lett.* **2015**, *107*, 171101.

(45) Raza, S. Slow light using magnetic and electric Mie resonances. *Opt. Lett.* **2020**, *45*, 1260–1263.

(46) Assadillayev, A.; Hinamoto, T.; Fujii, M.; Sugimoto, H.; Raza, S. Thermal near-field tuning of silicon Mie nanoparticles. *Nanophotonics* **2021**, *10*, 4161–4169.

(47) Dong, Z.; Wang, T.; Chi, X.; Ho, J.; Tserkezis, C.; Yap, S. L. K.; Rusydi, A.; Tjiptoharsono, F.; Thian, D.; Mortensen, N. A.; Yang, J. K. W. Ultraviolet interband plasmonics with Si nanostructures. *Nano Lett.* **2019**, *19*, 8040–8048.

(48) Schmidt, M. K.; Esteban, R.; Sáenz, J. J.; Suárez-Lacalle, I.; Mackowski, S.; Aizpurua, J. Dielectric antennas – a suitable platform for controlling magnetic dipolar emission. *Opt. Express* **2012**, *20*, 13636–13650.

(49) Stamatopoulou, P. E.; Tserkezis, C. Role of emitter position and orientation on silicon nanoparticle-enhanced fluorescence. *OSA Continuum* **2021**, *4*, 918–932.

(50) Sugimoto, H.; Fujii, M. Magnetic Purcell enhancement by magnetic quadrupole resonance of dielectric nanosphere antenna. *ACS Photonics* **2021**, *8*, 1794–1800.

(51) Tserkezis, C.; Gonçalves, P. A. D.; Wolff, C.; Todisco, F.; Busch, K.; Mortensen, N. A. Mie excitons: understanding strong coupling in dielectric nanoparticles. *Phys. Rev. B* **2018**, *98*, 155439.

(52) Todisco, F.; Malureanu, R.; Wolff, C.; Gonçalves, P. A. D.; Roberts, A. S.; Mortensen, N. A.; Tserkezis, C. Magnetic and electric Mie-exciton polaritons in silicon nanodisks. *Nanophotonics* **2020**, *9*, 803–814.

(53) Castellanos, G. W.; Murai, S.; Raziman, T. V.; Wang, S.; Ramezani, M.; Curto, A. G.; Gómez Rivas, J. Exciton-polaritons with magnetic and electric character in all-dielectric metasurfaces. *ACS Photonics* **2020**, *7*, 1226–1234.

(54) Stamatopoulou, P. E.; Yannopapas, V.; Mortensen, N. A.; Tserkezis, C. Manipulating the photonic Hall effect with hybrid Mie-exciton resonances. *Phys. Rev. B* **2020**, *102*, 195415.

(55) Sugimoto, H.; Fujii, M. Colloidal dispersion of subquarter micrometer silicon spheres for low-loss antenna in visible regime. *Adv. Opt. Mater.* **2017**, *5*, 1700332.

(56) van de Groep, J.; Polman, A. Designing dielectric resonators on substrates: combining magnetic and electric resonances. *Opt. Express* **2013**, *21*, 26285–26302.

(57) Fiedler, S.; Raza, S.; Ai, R.; Wang, J.; Busch, K.; Stenger, N.; Mortensen, N. A.; Wolff, C. Importance of substrates for the visibility of "dark" plasmonic modes. *Opt. Express* **2020**, *28*, 13938–13948.

(58) Ginzburg, V. L.; Frank, I. M. Radiation of a uniformly moving electron due to its transition from one medium to another. *J. Phys. USSR* **1945**, *9*, 353–362.

(59) Goldsmith, P.; Jelley, J. V. Optical transition radiation from protons entering metal surfaces. *Philos. Mag.* **1959**, *4*, 836–844.

(60) Yamamoto, N.; Toda, A.; Axaya, K. Imaging of transition radiation from thin films on a silicon substrate Using a light detection system combined with TEM. *J. Electron. Microsc.* **1996**, *45*, 64–72.

(61) Yamamoto, N.; Sugiyama, H.; Toda, A. Cherenkov and transition radiation from thin plate crystals detected in the transmission electron microscope. *Proc. R. Soc. Lond. A* **1996**, *452*, 2279–2301.

(62) Green, M. A. Self-consistent optical parameters of intrinsic silicon at 300 K including temperature coefficients. *Sol. Energy Mater. Sol. Cells* **2008**, *92*, 1305–1310.

Graphical TOC Entry

Paper C

Svendsen, M. K., Sugimoto, H., **Assadillayev, A.**, Shima, D., Fujii, M., Thygesen, K. S., Raza, S.

Ultraviolet Mie resonances in computationally discovered boron phosphide nanoparticles

Author Contributions

M.K.S. constructed the computational workflow, performed the screening, developed the f-sum approach, and prepared the figures. H.S. performed the structural and optical characterizations of nanoparticles. A.A. performed the EELS measurements, EELS analysis, EELS simulations, and prepared a figure. D.S. fabricated the nanoparticles and conducted laser shaping processes. M.F. contributed to analyses and interpretation of the data and supervised the fabrication and characterizations of nanoparticles. S.R. and K.S.T. conceived the idea and supervised the work. S.R. performed the optical simulations. All authors discussed the results and contributed to the preparation of the manuscript.

Ultraviolet Mie resonances in computationally discovered boron phosphide nanoparticles

Mark Kamper Svendsen,[†] Hiroshi Sugimoto,[‡] Artyom Assadillayev,[†] Daisuke Shima,[‡] Minoru Fujii,[‡] Kristian S. Thygesen,[*,†] and Søren Raza[*,†]

[†]*Department of Physics, Technical University of Denmark, Fysikvej, DK-2800 Kongens Lyngby, Denmark*
[‡]*Department of Electrical and Electronic Engineering, Kobe University, Rokkodai, Nada, Kobe 657-8501, Japan*

E-mail: thygesen@fysik.dtu.dk; sraz@dtu.dk

Abstract

Controlling ultraviolet light at the nanoscale using optical Mie resonances holds great promise for a diverse set of applications, such as lithography, sterilization, and biospectroscopy. However, Mie resonances hosted by dielectric nanoantennas are difficult to realize at ultraviolet wavelengths due to the lack of both suitable materials and fabrication methods. Here, we systematically search for improved materials by computing the frequency dependent optical permittivity of 338 binary semiconductors and insulators from first principles, and evaluate their potential performance as high refractive index materials using Mie theory. Our analysis reveals several interesting candidate materials among which boron phosphide (BP) appears particularly promising. We then prepare BP nanoparticles and demonstrate that they support Mie resonances at visible and ultraviolet wavelengths using both far-field optical measurements and near-field electron energy-loss spectroscopy. We also present a laser reshaping method to realize spherical Mie-resonant BP nanoparticles. With a refractive index above 3 and low absorption losses, BP nanostructures advance Mie optics to the ultraviolet.

Introduction

Achieving control over ultraviolet light with nanoscale materials is essential for improving surface-enhanced spectroscopies of biological molecules and enabling new ultraviolet optical components. Geometric Mie resonances supported by resonant nanoantennas made from materials that combine a high refractive index with low absorption losses offer efficient and tunable manipulation of the near- and far-field of optical waves.[1,2] Mie resonances have been realized at visible and infrared wavelengths thanks to the mature lithographic processing of suitable materials,[3] such as silicon,[4] gallium phosphide,[5] and titanium dioxide.[6] It would be desirable to extend the operation of these materials to the ultraviolet, but their small direct band gap energies ($\lesssim 3$ eV) lead to significant absorption losses in the ultraviolet. Recently, metasurfaces composed of an array of nanostructured materials with a wide band gap and moderate refractive index ($n \approx 2.1 - 2.3$) have demonstrated wave front manipulation in the ultraviolet using waveguide modes.[7–9] For ultraviolet Mie optics, diamond has been theoretically suggested as a potential material,[10,11] but diamond comes with significant nanofabrication challenges.[12] Consequently, extending the rich optical properties of Mie resonances observed in the visible to the ultraviolet requires identi-

fication of new high-index materials as well as development of suitable fabrication methods to realize Mie-resonant nanoantennas.

Concurrent advances in first-principles methodology and computing power have recently made it possible to design and discover new materials via high-throughput computations.[13–17] The approach has been successfully applied in several domains, including photovoltaics, transparent conductors, and photocatalysis.[18–20] However, to the best of our knowledge, computational discovery of new high-index materials remains largely unexplored. Relevant previous work in this direction has been limited to the static response regime[21,22] reflecting the fact that the major materials databases so far has focused on ground state properties.

Here we use high-throughput linear response density functional theory (DFT) to screen an initial set of 2743 elementary and binary materials with the aim to identify isotropic high-index, low loss, and broad band optical materials. For the most promising materials, the computed frequency-dependent complex refractive indices are used as input for Mie scattering calculations to evaluate their optical performance. In addition to the already known high-index materials we identify several new compounds. In particular, boron phosphide (BP) offers a refractive index above 3 with very low absorption losses in a spectral range spanning from the infrared to the ultraviolet. We then prepare BP nanoparticles and show, by means of dark-field optical measurements and electron energy-loss spectroscopy, that they support size-dependent Mie resonances in the visible and ultraviolet. Finally, we demonstrate a laser reshaping method to realize spherical BP nanoparticles, which host multiple Mie resonances in quantitative agreement with full-field optical simulations.

Results

High-throughput screening

Our high-throughput screening procedure is illustrated in Fig. 1a. We build the workflow using the Python-based Atomic Simulation Recipes (ASR)[23] framework and the MyQueue scheduling software[24] (see detailed workflow in Supplementary Note 1 and Supplementary Fig. 1). Starting from 2743 thermodynamically stable elementary and binary materials from the Open Quantum Materials Database (OQMD)[15] we extract the 1693 materials with up to 10 atoms in the unit cell and relax the atomic structure using DFT with the Perdew-Burke-Ernzerhof (PBE) exchange correlation functional[25] and the D3 correction to account for the van der Waals forces.[26] We perform DFT ground state calculations for all of the materials to determine their electronic band gaps. After discarding the metals, we are left with 338 semiconductors for which we calculate the optical dielectric function, $\epsilon(\omega)$, within the random phase approximation (RPA) and extract the refractive index and extinction coefficient as $n(\omega) = \mathrm{Re}\left\{\sqrt{\varepsilon(\omega)}\right\}$ and $k(\omega) = \mathrm{Im}\left\{\sqrt{\varepsilon(\omega)}\right\}$, respectively. All calculations are performed with the GPAW code.[27,28]

Next, we classify the materials according to the anisotropy of their refractive index tensor using a cut-off of 0.05 for the fractional anisotropy (see Supplementary Fig. 2). This leaves us with 207 isotropic material candidates, for which we show the static refractive index as a function of the direct band gap in Fig. 1b. The data points qualitatively follow the Moss formula[29] (dashed line in Fig. 1b); however, there are significant deviations from the general trend, which we ascribe to variations in oscillator strength and density of the transitions across the direct gap. It is well known that (semi)local functionals like the PBE employed in the present work systematically underestimates band gaps.[30] This effect is, however, to some extent compensated by the fact that the RPA neglects the attractive electron-hole interactions and consequently underesti-
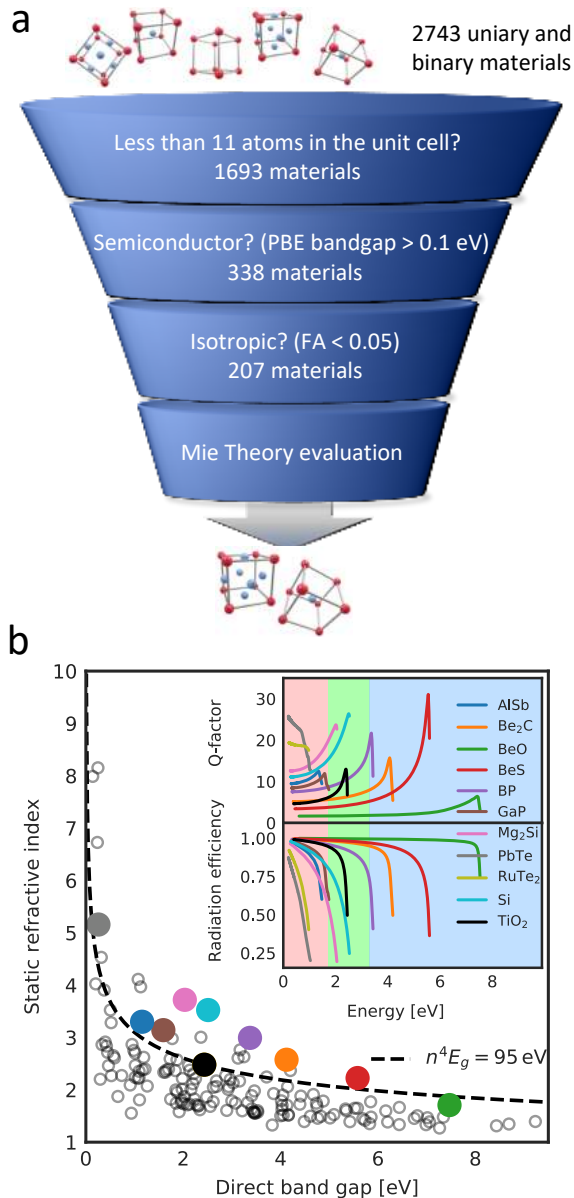
Fig. 1. High-throughput materials screening. a, Schematic of the screening steps and the number of materials that survive each of them. **b,** The static refractive index of the isotropic materials plotted as a function of their direct band gap energies along with the Moss formula. The colored dots highlight interesting materials and the inset shows the energy-dependent Q-factor and radiation efficiency, η, of the MD resonances in those materials. The background colors represent the infrared (red), visible (green) and ultraviolet (blue) spectral regions.

mates the spectral weight near the band edge. As a result, refractive indices obtained with RPA@PBE are typically in good agreement with experiments in the static limit[28] while deviations occur at higher frequencies near the band edge region (see Supplementary Note 2 and Supplementary Fig. 3-5). We shall return to this point later, but for now mention that for the materials that are identified as interesting based on this screening we will employ more accurate and computational expensive many-body perturbation methods.

We now turn to a more in-depth evaluation of the performance of the discovered materials. Specifically, we use Mie theory to calculate the scattering properties of a spherical nanoparticle made from the subset of isotropic materials. We focus on the lowest-order magnetic dipole (MD) resonance of the spheres and calculate energy-dependent quality factors, Q, and radiation efficiencies, η (see Supplementary Note 1).[3] This is achieved by continuously adjusting the size of the sphere to tune the energy of the MD resonance across the infrared, visible and ultraviolet regions. A high Q-factor is beneficial for boosting the local field enhancement of the nanoparticle, while a radiation efficiency close to unity points to low absorption losses. This analysis identifies all of the commonly used materials, such as Si, TiO_2, and GaP. However, we also find a number of other highly promising materials, some of which are highlighted in the inset of Fig. 1b. In particular, we identify BP, which has a refractive index exceeding that of TiO_2 and a radiation efficiency higher than both silicon and TiO_2 across the entire visible part of the spectrum. For these reasons, we believe BP stands out as an overlooked material with highly desirable optical properties and we will focus on BP in the rest of the paper.

Optical response of BP

BP crystals were successfully synthesized as early as 1957,[31] yet experimental measurements of its refractive index are limited to a couple of data points in the visible.[32,33] Refractive index measurements of BP thin films have also been conducted but with varying results.[34,35]
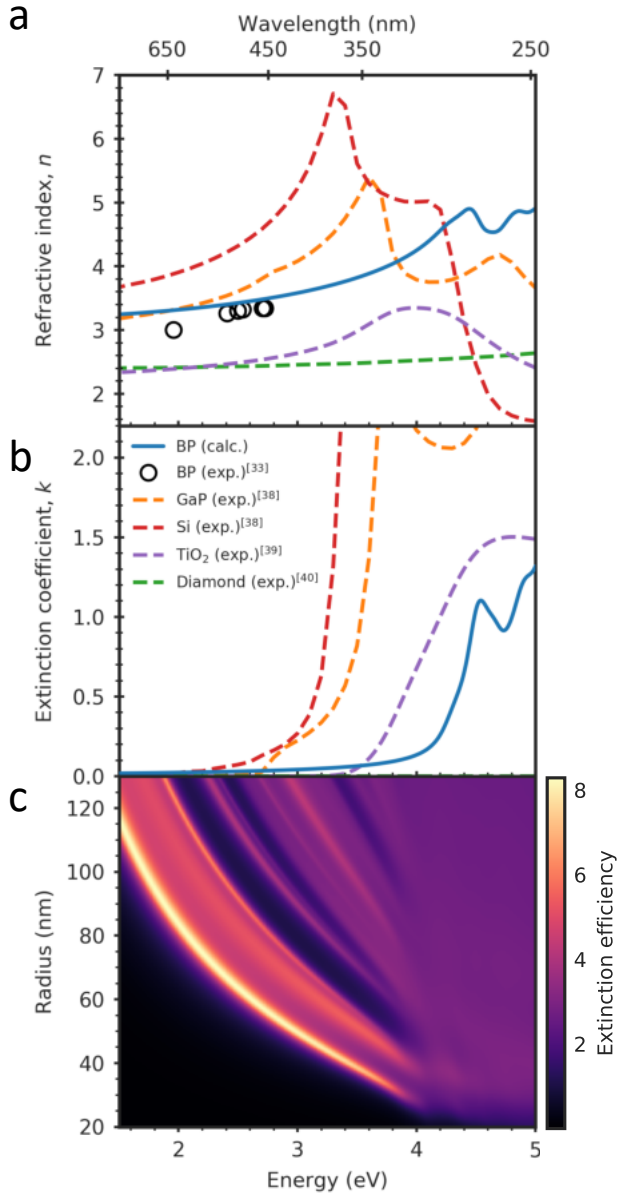
Fig. 2. Optical response and Mie resonances of BP. a,b Refractive index n and extinction coefficient k of BP calculated using the f-sum corrected BSE method compared with that of some of the commonly used dielectrics in the visible and ultraviolet spectral regions. **c,** Extinction efficiency map of BP spheres of varying radii calculated using Mie theory, which demonstrates that Mie resonances can be sustained in the visible and ultraviolet.

The RPA@PBE permittivities used for the initial screening are qualitatively accurate but suffer from underestimated band gaps and missing excitonic effects. To determine the refractive index of BP with quantitative accuracy, we solve the Bethe-Salpeter equation (BSE) to obtain the permittivity using single-particle transition energies obtained from a G_0W_0 band structure calculation. The band structure calculation reveals an indirect band gap of 2.1 eV and a direct band gap of 4.41 eV, which matches experimental measurements of the band gap energies for BP.[36,37] The square root dependence of the refractive index on the permittivity makes it crucial to converge both the real and imaginary parts of the latter. Unfortunately, the real part converges slowly with the number of bands making it impractical to obtain well converged results directly from the BSE. The problem can be alleviated by extending the imaginary part of the permittivity by an exponentially decaying tail whose weight is fixed by the f-sum rule (see Methods), and subsequently obtain the real part via the Kramers–Kronig relation. We benchmark this approach against experimental data for the refractive index of crystalline silicon and find excellent agreement (see Supplementary Note 3 and Supplementary Fig. 6).

With the f-sum rule fulfilling BSE-G_0W_0 method at hand, we are in a position to make a quantitative comparison of the refractive index of BP with some of the commonly used materials[38,39] in the visible as well as diamond,[40] which has been theoretically suggested for operation in the ultraviolet (Fig. 2a,b). We observe that the absorption edge of BP lies significantly higher than silicon, GaP, and TiO$_2$, while it retains a refractive index comparable to that of GaP. This suggests that BP provides low-loss operation across the entire visible spectrum. While this is also the case for TiO$_2$, its refractive index is significantly lower than that of BP. The higher refractive index of BP means that nanostructures can be made more compact[41] and packed more densely for enhanced metasurface performance.[42] Importantly, we note that BP offers a high refractive index with a low extinction coefficient not only in the visible but

4

also in the ultraviolet – a spectral region which is unreachable with the commonly-used materials. Diamond is transparent in the ultraviolet as well, but has a significantly lower refractive index. We illustrate the broadband performance of BP by performing extinction efficiency calculations using Mie theory for a BP sphere with varying radii, confirming that Mie resonances can be sustained across the visible and ultraviolet (Fig. 2c).

Far- and near-field characterization of BP nanoparticles

We now turn to an experimental demonstration of the potential of BP as a Mie-resonant nanostructure. BP has been synthesized in various forms such as crystals,[43,44] films,[35,45,46] and nanoparticles.[47–49] However, BP nanoparticles in the size range suitable for sustaining Mie resonances have not been reported. We prepare BP nanoparticles in the size range of a few hundred nanometers by grounding BP powder (Kojundo Chemicals) in a mortar and then dispersing it in methanol. The BP solution is subsequently dropcasted on a glass substrate.

We measure the far-field scattering efficiency of individual nanoparticles by illuminating the nanoparticles through a high-numerical-aperture dark-field objective and collecting the transmitted scattered light (see Fig. 3a). A similar measurement setup has been used to detect Mie resonances in silicon nanoparticles.[50] The scattering spectra recorded from a series of BP nanoparticles clearly show resonant peaks, which red shift with increasing particle size (Fig. 3b). Despite the irregular particle shapes, the scattering resonances are quite prominent and follow the trend observed in other Mie-resonant nanostructures, namely, that the smallest particle size support only the lowest-order Mie resonance while larger particle sizes also support higher-order Mie resonances.[51] We additionally confirm the crystallinity of the nanoparticles using micro-Raman spectroscopy from individual nanoparticles (see Supplementary Fig. 7). The particle radii are extracted from the scanning electron microscopy images under the assumption of a spherical shape and used as input for full-field simulations of the scattering efficiency of a BP nanosphere. The simulations account for the measurement setup as well as the glass substrate (see Methods). We find that the simulations accurately reproduce both the shift in resonance wavelengths with particle size as well as the number of resonant peaks (Fig. 3c). However, the particle sizes need to be adjusted to match the resonance wavelengths observed in the experiments. This suggests that the particle shape is better characterized as flakes with a thickness significantly smaller than the in-plane size. Nonetheless, the distinctive, multiple scattering peaks provide strong evidence for the interpretation that these are related to geometric Mie resonances.

To gain more insight into the nature of these resonances and to access the ultraviolet spectral region, we also perform near-field characterization on similar BP nanoparticles using electron energy-loss spectroscopy (EELS). EELS is performed in a transmission electron microscope and has been employed to access near-field properties of both metallic[52,53] and dielectric nanostructures[54–56] as well as optical devices.[57] The combined high spatial and spectral resolution of EELS provides unique nanoscale information on optical modes over a broad spectral range. For EELS measurements, the BP nanoparticles are deposited on a thin silicon oxide membrane. The EELS signal recorded from a triangular-shaped BP nanoparticle (Fig. 4a) at different beam positions is presented in Fig. 4c. The position of the beam is directly related to the excitation efficiency of the optical modes,[58] and thus, by judicious positioning of the beam we can selectively excite different Mie modes.[54] When the beam is positioned in the center of nanoparticle, we observe a distinct resonance in the ultraviolet at 3.99 eV. As the beam is moved closer to the surface of the nanoparticle, two additional resonances are observed at the energies 3.57 eV and 2.77 eV. To identify the nature of these resonances, we simulate the EELS signal of a BP nanodisk with the same effective radius as the measured BP nanoparticle (Fig. 4b). The thickness of the nanodisk is var-
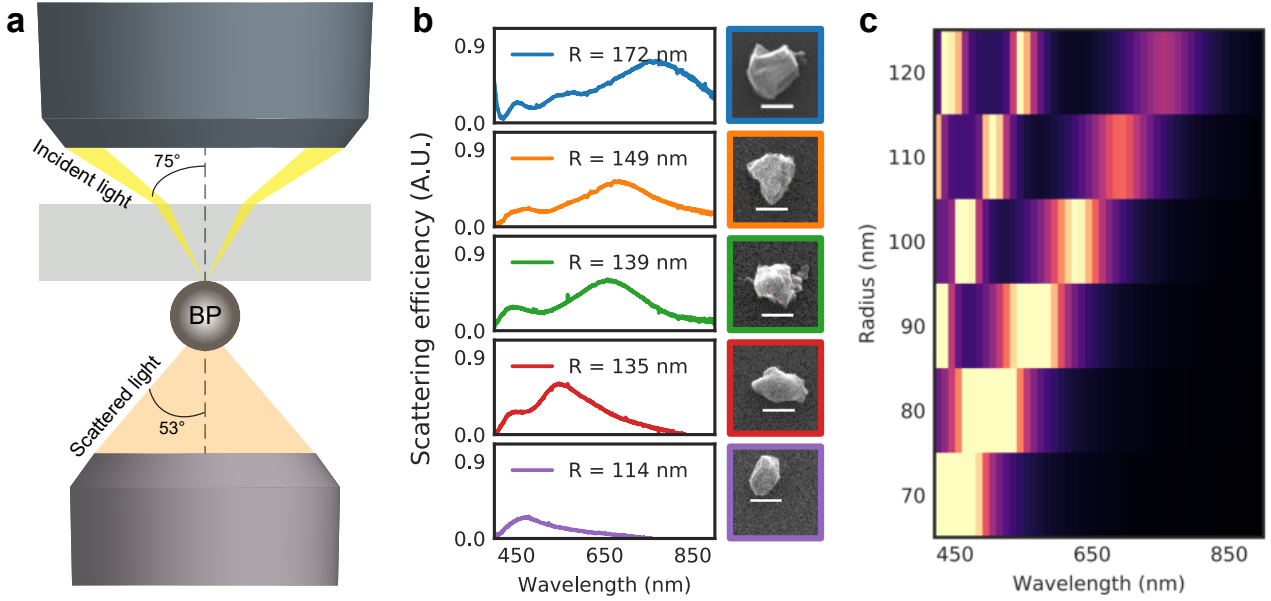
Fig. 3. Dark-field scattering of BP nanoparticles. a, Schematic of the dark-field scattering spectroscopy. The nanoparticles are excited by unpolarized, white light incident at an oblique angle and the transmitted scattered light is collected. **b,** Scattering efficiency spectra recorded from individual BP nanoparticles of different sizes showing clear scattering peaks due to resonant interaction. The effective radius R of the nanoparticle is determined from the area of the particles, assuming a spherical shape. **c,** Simulated scattering efficiency map of BP nanospheres with varying particle radii.

ied to achieve correspondence to the measured EELS resonance energies. The simulated EELS spectra for a nanodisk thickness of $h = 40$ nm at the same beam positions as in the experiments are shown in Fig. 4d. Here, we observe that the three lowest-energy EELS peaks have the same dependence on the impact parameter of the electron beam as seen experimentally. The simulated resonance energies of all three EELS peaks are also in quantitative agreement with the experiments, albeit the lowest-energy EELS peak is slightly shifted to higher energies in the simulations. The measured EELS peaks are broadened by the finite energy resolution of our EELS setup (see Methods). By performing a multipole decomposition of the induced field produced by the electron beam,[59] we identify the two lowest energy EELS peaks to be due to the Mie modes of the in-plane electric dipole $ED_{\parallel}$ and in-plane electric quadrupole $EQ_{\parallel}$. The highest energy EELS peak has contributions from both the in-plane magnetic dipole and and out-of-plane electric dipole $ED_{\perp}$, where the latter dominates in the

center of the particle (see Supplementary Fig. 8 for full decomposition). Simulated EELS intensity maps show that the electron beam couples efficiently to the in-plane modes, $ED_{\parallel}$ and $EQ_{\parallel}$ for beam positions near the surface of the particle, while the out-of-plane $ED_{\perp}$ is excited also for beam positions in the center of the particle (Fig. 4e-g). The experimental EELS intensity maps of these three Mie modes are in good agreement with the simulations (Fig. 4h-j) as well as previous EELS measurements performed on Mie-resonant silicon nanoparticles.[54,55] The near-field EELS measurements along with far-field dark-field optical measurements demonstrate that, despite their irregular shape, BP nanoparticles host a variety of multipolar size-dependent Mie resonances across the visible and ultraviolet, which are key attributes of low-loss high-index nanostructures.

Laser reshaping

To alleviate the irregular shape of the as-prepared BP nanoparticles, we generate spher-

6
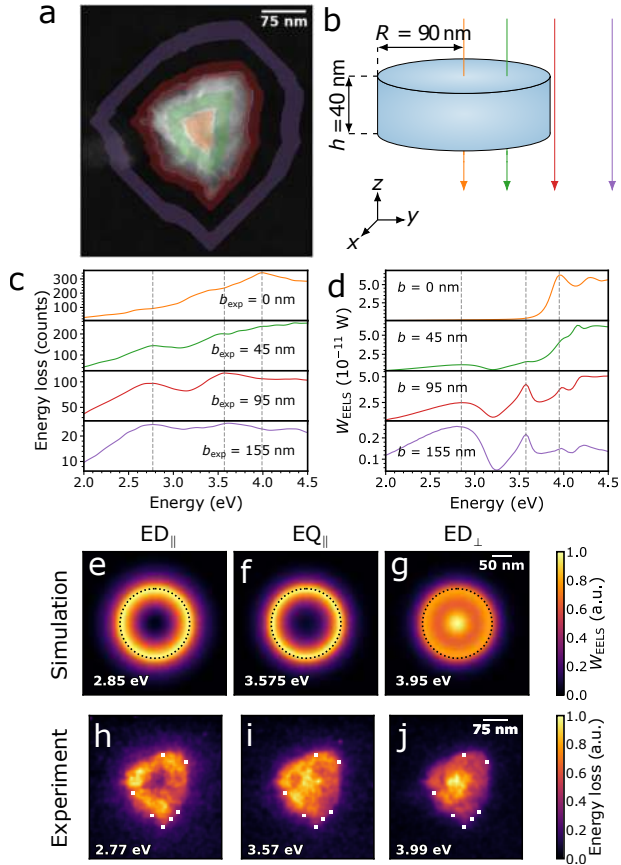
Fig. 4. Electron energy-loss spectroscopy of BP nanoparticles. a,b Experimental STEM image and theoretical set-up depicting the electron beam positions b used to acquire the measured and simulated EELS spectra of **c,d**, respectively. The triangular-shaped BP nanoparticle is characterized by an effective radius of $R = 90$ nm. Several EELS peaks due to Mie resonances are observed. **e-g** Simulated and **h-j** experimental EELS intensity maps at the Mie resonance energies. The Mie modes are identified as the in-plane electric dipole ($ED_\parallel$), in-plane electric quadrupole ($EQ_\parallel$), and out-of-plane electric dipole ($ED_\perp$) using a multipole decomposition.

ical BP nanoparticles by irradiating the unprocessed BP nanoparticles with a pulsed laser (see Fig. 5a and Methods). An example of a laser-processed BP nanoparticle is presented in Fig. 5b, confirming that the laser processing can be used for realizing spherical-shaped BP nanoparticles without affecting the nanoparti-

cle composition. In addition, we perform micro-Raman spectroscopy on the same particle and find that the crystallinity from the unprocessed BP nanoparticles is retained after laser reshaping (see Supplementary Fig. 7). The dark-field scattering spectrum from the BP nanoparticle in Fig. 5b is recorded and we observe multiple scattering peaks (Fig. 5c). The relatively large particle radius ($R = 184$ nm) places the lowest-order Mie resonances at wavelengths longer than our measurement range, while the scattering peaks observed can be attributed to higher-order Mie resonances. The full-field simulation of a BP nanosphere with a slightly smaller radius $R = 165$ nm, where we account for the substrate and the measurement setup, shows very good agreement with the measurement. We attribute the deviation in particle radius to shape imperfections and a slight variation between the calculated and experimental refractive index of BP. Multipole decomposition reveals that the scattering peaks are due to the excitation of the magnetic quadrupole MQ, the electric quadrupole EQ, and radial higher-order magnetic dipole MD^2, thereby confirming the Mie-resonant nature of BP nanoparticles. We also performed EELS measurements on a smaller laser-reshaped BP nanoparticle, where we observe Mie resonances in the ultraviolet (see Supplementary Fig. 9).

Discussion

Using a DFT-based high-throughput screening method combined with optical Mie theory of 338 dielectrics, we identify BP as a promising high-refractive-index material for ultraviolet nanooptics. We develop a new, quantitatively accurate many-body perturbation theory based methodology for calculating refractive indices and use it to reveal that BP has a high refractive index ($n > 3$) and low extinction coefficient ($k < 0.1$) up to ultraviolet photon energies of 4 eV. We present an approach to fabricate BP nanoparticles as well as a laser reshaping method to generate spherical BP nanoparticles. Through dark-field optical spectroscopy and EELS measurements, we confirm the pres-
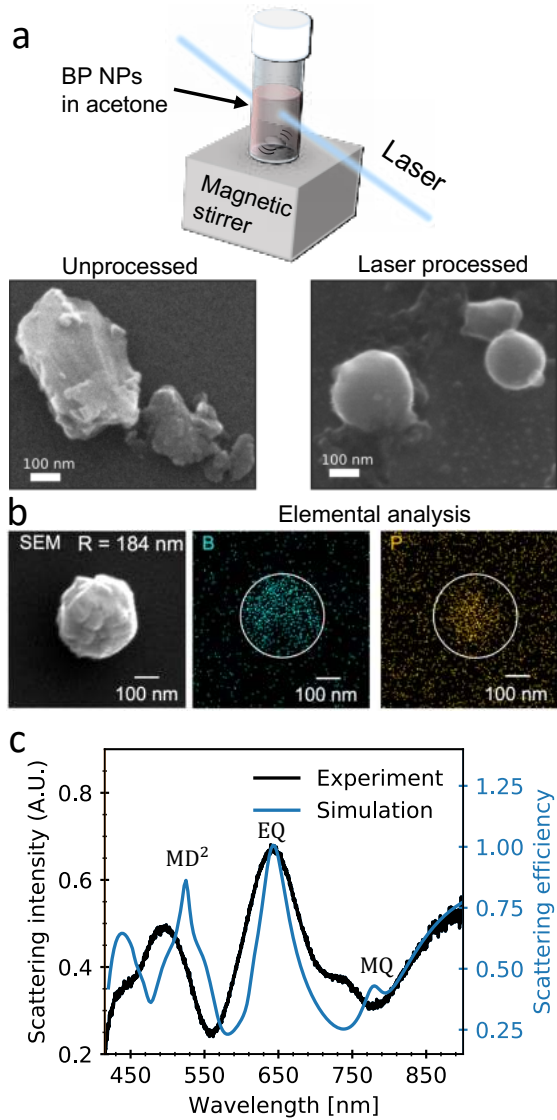
Fig. 5. Laser reshaping of BP nanoparticles. a, Reshaping of the BP nanoparticles is achieved by pulsed laser irradiation of unprocessed BP nanoparticles in acetone. After the irradiation, the BP nanoparticles obtain a spherical shape. **b,** Scanning electron microscopy image and energy-dispersive x-ray analysis of reshaped BP nanoparticle, showing a spherical shape without change in composition. **c,** Scattering spectrum recorded from the BP nanoparticle in **b** and simulated spectrum for a BP nanosphere with radius $R = 165$ nm with multipole decomposition revealing the excitation of the magnetic quadrupole (MQ), electric quadrupole (EQ), and radial higher-order magnetic dipole (MD^2).

ence of Mie resonances in BP nanoparticles across the visible and ultraviolet. Our work advances nanoscale Mie optics to the ultraviolet and may find applications in metasurface-enhanced spectroscopy of biological molecules and, more generally, in realizing metasurface optical components operating in the ultraviolet.

Methods

Computational workflow

Structural relaxation: All ground- and excited state calculations were performed with the GPAW electronic structure code.[27] We relaxed the atomic structure and the unit cell of the materials until the maximum force (stress) is below 10^{-4} eV/Å (0.002eV/Å^3). We use the PBE functional for exchange and correlation effects, a Γ-point centered k-point grid with a density of 6.0Å^{-3}, a 800 eV plane wave cutoff and a Fermi-Dirac smearing of 50 meV. Van der Waals interactions were taken into account by the D3 correction scheme.[26]

RPA calculations: We calculate the optical permittivity, $\varepsilon(\omega)$, within the Random Phase Approximation(RPA) using the dielectric function module in GPAW. From $\epsilon(\omega)$ we calculate the refractive index and extinction coefficient as $n(\omega) = \mathrm{Re}\left\{\sqrt{\varepsilon(\omega)}\right\}$ and $k(\omega) = \mathrm{Im}\left\{\sqrt{\varepsilon(\omega)}\right\}$ respectively. To ensure convergence across all materials we employ a k-point grid with a high density of 20.0 Å^{-3} and include conduction bands up to 5 times the number of valence bands. The calculations were performed on a nonlinear frequency grid with an initial frequency spacing of 0.5 meV, a broadening of 50 meV and a local field cutoff of 50 eV.

Many-body perturbation theory calculations

G_0W_0 calculations: The G_0W_0 calculations were performed on top of the ground state calculations. To ensure converged quasi-particle

8

gaps we perform extrapolation of both the plane wave cut-off and the k-point resolution to infinity.

BSE calculations: The BSE calculations were performed within the Tamm-Dancoff approximation on a k-point grid with a density of 20 Å^{-3}. The calculation included all valence and conduction bands within 2.3 eV of the valence band maximum and conduction minimum, respectively. The calculation of the screened interaction included all occupied bands and unoccupied bands up to 5 times the number of occupied bands, and we accounted for local field effects up to a plane wave cut-off of 50 eV. The calculation was performed on a linear 10001 point frequency grid spanning 0 to 8 eV.

BSE f-sum rule correction The optical polarizability has to obey the f-sum rule,

$$\int_0^\infty d\omega\,\omega \mathrm{Im}\chi(\omega) = \frac{\pi}{2}\frac{n_e e^2}{m}\,, \qquad (1)$$

where n_e is the electron density, e is the elementary charge and m is the electron mass. Since it is not obvious what to use for n_e in our PAW calculations, we use a different strategy to fix the left hand side, namely we obtain it from an RPA calculation (which can be readily converged)

$$\int_0^\infty d\omega\,\omega \mathrm{Im}\chi^{(\mathrm{RPA})}(\omega) = \int_0^\infty d\omega\,\omega \mathrm{Im}\chi^{(\mathrm{BSE})}(\omega)\,. \qquad (2)$$

Eq. 2 can be enforced if we artificially extend the imaginary part of the BSE polarizability. Denoting the largest transition energy included in the BSE calculation as w_c, we perform the following extension,

$$\mathrm{Im}\chi^{(\mathrm{BSE})}(\omega) = \begin{cases} \mathrm{Im}\chi^{(\mathrm{BSE})}(\omega), & \text{if } \omega \leq \omega_c, \\ C_0 e^{-\gamma(\omega-\omega_c)}, & \text{if } \omega > \omega_c. \end{cases} \qquad (3)$$

The constant C_0 is used to ensure continuity and the constant γ is fixed to give the correct spectral weight as fixed by Eq. 2. For benchmarks see Supplementary Information.

Optical simulations

The scattering efficiency and EELS simulations are both performed in COMSOL Multiphysics (ver. 5.6), which solves Maxwell's equations using finite-element modelling. For the scattering efficiency simulations in Fig. 3c, a BP sphere is placed on a semi-infinite glass substrate ($n_{\mathrm{sub}} = 1.45$) and excited by a plane wave incident from the substrate side at an oblique angle of $\theta_{\mathrm{inc}} = 42°$. We use the f-sum corrected refractive index for BP shown in Fig. 2. We then perform a near-to-far field transformation to extract the scattered far-field.[60] The Poynting flux of the scattered far-field in the air region is integrated over a solid angle spanning an azimuthal angle of 2π and a maximum polar angle of $\theta_{\mathrm{col}} = \arcsin(\mathrm{NA}) = 53°$ to retrieve the total scattered power collected by the collection objective (NA = 0.8). The total scattered power is normalized to the incident power and the geometrical cross sectional area of the particle to determine the scattering efficiency. To account for the unpolarized incident light in the experiments, we perform this simulation procedure for both transverse-electric and transverse-magnetic polarization of the incident wave. Finally, the scattering efficiency from both polarization states is averaged. The scattering efficiency simulation in Fig. 5c follows the same steps with the only change being that the plane wave is incident from the air side at an oblique angle of $\theta_{\mathrm{inc}} = 75°$.

For the EELS calculations, we simulate the electron beam as an edge current with an amplitude of 1 µA. The induced electromagnetic field is obtained by calculating the fields with and without the BP nanodisk in the simulation domain, and subsequently subtracting them. The energy loss is then calculated as the work rate done on the electron beam by the induced electromagnetic field.[54]

Dark-field scattering measurements

A custom-built inverted optical microscope was used for dark-field scattering spectroscopy of single nanoparticles (Fig. 3a). For the measurements presented in Fig. 3, the sample is illuminated from the top by a halogen lamp through a dark field condenser and the scattered light was collected by an objective (50×, NA = 0.8). For the spectrum in Fig. 5c, the sample was illuminated from the bottom through a dark-field objective (50×, NA = 0.8) and the scattered light was collected by the same objective. To measure the spectra, scattered light was transferred to the entrance slit of a monochromator (SpectraPro-300i, Princeton Instruments) and detected by a liquid-N_2 cooled CCD (Princeton Instruments). For Raman scattering measurements, the nanoparticles were excited by a 488 nm laser (Coherent Sapphire 488–50).

EELS measurements and analysis

The EELS measurements are performed in a monochromated and aberration-corrected FEI Titan operated in STEM mode at an acceleration voltage of 300 kV, providing a probe size of ∼0.5 nm and an energy resolution of 0.08 eV (as measured by the full-width-at-half-maximum of the zero-loss peak). We perform Richardson–Lucy deconvolution to remove the zero-loss peak. An EELS spectrum recorded in vacuum is used as an input for the point-spread function. Due to a small asymmetry in the zero-loss peak, the deconvolution algorithm produced an artificial EELS peak in the energy range below 0.5 eV. However, the artificial peak did not overlap with any of the observed resonances and could be safely removed using a first-order logarithmic polynomial.

The depicted EELS spectra are obtained by integrating the deconvoluted EELS data around the experimental impact parameter b_{exp}. This parameter is directly related to the effective radius of the particle R which is extracted as a radius of the circle with the effective area of the particle found from the STEM image. The effective area of the particle is the area which is enclosed by the boundaries obtained by Otsu's thresholding of the STEM image. The integration parameter itself is calculated as a radius of the circle with the adjusted effective area of expanded/reduced initial boundaries. For the integration region centered at the nanoparticle, the experimental impact parameter changes from 0 to $0.3R$ and denotes the nanoparticle center. For the annulus-shaped regions, the experimental impact parameter denotes the mean of the inner and outer radii with a typical radius spread of 0.3 (for example, the green region in Figure 4(a) encloses the regions from 0.35 to $0.65R$). The depicted EELS spectra are smoothed with a Gaussian function ($\sigma = 0.03$ eV).

The EELS maps are obtained by summing the deconvoluted EELS data in a spectral window of 0.02 eV width centered at the resonance energies. The signal-to-noise ratio is improved by spatially binning the map, reducing the total number of pixels by a factor of 4. A Gaussian filter with $\sigma = 0.8$ pixels is applied to smooth the image.

Laser reshaping

Unprocessed BP nanoparticles in acetone are irradiated with the third harmonic of a Nd:YAG laser (355 nm wavelength, 5 nm pulse width, 20 Hz repetition rate) with a fluence of 50 mJ/cm^2 per pulse for 10 min. **Author contributions** M. K. S. constructed the computational workflow, performed the screening, developed the f-sum approach, and

prepared the figures. H. S. performed the structural and optical characterizations of nanoparticles. A. A. performed the EELS measurements, EELS analysis, EELS simulations, and prepared a figure. D. S. fabricated the nanoparticles and conducted laser shaping processes. M. F. contributed to analyses and interpretation of the data and supervised the fabrication and characterizations of nanoparticles. S. R. and K. S. T. conceived the idea and supervised the work. S. R. performed the optical simulations. All authors discussed the results and contributed to the preparation of the manuscript. **Conflict of interests** The authors declare no competing financial interests. **Data and materials availability** All data needed to evaluate the conclusions in the paper are present in the paper and/or the Supplementary Information. Additional data related to this paper may be requested from the corresponding author.

References

(1) Kuznetsov, A. I.; Miroshnichenko, A. E.; Brongersma, M. L.; Kivshar, Y. S.; Luk'yanchuk, B. Optically resonant dielectric nanostructures. *Science* **2016**, *354*, aag2472.

(2) Kruk, S.; Kivshar, Y. Functional meta-optics and nanophotonics governed by Mie resonances. *ACS Photonics* **2017**, *4*, 2638–2649.

(3) Baranov, D. G.; Zuev, D. A.; Lepeshov, S. I.; Kotov, O. V.; Krasnok, A. E.; Evlyukhin, A. B.; Chichkov, B. N. All-dielectric nanophotonics: the quest for better materials and fabrication techniques. *Optica* **2017**, *4*, 814–825.

(4) Staude, I.; Schilling, J. Metamaterial-inspired silicon nanophotonics. *Nat. Photonics* **2017**, *11*, 274–284.

(5) Wilson, D. J.; Schneider, K.; Hönl, S.; Anderson, M.; Baumgartner, Y.; Czornomaz, L.; Kippenberg, T. J.; Seidler, P. Integrated gallium phosphide nonlinear photonics. *Nat. Photonics* **2020**, *14*, 57–62.

(6) Chen, W. T.; Zhu, A. Y.; Sanjeev, V.; Khorasaninejad, M.; Shi, Z.; Lee, E.; Capasso, F. A broadband achromatic metalens for focusing and imaging in the visible. *Nat. Nanotechnol.* **2018**, *13*, 220–226.

(7) Huang, K.; Deng, J.; Leong, H. S.; Yap, S. L. K.; Yang, R. B.; Teng, J.; Liu, H. Ultraviolet Metasurfaces of ≈80% Efficiency with Antiferromagnetic Resonances for Optical Vectorial Anti-Counterfeiting. *Laser Photon. Rev.* **2019**, *13*, 1800289.

(8) Zhang, C.; Divitt, S.; Fan, Q.; Zhu, W.; Agrawal, A.; Lu, Y.; Xu, T.; Lezec, H. J. Low-loss metasurface optics down to the deep ultraviolet region. *Light Sci. Appl.* **2020**, *9*, 55.

(9) Zhao, D.; Lin, Z.; Zhu, W.; Lezec, H. J.; Xu, T.; Agrawal, A.; Zhang, C.; Huang, K. Recent advances in ultraviolet nanophotonics: from plasmonics and metamaterials to metasurfaces. *Nanophotonics* **2021**, *10*, 2283–2308.

(10) Gutiérrez, Y.; Ortiz, D.; Saiz, J. M.; González, F.; Albella, P.; Moreno, F. The quest for low loss high refractive index dielectric materials for UV photonic applications. *Appl. Sci.* **2018**, *8*, 2065.

(11) Hu, J.; Lawrence, M.; Dionne, J. A. High Quality Factor Dielectric Metasurfaces for Ultraviolet Circular Dichroism Spectroscopy. *ACS Photonics* **2020**, *7*, 36–42.

(12) Aharonovich, I.; Greentree, A. D.; Prawer, S. Diamond photonics. *Nat. Photonics* **2011**, *5*, 397–405.

(13) Curtarolo, S.; Hart, G. L.; Nardelli, M. B.; Mingo, N.; Sanvito, S.; Levy, O. The high-throughput highway to computational materials design. *Nat. Mater.* **2013**, *12*, 191–201.

(14) Jain, A.; Ong, S. P.; Hautier, G.; Chen, W.; Richards, W. D.; Dacek, S.; Cholia, S.; Gunter, D.; Skinner, D.; Ceder, G., et al. Commentary: The Materials Project: A materials genome approach to accelerating materials innovation. *APL Mater.* **2013**, *1*, 011002.

(15) Kirklin, S.; Saal, J. E.; Meredig, B.; Thompson, A.; Doak, J. W.; Aykol, M.; Rühl, S.; Wolverton, C. The Open Quantum Materials Database (OQMD): assessing the accuracy of DFT formation energies. *NPJ Comput. Mater.* **2015**, *1*, 15010.

(16) Haastrup, S.; Strange, M.; Pandey, M.; Deilmann, T.; Schmidt, P. S.; Hinsche, N. F.; Gjerding, M. N.; Torelli, D.; Larsen, P. M.; Riis-Jensen, A. C., et al. The Computational 2D Materials Database: high-throughput modeling and discovery of atomically thin crystals. *2D Mater.* **2018**, *5*, 042002.

(17) Gjerding, M.; Taghizadeh, A.; Rasmussen, A.; Ali, S.; Bertoldo, F.; Deilmann, T.; Holguin, U.; Knøsgaard, N.; Kruse, M.; Manti, S., et al. Recent progress of the Computational 2D Materials Database (C2DB). *2D Materials* **2021**, *8*, 044002.

(18) Varley, J. B.; Miglio, A.; Ha, V.-A.; van Setten, M. J.; Rignanese, G.-M.; Hautier, G. High-throughput design of non-oxide p-type transparent conducting materials: Data mining, search strategy, and identification of boron phosphide. *Chem. Mater.* **2017**, *29*, 2568–2573.

(19) Yu, L.; Zunger, A. Identification of potential photovoltaic absorbers based on first-principles spectroscopic screening of materials. *Phys. Rev. Lett.* **2012**, *108*, 068701.

(20) Castelli, I. E.; Olsen, T.; Datta, S.; Landis, D. D.; Dahl, S.; Thygesen, K. S.; Jacobsen, K. W. Computational screening of perovskite metal oxides for optimal solar light capture. *Energy Environ. Sci.* **2012**, *5*, 5814–5819.

(21) Petousis, I.; Mrdjenovich, D.; Ballouz, E.; Liu, M.; Winston, D.; Chen, W.; Graf, T.; Schladt, T. D.; Persson, K. A.; Prinz, F. B. High-throughput screening of inorganic compounds for the discovery of novel dielectric and optical materials. *Sci. data* **2017**, *4*, 160134.

(22) Naccarato, F.; Ricci, F.; Suntivich, J.; Hautier, G.; Wirtz, L.; Rignanese, G.-M. Searching for materials with high refractive index and wide band gap: A first-principles high-throughput study. *Phys. Rev. Mater.* **2019**, *3*, 044602.

(23) Gjerding, M.; Skovhus, T.; Rasmussen, A.; Bertoldo, F.; Larsen, A. H.; Mortensen, J. J.; Thygesen, K. S. Atomic Simulation Recipes–a Python framework and library for automated workflows. *arXiv* **2021**, 2104.13431.

(24) Mortensen, J. J.; Gjerding, M.; Thygesen, K. S. MyQueue: Task and workflow scheduling system. *J. Open Source Softw.* **2020**, *5*, 1844.

(25) Perdew, J. P.; Burke, K.; Ernzerhof, M. Generalized gradient approximation made simple. *Phys. Rev. Lett.* **1996**, *77*, 3865.

(26) Grimme, S.; Antony, J.; Ehrlich, S.; Krieg, H. A consistent and accurate ab initio parametrization of density functional dispersion correction (DFT-D) for the 94 elements H-Pu. *J. Chem. Phys.* **2010**, *132*, 154104.

(27) Enkovaara, J.; Rostgaard, C.; Mortensen, J. J.; Chen, J.; Dułak, M.; Ferrighi, L.; Gavnholt, J.; Glinsvad, C.; Haikola, V.; Hansen, H., et al. Electronic structure calculations with GPAW: a real-space implementation of the projector augmented-wave method. *J. Phys. Condens. Matter* **2010**, *22*, 253202.

(28) Yan, J.; Mortensen, J. J.; Jacobsen, K. W.; Thygesen, K. S. Linear density response function in the projector augmented wave method: Applications to

solids, surfaces, and interfaces. *Phys. Rev. B* **2011**, *83*, 245122.

(29) Moss, T. Relations between the refractive index and energy gap of semiconductors. *physica status solidi (b)* **1985**, *131*, 415–427.

(30) Perdew, J. P. Density functional theory and the band gap problem. *Int. J. Quantum Chem.* **1985**, *28*, 497–523.

(31) Popper, P.; Ingles, T. A. Boron Phosphide, a III–V Compound of Zinc-Blende Structure. *Nature* **1957**, *179*, 1075.

(32) Takenaka, T.; Takigawa, M.; Shohno, K. Dielectric Constant and Refractive Index of Boron Monophosphide. *Jpn. J. Appl. Phys.* **1976**, *15*, 2021–2022.

(33) Wettling, W.; Windscheif, J. Elastic constants and refractive index of boron phosphide. *Solid State Commun.* **1984**, *50*, 33–34.

(34) Odawara, M.; Udagawa, T.; Shimaoka, G. Organometallic chemical vapor deposition growth of heterostructure of wide band gap and transparent boron phosphide on silicon. *Jpn. J. Appl. Phys.* **2005**, *44*, 681–683.

(35) Dalui, S.; Hussain, S.; Varma, S.; Paramanik, D.; Pal, A. K. Boron phosphide films prepared by co-evaporation technique: Synthesis and characterization. *Thin Solid Films* **2008**, *516*, 4958–4965.

(36) Archer, R. J.; Koyama, R. Y.; Loebner, E. E.; Lucas, R. C. Optical absorption, electroluminescence, and the band gap of BP. *Phys. Rev. Lett.* **1964**, *12*, 538–540.

(37) Schroten, E.; Goossens, A.; Schoonman, J. Photo- and electroreflectance of cubic boron phosphide. *J. Appl. Phys.* **1998**, *83*, 1660–1663.

(38) Aspnes, D. E.; Studna, A. Dielectric functions and optical parameters of si, ge, gap,

gaas, gasb, inp, inas, and insb from 1.5 to 6.0 ev. *Physical review B* **1983**, *27*, 985.

(39) Siefke, T.; Kroker, S.; Pfeiffer, K.; Puffky, O.; Dietrich, K.; Franta, D.; Ohlídal, I.; Szeghalmi, A.; Kley, E.-B.; Tünnermann, A. Materials pushing the application limits of wire grid polarizers further into the deep ultraviolet spectral range. *Advanced Optical Materials* **2016**, *4*, 1780–1786.

(40) Phillip, H.; Taft, E. Kramers-Kronig analysis of reflectance data for diamond. *Physical Review* **1964**, *136*, A1445.

(41) Yang, J.; Fan, J. A. Analysis of material selection on dielectric metasurface performance. *Opt. Express* **2017**, *25*, 23899–23909.

(42) Lalanne, P.; Chavel, P. Metalenses at visible wavelengths: past, present, perspectives. *Laser Photonics Rev.* **2017**, *11*, 1600295.

(43) Kumashiro, Y. Refractory semiconductor of boron phosphide. *J. Mater. Res.* **1990**, *5*, 2933–2947.

(44) Woo, K.; Lee, K.; Kovnir, K. BP: Synthesis and properties of boron phosphide. *Mater. Res. Express* **2016**, *3*, 074003.

(45) Kumashiro, Y.; Nakamura, K.; Enomoto, T.; Tanaka, M. Preparation and thermoelectric properties of BP films on SOI and sapphire substrates. *J. Mater. Sci. Mater. Electron.* **2011**, *22*, 966–973.

(46) Padavala, B.; Frye, C. D.; Wang, X.; Ding, Z.; Chen, R.; Dudley, M.; Raghothamachar, B.; Lu, P.; Flanders, B. N.; Edgar, J. H. Epitaxy of Boron Phosphide on Aluminum Nitride(0001)/Sapphire Substrate. *Cryst. Growth Des.* **2016**, *16*, 981–987.

(47) Sugimoto, H.; Fujii, M.; Imakita, K. Size-controlled growth of cubic boron phosphide nanocrystals. *RSC Adv.* **2015**, *5*, 8427–8431.

(48) Feng, M.; Zhang, J.; Zhou, H.; Jiang, P.; Zhang, D.; Wang, L.; Chen, S. Facile preparation of boron phosphide particles with high purity and high structural stability. *Mater. Res. Express* **2019**, *6*.

(49) Sugimoto, H.; Somogyi, B.; Nakamura, T.; Zhou, H.; Ichihashi, Y.; Nishiyama, S.; Gali, A.; Fujii, M. Size-dependent photocatalytic activity of cubic boron phosphide nanocrystals in the quantum confinement regime. *J. Phys. Chem. C* **2019**, *123*, 23226–23235.

(50) Sugimoto, H.; Fujii, M. Colloidal Dispersion of Subquarter Micrometer Silicon Spheres for Low-Loss Antenna in Visible Regime. *Adv. Opt. Mater.* **2017**, *5*, 1700332.

(51) Sugimoto, H.; Okazaki, T.; Fujii, M. Mie Resonator Color Inks of Monodispersed and Perfectly Spherical Crystalline Silicon Nanoparticles. *Adv. Opt. Mater.* **2020**, *8*, 2000033.

(52) García de Abajo, F. J. Optical excitations in electron microscopy. *Rev. Mod. Phys.* **2010**, *82*, 209–275.

(53) Colliex, C.; Kociak, M.; Stéphan, O. Electron Energy Loss Spectroscopy imaging of surface plasmons at the nanometer scale. *Ultramicroscopy* **2016**, *162*, A1–A24.

(54) Assadillayev, A.; Hinamoto, T.; Fujii, M.; Sugimoto, H.; Brongersma, M. L.; Raza, S. Plasmon Launching and Scattering by Silicon Nanoparticles. *ACS Photonics* **2021**, *8*, 1582–1591.

(55) Assadillayev, A.; Hinamoto, T.; Fujii, M.; Sugimoto, H.; Raza, S. Thermal near-field tuning of silicon Mie nanoparticles. *Nanophotonics* **2021**, *10*, 4161–4169.

(56) Alexander, D. T.; Flauraud, V.; Demming-Janssen, F. Near-Field Mapping of Photonic Eigenmodes in Patterned Silicon Nanocavities by Electron Energy-Loss Spectroscopy. *ACS Nano* **2021**, *15*, 16501–16514.

(57) Song, J. H.; Raza, S.; van de Groep, J.; Kang, J. H.; Li, Q.; Kik, P. G.; Brongersma, M. L. Nanoelectromechanical modulation of a strongly-coupled plasmonic dimer. *Nat. Commun.* **2021**, *12*, 48.

(58) Raza, S.; Esfandyarpour, M.; Koh, A. L.; Mortensen, N. A.; Brongersma, M. L.; Bozhevolnyi, S. I. Electron energy-loss spectroscopy of branched gap plasmon resonators. *Nat. Commun.* **2016**, *7*, 13790.

(59) Alaee, R.; Rockstuhl, C.; Fernandez-Corbaton, I. An electromagnetic multipole expansion beyond the long-wavelength approximation. *Opt. Commun.* **2018**, *407*, 17–21.

(60) Yang, J.; Hugonin, J. P.; Lalanne, P. Near-to-Far Field Transformations for Radiative and Guided Waves. *ACS Photonics* **2016**, *3*, 395–402.

Paper D

Assadillayev, A., Hinamoto, T., Fujii, M., Sugimoto, H., Raza, S.

Thermal near-field tuning of silicon Mie nanoparticles

Author Contributions

S. R. conceived the experiments and supervised the project. A. A. fabricated the samples, performed the EELS measurements, the image and EELS data analyses, the simulations. T. H., H. S., and M. J. fabricated the silicon nanoparticles. A. A. and S. R. prepared figures and wrote the manuscript. All authors discussed the results and contributed to the preparation of the manuscript.

Research Article

Artyom Assadillayev, Tatsuki Hinamoto, Minoru Fujii, Hiroshi Sugimoto and Søren Raza*

Thermal near-field tuning of silicon Mie nanoparticles

Abstract: Tunable high-refractive-index nanostructures are highly desired for realizing photonic devices with a compact footprint. By harnessing the large thermo-optic effect in silicon, we show reversible and wide thermal tuning of both the far- and near-fields of Mie resonances in isolated silicon nanospheres in the visible range. We perform *in situ* heating in a transmission electron microscope and electron energy-loss spectroscopy to show that the Mie resonances exhibit large spectral shifts upon heating. We leverage the spectral shifts to demonstrate near-field tuning between different Mie resonances. By combining electron energy-loss spectroscopy with energy-dispersive X-ray analysis, we show a reversible and stable operation of single silicon nanospheres up to a temperature of 1073 K. Our results demonstrate that thermal actuation offers dynamic near-field tuning of Mie resonances, which may open up applications in tunable nonlinear optics, Raman scattering, and light emission.

Keywords: electron energy-loss spectroscopy; high-refractive-index nanostructures; Mie resonances; near-field tuning; thermo-optic tuning.

1 Introduction

Dielectric and semiconductor nanostructures are rapidly becoming one of the main constituents in nanoscale optical devices. Due to their high refractive index and low nonradiative losses, they support magnetic and electric multipole Mie resonances on subwavelength scales [1]. Dielectric nanoparticles have been exploited for a number of applications, such as dielectric nanoantennas [2–5], resonant nonlinear optics [6–8], and metasurfaces [9–12]. In most cases, nanoresonators or metasurfaces are operated statically, i.e., the optical response of the system is fixed upon fabrication. However, many applications require tunable optical elements, where the optical response can be controlled with an external stimulus [13, 14]. This has prompted a strong interest in realizing dielectric optical components with a tunable far-field functionality and has led to the successful demonstrations of different tuning mechanisms, including photothermal [15, 16], electromechanical [17, 18], via photocarrier generation [19, 20], coupling to liquid crystals [21–23], using phase change materials [24–26], and through the thermo-optic effect [27, 28]. In this regard, the thermo-optic effect, i.e., the change in the refractive index n with temperature T, is an appealing tuning mechanism as it provides reversible, continuous and large spectral shifts of optical Mie resonances by simply tuning the temperature. Recent work has demonstrated that it is possible to thermally tune the far-field optical response of nanoparticles and metasurfaces made of silicon, germanium, lead telluride [27, 29–32], and hybrid silicon–gold [33]. Silicon is particularly interesting for dynamic thermal tuning due to its combination of high refractive index, complementary metal-oxide-semiconductor (CMOS) compatibility, and high thermo-optic coefficient dn/dT [31]. However, thermal tuning of silicon has so far been limited to nano- and micron-sized structures with resonances in the infrared spectral ranges, where a modest tunability of Mie resonances is observed. Shifting the resonances into the visible is expected to increase the tuning range due to an increased thermo-optic coefficient near the direct bandgap edge of silicon. In

*Corresponding author: **Søren Raza**, Department of Physics, Technical University of Denmark, Fysikvej, DK-2800 Kongens Lyngby, Denmark, E-mail: sraz@dtu.dk. https://orcid.org/0000-0002-0296-7202
Artyom Assadillayev, Department of Physics, Technical University of Denmark, Fysikvej, DK-2800 Kongens Lyngby, Denmark, E-mail: artas@dtu.dk. https://orcid.org/0000-0002-5117-2748
Tatsuki Hinamoto, Minoru Fujii and Hiroshi Sugimoto, Department of Electrical and Electronic Engineering, Kobe University, Rokkodai, Nada, Kobe 657-8501, Japan, E-mail: tatsuki.hinamoto@gmail.com (T. Hinamoto), fujii@eedept.kobe-u.ac.jp (M. Fujii), sugimoto@eedept.kobe-u.ac.jp (H. Sugimoto). https://orcid.org/0000-0001-6607-2574 (T. Hinamoto)

addition, tunable dielectric components have been heavily focused on far-field functionalities with little attention devoted to the near-field. Yet, many important optical processes rely on the properties and enhancement of the near-field, such as nonlinear processes [8, 34], Raman scattering [35–37], and light emission [38–40], and, as such, dynamic tuning of the near-field in high-index nanostructures could open up for new applications in these areas.

Here, we demonstrate reversible and wide thermal tuning of both the far- and near-fields of Mie resonances in isolated silicon nanoparticles in the visible range. We perform *in situ* heating with temperatures reaching 1073 K in a scanning transmission electron microscope (STEM) and map the spatial and spectral changes of the Mie resonances using electron energy loss spectroscopy (EELS). The extreme spatial resolution of EELS along with its capability to characterize both the near- and far-field optical response [41–43] have been exploited to study a variety of optical nanostructures [44–48] and recently also nanodevices [49]. Using *in situ* EELS, we show that the Mie resonances exhibit large spectral shifts upon heating and that the

near-field can be dramatically altered at fixed energies. In particular, we show that we can tune between the near-fields of different Mie resonances. Furthermore, we extend our EELS and STEM measurements with energy-dispersive X-ray (EDX) analysis, which allows us to correlate structural and chemical changes to the near- and far-field optical response. We find that the silicon nanoparticles can be repeatedly heated to temperatures up to 1073 K without any structural, chemical, or optical degradation. Our *in situ* EELS results provide a unique insight into thermal-induced near-field tuning at the scale of individual silicon Mie nanoparticles.

2 Results

2.1 Thermal tuning of Mie resonances

Crystalline silicon nanoparticles with a spherical shape are prepared in a colloidal suspension [5] and deposited on top of commercially available TEM chips [48], which use ceramic elements for heating. Figure 1(a) shows a
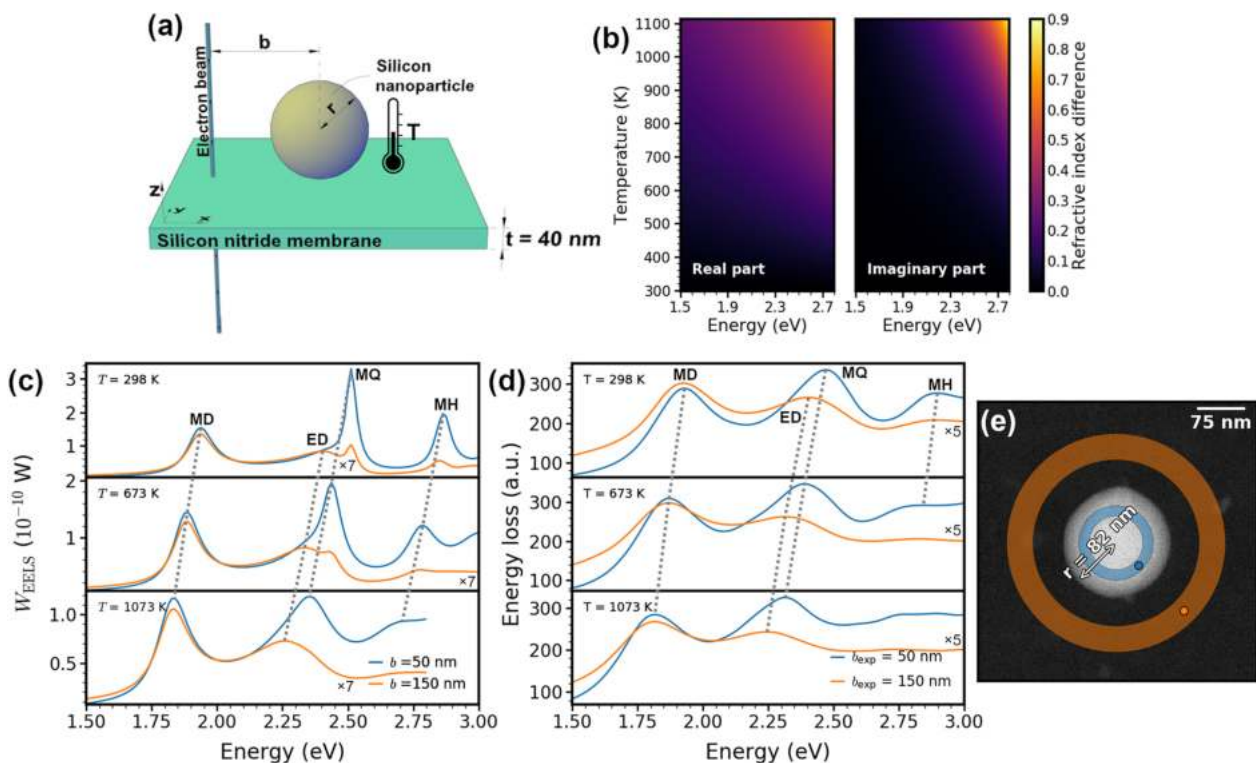
Figure 1: Thermal tuning of Mie resonances in silicon nanoparticles. (a) Schematic of a silicon nanoparticle of radius *r* placed on a silicon nitride membrane and excited by an electron beam. The impact parameter *b* denotes the distance between the electron beam and the center of the nanoparticle. The temperature is applied to the nanoparticle by a ceramic heater located around the nitride membrane. (b) Temperature modulation of the refractive index of silicon. (c) Simulated and (d) experimental EELS spectra of a silicon nanoparticle with a radius $r = 82.4 \pm 1.9$ nm acquired from the electron beam positions shown in (e). (e) STEM image of the nanoparticle, where the colored areas represent the integration regions for the experimental EELS signal, and the colored points are the position of the electron beam in the simulation.

schematic of the resulting structure, where an isolated silicon nanoparticle is on top of a silicon nitride membrane. The ceramic heater is located several micrometers from the nanoparticle (not shown). Upon heating, the refractive index of silicon is modified due to the thermo-optic effect (Figure 1(b)). Silicon has a positive thermo-optic coefficient in the energy region from 1.5 to 3 eV due to the temperature-induced changes in the electronic transitions in silicon [50], which leads to an increase of the real part of the refractive index by up to 0.6 at 1100 K in comparison to room temperature. Silicon also exhibits a negative thermo-optic coefficient for energies higher than the temperature-dependent direct bandgap edge (3.4 eV at room temperature [51]), or a nonnegligible concentration of thermally-generated free carriers [30]. Figure 1(b) also shows the increase in the imaginary part of the refractive index that is mainly due to increased phonon population at elevated temperatures, which results in an increase in the probability of indirect transitions and, hence, to increased light absorption [52]. This effect is most pronounced in the violet part of the spectrum since this is close to the direct bandgap energy of silicon.

We perform EELS characterization both via simulation and experiment of a silicon nanoparticle with a radius $r = 82.4 \pm 1.9$ nm (Figure 1(c) and (d)). The electron beam excites the nanoparticle at the positions indicated in Figure 1(e). These positions are selected based on the fact that the electric dipole (ED) has a larger EELS response outside the particle, while the magnetic quadrupole (MQ) and magnetic hexapole (MH) are predominantly excited inside the particle, halfway to the edge [48]. We observe redshifts of all Mie modes (magnetic dipole (MD), ED, and MQ) in the silicon nanoparticle in both experiment and simulation with increasing temperature. The redshift is due to the increasing real part of the refractive index at elevated temperatures. The MD resonance energy is shifted by 0.1 eV as the temperature is elevated to 1073 K, while the higher-order ED, MQ, and MH modes show larger shifts of around 0.15 eV each. The electric quadrupole (EQ), which is predominantly excited in the middle of the particle [48], has a comparable shift of 0.15 eV (see Supplementary Figure S1). In addition, the thermally-induced increase in the imaginary part of the refractive index of silicon near the direct bandgap edge leads to a significant broadening of the MH mode. Combined with the spectral resolution of the EELS setup, it is not possible to safely identify the MH mode at temperatures above 673 K. The EQ mode behaves similarly (see Supplementary Figure S1).

The analysis of the thermal tuning of Mie resonances is further extended to various particle sizes in Figure 2(a). The
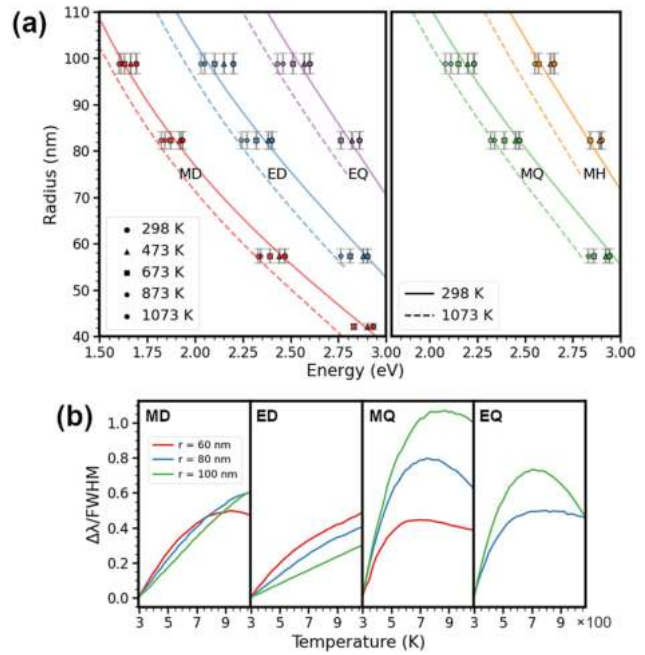
Figure 2: Tunability of Mie resonances. (a) Measured resonance energies as a function of particle radius and temperature for the first five Mie resonances in silicon nanoparticles. The color points represent experimental values, and the color lines show the first maxima of the different Mie scattering coefficients. ED/EQ and MQ/MH resonances are separated into two plots for clarity. (b) Simulated linewidth tunability as a function of temperature for the first four Mie modes supported by silicon nanoparticles with different radii.

change in the first five Mie mode (MD, ED, MQ, EQ, and MH) resonance energies of the nanoparticles with 40–100 nm radii are analyzed experimentally and compared to theoretical predictions. The close match between the theory and experiment for broad nanoparticles size range shows the possibility to thermally tune all nanoparticle Mie modes by up to 0.15 eV when the temperature is increased to 1073 K. The modes which are closer to the red side of the spectrum experience the lower shift of around 0.1 eV. Different spectral shifts as a function of resonances excited are due to nonlinear dependence of the refractive index with energy and temperature. From Figure 1(b), it can be seen that there is a larger change in the real part of the refractive index in comparison to the room temperature at higher energies. This leads to larger spectral shifts at higher energies; consequently, Mie modes with higher resonance energy (e.g., higher-order modes) experience larger spectral shifts.

Due to the mode broadening caused by the increase in the imaginary part of the refractive index and the energy resolution of our EELS setup, some Mie modes located above 2.5 eV at high temperatures cannot be experimentally resolved. In particular, at temperatures above 673 K,

the MD mode disappears for the smallest particle (42 nm radius), the MH and EQ resonances disappear in the middle nanoparticle size region (82 nm radius), while larger particles (99 nm radius) are not affected.

The thermal tunability of the Mie resonances depends on their resonance energy (defined by the particle size) since resonance energies close to the direct bandgap energy of silicon will be subject to both large refractive index changes and increased optical losses at elevated temperatures. In the following, we quantify this effect by using linewidth tunability as a measure for the thermal tunability of the Mie resonances. The linewidth tunability is defined as the spectral shift of the Mie resonance energy at elevated temperatures relative to the room temperature, normalized by the resonance full-width at half-maximum at the elevated temperature (see Methods). A linewidth tunability above one, therefore, corresponds to tuning the resonance energy more than one linewidth. We numerically show the linewidth tunability of the first four Mie modes supported by silicon nanospheres in the 60–100 nm radii range (Figure 2(b)). The MD mode shows a continuous increase by up to 0.6 tuning with the exception of the 60 nm particle, which peaks at 923 K and shows a slight decrease. The ED follows a similar increase trend with larger particles having smaller overall tunability. The higher-order MQ mode shows the largest linewidth tunability, reaching its maximal value at a higher temperature when the particle size is increased (700 K and 0.44 tuning for 60 nm particle, 820 K and 1.07 tuning for 100 nm particle). Increasing the temperature even further leads to a drop in the linewidth tunability due to thermally-induced broadening of the direct bandgap edge in silicon. The EQ tuning shows a similar lineshape with the peak value being approximately 1.5 times smaller. These results demonstrate that even fundamental Mie resonances can be optimized to achieve large thermal tunability with linewidth tunabilities reaching above unity.

2.2 Thermal near-field tuning of silicon Mie modes

A unique feature of *in situ* EELS is that it allows us to track the near-field changes in the EELS maps of the silicon nanoparticles with temperature. Using the characteristic EELS maps for different Mie modes at elevated temperatures (see Supplementary Figure S2), we demonstrate significant tuning of the near-field profiles at an energy of interest. We consider two cases of thermal near-field tuning for two different particle sizes. For a silicon particle with radius $r = 80$ nm, a multipole decomposition of the

EELS spectrum [53] reveals that the main spectral contributions come from the two first azimuthal components $l = 1$ and $l = 2$ (Figure 3(a)). It is worth noting that $l = 1$ ($l = 2$) contains the resonant features of both the MD and ED (MQ and EQ). We fix the energy of interest at 2.4 eV which is the ED resonance energy at room temperature. By increasing the temperature to 1073 K, we can see from the multipole decomposition that the energy crosses the MQ peak. This is accompanied by significant changes in the experimental EELS maps presented in Figure 2(b) and (d). Indeed, we observe that the near field is tuned from the ED mode (at room temperature) to the MQ mode at $T = 1073$ K (see also Supplementary Figure S2 for characteristic maps).

We also perform a multipole decomposition of the EELS spectrum for a smaller nanoparticle with radius $r = 40$ nm in Figure 3(e). For this particle size, the EELS spectrum is dominated by the $l = 1$ contribution at both room temperature and $T = 1073$ K. We fix the energy of interest at 2.91 eV which is the MD resonance energy at the room temperature. By elevating the temperature to 1073 K, the energy of interest is now located in the flat region of the spectrum. Despite no observable peak from the ED in the EELS spectrum, we still observe experimentally that the near field dramatically changes from the MD mode to that characteristic of the ED mode as the temperature is elevated (Figure 3(f)–(h)). Importantly, this serves to show that near-field tuning remains accessible despite weak or lacking spectral features.

2.3 Stability

In situ EELS allows us to track morphological changes of the nanoparticles at elevated temperatures. These changes can be attributed to the possible changes in the nanoparticle size and geometry due to temperature, such as nanoparticle melting. This, combined with the EELS data, can be used to ensure a stable and reversible operation of the silicon nanoparticles when exposed to high temperatures.

We track the changes in the nanoparticle shape and size in Figure 4(a)–(d). The STEM images are taken at time gaps of several minutes between each other to ensure the thermally stable condition of the TEM chip. By careful image analysis, we determine the radius of the particle at different temperatures and find that the particle radius does not change for temperatures up to 1073 K. This demonstrates that there is no observable thermal expansion of the silicon nanoparticle. When the particle temperature increases beyond 1073 K we observe that the particle reshapes and becomes faceted (see Figure 4(d)). We extend this procedure to 31 different nanoparticles of various sizes
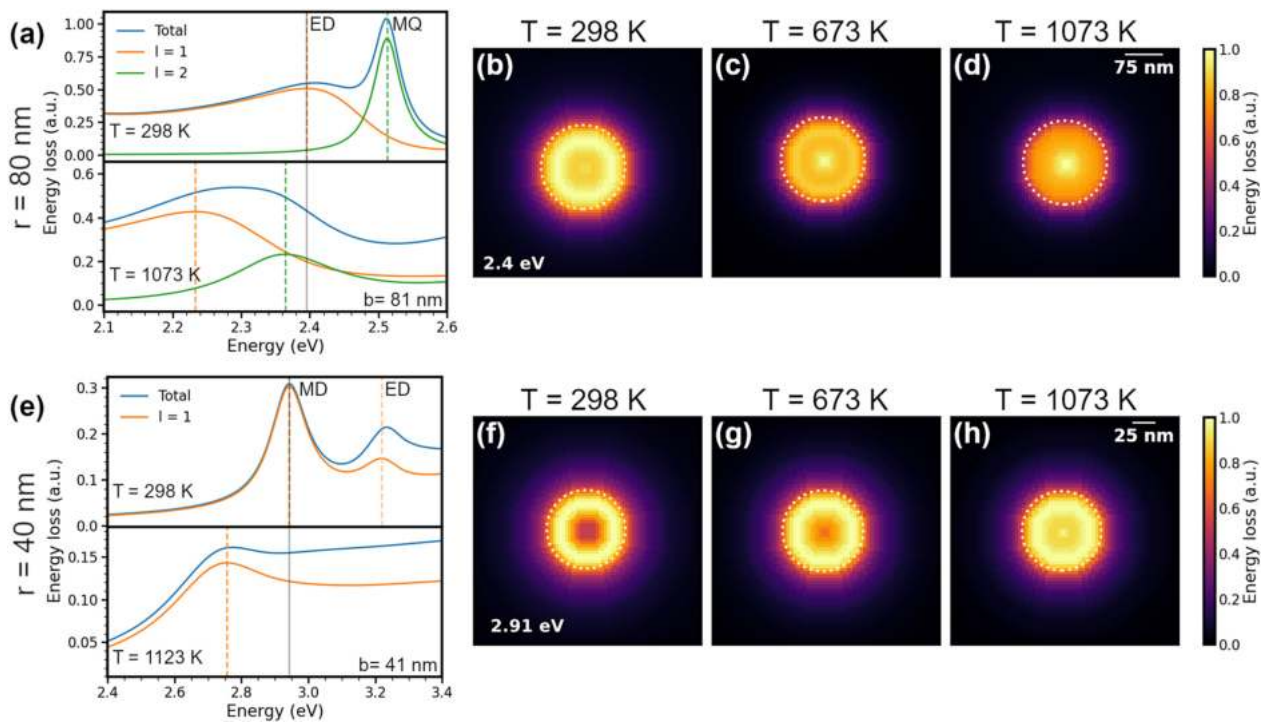
Figure 3: Thermal near-field tuning of silicon Mie modes. (a) Multipole decomposition of the EELS signal into different azimuthal contributions l for a particle with $r = 80$ nm. The decomposition is performed at two temperatures for the impact parameter $b = 81$ nm. (b)−(d) Experimental EELS maps of a particle with $r = 82.4 \pm 1.9$ nm for a fixed energy of 2.4 eV (ED at the room temperature) at different temperatures. (e) Multipole EELS decomposition at two temperatures for a particle with $r = 40$ nm with impact parameter $b = 41$ nm. (f)−(h) Experimental EELS maps of a particle with $r = 42.2 \pm 0.7$ nm for a fixed energy of 2.91 eV (MD at the room temperature) at different temperatures.

(Figure 4(e)). Approximately two-thirds of the particles remain stable up to 1073 K, while the remaining particles reshape approximately 100 K below this temperature. This demonstrates that the majority of the particles can be operated at temperatures up to 1073 K without changes in the nanoparticle morphology. To the best of our knowledge, this marks the highest operating temperature of silicon nanoparticles for thermal actuation but is nonetheless smaller than the crystalline silicon melting point (1688 K). Nanoparticles larger than the 40 nm radii range should not display a size-dependent decrease in their melting temperatures [54]. Although the electron beam is also known to induce heating [55], we can safely dismiss this effect as the cause for the reshaping, since particles that were not imaged by the electron beam during the heating also underwent shape changes. We attribute the lower reshaping temperature to the polycrystallinality and doping of our nanoparticles (see Methods). Grain growth in doped polycrystalline silicon starts at relatively low temperatures (below 1173 K) since doping enhances the self-diffusion of

silicon [56]. In addition, the highly spherical nature of our nanoparticles entails that crystal planes with high Miller indices are present on the surface, which are known to develop into low-index planes upon heating [57]. Indeed, the reported temperatures for grain growth and reconstruction into low-index planes in silicon (near or above 1073 K) are consistent with the shape and facet changes observed in our experiments.

To demonstrate reversible thermal tuning at such high temperatures, we applied four heating and cooling procedures and recorded the EELS spectra before and after the whole process to detect any changes in the EELS response (Figure 4(f)). As can be seen, the nanoparticle remains stable and the Mie modes are not affected by the multiple heating procedures. This shows that the nanoparticles can be operated in the proposed temperature range up to 1073 K without their operation failure. This is further supported by STEM EDX measurements (see Supplementary Figure S3), where we observe no changes in the chemical composition of the particles when they are heated to 1073 K.
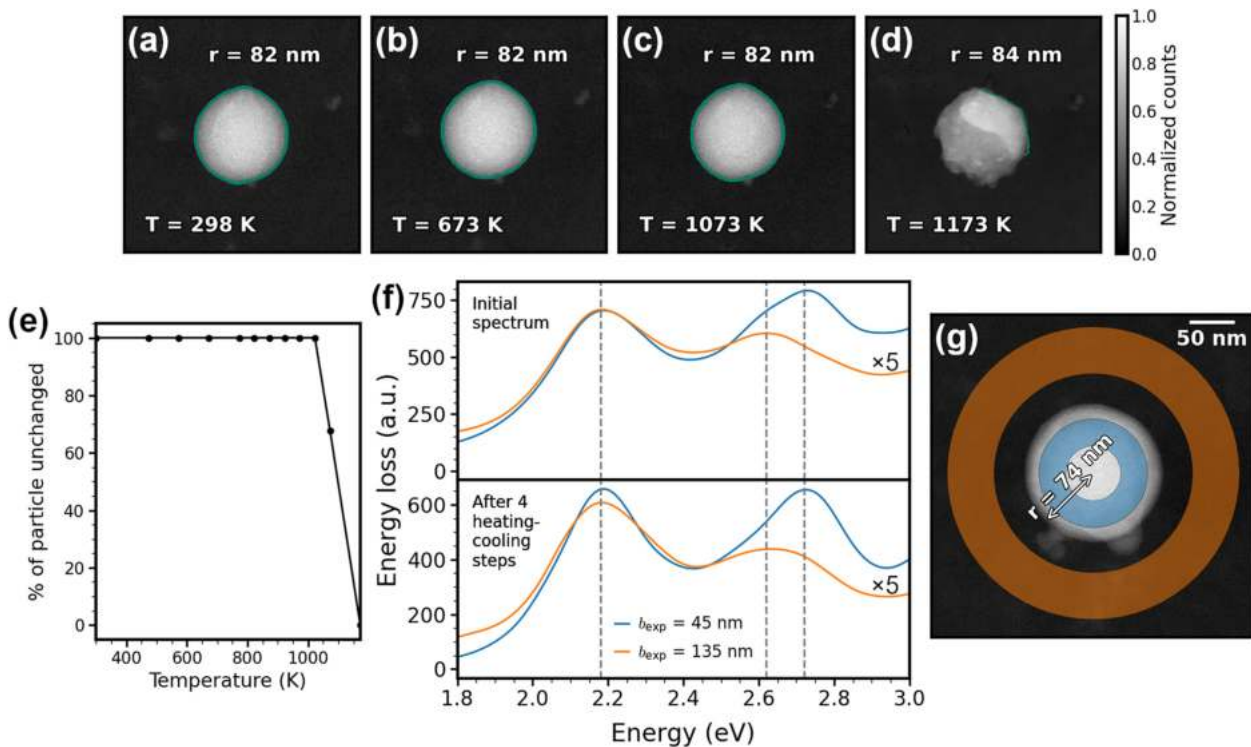
Figure 4: Stability of thermally tuned nanoparticles. (a)–(d) STEM images of a silicon nanoparticle with $r = 82.4 \pm 1.9$ nm at different temperatures. The green selection represents the boundary of the particle. (e) Systematic investigation of morphology changes for 31 different nanoparticles with radii spanning 40–100 nm at elevated temperatures. (f) Experimental EELS spectra of a silicon nanoparticle with a radius $r = 73.8 \pm 2.3$ nm (top) with no heating applied and (bottom) after four heating to 1073 K-cooling to 298 K procedures. The spectra are acquired from the electron beam positions shown in (g). (g) STEM image of the nanoparticle, where the colored areas represent the integration regions for the EELS signal.

3 Conclusions

We have experimentally demonstrated that the Mie modes of silicon nanoparticles in a broad size range can be tuned using the thermo-optic effect. The effect allows tuning the Mie modes of the nanoparticle in the visible spectral range by up 0.15 eV (40 nm). By optimizing the particle size, we show that the MQ mode can be tuned beyond one linewidth, while the MD, ED, and EQ modes offer linewidth tunability ranging from 0.3 to 0.7. The silicon losses at high energies (2.8–3 eV), which ultimately limit further linewidth tunability, can be beneficial for switching applications, i.e., by providing turn on-off functionality.

We leveraged the significant spectral shifts of Mie resonances to demonstrate that near-field profiles of Mie modes can be tuned with temperature and showed that we can effectively switch between two different Mie modes. Despite the lack of spectral peaks for some modes, we still observe significant changes in the near-field profiles. This demonstrates that thermal tuning can be effectively

utilized in applications, where the near-field switching between different Mie modes is desired.

By combining *in situ* STEM imaging and EELS, we show there are no significant changes in the spectral response or morphology for the majority of silicon nanoparticles as they are heated to temperatures up to 1073 K, with all particles being stable up to 973 K. Moreover, EDX analysis reveals no chemical changes in the nanoparticle composition. Therefore, the thermal tuning of the Mie resonance with our silicon nanoparticles can be effectively performed up to 1073 K temperature.

4 Methods

4.1 Fabrication

The crystalline silicon nanoparticles of spherical shape are produced by thermal annealing of silicon suboxide (SiO_x) and extraction into methanol [5]. In optical measurement, it has been shown that the scattering spectrum of the nanoparticle perfectly agrees with the Mie theory [58].

A 10 µL solution of silicon nanoparticles in methanol is dropcasted onto commercially available thermal E-chips produced by Protochips, which are nitrogen dried after a 1 min wait time. The chip has a membrane composed of a ceramic layer on top of a 40 nm thick silicon nitride layer. The ceramic layer is used for heating and can be heated up to 1473 K with a temperature accuracy over 95.5% (example: 1073 ± 48 K) and a 99.5% homogeneous temperature profile across the entire chip. It has nine 8 µm holes where only the nitride layer is present. The STEM imaging and EELS characterization is performed in these areas.

4.2 Image analysis

The sizes of the silicon nanoparticles are determined from the STEM images by a previously reported procedure [48]. Using image processing operations with the Python scikit-image library, a canny filter is applied to the STEM image to find the particle edges. A Hough circle transform is applied on the edge map to find the best fit for the radius and particle center. The uncertainty in the radius is determined by fitting the number of intersections-radius dependence with a bimodal distribution of 2 Gaussians.

4.3 EELS measurements and analysis

The EELS measurements are performed in a monochromated and aberration-corrected FEI Titan operated in STEM mode at an acceleration voltage of 300 kV, providing a probe size of ~ 0.5 nm and an energy resolution of 0.08 eV (as measured by the full-width-at-half-maximum of the zero-loss peak). We perform Richardson–Lucy deconvolution to remove the zero-loss peak. An EELS spectrum obtained in a vacuum is used as an input for the point-spread function. Due to a small asymmetry in the zero-loss peak, the deconvolution algorithm produced an artificial EELS peak in the energy range below 0.6 eV. However, the artificial peak did not overlap with any of the observed resonances and could be safely removed using a first-order logarithmic polynomial.

The depicted EELS spectra are obtained by integrating the deconvoluted EELS data around the experimental impact parameter b_{exp}. For the disk-shaped integration regions, the experimental impact parameter denotes the center of the disk. For the annulus-shaped regions, the experimental impact parameter denotes the mean of the inner and outer radii. The depicted EELS spectra are smoothed with a Gaussian function ($\sigma = 0.03$ eV).

The EELS maps are obtained by summing the deconvoluted EELS data in a spectral window of 0.02 eV width centered at the resonance energies. To improve the signal-to-noise ratio, the map is spatially binned, reducing the effective number of pixels by a factor of 2 in each row and column, i.e., a factor of 4 in total. A Gaussian filter with $\sigma = 0.8$ pixels is applied to smooth the image. Exploiting the spherical symmetry of the nanoparticles, the maps are integrated along the azimuth angle at the coordinates located at the same distance from the nanoparticle center.

4.4 EELS simulations and theory

The EELS simulations are performed in COMSOL Multiphysics, which solves Maxwell's equations using finite-element modeling. We simulate the electron beam as an edge current with an amplitude of 1 µA. The induced electromagnetic field is determined by calculating the fields with and without the silicon nanoparticle in the simulation domain, and subsequently subtracting them. Using the obtained induced electric field, the energy loss can be calculated as the work rate done on the electron beam by the electromagnetic field induced by the optical structure [59]. The temperature-dependent complex refractive index for silicon is taken from Reference [51]. The silicon nitride layer is not included in the simulation since it has negligible influence on the optical properties of Mie resonances throughout the visible spectral range [48].

The multipole decomposition of the EELS spectra is obtained via a multipole expansion of the electromagnetic field produced by an electron exciting a dielectric sphere in a vacuum [53]. The refractive index data is taken from Reference [51], while in Figure 3(e) it is taken from Reference [60]. This is due to a limited energy range of the refractive index data in the former case.

The linewidth tunability $\Delta\lambda$/FWHM of Mie resonances in Figure 2 is calculated from the theoretical EELS spectra of a sphere at a fixed impact parameter $b = 2r$. The theoretical EELS spectra are calculated for separate azimuthal coefficients $l = 1, 2$. Then, they are fitted with two Lorentzian functions, resulting in the parameters for different couples of multipoles (MD and ED for $l = 1$, MQ and EQ for $l = 2$). The resonance wavelength is fixed and is defined as the first maxima of the Mie scattering coefficient for a respective multipole, and the full-width at half-maximum of the Lorentzian is found from the fit. A split Lorentzian function (width of the distribution is different between left and right slopes) is used for the ED mode, while a symmetrical Lorentzian function is used for the rest of the modes. The fit is performed using the python package LMFIT.

References

[1] A. I. Kuznetsov, A. E. Miroshnichenko, M. L. Brongersma, Y. S. Kivshar, and B. Luk'yanchuk, "Optically resonant dielectric nanostructures," *Science*, vol. 354, p. aag2472, 2016.

[2] A. E. Krasnok, A. E. Miroshnichenko, P. A. Belov, and Y. S. Kivshar, "All-dielectric optical nanoantennas," *Opt. Express*, vol. 20, pp. 20599–20604, 2012.

[3] A. E. Krasnok, C. R. Simovski, P. A. Belov, and Y. S. Kivshar, "Superdirective dielectric nanoantennas," *Nanoscale*, vol. 6, pp. 7354−7361, 2014.

[4] T. Feng, W. Zhang, Z. Liang, and Y. Xu, "Unidirectional emission in an all-dielectric nanoantenna," *J. Phys. Condens. Matter*, vol. 30, p. 124002, 2018.

[5] H. Sugimoto and M. Fujii, "Colloidal dispersion of subquarter micrometer silicon spheres for low-loss antenna in visible regime," *Adv. Opt. Mater.*, vol. 5, p. 1700332, 2017.

[6] M. R. Shcherbakov, D. N. Neshev, B. Hopkins, et al., "Enhanced third-harmonic generation in silicon nanoparticles driven by magnetic response," *Nano Lett.*, vol. 14, pp. 6488−6492, 2014.

[7] D. Smirnova, A. I. Smirnov, and Y. S. Kivshar, "Multipolar second-harmonic generation by Mie-resonant dielectric nanoparticles," *Phys. Rev. A*, vol. 97, p. 013807, 2018.

[8] K. Koshelev, S. Kruk, E. Melik-Gaykazyan, et al., "Subwavelength dielectric resonators for nonlinear nanophotonics," *Science*, vol. 367, pp. 288−292, 2020.

[9] P. Moitra, B. A. Slovick, W. li, et al., "Large-scale all-dielectric metamaterial perfect reflectors," *ACS Photonics*, vol. 2, pp. 692−698, 2015.

[10] A. Arbabi, Y. Horie, M. Bagheri, and A. Faraon, "Dielectric metasurfaces for complete control of phase and polarization with subwavelength spatial resolution and high transmission," *Nat. Nanotechnol.*, vol. 10, pp. 937−943, 2015.

[11] M. Khorasaninejad, W. T. Chen, R. C. Devlin, J. Oh, A. Y. Zhu, and F. Capasso, "Metalenses at visible wavelengths: diffraction-limited focusing and subwavelength resolution imaging," *Science*, vol. 352, pp. 1190−1194, 2016.

[12] A. Vaskin, S. Mashhadi, M. Steinert, et al., "Manipulation of magnetic dipole emission from Eu^{3+} with Mie-resonant dielectric metasurfaces," *Nano Lett.*, vol. 19, pp. 1015−1022, 2019.

[13] A. M. Shaltout, V. M. Shalaev, and M. L. Brongersma, "Spatiotemporal light control with active metasurfaces," *Science*, vol. 364, p. eaat3100, 2019.

[14] C. Zou, J. Sautter, F. Setzpfandt, and I. Staude, "Resonant dielectric metasurfaces: active tuning and nonlinear effects," *J. Phys. D Appl. Phys.*, vol. 52, p. 373002, 2019.

[15] G. P. Zograf, M. I. Petrov, D. A. Zuev, et al., "Resonant nonplasmonic nanoparticles for efficient temperature-feedback optical heating," *Nano Lett.*, vol. 17, pp. 2945−2952, 2017.

[16] T. Zhang, Y. Che, K. Chen, et al., "Anapole mediated giant photothermal nonlinearity in nanostructured silicon," *Nat. Commun.*, vol. 11, p. 3027, 2020.

[17] P. Gutruf, C. Zou, W. Withayachumnankul, M. Bhaskaran, S. Sriram, and C. Fumeaux, "Mechanically tunable dielectric resonator metasurfaces at visible frequencies," *ACS Nano*, vol. 10, pp. 133−141, 2015.

[18] A. L. Holsteen, S. Raza, P. Fan, P. G. Kik, and M. L. Brongersma, "Purcell effect for active tuning of light scattering from semiconductor optical antennas," *Science*, vol. 358, pp. 1407−1410, 2017.

[19] K. Lee, J. Son, J. Park, et al., "Linear frequency conversion via sudden merging of meta-atoms in time-variant metasurfaces," *Nat. Photonics*, vol. 12, pp. 765−773, 2018.

[20] J. Xiang, J. Chen, Q. Dai, S. Tie, S. Lan, and A. E. Miroshnichenko, "Modifying Mie resonances and carrier dynamics of silicon nanoparticles by dense electron-hole plasmas," *Phys. Rev. Appl.*, vol. 13, p. 014003, 2020.

[21] J. Sautter, I. Staude, M. Decker, et al., "Active tuning of all-dielectric metasurfaces," *ACS Nano*, vol. 9, pp. 4308−4315, 2015.

[22] M. Parry, A. Komar, B. Hopkins, et al., "Active tuning of high-Q dielectric metasurfaces," *Appl. Phys. Lett.*, vol. 111, p. 053102, 2017.

[23] S. Q. Li, X. Xu, R. Maruthiyodan Veetil, V. Valuckas, R. Paniagua-Domínguez, and A. I. Kuznetsov, "Phase-only transmissive spatial light modulator based on tunable dielectric metasurface," *Science*, vol. 364, pp. 1087−1090, 2019.

[24] Q. Wang, E. T. F. Rogers, B. Gholipour, et al., "Optically reconfigurable metasurfaces and photonic devices based on phase change materials," *Nat. Photonics*, vol. 10, pp. 60−65, 2016.

[25] J. Tian, H. Luo, Y. Yang, et al., "Active control of anapole states by structuring the phase-change alloy Ge$_2$Sb$_2$Te$_5$," *Nat. Commun.*, vol. 10, p. 396, 2019.

[26] Y. Zhang, C. Fowler, J. Liang, et al., "Electrically reconfigurable non-volatile metasurface using low-loss optical phase-change material," *Nat. Nanotechnol.*, vol. 16, pp. 661−666, 2021.

[27] T. Lewi, H. A. Evans, N. A. Butakov, and J. A. Schuller, "Ultrawide thermo-optic tuning of PbTe meta-atoms," *Nano Lett.*, vol. 17, pp. 3940−3945, 2017.

[28] P. Berto, L. Philippet, J. Osmond, et al., "Tunable and free-form planar optics," *Nat. Photonics*, vol. 13, pp. 649−656, 2019.

[29] M. Rahmani, L. Xu, A. E. Miroshnichenko, et al., "Reversible thermal tuning of all-dielectric metasurfaces," *Adv. Funct. Mater.*, vol. 27, p. 1700580, 2017.

[30] T. Lewi, N. A. Butakov, and J. A. Schuller, "Thermal tuning capabilities of semiconductor metasurface resonators," *Nanophotonics*, vol. 8, pp. 331−338, 2019.

[31] T. Lewi, N. A. Butakov, H. A. Evans, et al., "Thermally reconfigurable meta-optics," *IEEE Photon. J.*, vol. 11, pp. 1−16, 2019.

[32] K. Z. Kamali, L. Xu, J. Ward, et al., "Reversible image contrast manipulation with thermally tunable dielectric metasurfaces," *Small*, vol. 15, p. 1805142, 2019.

[33] J. Ward, K. Zangeneh Kamali, L. Xu, G. Zhang, A. E. Miroshnichenko, and M. Rahmani, "High-contrast and reversible scattering switching via hybrid metal-dielectric metasurfaces," *Beilstein J. Nanotechnol.*, vol. 9, pp. 460−467, 2018.

[34] G. Grinblat, H. Zhang, M. P. Nielsen, et al., "Efficient ultrafast all-optical modulation in a nonlinear crystalline gallium phosphide nanodisk at the anapole excitation," *Sci. Adv.*, vol. 6, p. eabb3123, 2020.

[35] M. Caldarola, P. Albella, E. Cortés, et al., "Non-plasmonic nanoantennas for surface enhanced spectroscopies with ultra-low heat conversion," *Nat. Commun.*, vol. 6, p. 7915, 2015.

[36] D. G. Baranov, R. Verre, P. Karpinski, and M. Käll, "Anapole-enhanced intrinsic Raman scattering from silicon nanodisks," *ACS Photonics*, vol. 5, pp. 2730−2736, 2018.

[37] S. Raza and A. Kristensen, "Raman scattering in high-refractive-index nanostructures," *Nanophotonics*, vol. 10, pp. 1197–1209, 2021.

[38] A. F. Cihan, A. G. Curto, S. Raza, P. G. Kik, and M. L. Brongersma, "Silicon Mie resonators for highly directional light emission from monolayer MoS$_2$," *Nat. Photonics*, vol. 12, pp. 284–290, 2018.

[39] S. Liu, A. Vaskin, S. Addamane, et al., "Light-emitting metasurfaces: simultaneous control of spontaneous emission and far-field radiation," *Nano Lett.*, vol. 18, pp. 6906–6914, 2018.

[40] A. Vaskin, J. Bohn, K. E. Chong, et al., "Directional and spectral shaping of light emission with Mie-resonant silicon nanoantenna arrays," *ACS Photonics*, vol. 5, pp. 1359–1364, 2018.

[41] R. F. Egerton, "Electron energy-loss spectroscopy in the TEM," *Rep. Prog. Phys.*, vol. 72, p. 016502, 2009.

[42] F. J. García de Abajo, "Optical excitations in electron microscopy," *Rev. Mod. Phys.*, vol. 82, pp. 210–256, 2010.

[43] C. Colliex, M. Kociak, and O. Stéphan, "Electron energy loss spectroscopy imaging of surface plasmons at the nanometer scale," *Ultramicroscopy*, vol. 162, pp. A1–A24, 2016.

[44] S. Raza, M. Esfandyarpour, A. L. Koh, N. A. Mortensen, M. L. Brongersma, and S. I. Bozhevolnyi, "Electron energy-loss spectroscopy of branched gap plasmon resonators," *Nat. Commun.*, vol. 7, p. 13790, 2016.

[45] E. P. Bellido, G. D. Bernasconi, D. Rossouw, J. Butet, O. J. F. Martin, and G. A. Botton, "Self-similarity of plasmon edge modes on Koch fractal antennas," *ACS Nano*, vol. 11, pp. 11240–11249, 2017.

[46] V. Flauraud, G. D. Bernasconi, J. Butet, D. T. L. Alexander, O. J. F. Martin, and J. Brugger, "Mode coupling in plasmonic heterodimers probed with electron energy loss spectroscopy," *ACS Nano*, vol. 11, pp. 3485–3495, 2017.

[47] D. Kordahl, D. T. Alexander, and C. Dwyer, "Waveguide modes spatially resolved by low-loss STEM-EELS," *Phys. Rev. B*, vol. 103, p. 134109, 2021.

[48] A. Assadillayev, T. Hinamoto, M. Fujii, H. Sugimoto, M. L. Brongersma, and S. Raza, "Plasmon launching and scattering by silicon nanoparticles," *ACS Photonics*, vol. 8, p. 48, 2021.

[49] J. H. Song, S. Raza, J. van de Groep, et al., "Nanoelectro-mechanical modulation of a strongly-coupled plasmonic dimer," *Nat. Commun.*, vol. 12, p. 48, 2021.

[50] P. Lautenschlager, M. Garriga, L. Vina, and M. Cardona, "Temperature dependence of the dielectric function and interband critical points in silicon," *Phys. Rev. B*, vol. 36, p. 4821, 1987.

[51] G. E. Jellison, J. Modine, and F. A. Modine, "Optical functions of silicon at elevated temperatures," *J. Appl. Phys.*, vol. 76, pp. 3758–3761, 1994.

[52] G. E. Jellison, Jr and F. A. Modine, "Optical absorption of silicon between 1.6 and 4.7 eV at elevated temperatures," *Appl. Phys. Lett.*, vol. 41, p. 180, 1982.

[53] F. J. García de Abajo, "Relativistic energy loss and induced photon emission in the interaction of a dielectric sphere with an external electron beam," *Phys. Rev. B*, vol. 59, pp. 3095–3107, 1999.

[54] I. V. Talyzin, M. V. Samsonov, V. M. Samsonov, M. Y. Pushkar, and V. V. Dronnikov, "Size dependence of the melting point of silicon nanoparticles: molecular dynamics and thermodynamic simulation," *Semiconductors*, vol. 53, pp. 947–953, 2019.

[55] M. A. Asoro, D. Kovar, and P. J. Ferreira, "In situ transmission electron microscopy observations of sublimation in silver nanoparticles," *ACS Nano*, vol. 7, pp. 7844–7852, 2013.

[56] Y. Wada and S. Nishimatsu, "Grain growth mechanism of heavily phosphorus-implanted polycrystalline silicon," *J. Electrochem. Soc.*, vol. 125, p. 1499, 1978.

[57] T. Tsong, D. Feng, and H. Liu, "Atomic structures in reconstruction of high index surfaces of silicon," *Surf. Sci.*, vol. 199, pp. 421–438, 1988.

[58] H. Sugimoto, T. Hinamoto, and M. Fujii, "Forward to backward scattering ratio of dielectric–metal heterodimer suspended in almost free-space," *Adv. Opt. Mater.*, vol. 7, p. 1900591, 2019.

[59] A. L. Koh, A. I. Fernández-Domínguez, D. W. McComb, S. A. Maier, and J. K. W. Yang, "High-resolution mapping of electron-beam-excited plasmon modes in lithographically defined gold nanostructures," *Nano Lett.*, vol. 11, pp. 1323–1330, 2011.

[60] J. Šik, J. Hora, and J. Humlíček, "Optical functions of silicon at high temperatures," *J. Appl. Phys.*, vol. 84, pp. 6291–6298, 1998.

Research Article

Artyom Assadillayev, Tatsuki Hinamoto, Minoru Fujii, Hiroshi Sugimoto, and Søren Raza*

Supplementary Materials: Thermal near-field tuning of silicon Mie nanoparticles
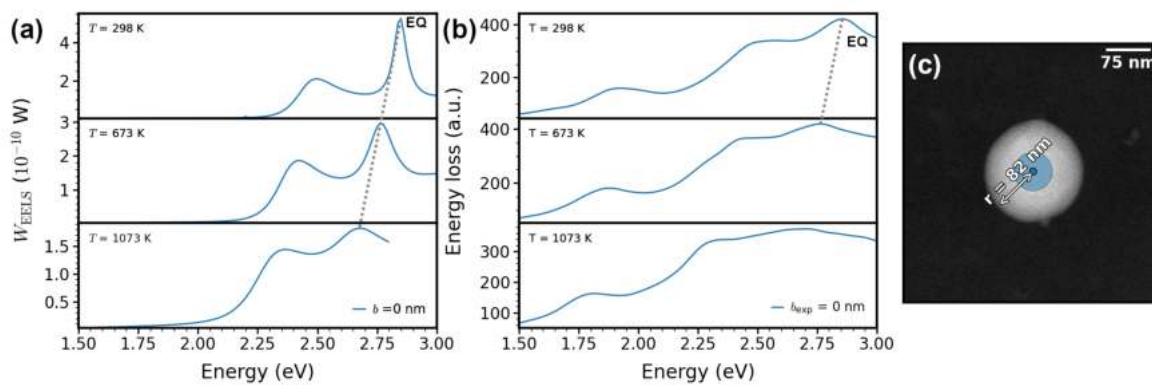
Supplementary Fig. S1: Thermal tuning of the EQ Mie resonance in a silicon nanoparticle (c) Simulated and (d) experimental EELS spectra of a silicon nanoparticle with a radius $r = 82.4 \pm 1.9$ nm acquired from the electron beam positions shown in (e). (e) STEM image of the nanoparticle, where the colored area represents the integration region for the experimental EELS signal, and the colored point is the position of the electron beam in the simulation.

Artyom Assadillayev, Søren Raza, Department of Physics, Technical University of Denmark, Fysikvej, DK-2800 Kongens Lyngby, Denmark, e-mail: artas@dtu.dk (A. Assadillayev), sraz@dtu.dk (S. Raza)
Tatsuki Hinamoto, Minoru Fujii, Hiroshi Sugimoto, Department of Electrical and Electronic Engineering, Kobe University, Rokkodai, Nada, Kobe 657-8501, Japan, e-mail: tatsuki.hinamoto@gmail.com (T. Hinamoto), fujii@eedept.kobe-u.ac.jp (M. Fujii), sugimoto@eedept.kobe-u.ac.jp (H. Sugimoto)
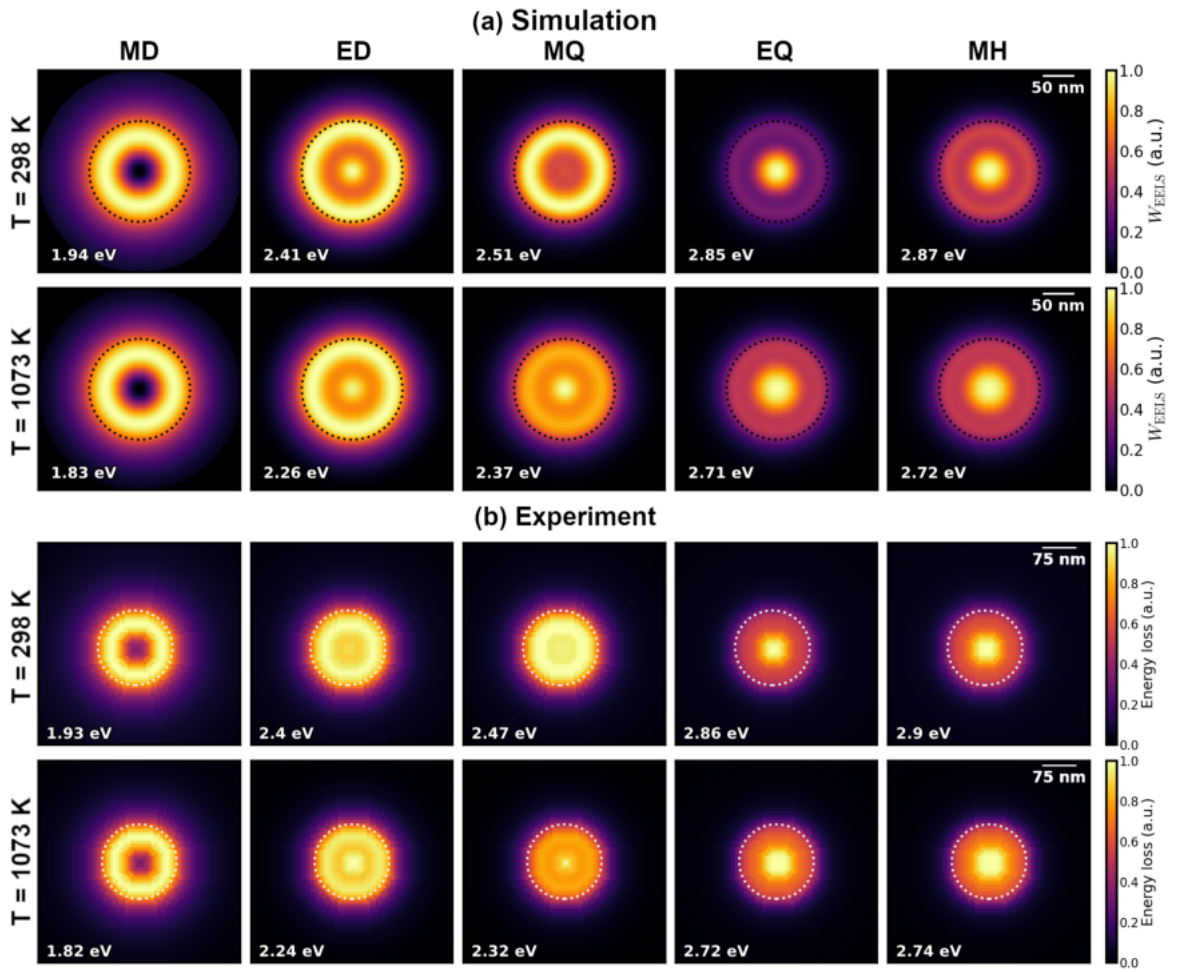
Supplementary Fig. S2: EELS mapping of a silicon nanoparticle Mie modes at different temperatures. (a) Simulated EELS maps of a silicon nanoparticle with a radius $r = 80$ nm at different temperatures (rows) and different Mie resonances (columns). (b) Experimental EELS maps of a silicon nanoparticle with a radius $r = 82.4 \pm 1.9$ nm at different temperatures (rows) and different Mie resonances (columns). Spherical symmetry of the nanoparticle is used in the experiment to obtain high signal-to-noise ratio images, where we azimuthally integrate the experimental spectrum and show it as a 2D map for an easy comparison with the simulated maps. Simulations and experiments closely follow each other, however, there are some differences caused by the energy resolution of the EELS setup, which influences the experimental field profiles of spectrally-close Mie modes. The experimental EELS maps are acquired in a ± 0.01 eV energy window centered around the Mie resonance energy. Note that, as stated in the manuscript, the EQ and MH resonance energies at $T = 1073$ K can not be resolved in the experimental spectra due to thermal-induced damping of the modes. Hence, we assume that the EQ and MH modes undergo the same thermally-induced spectral shift as seen in the simulations and depict the experimental EELS signal at the energies 2.72 eV and 2.74 eV, respectively.
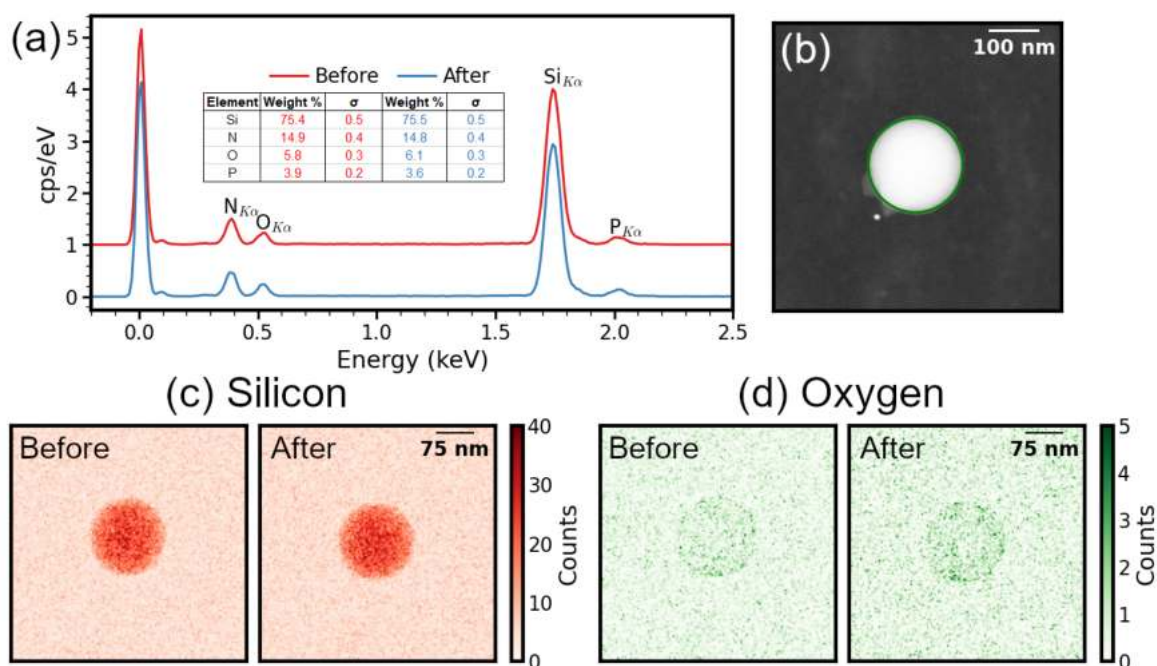
Supplementary Fig. S3: STEM EDX analysis of a silicon nanoparticle. (a) EDX spectra before the heating to 1073 K and after the cooling to 298 K obtained in the region indicated in (b). Note, that the top spectral line is shifted by one unit for clarity. (b) STEM image of the nanoparticle, where the green circular region represents the integration region for the EDX signal. (c-d) EDX mapping of (c) silicon and (d) oxygen before the heating and after the cooling. From both, spectral and mapping EDX data, it can be concluded that there is no significant modification in the chemical composition of the particle after its heating to 1073 K.

Technical
University of
Denmark

Fysikvej, Building 311
2800 Kgs. Lyngby
Tlf. 4525 1700

fysik.dtu.dk